



TECHNISCHE
UNIVERSITÄT
WIEN

DISSERTATION

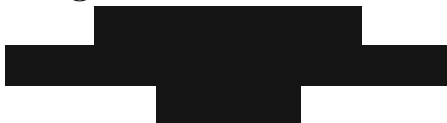
Classical and Quantum Waves in Complex Environments

Ausgeführt zum Zwecke der Erlangung des akademischen Grades eines
Doktors der technischen Wissenschaften

unter der Leitung von
Univ.Prof. Dipl.-Ing. Dr.techn. Stefan Rotter
Institut für Theoretische Physik, E136

eingereicht an der
Technischen Universität Wien
Fakultät für Physik

von
Dipl.-Ing. Lukas Michael Rachbauer



Wien, am 11.01.2024

Unterschrift

Erklärung zur Verfassung der Arbeit

Dipl.-Ing. Lukas Michael Rachbauer
Landstraßer Hauptstraße 48/2/5
1030 Wien

Hiermit erkläre ich, dass ich diese Arbeit selbständig verfasst habe, dass ich die verwendeten Quellen und Hilfsmittel vollständig angegeben habe und dass ich die Stellen der Arbeit (einschließlich Abbildungen und Tabellen), die anderen Werken oder dem Internet im Wortlaut oder dem Sinn nach entnommen sind, auf jeden Fall unter Angabe der jeweiligen Quelle als Entlehnung kenntlich gemacht habe.

Wien, am 11.01.2024

Unterschrift

Deutsche Kurzfassung

In der vorliegenden Dissertationsarbeit werden verschiedenste Themengebiete behandelt, die alle unter „Wellenpropagation in komplexen Umgebungen“ subsumiert werden können.

Zunächst werden die Streutheorie in der klassischen Optik sowie die Grundlagen der Quantenoptik rekapituliert, bevor das Streuverhalten von quantenmechanischen Lichtzuständen durch komplexe lineare klassische Medien beschrieben wird, was rein mithilfe der klassischen Streumatrix möglich ist. Dieser Formalismus legt den Grundstein zur wichtigsten Kerngröße der Arbeit: dem Quanten-Wigner-Smith (QWS) Operator. Er stellt die quantenmechanische Verallgemeinerung der zuvor bekannten klassischen generalisierten Wigner-Smith-Matrix dar. Mit dem QWS-Operator lassen sich verallgemeinerte Kräfte (Impulsübertrag, Drehimpulsübertrag, Druck) beschreiben, die Quantenlicht auf klassische Zielobjekte ausübt. Dabei werden nicht nur die Quanteneigenschaften des Lichtes, sondern zugleich auch seine räumliche Struktur berücksichtigt. Die einzige physikalische Größe, die man zum Aufstellen des QWS-Operators benötigt, ist die klassische Streumatrix, die experimentell im Fernfeld messbar ist, sowie ihre Abhängigkeit vom entsprechenden lokalen Parameter. Daraus lässt sich auf den Effekt von Quantenlicht im Nahfeld (in der Nähe des Zielobjektes) schließen. Der entwickelte Formalismus erlaubt es, quantenmechanische Lichtzustände zu identifizieren, die eine optimale Wirkung (möglichst große Kraft, möglichst geringe Kraft, möglichst wenig Quantenrauschen in der Kraft) auf das Zielobjekt haben. Befindet sich das Lichtfeld im Vakuumzustand, so liefert der Formalismus auf natürliche Weise die Vakuumbeiträge zu den Kräften, die auch als Casimir-Kräfte bekannt sind.

Eine weitere Anwendung des QWS-Operators besteht in der Quanten-Metrologie. Für reine Zustände ist die Varianz des QWS-Operators proportional zur Quanten-Fisher-Information (QFI), die wiederum Auskunft darüber gibt, wie präzise ein Parameter des Streusystems (z.B. die Position eines Streuers oder seine Orientierung) gemessen werden kann. Die Optimierung der QFI bestimmt — selbst in komplexen, offenen Streusystemen — wie die räumliche Struktur und die Quantenfreiheitsgrade des Lichtes gestaltet sein müssen, um die physikalisch bestmögliche Messgenauigkeit zu erreichen.

Für klassisches, kohärentes Licht kann sogar ein räumlicher Fluss von Fisher-Information definiert werden. Dieser erfüllt eine Kontinuitätsgleichung, d.h. die Quellen und Senken der Fisher-Information sind eindeutig identifizierbar, und abseits davon ist die Fisher-Information eine Erhaltungsgröße, die durch die Propaga-

tion des Lichtes durch ein stark streuendes Medium weder verringert noch erhöht wird.

Abseits von der Schätzung kontinuierlicher Parameter werden klassische, kohärente Lichtzustände identifiziert, die mit minimaler Fehlerwahrscheinlichkeit unterscheiden können, in welchem von zwei möglichen Konfigurationen sich das Streumedium befindet. Das ermöglicht es zum Beispiel, im Streusystem eingelagerte Elemente mit äußerst geringer Lichtintensität zuverlässig zu erkennen.

Darüber hinaus wird die Propagation von Ultraschallwellen durch komplexe Medien (wie z.B. menschliches Gewebe) untersucht. Auf Basis theoretischer Überlegungen werden neue nicht-invasive Methoden vorgeschlagen, die die Identifikation und Lokalisierung von bestimmten Strukturen (z.B. Einlagerungen) ermöglichen, die tiefer unter der Oberfläche (Haut) liegen, als es mit bisherigen Methoden möglich war. Die Prozedur wird im Rahmen von Experimenten an Modellsystemen überprüft.

Nicht zuletzt werden Projekte im Bereich des maschinellen Lernens vorgestellt, die der Autor dieser Dissertation im Rahmen seines Doktoratsstudiums betreut hat. Drei der Projekte befassen sich mit Problemen, die bei der Propagation von Wellen in komplexen Medien auftauchen und mithilfe künstlicher neuronaler Netzwerke zufriedenstellend gelöst werden können. In einem weiteren Projekt werden Machine-Learning-Methoden zum bestmöglichen Schätzen von Parametern benutzt, die sich auf klassische Objekte beziehen, die sich hinter einem stark streuenden Diffuser befinden. Das abschließend dargestellte Projekt untersucht — inspiriert durch den räumlichen Fisher-Informations-Fluss, der von elektromagnetischen Wellen getragen wird — wie sich Information durch künstliche neuronale Netzwerke ausbreitet und wie die dadurch gewonnenen Einsichten verwendet werden können, um solche Netzwerke effizienter trainieren zu können.

Das vereinheitlichende Rahmenwerk, welches in der vorliegenden Dissertation vorgestellt wird, bringt verschiedene Perspektiven in Einklang und schlägt so eine Brücke zwischen verschiedenen Gebieten der Wellenphysik, die bisher vergleichsweise separat betrachtet wurden. Dazu zählen der Streumatrix-Formalismus, Wellenkontrolle, Mikromanipulation, bildgebende Verfahren, Quantenoptik, Quantenmetrologie und Vakuumphysik.

Abstract

This dissertation deals with a wide variety of topics, all of which can be subsumed under “wave propagation in complex environments”.

At first, the scattering theory in classical optics and the basics of quantum optics are recapitulated before the scattering behaviour of quantum light states through complex linear classical media is described, which requires the knowledge of only the classical scattering matrix. This formalism lays the foundation for the essential quantity of the work: the quantum Wigner-Smith (QWS) operator. It represents the quantum version of the previously known classical generalized Wigner-Smith matrix. The QWS operator can be used to describe generalized forces (momentum transfer, angular momentum transfer, pressure) that quantum light exerts on classical target objects. Not only are the quantum properties of the light taken into account, but at the same time also its spatial structure. The only physical quantity needed to establish the QWS operator is the classical scattering matrix, which can be measured experimentally in the far field, and its dependence on the corresponding local parameter. From this, the effect of quantum light in the near field (in the vicinity of the target object) can be inferred. The formalism developed makes it possible to identify quantum light states that have an optimal effect (the greatest possible force, the least possible force, the least possible quantum noise in the force) on the target object. If the light field is in the vacuum state, the formalism naturally provides the vacuum contributions to the forces, also known as Casimir forces.

The QWS operator has another application in quantum metrology. For pure states, the variance of the QWS operator is proportional to the quantum Fisher information (QFI), which in turn provides information on how precisely a parameter of the scattering system (e.g., the position of a scatterer or its orientation) can be measured. The optimization of the QFI determines — even in complex, open scattering systems — how the spatial structure and the quantum degrees of freedom of the employed light must be designed in order to achieve the physically best possible measurement precision.

For classical coherent light, even a spatial flow of Fisher information can be defined. It satisfies a continuity equation, i.e., the sources and sinks of Fisher information are uniquely identifiable. Away from the sources and sinks, Fisher information is a conserved quantity that is neither reduced nor increased by the propagation of light through a strongly scattering medium.

Aside from the estimation of continuous parameters, classical coherent light states

are identified that can distinguish with minimal error probability, which of two possible configurations is realized by the scattering medium. This makes it possible, for example, to reliably detect elements embedded within a scattering system with extremely low light intensity.

Furthermore, the propagation of ultrasound waves through complex media (such as human tissue) is investigated. Based on theoretical considerations, new non-invasive methods are proposed that enable the identification and localization of certain structures (e.g., deposits) that lie deeper beneath the surface (skin) than was possible with previous methods. The procedure is tested in experiments on model systems.

Last but not least, projects in the field of machine learning are presented, which the author of this dissertation supervised during his doctoral studies. Three of the projects deal with problems that arise in the propagation of waves in complex media and can be solved satisfactorily with the help of artificial neural networks. In another project, machine learning methods are used to optimally estimate parameters related to classical objects located behind a strongly scattering diffuser. The final project presented investigates — inspired by the spatial flow of Fisher information carried by electromagnetic waves — how information propagates through artificial neural networks and how the insights gained can be used to train such networks more efficiently.

The unifying framework presented in this dissertation brings different perspectives into alignment and thus builds a bridge between different areas of wave physics that were previously considered comparatively separately. These include the scattering matrix formalism, wave control, micromanipulation, imaging techniques, quantum optics, quantum metrology and vacuum physics.

Contents

Deutsche Kurzfassung	v
Abstract	vii
List of Acronyms	xiii
Introduction	1
1 Scattering Theory	5
1.1 Scattering in Classical Optics	5
1.1.1 Classical Scattering Matrix	5
1.1.2 Electromagnetic Waveguide	6
1.2 Fundamentals of Quantum Optics	10
1.2.1 Quantization of the Electromagnetic Field	11
1.2.2 Coherent States	13
1.2.3 Squeezed States	13
1.2.4 Fock States and Photon Number States	15
1.3 Scattering in Quantum Optics	17
2 Micromanipulation	21
2.1 Classical Optical Micromanipulation	21
2.2 Quantum Optical Micromanipulation	27
2.2.1 The Quantum Wigner-Smith Operator in General	27
2.2.2 The QWS Operator for Passive Linear Systems	29
2.2.3 Optimal Micromanipulation	30
2.3 Vacuum Forces	36
3 Metrology	43
3.1 Classical Fisher Information	43
3.2 Quantum Fisher Information	45
3.3 Unitary Quantum Metrology	48
3.3.1 Coherent Probe States	49
3.3.2 Squeezed Probe States	50

3.3.3	Photon Number Probe States	52
3.3.4	Optimal POVM	53
3.4	Subunitary Quantum Metrology	55
3.4.1	Coherent Probe States	56
3.4.2	Squeezed Probe States	57
3.4.3	Photon Number Probe States	59
3.5	Coherent Quantum Fisher Information Flow	65
3.6	Coherent Discrimination	70
4	Imaging	75
4.1	Confocal Imaging	75
4.2	Fingerprint Imaging	82
5	Machine Learning	89
5.1	Two-Dimensional Inverse Scattering	89
5.2	Design of Refractive Index for Constant-Intensity Waves	93
5.3	Completing Classical Scattering Matrices for Micromanipulation	97
5.4	Artificial Neural Networks as Efficient Estimators	98
5.5	Fisher Information Flow Through Artificial Neural Networks	104
	Conclusions and Outlook	107
A	Expectation Values for Gaussian States	111
B	QWS Operator in Terms of the GWS Matrix	117
B.1	First Lemma	117
B.2	Second Lemma	117
B.3	The Proof	119
C	Variance of the QWS Operator for Gaussian States	121
D	QFI of Coherent States	125
E	General Reduced Photon Number States	127
F	QFI of Reduced Pure States	131
G	Multi-Photon GWS and FI Matrix	133
G.1	Multi-Photon GWS Matrix	133
G.2	Multi-Photon FI Matrix	135
	Acknowledgements	139
	References	141

List of Publications	159
Curriculum Vitae	161

List of Acronyms

ANN	Artificial Neural Network
CI	Constant-Intensity
CNN	Convolutional Neural Network
CRLB	Cramér-Rao Lower Bound
DL	Deep Learning
FCNN	Fully Connected Neural Network
FI	(Classical) Fisher Information
GWS	Generalized Wigner-Smith
HL	Heisenberg Limit
ICA	Independent Component Analysis
LFI	Linear Fisher Information
LSTM	Long Short-Term Memory
ML	Machine Learning
MLE	Maximum Likelihood Estimator
MSE	Mean Squared Error
NA	Numerical Aperture
PCA	Principal Component Analysis
POVM	Positive Operator-Valued Measure
QFI	Quantum Fisher Information
QWS	Quantum Wigner-Smith
RIM	Reflection Invariant Mode
SIM	Scattering Invariant Mode
SLD	Symmetric Logarithmic Derivative
SOP	Speed Of Propagation
SQL	Standard Quantum Limit

Introduction

Waves are an omnipresent phenomenon in the physical world we live in. This includes manifestations common in everyday life like water waves, sound and light, but also less familiar forms like seismic¹, gravitational and quantum matter waves. A wave is a delocalized phenomenon that propagates freely through homogeneous media and undergoes scattering in inhomogeneous media. A wave is able to superimpose with itself, leading to intricate spatial interference patterns, especially in disordered environments [1, 2]. At first sight, those patterns might seem random, offering no possibility of leveraging their structure for targeted purposes. However, research pushed the boundaries for controlling and utilizing multiple scattering of waves in complex media.

In optics, one of the first applications going in that direction was adaptive optics used for astronomical observations [3]. With the aid of a known guide star, one can correct for distortions in the wavefront caused by turbulences in the atmosphere. A real milestone in the field was the insight that light can be focused behind a strongly scattering slab without the need for a guide star, but by using optimization techniques instead [4]. For more advanced tasks, such as the transmission of images across turbid media [5], the disordered medium first needs to be characterized by its scattering matrix which connects the in- to the outgoing light fields [6–8]. The experimental feasibility of measuring scattering matrices of optical systems opened up a wide range of possibilities for tailoring light states and light-matter interactions as required [9–11]. Recently, this led to several practical applications like focusing light in a complex environment [12–14], trapping and levitating microscopic objects with light [15–17], exerting specific optical forces and torques onto microscopic particles [18–20], measuring physical properties of targets by means of their interaction with light [21–23], imaging through complex media [9, 24, 25] and generating waves with special spatial structures, including particle-like patterns [26, 27] and branched flow [28].

Apart from wavefront shaping, which is primarily concerned with the spatial structure of light waves and their control, vast progress has also been made in the domain of quantum optics, which deals with the quantum character of light and how to make it exploitable in practice. Several accomplishments have been made in this field, including cooling optically trapped particles down into their quantum ground states [29–31], obtaining squeezed light from micromechanical resonators [32] and

¹Austria shows only a moderate seismic activity.

tailoring the quantum parameters of light fields to achieve exceeding sensitivity for precision measurements in laser optics [33], biological microrheology [34] and gravitational wave detection [35], to provide a few examples. Furthermore, also the field of imaging has benefited from the advances accomplished in quantum optics [36–38].

The developments in these two research directions, namely classical wavefront shaping and quantum state engineering, have, until very recently, been largely disconnected from each other. This separation is all the more surprising since the areas of applications overlap significantly as can be seen from the two preceding paragraphs. In the last decade, several works have appeared with the clear intention of bridging the gap between the exciting advances that have been made in the respective communities. Notable results are here, e.g., the precompensation of multiple photon scattering in complex media [39, 40], the spatial modulation of entangled photon pairs for tailoring high-dimensional quantum entanglement [41] and the combination of the phase sensitivity of NOON states with the orbital angular momentum of photons [42]. The controlled propagation of single-photon states through complex media [43–45] has meanwhile also been extended to the programmable propagation of two-photon states through multi-mode fibers for advanced quantum information processing [39, 46]. Further results in this vein include the distillation of quantum images [47], the real-time shaping of entangled photons using classical light [48] and the successful unscrambling of entanglement through a complex medium [49].

In this thesis, we identify and match concepts that are central both to wave control in complex media and to quantum metrology. For the former, this concept is known as the generalized Wigner-Smith matrix [14, 20], whereas for the latter, the relevant concept is the generator of parameter translations [50, 51]. We can thereby provide a unified picture that portrays those two aspects as two mutually beneficial sides of a single coin. The wave front shaping community can learn how to include the quantum parameters of light in their protocols. The quantum metrology community, on the other hand, can transfer and apply their knowledge to multi-mode complex scattering systems. As it turns out, the insights gained from the combination of the spatial and the quantum degrees of freedom of light are also useful for yet another community, namely the one dealing with vacuum forces [52–54].

When it comes to imaging in biological specimen, employing ultrasound waves may be preferred over optical techniques due to low equipment costs, easy portability and an increased imaging depth, which, however, comes at the price of a compromised resolution [55, 56]. Ultrasound imaging is both a well-established approach [56–58] and an active field of research [59–61]. The scattering matrix, concisely encoding the scattering behaviour of the object under study, turns out to be a valuable tool not only for optical imaging, but also for ultrasound imaging [62–64]. In this work, we present a novel imaging modality in line with this spirit of

utilizing the measured scattering matrix. This method is inspired by a discretized version of the previously mentioned generalized Wigner-Smith matrix. It allows the identification and location of specific, pre-characterized targets inside inhomogeneous samples. Special beamshaping is not required since the image is computed in post-processing.

Due to its deterministic complexity, wave propagation in disordered media is predestined to be treated with machine learning methods. Deep learning has successfully been employed for wavefront shaping [65], optical imaging [66–69], ultrasound imaging [70, 71], three-dimensional localization microscopy [72, 73] and the inverse design of nanophotonic structures [74–77]. Conversely, the propagation of light has been utilized to implement high-speed, energy-efficient optical neural networks as opposed to electronic-based hardware [78–80]. The vital nonlinearities in optical neural networks can be realized, e.g., by programmable electro-optic architectures [81], integrated Kerr microcomb sources [82] or multiple scattering in a reverberating cavity [83]. Methods for training optical neural networks in situ have also been devised [84–86]. In the corresponding chapter of this thesis, we put our focus mainly on the usage of artificial neural networks to solve problems appearing in wave scattering. In addition, we will also study the inner workings of such networks with tools inspired by wave propagation in disordered media.

It is evident that the various research topics mentioned above are closely interconnected. This dissertation aims to make a contribution to the mutually enriching network of these areas.

This thesis is organized as follows: Chapter 1 summarizes the scattering of classical and quantum light through linear media. In Sec. 1.1, classical scattering in a waveguide, the system of choice, is explained and the classical scattering matrix is introduced. After portraying the fundamentals of quantum optics and the used quantum states of light in Sec. 1.2, it is shown in Sec. 1.3 how such quantum states of light scatter through linear media.

Chapter 2 deals with micromanipulation. After describing the known case of classical light in Sec. 2.1, the case of quantum light is elaborated in Sec. 2.2, where also a key quantity of this thesis, namely the quantum Wigner-Smith operator, is introduced. In Sec. 2.3, the vacuum contributions to the optical forces are considered.

Chapter 3 covers all contributions related to metrology. After explaining the notions of classical Fisher information and quantum Fisher information in Secs. 3.1 and 3.2, optical metrology for unitary and subunitary systems is discussed in Secs. 3.3 and 3.4, respectively. For classical states of light, the spatial propagation of Fisher information is formulated in Sec. 3.5. In Sec. 3.6, classical states that perform optimally in binary decision problems are identified.

Chapter 4 deals with imaging methods based on the reflection matrix of the system under study. Confocal imaging, an established procedure, is formulated using the reflection matrix in Sec. 4.1. A novel target-specific matrix imaging

method is explained in Sec. 4.2.

Chapter 5 encompasses the projects related to machine learning. The author of this thesis supervised diverse student projects using artificial neural networks to solve problems in wave scattering. These projects are outlined in Secs. 5.1, 5.2 and 5.3. In Sec. 5.4, we demonstrate that artificial neural networks can serve as nearly efficient estimators when estimating the position of a target from a single speckle image that emerges behind a dynamically changing scattering layer. In Sec. 5.5, we take up the idea of spatial Fisher information flow and transfer it to artificial neural networks.

The [conclusion](#) provides a wrap-up of the different topics and projects covered by this thesis. The appendices [A–G](#) contain technical details.

Chapter 1

Scattering Theory

1.1 Scattering in Classical Optics

We start out by reviewing how the scattering of light can be formalized in classical optics. By “classical” light we mean — in the language of quantum optics — coherent states of light (see Subsec. 1.2.2). If there are $N \in \mathbb{N}$ channels for propagation (throughout this thesis, we use the words “channel” and “mode” interchangeably), then classical light can be described by N coherent amplitudes $\alpha_m \in \mathbb{C}$, one for each channel, or — more conveniently — by the vector $\boldsymbol{\alpha} \in \mathbb{C}^N$. The energy flux of the coherent state $\boldsymbol{\alpha}$ is given by $\|\boldsymbol{\alpha}\|^2$. In an experiment, a detector typically measures the number of photons hitting the camera surface, which corresponds to the integrated energy flux [10]. For this reason we will call $\|\boldsymbol{\alpha}\|^2$ the intensity of the coherent state $\boldsymbol{\alpha}$.

1.1.1 Classical Scattering Matrix

In general, we describe the scattering of light in the following framework: We distinguish the far field from the near field, see also Fig. 1.1. The objects that govern the non-trivial propagation of the wave and thus determine the scattering process are located in the near field. The far field, on the other hand, is characterized by free space propagation. The far field is chosen sufficiently far away from the scattering region such that all evanescent waves have vanished. In experiments, light sources and detectors are usually placed in the far field. If the far field carries N propagating modes (in both directions: into and out of the system), a coherent wavefront that is injected into the system is described by the vector of coherent amplitudes $\boldsymbol{\alpha}^{\text{in}} \in \mathbb{C}^N$. Likewise, the light that exits the system is described by the vector $\boldsymbol{\alpha}^{\text{out}} \in \mathbb{C}^N$.

The system is said to be linearly scattering if the media that the objects are made of have linear constitutive equations $\mathbf{P}(\omega) = \varepsilon_0 \boldsymbol{\chi}_e(\omega) \mathbf{E}(\omega)$, where ω is angular frequency, $\mathbf{P}(\omega)$ is the dielectric polarization density, $\boldsymbol{\chi}_e(\omega)$ the electric susceptibility tensor of the medium and $\mathbf{E}(\omega)$ the electric field [87]. Many “ordinary” optical elements are linear, e.g., mirrors, lenses, prisms, gratings, cavities, optical fibers

or common quantum logic gates like cNOT, the Hadamard gate and the Toffoli gate [88]. The optical Kerr effect, optical phase conjugation and frequency mixing (e.g., harmonic generation and spontaneous parametric down-conversion) are typical examples for nonlinearities [89]. Nonlinear effects occur only at high intensities, when the electric field becomes comparable to the atomic electric field strength $e/(4\pi\epsilon_0 a_0^2) \approx 5 \cdot 10^{11}$ V/m [89]. A linear scattering system is fully characterized by the frequency-dependent, so-called (classical) scattering matrix $\mathbf{S}(\omega) \in \mathbb{C}^{N \times N}$, which maps incoming monochromatic states of light $\boldsymbol{\alpha}^{\text{in}}(\omega)$ to the corresponding output states $\boldsymbol{\alpha}^{\text{out}}(\omega)$ [10]:

$$\boldsymbol{\alpha}^{\text{out}}(\omega) = \mathbf{S}(\omega) \boldsymbol{\alpha}^{\text{in}}(\omega). \quad (1.1)$$

In absence of loss and gain, the scattering matrix is unitary and the output intensity equals the input intensity:

$$\mathbf{S}^\dagger(\omega) \mathbf{S}(\omega) = \mathbf{1} \implies \|\boldsymbol{\alpha}^{\text{out}}(\omega)\|^2 = \|\boldsymbol{\alpha}^{\text{in}}(\omega)\|^2. \quad (1.2)$$

Another fundamental property of scattering matrices is established in case of reciprocity [10]: The amplitude $S_{m',m}(\omega)$ for propagating from the incoming mode m to the outgoing mode m' is the same as the amplitude $S_{m,m'}(\omega)$ for the reverse process. This implies that the scattering matrix is symmetric:

$$\mathbf{S}^\top(\omega) = \mathbf{S}(\omega). \quad (1.3)$$

Reciprocity is typically broken in presence of nonlinearities, time-varying media or magnetic fields. Usually, time-reversal symmetry is a sufficient, but not a necessary condition for reciprocity. For instance, an absorptive medium clearly violates time-reversal symmetry, but it may still be reciprocal. But there are also instances of metamaterials that are time-reversal symmetric but not reciprocal [90].

Standard sources of coherent light are lasers. Forming a specific input state $\boldsymbol{\alpha}^{\text{in}}(\omega)$ is called “wavefront shaping”. This is achieved by employing tools like spatial light modulators, digital micromirror devices or deformable mirrors in combination with lenses [4, 9, 11, 13, 91–93]. Conventional detectors are charge-coupled device cameras. Homodyne detection provides a scheme to measure both the amplitude and the phase of an optical light field [94] (see also last paragraph of Subsec. 1.2.4).

1.1.2 Electromagnetic Waveguide

In the following, we present and discuss a physical setup, which will appear as an example at times throughout the rest of this thesis. We consider an infinite metallic waveguide along the x -axis with cross-section $W_y \times W_z$, see Fig. 1.1. The interior is filled with an isotropic, time- and z -independent medium described by the scalar electric susceptibility $\chi_e(\omega; x, y)$. We assume a vanishing magnetic susceptibility $\chi_m = 0$, such that the refractive index landscape is given by $n(\omega; x, y) =$

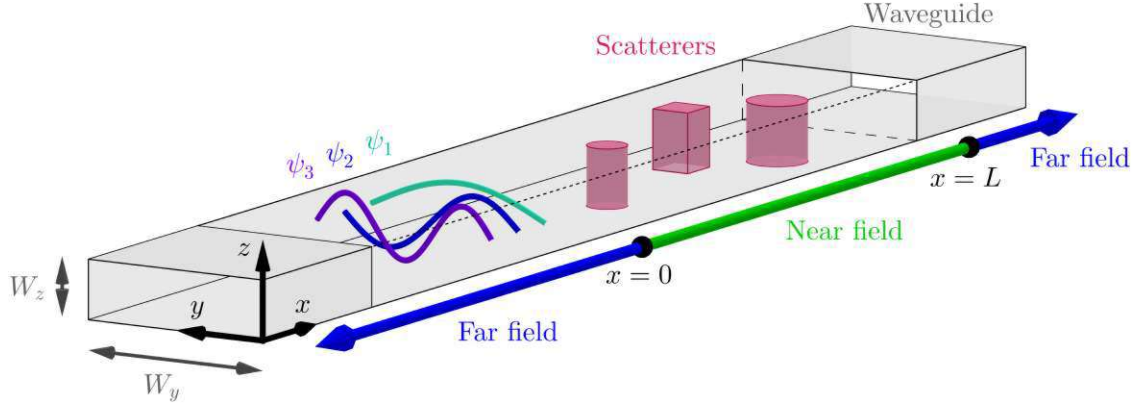


Figure 1.1: Electromagnetic waveguide (grey) with rectangular cross-section $W_y \times W_z$, extending along the x -axis. A section of the front side wall and the top plate are not shown to reveal a view of the interior. Scatterers (red) with different shapes and refractive indices constitute a scattering landscape inside the waveguide. The near field (green) covers the spatial area where the scatterers are located. Its borders are defined as $x = 0$ and $x = L$. The region outside the near field is called the far field (blue). The transverse profiles of the first three electromagnetic waveguide modes in y -direction, ψ_1 , ψ_2 and ψ_3 , are indicated in turquoise, blue and purple, respectively.

$\sqrt{1 + \chi_e(\omega; x, y)}$. Apart from this, there are no free charges or currents. For monochromatic waves $\mathbf{E}(\mathbf{r}, t) = \mathbf{E}(\omega; \mathbf{r}) e^{-i\omega t}$ with frequency ω and wavenumber $k = \omega/c$, Maxwell's equations lead to the vector Helmholtz equation

$$\nabla \times (\nabla \times \mathbf{E}(\omega; \mathbf{r})) - k^2 n^2(\omega; x, y) \mathbf{E}(\omega; \mathbf{r}) = \mathbf{0}. \quad (1.4)$$

In an empty waveguide with $n(\omega; x, y) = 1$, the well-known TE and TM modes form a complete set of solutions [87]. We demand that the waveguide is so narrow in the z -direction that only TE_{m_y, m_z} modes with $m_z = 0$ can propagate. This is the case whenever $W_z < \pi/k$. In the following, we write $W \equiv W_y$ and $m \equiv m_y$. The $\text{TE}_{m,0}$ modes are independent of the z coordinate and they are polarized in the z -direction,

$$\mathbf{E}(\omega; \mathbf{r}) =: \psi(\omega; x, y) \mathbf{e}_z. \quad (1.5)$$

We make use of

$$\nabla \times (\nabla \times \mathbf{E}) = \nabla(\nabla \cdot \mathbf{E}) - \Delta \mathbf{E} \quad (1.6)$$

and

$$\nabla \cdot \mathbf{D} = 0 \implies \nabla \cdot \mathbf{E} = \nabla \cdot (\varepsilon_0^{-1} n^{-2} \mathbf{D}) = \varepsilon_0^{-1} (\nabla n^{-2}) \cdot \mathbf{D} = n^2 (\nabla n^{-2}) \cdot \mathbf{E} = 0, \quad (1.7)$$

where in the last step we used the fact that n is independent of z and \mathbf{E} is parallel to \mathbf{e}_z . With this we arrive at the scalar two-dimensional Helmholtz equation

$$(\partial_x^2 + \partial_y^2 + k^2 n^2(\omega; x, y)) \psi(\omega; x, y) = 0 \quad (1.8)$$

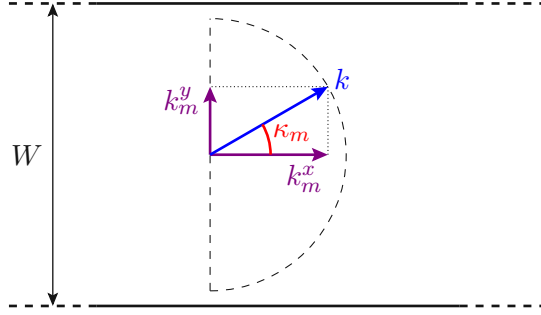


Figure 1.2: An empty waveguide of width W that is fed with electromagnetic waves with the wavenumber k can support $\lfloor kW/\pi \rfloor$ open modes for each direction of propagation. Each open mode m has an associated wave vector (k_m^x, k_m^y) with evenly spaced $k_m^y = m\pi/W$ and $k_m^x = (k^2 - (k_m^y)^2)^{1/2}$. The corresponding angle $\kappa_m = \arcsin(k_m^y/k)$ determines the inclination of the associated classical trajectory.

with the boundary conditions

$$\psi(\omega; x, 0) = 0, \quad (1.9)$$

$$\psi(\omega; x, W) = 0. \quad (1.10)$$

In the far field, where $n(\omega; x, y) = 1$, the waveguide modes are given by

$$\psi_m^\pm(\omega; x, y) = \sqrt{\frac{2}{W}} \sin\left(\frac{m\pi y}{W}\right) \frac{e^{\pm ik_m^x x}}{\sqrt{k_m^x}}, \quad (1.11)$$

where the sign \pm indicates the direction of travel (+ for propagation in x direction, – against x) and

$$k_m^x = \sqrt{k^2 - \frac{m^2\pi^2}{W^2}} \quad (1.12)$$

is the wavenumber in the direction of propagation. The mode m is called “open”, “propagating” or “flux-carrying” when k_m^x is real, i.e., $m < kW/\pi$. The mode m is called “evanescent” when k_m^x is imaginary, i.e., $m > kW/\pi$. Such modes decay exponentially fast and are not able to propagate into the far field. For a given frequency $\omega = ck$ and waveguide width W , there are $N' := \lfloor \omega W/\pi c \rfloor$ open modes for each direction of propagation. Each open mode m can be identified with a classical trajectory tilted at an angle $\kappa_m = \arcsin(m\pi/kW)$, see Fig. 1.2.

In the near field, the scattering medium with $n(\omega; x, y) \neq 1$ should lie within $x \in [0, L]$. The two lines $x = 0$ and $x = L$ mark the transition from the near field to the far field and serve as references for the scattering matrix (i.e., the numerical entries of \mathbf{S} will depend on the choice of L). In the far field, a general solution of Eqs. (1.8), (1.9) and (1.10) can be decomposed according to

$$\psi(\omega; x \leq 0, y) = \sum_{m=1}^{N'} \alpha_{l,m}^+(\omega) \psi_m^+(\omega; x, y) + \sum_{m=1}^{N'} \alpha_{l,m}^-(\omega) \psi_m^-(\omega; x, y), \quad (1.13)$$

$$\begin{aligned} \psi(\omega; x \geq L, y) &= \sum_{m=1}^{N'} \alpha_{r,m}^+(\omega) \psi_m^+(\omega; x-L, y) \\ &\quad + \sum_{m=1}^{N'} \alpha_{r,m}^-(\omega) \psi_m^-(\omega; x-L, y). \end{aligned} \quad (1.14)$$

The input and output amplitudes are collected in the vectors

$$\boldsymbol{\alpha}^{\text{in}}(\omega) = \begin{pmatrix} \boldsymbol{\alpha}_l^+(\omega) \\ \boldsymbol{\alpha}_r^-(\omega) \end{pmatrix}, \quad \boldsymbol{\alpha}^{\text{out}}(\omega) = \begin{pmatrix} \boldsymbol{\alpha}_l^-(\omega) \\ \boldsymbol{\alpha}_r^+(\omega) \end{pmatrix}, \quad (1.15)$$

respectively. In total, there are $N = 2N'$ input and output modes. The scattering matrix $\mathbf{S}(\omega)$ is defined through Eq. (1.1). The factor $1/\sqrt{k_m^x}$ in Eq. (1.11) is necessary in order for the modes ψ_m^\pm to be normalized w.r.t. the longitudinal flux [10]. The scattering matrix $\mathbf{S}(\omega)$ is unitary only with this normalization.

The scattering matrix can be determined column-wise: We successively inject the modes $\alpha_{l,m}^+(\omega)$ and $\alpha_{r,m}^-(\omega)$ into the system and calculate (or measure) the emerging field at the reference lines $x = 0$ and $x = L$. Since the transverse mode profiles

$$\psi_m(y) = \sqrt{\frac{2}{W}} \sin\left(\frac{m\pi y}{W}\right) \quad (1.16)$$

are orthonormal,

$$\int_0^W \psi_m^*(y) \psi_{m'}(y) dy = \delta_{m,m'}, \quad (1.17)$$

the outgoing amplitudes can be found via

$$\sqrt{k_m^x} \int_0^W \psi_m^*(y) \psi(\omega; 0, y) dy = \alpha_{l,m}^+(\omega) + \alpha_{l,m}^-(\omega), \quad (1.18)$$

$$\sqrt{k_m^x} \int_0^W \psi_m^*(y) \psi(\omega; L, y) dy = \alpha_{r,m}^+(\omega) + \alpha_{r,m}^-(\omega). \quad (1.19)$$

By setting only the m^{th} component of $\boldsymbol{\alpha}^{\text{in}}(\omega) = (\boldsymbol{\alpha}_l^+(\omega), \boldsymbol{\alpha}_r^-(\omega))^\top$ equal to one and all the other ones to zero, we can identify the corresponding output vector $\boldsymbol{\alpha}^{\text{out}}(\omega) = (\boldsymbol{\alpha}_l^-(\omega), \boldsymbol{\alpha}_r^+(\omega))^\top$ as the m^{th} column of $\mathbf{S}(\omega)$. Note that the transverse profiles of the evanescent modes are orthogonal to the transverse profiles of all the propagating modes. Therefore, the contribution of the evanescent modes are automatically dropped in Eqs. (1.18) and (1.19). This means that L does not have to be so large that all evanescent modes have become negligible at $x = L$.

Due to the specific geometry of the waveguide, having a lead to the left of the scattering medium and another one to the right of it, one often separates the scattering matrix into four $N' \times N'$ blocks:

$$\mathbf{S}(\omega) = \begin{pmatrix} \mathbf{R}(\omega) & \mathbf{T}'(\omega) \\ \mathbf{T}(\omega) & \mathbf{R}'(\omega) \end{pmatrix}. \quad (1.20)$$

$\mathbf{R}^{(l)}(\omega)$ is called the reflection matrix from left to left (from right to right) and $\mathbf{T}^{(l)}(\omega)$ is called the transmission matrix from left to right (from right to left).

A completely empty waveguide has vanishing reflection matrices and diagonal transmission matrices with

$$T_{m,m}(\omega) = T'_{m,m}(\omega) = e^{ik_m^x L}. \quad (1.21)$$

When the waveguide is not empty, we solve the Helmholtz equation (1.8) numerically using a finite element method. As opposed to finite difference methods, this allows for the modelling of arbitrary geometrical shapes and adaptive mesh refinement depending on the local refractive index, which determines the local wavelength. The author employed the software “NGSolve” [95], to which Matthias Kühmayer programmed a handy frontend that is customized for application to the Helmholtz equation [96].

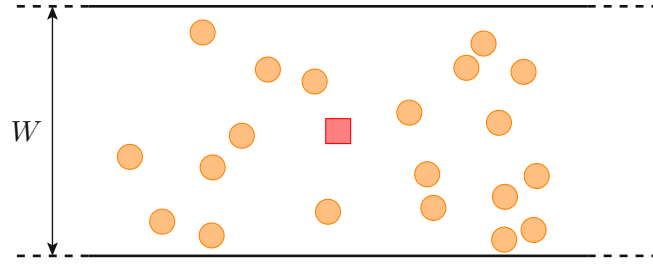
Experimentally, the optical transmission matrix has been measured in “open” environments (i.e., without a waveguide) [6–8]. In optical fibers, one can measure the full scattering matrix [97].

In the following, we explain the physical setup that we will consider in all numerical examples appearing throughout the rest of this thesis. We deliberately choose a generic setup to demonstrate the generality of the presented concepts, see also Fig. 1.3(a). The system under study consists of a waveguide of width W as described above. A target scatterer in the shape of a square with side length $W/10$ is placed at the center of the waveguide. The target is metallic, which means that we impose homogeneous Dirichlet boundary conditions along its border. The target is surrounded by 20 randomly placed circular scatterers with radius $W/20$, providing a complex scattering environment. The refractive index of those scatterers is chosen as 1.44. We numerically calculate the scattering matrix of this system for the wavenumber $k = 20.5\pi/W$ such that $N' = 20$ modes are open for each direction of propagation, i.e., there are $N = 40$ open modes in total. Figure 1.3(b) shows the absolute values of the entries of the scattering matrix. The symmetry of the scattering matrix (see Eq. (1.3)) is evident. The fact that the entries of the matrix seem to be random and far from a diagonal structure as in the case of an empty waveguide, see Fig. 1.3(c), is a hallmark for complex scattering. The total reflectance of the system amounts to $\text{tr}(\mathbf{R}^\dagger \mathbf{R})/N' \approx 0.514$, whereas the total transmittance is given by $\text{tr}(\mathbf{T}^\dagger \mathbf{T})/N' \approx 0.486$.

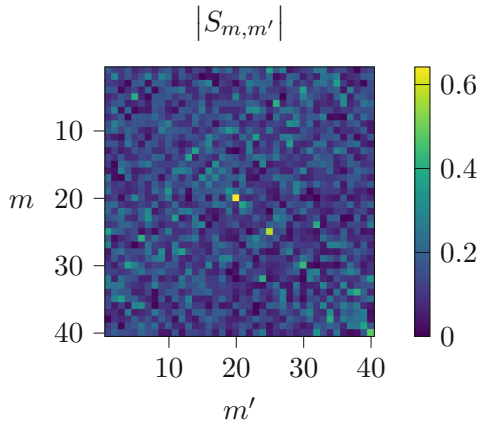
1.2 Fundamentals of Quantum Optics

In Subsec. 1.2.1, we outline the basic ideas and the most relevant results for the quantization of the electromagnetic field. For a more in-depth treatment, the reader is referred to Ref. [98]. After presenting multi-mode Gaussian and photon number states in Subsecs. 1.2.2, 1.2.3 and 1.2.4, we discuss the scattering behaviour of those

(a) Geometrical configuration



(b) Scattering matrix of full system



(c) Scattering matrix of empty waveguide

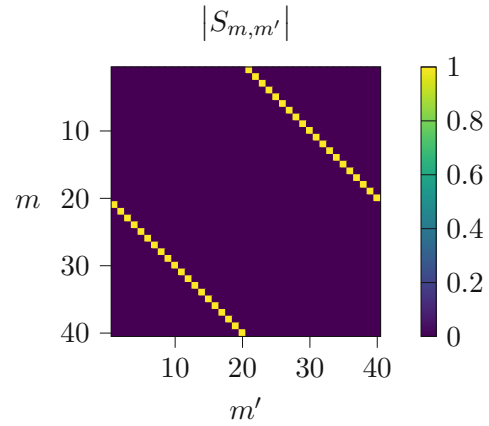


Figure 1.3: Physical setup of the generically chosen system. (a) A metallic target (red square) is placed inside a waveguide of width W . The target is surrounded by randomly placed circular scatterers (orange) with refractive index $n = 1.44$. (b) The plot shows the absolute values of the entries of the numerically calculated scattering matrix for the wavenumber $k = 20.5\pi/W$, where $N = 40$ waveguide modes are open. The symmetry (see Eq. (1.3)) of the matrix is apparent. The seemingly random distribution of values in the matrix indicates complex scattering. (c) For comparison, the scattering matrix of the empty waveguide is shown.

quantum states of light in Sec. 1.3. Reference [99] gives an excellent overview over multi-mode quantum optics.

1.2.1 Quantization of the Electromagnetic Field

The classical magnetic vector potential \mathbf{A} is usually decomposed in a suitable basis of monochromatic modes \mathbf{A}_m with respective frequencies ω_m :

$$\mathbf{A}(\mathbf{r}, t) = \sum_m (a_m \mathbf{A}_m(\mathbf{r}) e^{-i\omega_m t} + a_m^* \mathbf{A}_m^*(\mathbf{r}) e^{i\omega_m t}). \quad (1.22)$$

The so-called “second quantization” or “canonical quantization” consists in replacing the coefficients a_m by the annihilation operators \hat{a}_m of the respective modes:

$$\hat{\mathbf{A}}(\mathbf{r}, t) = \sum_m^f (\hat{a}_m \mathbf{A}_m(\mathbf{r}) e^{-i\omega_m t} + \hat{a}_m^\dagger \mathbf{A}_m^*(\mathbf{r}) e^{i\omega_m t}). \quad (1.23)$$

The Hermitian conjugates \hat{a}_m^\dagger of the annihilation operators are called “creation operators”. The annihilation and creation operators fulfil the bosonic commutation relations

$$[\hat{a}_m, \hat{a}_{m'}^\dagger] = \delta_{m,m'}, \quad [\hat{a}_m, \hat{a}_{m'}] = 0, \quad [\hat{a}_m^\dagger, \hat{a}_{m'}^\dagger] = 0. \quad (1.24)$$

Physically speaking, the annihilation and creation operators destroy and create single quanta of light, i.e. photons, respectively, as will be discussed below in Subsec. 1.2.4. We denote the column vector consisting of the annihilation operators by

$$[\hat{a}] := \begin{pmatrix} \hat{a}_1 \\ \hat{a}_2 \\ \vdots \end{pmatrix} \quad (1.25)$$

and likewise $[\hat{a}^\dagger]$ for the creation operators. The observables

$$\hat{n}_m := \hat{a}_m^\dagger \hat{a}_m, \quad (1.26)$$

$$\hat{n} := \sum_m^f \hat{n}_m \quad (1.27)$$

measure the number of photons in mode m and the total number of photons, respectively. The Hamiltonian of the electromagnetic field turns out to be

$$\hat{H}_{\text{EM}} = \sum_m^f \hbar\omega_m \left(\hat{n}_m + \frac{1}{2} \right). \quad (1.28)$$

This means that the quantized electromagnetic field can be pictured as a collection of independent harmonic oscillators, one for each mode. Similar to the position and momentum of a harmonic oscillator, the so-called “quadratures” of mode m are introduced as

$$\hat{q}_m := \frac{1}{\sqrt{2}} (\hat{a}_m + \hat{a}_m^\dagger), \quad (1.29)$$

$$\hat{p}_m := \frac{-i}{\sqrt{2}} (\hat{a}_m - \hat{a}_m^\dagger). \quad (1.30)$$

A rotation in the phase space spanned by \hat{q}_m and \hat{p}_m yields the rotated quadratures (also often called just “quadratures”)

$$\hat{q}_m(\varphi) := \cos(\varphi) \hat{q}_m + \sin(\varphi) \hat{p}_m = \frac{1}{\sqrt{2}} (e^{-i\varphi} \hat{a}_m + e^{i\varphi} \hat{a}_m^\dagger), \quad (1.31)$$

$$\hat{p}_m(\varphi) := -\sin(\varphi)\hat{q}_m + \cos(\varphi)\hat{p}_m = \frac{-i}{\sqrt{2}}(e^{-i\varphi}\hat{a}_m - e^{i\varphi}\hat{a}_m^\dagger). \quad (1.32)$$

Correspondingly, multi-mode light can take the same quantum states as a multi-dimensional harmonic oscillator. Below, we discuss a physically relevant selection of such quantum states of light with N modes. To make it clear that the representation is rooted in the “standard” modes (e.g., the waveguide modes (1.11)), we use the superscript \mathcal{M} in the notation. Later on, we will use other representations as well.

1.2.2 Coherent States

Coherent states $|\boldsymbol{\alpha}\rangle^{\mathcal{M}}$ are parameterized by a vector of coherent amplitudes $\boldsymbol{\alpha} \in \mathbb{C}^N$. Introducing the unitary displacement operator (the index “ a ” indicates that the operators \hat{a}_m and \hat{a}_m^\dagger are used)

$$\hat{D}_a(\boldsymbol{\alpha}) := \exp(\boldsymbol{\alpha}^\top [\hat{a}^\dagger] - \boldsymbol{\alpha}^\dagger [\hat{a}]), \quad (1.33)$$

the coherent state $|\boldsymbol{\alpha}\rangle^{\mathcal{M}}$ is created from the vacuum state $|\mathbf{0}\rangle$ via displacement, see also Fig. 1.4(a):

$$|\boldsymbol{\alpha}\rangle^{\mathcal{M}} := \hat{D}_a(\boldsymbol{\alpha})|\mathbf{0}\rangle. \quad (1.34)$$

Coherent states are eigenstates of the annihilation operators,

$$\hat{a}_m|\boldsymbol{\alpha}\rangle^{\mathcal{M}} = \alpha_m|\boldsymbol{\alpha}\rangle^{\mathcal{M}}, \quad (1.35)$$

and they have mean photon numbers

$${}^{\mathcal{M}}\langle\boldsymbol{\alpha}|\hat{n}_m|\boldsymbol{\alpha}\rangle^{\mathcal{M}} = |\alpha_m|^2, \quad (1.36)$$

$${}^{\mathcal{M}}\langle\boldsymbol{\alpha}|\hat{n}|\boldsymbol{\alpha}\rangle^{\mathcal{M}} = \|\boldsymbol{\alpha}\|^2. \quad (1.37)$$

Coherent states are considered the “most classical” states of quantum light since they exhibit equal minimum uncertainty (i.e. variance) in all quadratures:

$$\forall m \in \{0, \dots, N\} \forall \varphi \in [0, 2\pi) : \mathbb{V}_{|\boldsymbol{\alpha}\rangle^{\mathcal{M}}}[\hat{q}_m(\varphi)] = \frac{1}{2}. \quad (1.38)$$

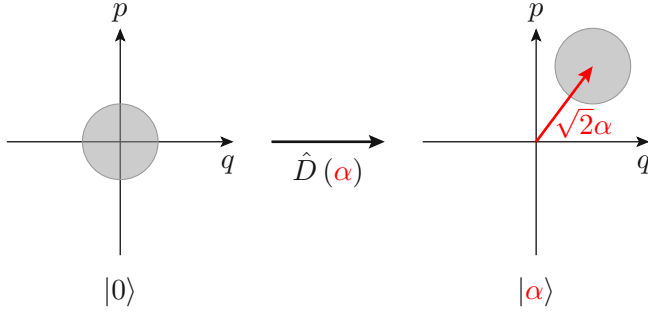
In the experiment, lasers serve as sources of coherent states of light, as discussed in Subsec. 1.1.1.

1.2.3 Squeezed States

Squeezed states $|\boldsymbol{\alpha}, \mathbf{Z}\rangle^{\mathcal{M}}$ are parameterized by a vector of coherent amplitudes $\boldsymbol{\alpha} \in \mathbb{C}^N$ and a symmetric squeezing matrix $\mathbf{Z} \in \mathbb{C}^{N \times N}$ [100]. Introducing the unitary squeezing operator (note the different sign convention in Ref. [100])

$$\hat{S}_a(\mathbf{Z}) := \exp\left(\frac{1}{2}\left([\hat{a}]^\top \mathbf{Z}^* [\hat{a}] - [\hat{a}^\dagger]^\top \mathbf{Z} [\hat{a}^\dagger]\right)\right), \quad (1.39)$$

(a) Coherent state



(b) Squeezed state

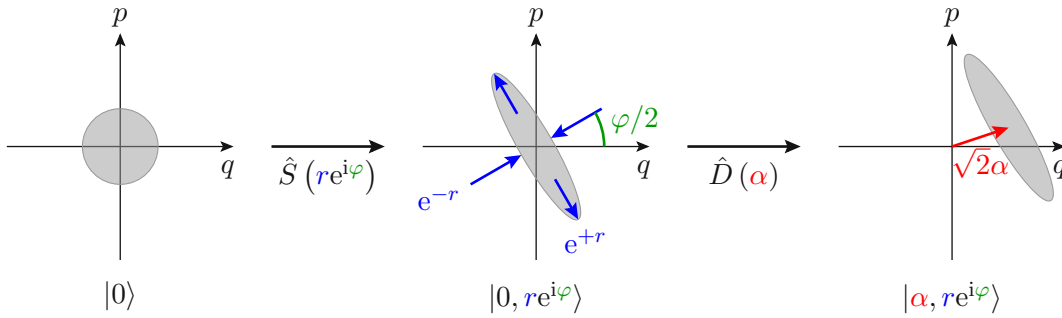


Figure 1.4: Phase space representation of single-mode Gaussian states of light. The grey circles and ellipses represent contour sections of the Wigner functions. **(a)** A coherent state $|\alpha\rangle$ is created from the vacuum state $|0\rangle$ by applying the displacement operator $\hat{D}(\alpha)$. **(b)** A squeezed state $|\alpha, z\rangle$ with $z = re^{i\varphi}$ is created from the vacuum state $|0\rangle$ by first applying the squeezing operator $\hat{S}(z)$ and then the displacement operator $\hat{D}(\alpha)$. Here, the squeezing parameters are chosen as $r = 0.8$ and $\varphi = 60^\circ = \pi/3$.

the squeezed state $|\alpha, \mathbf{Z}\rangle^{\mathcal{M}}$ is obtained from the vacuum state by squeezing it by \mathbf{Z} first and then displacing it by α , see also Fig. 1.4(b):

$$|\alpha, \mathbf{Z}\rangle^{\mathcal{M}} := \hat{D}_a(\alpha) \hat{S}_a(\mathbf{Z}) |0\rangle. \quad (1.40)$$

The Wigner function of a squeezed state is a Gaussian [98]. For this reason, squeezed states (including coherent states) are also often called ‘‘Gaussian states’’.

We now discuss a specific decomposition of the squeezing matrix \mathbf{Z} which will be useful in later calculations. This decomposition is the counterpart to the polar representation of a scalar complex number, $z = re^{i\varphi}$, and is thus called ‘‘polar decomposition’’: Any finite-dimensional square matrix can be decomposed into a product of a Hermitian and a unitary matrix [100]:

$$\mathbf{Z} = \mathbf{R}e^{i\Phi}. \quad (1.41)$$

Both matrices \mathbf{R} and Φ are Hermitian with the properties² $\mathbf{R} \succeq \mathbf{0}$, $\mathbf{R} \succ \mathbf{0} \iff \det(\mathbf{Z}) \neq 0$, and $\mathbf{0} \preceq \Phi \prec 2\pi\mathbf{1}$. \mathbf{R} is always unique, but Φ is unique iff $\det(\mathbf{Z}) \neq 0$. The polar decomposition can be obtained from the singular value decomposition $\mathbf{Z} = \mathbf{U}\Sigma\mathbf{V}^\dagger$ as $\mathbf{R} = \mathbf{U}\Sigma\mathbf{U}^\dagger$ and $e^{i\Phi} = \mathbf{U}\mathbf{V}^\dagger$.

In App. A we show that the mean photon numbers of a squeezed state are

$${}^{\mathcal{M}}\langle \boldsymbol{\alpha}, \mathbf{Z} | \hat{n}_m | \boldsymbol{\alpha}, \mathbf{Z} \rangle^{\mathcal{M}} = |\alpha_m|^2 + (\sinh^2(\mathbf{R}))_{m,m}, \quad (1.42)$$

$${}^{\mathcal{M}}\langle \boldsymbol{\alpha}, \mathbf{Z} | \hat{n} | \boldsymbol{\alpha}, \mathbf{Z} \rangle^{\mathcal{M}} = \|\boldsymbol{\alpha}\|^2 + \text{tr}(\sinh^2(\mathbf{R})), \quad (1.43)$$

where \sinh^2 is to be applied as a proper matrix function.

If the squeezing matrix is diagonal, $\mathbf{Z} = \text{diag}(\zeta_1, \dots, \zeta_N)$ with $\zeta_m = r_m e^{i\varphi_m}$, the squeezed state factorizes into a product of single-mode squeezed states. In phase space, the physical interpretation of the parameters r_m and $\varphi_m/2$ is squeezing strength and squeezing angle, respectively, see also Fig. 1.4(b). The squeezing strength determines the uncertainties in the rotated quadratures (for a derivation see App. A):

$$\mathbb{V}_{|\boldsymbol{\alpha}, \mathbf{Z}\rangle^{\mathcal{M}}}[\hat{q}_m(\varphi_m/2)] = \frac{e^{-2r_m}}{2}, \quad (1.44)$$

$$\mathbb{V}_{|\boldsymbol{\alpha}, \mathbf{Z}\rangle^{\mathcal{M}}}[\hat{p}_m(\varphi_m/2)] = \frac{e^{2r_m}}{2}. \quad (1.45)$$

The squeezing strength is often stated in units of decibel. A value of r corresponds to $\frac{20}{\ln(10)}r \text{ dB} \approx 8.686r \text{ dB}$. The highest squeezing strength currently accomplished experimentally is 15 dB or $r \approx 1.73$ [101].

There are many ways of generating single-mode squeezing [102–104]. Single-mode squeezed light can be reshaped into different spatial modes using deformable mirrors in combination with lenses [105] or spatial light modulators [106, 107]. The preparation of a product of single-mode squeezed states is demonstrated in Ref. [108]. Such product states can be converted to general multi-mode squeezed states by virtue of linear optical networks [99, 109], see also Sec. 1.3. Arbitrary linear optical networks can be realized by suitable combinations of finitely many simple optical elements [91, 110, 111]. Multiple four-wave mixing processes provide a more direct way of producing multi-mode squeezed states [112].

1.2.4 Fock States and Photon Number States

Fock states $|\mathbf{n}\rangle^{\mathcal{M}}$ are parameterized by a vector of photon numbers $\mathbf{n} \in \mathbb{N}_0^N$. They are created from the vacuum state by repeated application of the creation operators:

$$|\mathbf{n}\rangle^{\mathcal{M}} := \frac{1}{C_{\mathbf{n}}} \prod_{m=1}^N (\hat{a}_m^\dagger)^{n_m} |\mathbf{0}\rangle, \quad (1.46)$$

²For Hermitian matrices \mathbf{A}, \mathbf{B} we denote $\mathbf{A} \succ \mathbf{B}$ if $\mathbf{A} - \mathbf{B}$ is positive definite and $\mathbf{A} \succeq \mathbf{B}$ if $\mathbf{A} - \mathbf{B}$ is positive semidefinite. The symbols \prec and \preceq are defined likewise.

where we defined the combinatorial factor

$$C_{\mathbf{n}} := \sqrt{\prod_{m=1}^N n_m!}. \quad (1.47)$$

Fock states are eigenstates of the photon number operators, i.e., they contain a well-defined number of photons in each mode:

$$\hat{n}_m |\mathbf{n}\rangle^{\mathcal{M}} = n_m |\mathbf{n}\rangle^{\mathcal{M}}, \quad (1.48)$$

$$\hat{n} |\mathbf{n}\rangle^{\mathcal{M}} = \sum_{m=1}^N n_m |\mathbf{n}\rangle^{\mathcal{M}}. \quad (1.49)$$

The application of \hat{a}_m or \hat{a}_m^\dagger destroys or creates a photon in mode m , respectively:

$$\hat{a}_m |\mathbf{n}\rangle^{\mathcal{M}} = \sqrt{n_m} |\mathbf{n} - \mathbf{e}_m\rangle^{\mathcal{M}}, \quad (1.50)$$

$$\hat{a}_m^\dagger |\mathbf{n}\rangle^{\mathcal{M}} = \sqrt{n_m + 1} |\mathbf{n} + \mathbf{e}_m\rangle^{\mathcal{M}}. \quad (1.51)$$

Here, \mathbf{e}_m denotes the m^{th} unit vector. There is a wide range of possibilities to prepare single-photon Fock states [113]. Fock states with two photons can be generated in high- Q cavities [114]. While it is still possible to produce three-photon Fock states [115], there are proposals for schemes that yield larger Fock states with up to 100 photons [116–118].

Mathematically, Fock states form an orthonormal basis of the Hilbert space of N -mode quantum states:

$$\langle \mathbf{n} | \mathbf{n}' \rangle^{\mathcal{M}} = \delta_{\mathbf{n}, \mathbf{n}'}, \quad (1.52)$$

$$\sum_{\mathbf{n} \in \mathbb{N}_0^N} |\mathbf{n}\rangle^{\mathcal{M}} \langle \mathbf{n}|^{\mathcal{M}} = \hat{1}. \quad (1.53)$$

The subspace spanned by the Fock states with the same total photon number n is the space of so-called “photon number states” (with n photons). In general, such states exhibit an entanglement between the different spatial modes. A basis for this subspace is given by the set

$$\mathcal{F}_n^N := \left\{ \mathbf{n} \in \mathbb{N}_0^N : \sum_{m=1}^N n_m = n \right\}. \quad (1.54)$$

To each of the n photons we have to assign a mode $m \in \{1, \dots, N\}$. There are $\binom{N+n-1}{n}$ possible ways of drawing n times from the set $\{1, \dots, N\}$ with repetition, therefore the dimensionality of the space of photon number states is

$$|\mathcal{F}_n^N| = \binom{N+n-1}{n}. \quad (1.55)$$

Any photon number state is parameterized by its coefficient vector $\boldsymbol{\psi} \in \mathbb{C}^{\binom{N+n-1}{n}}$:

$$|\boldsymbol{\psi}\rangle^{\mathcal{M}} = \sum_{\mathbf{n} \in \mathcal{F}_n^N} \langle \mathbf{n} | \boldsymbol{\psi} \rangle^{\mathcal{M}} |\mathbf{n}\rangle^{\mathcal{M}} =: \sum_{\mathbf{n} \in \mathcal{F}_n^N} \psi_{\mathbf{n}} |\mathbf{n}\rangle^{\mathcal{M}}. \quad (1.56)$$

In the experiment, the spatial waveform of entangled photon pairs can be shaped by applying wavefront shaping to the pump beam [48, 119, 120]. The spatial coherence of the pump beam influences the degree of correlations between the entangled photons [121, 122].

We finish this section by shortly reviewing means to measure Gaussian and photon number states. Quantum state tomography is a method to reconstruct the Wigner function (a unique representation) of a quantum state from measurements on the rotated quadratures [94, 98, 123, 124]. The latter are typically measured in a homodyne detection scheme [104, 125, 126]. Further measurement schemes are described in Refs. [99, 113].

1.3 Scattering in Quantum Optics

Analogously to Eq. (1.1), which describes unitary classical scattering, we declare a unitary quantum scattering process to be defined by a unitary operator \hat{U} mapping pure input states to pure output states:

$$|\boldsymbol{\psi}^{\text{out}}\rangle = \hat{U} |\boldsymbol{\psi}^{\text{in}}\rangle. \quad (1.57)$$

This operator \hat{U} is determined by the input-output relation of the mode operators \hat{a}_m and \hat{a}_m^\dagger . We assume a linear input-output relation, allowing for annihilation operators to be transformed into creation operators and vice versa. This includes active linear elements like phase conjugation mirrors or parametric amplifiers, as well as all passive linear elements as discussed in Subsec. 1.1.1 [127, 128]. For optomechanical and micromechanical systems which do not satisfy this condition, our framework is restricted to the linear regime (as realized, e.g., for sufficiently low intensities). This kind of transformation is also known as a Bogoliubov transformation:

$$\left[\hat{U}^\dagger \hat{a} \hat{U} \right] = \mathbf{A} [\hat{a}] + \mathbf{B} [\hat{a}^\dagger]. \quad (1.58)$$

The physical meaning of the matrices \mathbf{A} and \mathbf{B} is explained below. The conditions

$$\mathbf{A}\mathbf{A}^\dagger - \mathbf{B}\mathbf{B}^\dagger = \mathbf{1}, \quad (1.59)$$

$$\mathbf{A}\mathbf{B}^\top = \mathbf{B}\mathbf{A}^\top, \quad (1.60)$$

ensure that the transformed operators still fulfil the commutation relations (1.24). In terms of the transformation matrices \mathbf{A} and \mathbf{B} , the unitary operator \hat{U} is given

as [127, 128]

$$\hat{U} = \exp\left(\frac{1}{2}\left([\hat{a}^\dagger]^\top \quad [\hat{a}]^\top\right)\begin{pmatrix} \mathbf{1} & \mathbf{0} \\ \mathbf{0} & -\mathbf{1} \end{pmatrix}\ln\begin{pmatrix} \mathbf{A} & \mathbf{B} \\ \mathbf{B}^* & \mathbf{A}^* \end{pmatrix}\begin{pmatrix} [\hat{a}] \\ [\hat{a}^\dagger] \end{pmatrix}\right). \quad (1.61)$$

In the case where there are no active elements, annihilation operators of modes with frequency $\omega_m = \omega$ are mapped to annihilation operators with the same frequency only. This means that we can treat each frequency ω individually, which is why in the following we omit to explicitly write the ω -dependence. Furthermore, $\mathbf{B} = \mathbf{0}$ and \mathbf{A} can be identified with the classical scattering matrix \mathbf{S} , which will be justified below, see Eq. (1.65). (For active linear elements, $\mathbf{B} \neq \mathbf{0}$ and the transformation \hat{U} needs to be described by a squeezing matrix on top of the scattering matrix, and those two matrices need to be combined in a specific way to obtain \mathbf{A} and \mathbf{B} [100].) Using the unitarity of \mathbf{S} and the commutator relations (1.24), we obtain

$$\hat{U} = \sqrt{\det(\mathbf{S})} \exp\left([\hat{a}^\dagger]^\top \ln(\mathbf{S}) [\hat{a}]\right). \quad (1.62)$$

Apart from the global phase factor $\sqrt{\det(\mathbf{S})}$, this corresponds to what is called a “rotation operator” in Ref. [100]. Here, it is immediately clear that the quantum operator \hat{U} is uniquely specified by the classical scattering matrix \mathbf{S} . In general, the task of determining a quantum unitary gate by probing it with different (often coherent) states is called “quantum process tomography” [97, 129–131].

A first important observation is that such a quantum process does not change the total photon number, i.e., $\hat{n}\hat{U} = \hat{U}\hat{n}$. This can be shown by using Eqs. (1.26), (1.27), (1.58) and (1.59):

$$\begin{aligned} \hat{U}^\dagger \hat{n} \hat{U} &= \hat{U}^\dagger [\hat{a}^\dagger]^\top [\hat{a}] \hat{U} = \left[\hat{U}^\dagger \hat{a}^\dagger \hat{U}\right]^\top \left[\hat{U}^\dagger \hat{a} \hat{U}\right] = (\mathbf{S}^* [\hat{a}^\dagger])^\top \mathbf{S} [\hat{a}] \\ &= [\hat{a}^\dagger]^\top \mathbf{S}^\dagger \mathbf{S} [\hat{a}] = [\hat{a}^\dagger]^\top [\hat{a}] = \hat{n}. \end{aligned} \quad (1.63)$$

According to Ref. [100], the scattering behaviour of a Gaussian state is given by

$$\hat{U} |\boldsymbol{\alpha}, \mathbf{Z}\rangle^{\mathcal{M}} = \sqrt{\det(\mathbf{S})} |\mathbf{S}\boldsymbol{\alpha}, \mathbf{S}\mathbf{Z}\mathbf{S}^\top\rangle^{\mathcal{M}}. \quad (1.64)$$

Coherent states are transformed according to the classical scattering matrix:

$$\hat{U} |\boldsymbol{\alpha}\rangle^{\mathcal{M}} = \sqrt{\det(\mathbf{S})} |\mathbf{S}\boldsymbol{\alpha}\rangle^{\mathcal{M}}. \quad (1.65)$$

As mentioned in Subsec. 1.2.3, the transformation (1.64) can be used to produce an arbitrary multi-mode squeezed state $|\boldsymbol{\alpha}, \mathbf{Z}\rangle^{\mathcal{M}}$ from a product consisting of single-mode squeezed states. Such a product state is characterized by a diagonal squeezing matrix. Considering the so-called Takagi factorization $\mathbf{Z} = \mathbf{U}\boldsymbol{\Sigma}\mathbf{U}^\top$, a special singular value decomposition for symmetric matrices [132, 133], we see that

the product state $\det(\mathbf{U})^{-1/2} |\mathbf{U}^\dagger \boldsymbol{\alpha}, \boldsymbol{\Sigma}\rangle^{\mathcal{M}}$ gets mapped to $|\boldsymbol{\alpha}, \mathbf{Z}\rangle^{\mathcal{M}}$ after propagation through a linear optical network with classical scattering matrix \mathbf{U} [91, 110, 111].

Since the scattering operator \hat{U} commutes with the total photon number operator \hat{n} , photon number states with n photons get scattered into photon number states with the same number of photons. Therefore, in the Fock basis the quantum unitary \hat{U} has block structure and we can deal with the scattering behaviour of photon number states separately, according to n . Introducing the n -photon scattering matrix $\mathbf{S}^{(n)} \in \mathbb{C}^{\binom{N+n-1}{n} \times \binom{N+n-1}{n}}$ with elements

$$\forall \mathbf{n}, \mathbf{n}' \in \mathcal{F}_n^N : S_{\mathbf{n}, \mathbf{n}'}^{(n)} := \frac{1}{\sqrt{\det(\mathbf{S})}} {}^{\mathcal{M}} \langle \mathbf{n} | \hat{U} | \mathbf{n}' \rangle^{\mathcal{M}}, \quad (1.66)$$

the scattering of the photon number state $|\boldsymbol{\psi}\rangle^{\mathcal{M}}$ is straightforwardly described as

$$\hat{U} |\boldsymbol{\psi}\rangle^{\mathcal{M}} = \sqrt{\det(\mathbf{S})} \sum_{\mathbf{n}, \mathbf{n}' \in \mathcal{F}_n^N} |\mathbf{n}\rangle^{\mathcal{M}} S_{\mathbf{n}, \mathbf{n}'}^{(n)} \psi_{\mathbf{n}'} = \sqrt{\det(\mathbf{S})} |\mathbf{S}^{(n)} \boldsymbol{\psi}\rangle^{\mathcal{M}}. \quad (1.67)$$

The unitarity of $\mathbf{S}^{(n)}$ follows from the unitarity of \hat{U} :

$$\begin{aligned} \left((\mathbf{S}^{(n)})^\dagger \mathbf{S}^{(n)} \right)_{\mathbf{n}, \mathbf{n}'} &= \sum_{\mathbf{n}'' \in \mathcal{F}_n^N} S_{\mathbf{n}'', \mathbf{n}}^{(n)*} S_{\mathbf{n}'', \mathbf{n}'}^{(n)} = \sum_{\mathbf{n}'' \in \mathcal{F}_n^N} {}^{\mathcal{M}} \langle \mathbf{n} | \hat{U}^\dagger | \mathbf{n}'' \rangle^{\mathcal{M}} {}^{\mathcal{M}} \langle \mathbf{n}'' | \hat{U} | \mathbf{n}' \rangle^{\mathcal{M}} \\ &= {}^{\mathcal{M}} \langle \mathbf{n} | \hat{U}^\dagger \hat{U} | \mathbf{n}' \rangle^{\mathcal{M}} = \delta_{\mathbf{n}, \mathbf{n}'}. \end{aligned} \quad (1.68)$$

The n -photon scattering matrix is expressible in terms of the classical scattering matrix \mathbf{S} [134, 135]:

$$S_{\mathbf{n}, \mathbf{n}'}^{(n)} = \frac{1}{C_{\mathbf{n}} C_{\mathbf{n}'}} \text{perm} \begin{pmatrix} S_{11} \mathbf{1}_{n_1 \times n'_1} & \cdots & S_{1N} \mathbf{1}_{n_1 \times n'_N} \\ \vdots & \ddots & \vdots \\ S_{N1} \mathbf{1}_{n_N \times n'_1} & \cdots & S_{NN} \mathbf{1}_{n_N \times n'_N} \end{pmatrix}, \quad (1.69)$$

where $\mathbf{1}_{n \times n'}$ is the constant $n \times n'$ matrix with all entries equal to 1. In order to explicitly expand this permanent, we decompose any “photon occupation vector” $\mathbf{n} \in \mathcal{F}_n^N$ into its n “single occupation contributions” $\mathbf{n}_k \in \mathcal{F}_1^N$:

$$\mathbf{n} = \sum_{k=1}^n \mathbf{n}_k. \quad (1.70)$$

The general convention used in this thesis is that the “single occupation contributions” are indicated by an index k or l (potentially with additional primes ι) attached to the vector symbol of the full “photon occupation vector”. This decomposition is not unique, but this is irrelevant since in the following expressions

there will always be a symmetrization over k and l . Additionally, we introduce the notation $S_{\mathbf{n}_k, \mathbf{n}'_l} \equiv S_{m, m'}$ for $\mathbf{n}_k = \mathbf{e}_m$ and $\mathbf{n}'_l = \mathbf{e}_{m'}$, i.e., we use the “photon occupation vector” as an index instead of the mode number. Now we can expand the permanent in Eq. (1.69) as a sum over the set \mathfrak{S}_n of all permutations of n -tuples:

$$S_{\mathbf{n}, \mathbf{n}'}^{(n)} = \frac{1}{C_{\mathbf{n}} C_{\mathbf{n}'}} \sum_{\sigma \in \mathfrak{S}_n} \prod_{k=1}^n S_{\mathbf{n}_k, \mathbf{n}'_{\sigma(k)}}. \quad (1.71)$$

The single-photon scattering matrix coincides with the classical scattering matrix: For $\mathbf{n} \in \mathcal{F}_1^N$ we find $C_{\mathbf{n}} = 1$ and thus $\mathbf{S}^{(1)} = \mathbf{S}$. Yet, the scattering of coherent states is physically different from the scattering of single-photon states. In the former case, the scattering matrix acts on the space of coherent amplitudes $\boldsymbol{\alpha} \in \mathbb{C}^N$, whereas in the latter case, the scattering matrix acts on the space of normalized coefficient vectors $\boldsymbol{\psi} \in \mathbb{C}^N$.

Chapter 2

Micromanipulation

2.1 Classical Optical Micromanipulation

The development of optical tweezers [136–139] triggered a whole research area concerned with manipulating, pushing, trapping or cooling small particles with light. The fields of application range from physics to biology and medicine [19, 140–145]. Micromanipulation of targets located behind or within a complex scattering medium is a challenging task, which can be tackled using the wavefront shaping techniques mentioned in Subsec. 1.1.1 [16, 18, 20, 146].

In the remaining section, we especially focus on the approach developed in Refs. [14, 20] using the so-called generalized Wigner-Smith matrix. The discussion in this chapter is largely based on Ref. [147], where the analytical and numerical calculations were carried out by the author of this thesis, the project was proposed by Stefan Rotter and Ulf Leonhardt and the manuscript was written by the author of this thesis with input from Ulf Leonhardt, Stefan Rotter and Dorian Bouchet.

As was first shown in the pioneering work by Eisenbud, Wigner and Smith [148–150], the scattering matrix provides unique access to the time spent by waves in the scattering process through the Wigner-Smith time delay matrix,

$$\mathbf{Q}_\omega := -i\mathbf{S}^\dagger \partial_\omega \mathbf{S}, \quad (2.1)$$

involving the frequency derivative of the scattering matrix. The so-called “proper delay times” are defined as the eigenvalues of this Hermitian matrix [151, 152] and the corresponding eigenstates, also known as “principal modes” [153], are the input vectors for the scattering states associated with these well-defined delay times. For instance, in an empty waveguide (see Eq. (1.21)) the Wigner-Smith time delay matrix is diagonal, $(\mathbf{Q}_\omega)_{m,m} = (L/c)(k/k_m^x)$, which means that the principal modes are given by the standard waveguide modes (1.11) and the proper delay times are the ballistic times of the corresponding classical trajectories, see Fig. 1.2.

It turns out that the Wigner-Smith time delay matrix can be generalized to involve, instead of the frequency derivative, a derivative with respect to any other parameter θ that the scattering matrix depends on. The generalized Wigner-Smith

(GWS) matrix³, defined as

$$\mathbf{Q}_\theta := -i\mathbf{S}^\dagger \partial_\theta \mathbf{S}, \quad (2.2)$$

is a Hermitian matrix if \mathbf{S} is unitary:

$$\partial_\theta (\mathbf{S}^\dagger \mathbf{S}) = (\partial_\theta \mathbf{S})^\dagger \mathbf{S} + \mathbf{S}^\dagger \partial_\theta \mathbf{S} = \mathbf{0} \implies \mathbf{Q}_\theta^\dagger = i(\partial_\theta \mathbf{S})^\dagger \mathbf{S} = -i\mathbf{S}^\dagger \partial_\theta \mathbf{S} = \mathbf{Q}_\theta. \quad (2.3)$$

Instead of the time delay — as the conjugate quantity to frequency — the GWS matrix provides access to the physical observable associated with the conjugate quantity to θ [14, 20]. Let θ , e.g., be a certain geometric parameter of the scattering system like the position or the rotation angle of a target. In this case, the expectation value $\boldsymbol{\alpha}^\dagger \mathbf{Q}_\theta \boldsymbol{\alpha}$ is proportional to the mean force or torque, respectively, acting on this target, given the input state $\boldsymbol{\alpha}$.

Since \mathbf{Q}_θ is Hermitian, its eigenvalues λ_i are real-valued and its eigenvectors \mathbf{w}_i form an orthonormal basis of \mathbb{C}^N :

$$\mathbf{Q}_\theta \mathbf{w}_i = \lambda_i \mathbf{w}_i \iff \mathbf{Q}_\theta = \mathbf{W} \boldsymbol{\Lambda} \mathbf{W}^\dagger. \quad (2.4)$$

The eigenvectors \mathbf{w}_i are the input states that deliver a certain generalized force conjugate to θ that is proportional to the corresponding eigenvalues λ_i . Consequently, the eigenvector of the GWS matrix with the largest eigenvalue provides the incoming wavefront that couples to the parameter θ most strongly and thus constitutes the optimal wave state for micromanipulating this target, as demonstrated also in a recent experiment [20]. The GWS matrix can, however, also be applied in a much broader context such as for the optimal cooling of an ensemble of particles [154], for the identification of channels that are resilient to disorder [155], or for the optimal retrieval of information on the system parameter θ in an arbitrarily complex scattering environment [23]. Building on the concept of Fisher information, it turns out that the matrix that quantifies this information is given by the square of the GWS matrix — thereby providing a strong link between information theory and measurement backaction, as is elaborated in Sec. 3.3.

Quite remarkably, the GWS matrix provides access to the pivotal quantities for manipulating a target without any knowledge of the target’s near field; only the scattering amplitudes in the far field and their dependence on the relevant parameter θ are required. Since no direct access to the target scatterer is necessary in this way, this target may also be hidden behind or inside a complex medium like a disordered material. Note that, for accessing the θ -dependence of the scattering matrix, a small, controlled variation of θ must occur in the system. There are many ways of how this can be achieved in practice, such as by externally induced forces (using acoustic, magnetic or gravitational fields [156–159]) or by autonomous movement [154, 160, 161].

³In Refs. [14, 20] this quantity is referred to as the “generalized Wigner-Smith operator”, but we rather call it a *matrix* and we reserve the term *operator* to true quantum operators.

The findings above hold for monochromatic light. In case of a broadband signal $\alpha(\omega)$, one has to integrate over the individual spectral components in order to obtain the total conjugate force (see also Eq. (2.17) in Subsec. 2.2.1)

$$K_\theta = \frac{\hbar}{2\pi} \int_0^\infty \alpha^\dagger(\omega) \mathbf{Q}_\theta(\omega) \alpha(\omega) d\omega. \quad (2.5)$$

In most experiments it is unfeasible to measure the complete unitary scattering matrix due to the limited numerical aperture (NA) of the illumination or the detectors. However, starting from a subunitary scattering matrix, one can still find good approximations for optimal states for micromanipulation [20].

To illustrate explicitly how the GWS matrix is employed for micromanipulation, we turn to the generic example introduced at the end of Subsec. 1.1.2. For the parameter θ we choose three realizations that we consider separately: horizontal displacement of the target ($\theta = x$), vertical displacement of the target ($\theta = y$) and counterclockwise rotation of the target about its center ($\theta = \varphi$). In the numerical simulation, we have to implement a small change $\delta\theta$ in order to obtain the GWS matrix \mathbf{Q}_θ using a finite difference approximation for the θ -derivative. This change must be small enough such that the finite difference approximation is appropriate, but it must not be too small, because otherwise numerical inaccuracies would become dominant. To find good values for $\delta\theta$, we make use of the Hermiticity of \mathbf{Q}_θ . We calculate the Frobenius norm $\|\mathbf{Q}_\theta - \mathbf{Q}_\theta^\dagger\|_F$, which should ideally be zero, for different values of $\delta\theta$ and choose the one that leads to a minimum, see Fig. 2.1(a).

Figures 2.1(b), 2.1(c) and 2.1(d) show the spatial intensity distribution of the wave that emerges when injecting eigenstates of \mathbf{Q}_x into the system corresponding to the maximum, minimum and closest-to-zero eigenvalue, respectively. In the immediate vicinity of the target, regions of high intensity exert a force onto the target. It is apparent that the waves in Figs. 2.1(b) and 2.1(c) lead to a force pointing to the right and left, respectively. The wave in Fig. 2.1(d) avoids any interaction with the target. This is also the case for $\theta = y$ and $\theta = \varphi$, which is why we show the case of avoided interaction only for $\theta = x$.

Figures 2.2(a) and 2.2(b) show the eigenstates of \mathbf{Q}_y corresponding to the maximum and minimum eigenvalue, respectively. It turns out that the minimum eigenstate also exerts a substantial horizontal force $\langle \mathbf{Q}_x \rangle$ onto the target. (In the following, we use the shorthand notation $\langle \mathbf{Q}_\theta \rangle = \alpha^\dagger \mathbf{Q}_\theta \alpha$ for mean conjugate forces — the state α should be clear from the context.) The 2nd minimum eigenstate shown in Fig. 2.2(c) also exhibits a finite horizontal force, but in the opposite direction. Thus, we can take a suitable (classical) superposition of the minimum and the 2nd minimum eigenstate to achieve $\langle \mathbf{Q}_x \rangle = 0$, see Fig. 2.2(d).

Figures 2.3(a), 2.3(b) and 2.3(c) show the eigenstates of \mathbf{Q}_φ corresponding to the maximum, minimum and 3rd maximum eigenvalue, respectively. The latter is (classically) superimposed with the maximum eigenstate such that the total force $(\langle \mathbf{Q}_x \rangle^2 + \langle \mathbf{Q}_y \rangle^2)^{1/2}$ onto the target is minimized, see Fig. 2.3(d).

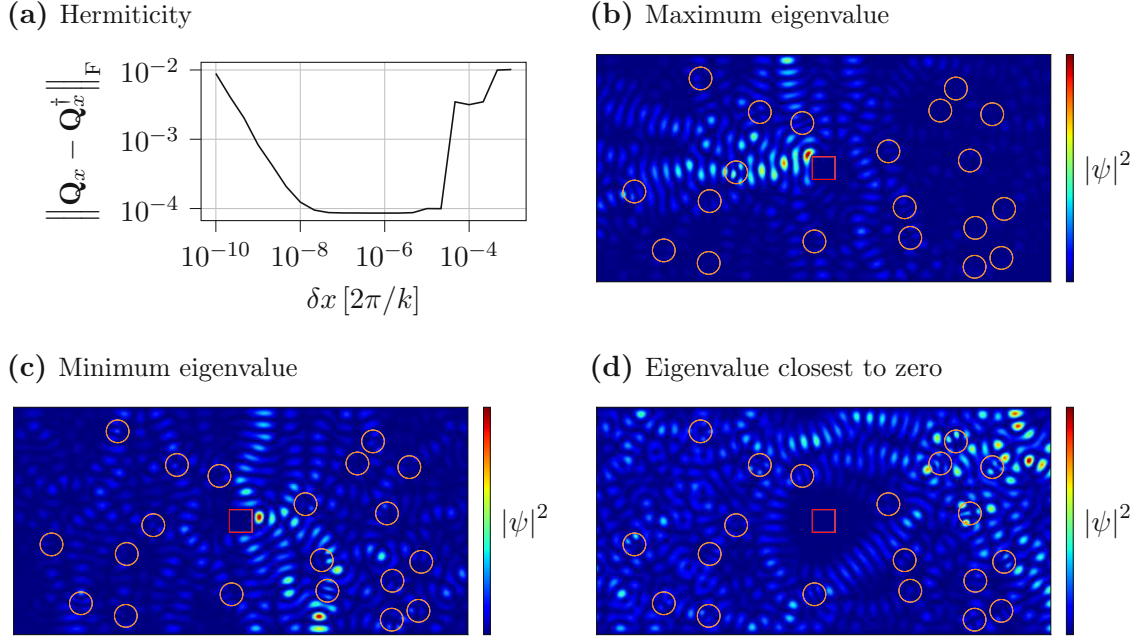


Figure 2.1: Classical optical micromanipulation with $\theta = x$ being the horizontal position of the target (red square). The corresponding GWS matrix \mathbf{Q}_x and its eigenvalues quantify the horizontal momentum transfer onto the target. (a) The small finite shift δx needed for the numerical calculation of the GWS matrix \mathbf{Q}_x is chosen such that \mathbf{Q}_x is Hermitian with as little error as possible. This is achieved by minimizing the Frobenius norm $\|\mathbf{Q}_x - \mathbf{Q}_x^\dagger\|_F$. (b) Spatial intensity distribution of the emerging wave when the eigenstate corresponding to the maximum eigenvalue $\lambda_i \approx 137.8 W^{-1}$ is injected into the system. In the regions of high intensity close to the target, the wave exerts a local force onto the target. (c) Same as (b), but for the minimum eigenvalue $\lambda_i \approx -92.04 W^{-1}$. (d) Same as (b), but for the eigenvalue closest to zero, $\lambda_i \approx 3.289 \cdot 10^{-7} W^{-1}$.

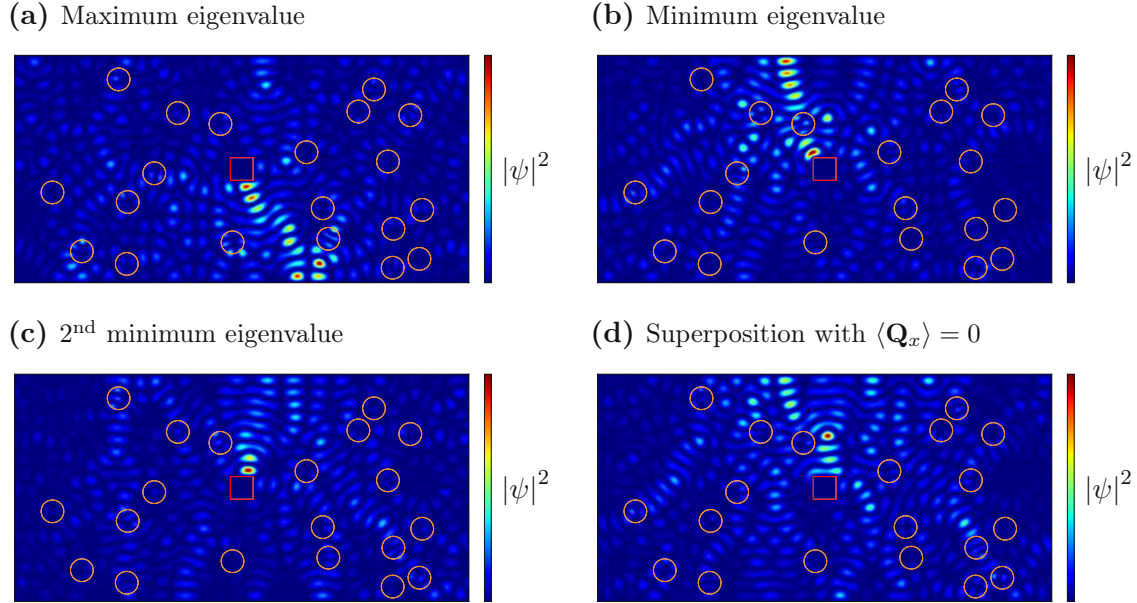


Figure 2.2: Classical optical micromanipulation with $\theta = y$ being the vertical position of the target (red square). The corresponding GWS matrix \mathbf{Q}_y and its eigenvalues quantify the vertical momentum transfer onto the target. **(a)** Spatial intensity distribution of the emerging wave when the eigenstate corresponding to the maximum eigenvalue $\lambda_i \approx 123.3 W^{-1}$ is injected into the system. In the regions of high intensity close to the target, the wave exerts a local force onto the target. **(b)** Same as **(a)**, but for the minimum eigenvalue $\lambda_i \approx -137.2 W^{-1}$. The horizontal momentum transfer is proportional to $\langle \mathbf{Q}_x \rangle \approx 70.77 W^{-1}$. **(c)** Same as **(a)**, but for the second minimum eigenvalue $\lambda_i \approx -116.5 W^{-1}$. Here, $\langle \mathbf{Q}_x \rangle \approx -13.26 W^{-1}$. **(d)** Classical superposition of the states shown in **(b)** and **(c)** such that $\langle \mathbf{Q}_x \rangle = 0$. The vertical momentum transfer is proportional to $\langle \mathbf{Q}_y \rangle \approx -127.8 W^{-1}$.

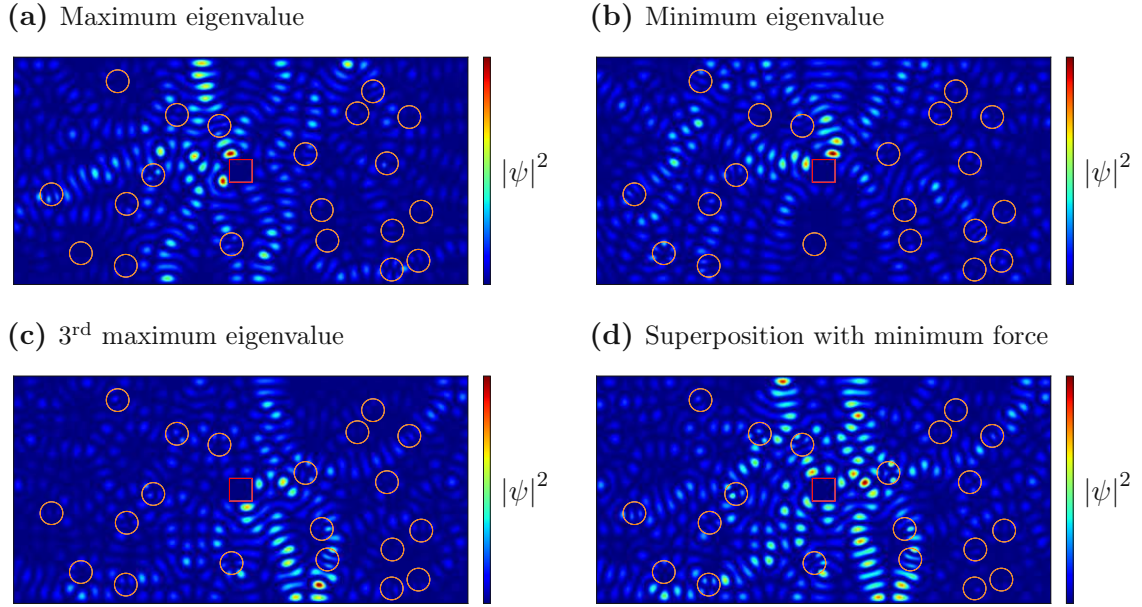


Figure 2.3: Classical optical micromanipulation with $\theta = \varphi$ being the angular orientation of the target (red square). The corresponding GWS matrix \mathbf{Q}_φ and its eigenvalues quantify the counterclockwise angular momentum transfer onto the target. (a) Spatial intensity distribution of the emerging wave when the eigenstate corresponding to the maximum eigenvalue $\lambda_i \approx 3.491$ is injected into the system. In the regions of high intensity close to the target, the wave exerts a local force onto the target. These local forces act near the corners of the target, thereby resulting in a torque. The horizontal and vertical momentum transfer is proportional to $\langle \mathbf{Q}_x \rangle \approx 55.35 W^{-1}$ and $\langle \mathbf{Q}_y \rangle \approx -37.89 W^{-1}$, respectively. (b) Same as (a), but for the minimum eigenvalue $\lambda_i \approx -3.265$. (c) Same as (a), but for the third maximum eigenvalue $\lambda_i \approx 2.139$. Here, $\langle \mathbf{Q}_x \rangle \approx -35.30 W^{-1}$ and $\langle \mathbf{Q}_y \rangle \approx 64.54 W^{-1}$. (d) Classical superposition of the states shown in (a) and (c) such that $(\langle \mathbf{Q}_x \rangle^2 + \langle \mathbf{Q}_y \rangle^2)^{1/2}$ is minimized. One obtains $\langle \mathbf{Q}_x \rangle \approx 10.35 W^{-1}$ and $\langle \mathbf{Q}_y \rangle \approx 8.698 W^{-1}$. The applied torque is proportional to $\langle \mathbf{Q}_\varphi \rangle \approx 2.386$.

2.2 Quantum Optical Micromanipulation

As discussed in Sec. 1.2, the optical light field is characterized by its quantum degrees of freedom on top of its spatial shape, thus widening the window of possibilities also in micromanipulation. In this section, we show how to integrate these quantum degrees of freedom into the framework established by the GWS matrix, and we explore how to harness them for improved micromanipulation procedures.

2.2.1 The Quantum Wigner-Smith Operator in General

Comparing Eq. (1.57) with Eq. (1.1), we see that the quantum unitary operator \hat{U} takes on the role of the classical scattering matrix \mathbf{S} for quantum states of light. This correspondence is emphasized by the close link between those two quantities as given in Eq. (1.65). Accordingly, we translate the GWS matrix \mathbf{Q}_θ from Eq. (2.2) into the quantum realm by replacing \mathbf{S} with \hat{U} to arrive at what we refer to as the quantum Wigner-Smith (QWS) operator:

$$\hat{Q}_\theta := -i\hat{U}^\dagger \partial_\theta \hat{U}. \quad (2.6)$$

In Lie group theory and quantum metrology this operator is known as a generator and has already been studied in detail [50, 51, 162]. The QWS operator directly inherits useful properties from the GWS matrix, like being Hermitian for unitary systems and its ability to express local phenomena in terms of the far field scattering amplitudes.

A first and natural application of the QWS operator lies in micromanipulation, in which domain the quantum degrees of freedom of light have, e.g., been used already to improve cooling protocols [163–166]. Here, we are interested in finding a state of light that, when injected into the scattering system, optimally couples to the system property described by θ , which can be any geometric or material parameter characterizing the scattering system as a whole or any part of it. Physically speaking, a coupling to θ implies that the quantity conjugate to θ is transferred between the light field and the scattering system. For instance, if θ represents a position, rotational angle or radius of a scatterer, the conjugate quantity is the linear momentum, angular momentum or pressure, respectively. In the following, we establish this physical interpretation of the QWS operator \hat{Q}_θ as the quantum operator describing the generalized force conjugate to θ . In general, a force is defined as the negative gradient of the Hamiltonian with respect to the parameter θ . So in order to arrive at the desired correspondence, we have to express the unitary quantum scattering operator \hat{U} in terms of the underlying Hamiltonian \hat{H} . This is a well-known result from formal scattering theory, typically formulated in terms of a scattering matrix [167], but it holds equally for the quantum operator \hat{U} following Refs. [168, 169],

$$\hat{U} = \hat{1} - 2\pi i \hat{W}^\dagger \hat{G} \hat{W}, \quad (2.7)$$

$$\hat{G} = \left(E - \hat{H}_{\text{eff}} \right)^{-1}, \quad (2.8)$$

$$\hat{H}_{\text{eff}} = \hat{H} - \pi i \hat{W} \hat{W}^\dagger, \quad (2.9)$$

where \hat{G} is the Green's operator in the interior of the scattering region, \hat{W} describes the coupling between the mode basis in the asymptotic region and the local basis at the boundary of the scattering region, $E = \hbar\omega$ is the photonic energy corresponding to the frequency ω and \hat{H}_{eff} is the effective Hamiltonian. In order to comprehend the connection to Ref. [169], we rewrite $\hat{U} = (\hat{1} - i\hat{K})(\hat{1} + i\hat{K})^{-1}$ with $\hat{K} = \pi\hat{W}^\dagger(E - \hat{H})^{-1}\hat{W}$. This representation is identical to Eqs. (2.50) and (2.51) from [169] by virtue of identifying $\hat{W} = Q\mathcal{H}P$ and $\hat{H} = Q\mathcal{H}Q$, where \mathcal{H} is the “full” Hamiltonian and Q and P are the projection operators onto the subspace of “bound” and “scattering” states, respectively.

Proceeding, we observe the following:

$$\begin{aligned} \hat{1} &= \left(E - \hat{H}_{\text{eff}} \right) \hat{G} \\ \implies \hat{G}^\dagger &= E\hat{G}^\dagger\hat{G} - \hat{G}^\dagger\hat{H}_{\text{eff}}\hat{G}, \end{aligned} \quad (2.10)$$

$$\begin{aligned} \hat{1} &= \hat{G}^\dagger \left(E - \hat{H}_{\text{eff}}^\dagger \right) \\ \implies \hat{G} &= E\hat{G}^\dagger\hat{G} - \hat{G}^\dagger\hat{H}_{\text{eff}}^\dagger\hat{G}, \end{aligned} \quad (2.11)$$

$$\begin{aligned} \implies \hat{G}^\dagger - \hat{G} &= \hat{G}^\dagger \left(\hat{H}_{\text{eff}}^\dagger - \hat{H}_{\text{eff}} \right) \hat{G} \\ &= 2\pi i \hat{G}^\dagger \hat{W} \hat{W}^\dagger \hat{G}. \end{aligned} \quad (2.12)$$

In the last step we used the Hermiticity of \hat{H} .

We assume that the coupling operator \hat{W} is independent of θ and thus

$$\partial_\theta \hat{U} = 2\pi i \hat{W}^\dagger \hat{G} \left(-\partial_\theta \hat{H} \right) \hat{G} \hat{W}. \quad (2.13)$$

Using Eqs. (2.12) and (2.13), it is straightforward to show that

$$\hat{Q}_\theta = 2\pi \hat{W}^\dagger \hat{G}^\dagger \left(-\partial_\theta \hat{H} \right) \hat{G} \hat{W}. \quad (2.14)$$

This equation already allows for the desired interpretation: The operator \hat{W} maps the asymptotic region to the boundary of the scattering system and the Green's operator \hat{G} describes the propagation inside the system. So indeed the QWS operator \hat{Q}_θ can be interpreted as the “asymptotic counterpart” to the local force $-\partial_\theta \hat{H}$. To illustrate this relation even further, it is convenient to write

$$|\psi^{\text{scat}}\rangle := \sqrt{\varepsilon} \hat{G} \hat{W} |\psi^{\text{in}}\rangle, \quad (2.15)$$

where $|\psi^{\text{in}}\rangle$ is the input state in the asymptotic region, $|\psi^{\text{scat}}\rangle$ is the scattering state in the interior of the system and ε is an auxiliary quantity with the physical unit of energy with the purpose of cancelling the physical units of \hat{G} (J^{-1}) and \hat{W} ($J^{1/2}$).

Combining Eqs. (2.14) and (2.15) yields

$$\langle \psi^{\text{scat}} | \left(-\partial_\theta \hat{H} \right) | \psi^{\text{scat}} \rangle = \frac{\varepsilon}{2\pi} \langle \psi^{\text{in}} | \hat{Q}_\theta | \psi^{\text{in}} \rangle, \quad (2.16)$$

which generalizes the central Eq. (2) in Ref. [20]. Note that this relation is evaluated at a single energy E . So in order to get the total force \hat{K}_θ , we have to integrate over the whole electromagnetic spectrum. The auxiliary ε is conveniently replaced by the infinitesimal measure dE :

$$\hat{K}_\theta = \frac{1}{2\pi} \int_0^\infty \hat{Q}_\theta dE. \quad (2.17)$$

One might very well question why we replace ε by dE without any further numerical factors. In Sec. 2.3 (see Eq. (2.71)) we derive the vacuum contribution to \hat{K}_θ with an independent calculation, which fixes the prefactor to $(2\pi)^{-1}$.

The relation (2.17) is fundamental and concise. It shows that the QWS operator is the proper object to describe the action of quantum light onto the scattering system. To be precise, the QWS operator is the spectral density of the generalized force.

2.2.2 The Quantum Wigner-Smith Operator for Passive Linear Systems

For general complex scattering systems it is practically impossible to assemble the QWS operator as defined in Eq. (2.6) since the evolution operator \hat{U} is typically unknown and also inaccessible experimentally — a problem addressed by quantum process tomography [97, 129–131]. Our idea to resolve this fundamental issue is to express Eq. (2.6) using the scattering matrix formalism given by Eq. (1.62). This is permissible for setups with passive linear optical elements only, where all the quantities are expressible in terms of the experimentally accessible scattering matrix. Note that the definition (2.6) of the QWS operator does not depend on whether it represents a linear or nonlinear optical process. Also, the connections between the QWS operator and the major quantities in this work, like the generalized force in Eq. (2.17) and the quantum Fisher information in Eq. (3.21), are still valid for nonlinear optical systems.

For passive linear processes, inserting the relation (1.62) yields one of the most important results of this thesis (a detailed derivation is given in App. B):

$$\hat{Q}_\theta = [\hat{a}^\dagger]^\top \mathbf{Q}_\theta [\hat{a}] + \frac{1}{2} \text{tr}(\mathbf{Q}_\theta). \quad (2.18)$$

This remarkably simple relation provides a straightforward operational procedure for translating the classical scattering amplitudes in the GWS matrix \mathbf{Q}_θ to a corresponding quantum operator \hat{Q}_θ . This is most directly seen in the first term on

the right hand side of Eq. (2.18), which simply couples the elements of the classical GWS matrix to the corresponding quantum channels, similar to the Jordan-Schwinger map [170, 171]. However, as a result of the nonlinear relation in Eq. (1.62), the normal ordering in Eq. (2.18) and the non-commutativity of the mode operators, we do find an additional scalar trace term that may seem irrelevant at first glance as it does not depend on the input channels, but it provides us with a powerful way of describing vacuum forces. This will be discussed in more detail in Sec. 2.3.

Next, we insert Eq. (2.18) into Eq. (2.17) and take the expectation value with respect to some input state of light $|\Psi^{\text{in}}\rangle$. It is to be understood that $|\Psi^{\text{in}}\rangle$ is composed of spectral components $|\psi_E^{\text{in}}\rangle$ from the whole energy spectrum. We can identify two contributions to the mean generalized force:

$$\langle \Psi^{\text{in}} | \hat{K}_\theta | \Psi^{\text{in}} \rangle = \frac{1}{2\pi} \int_0^\infty \langle \psi_E^{\text{in}} | [\hat{a}^\dagger]^\top \mathbf{Q}_\theta [\hat{a}] | \psi_E^{\text{in}} \rangle dE + \frac{1}{4\pi} \int_0^\infty \text{tr}(\mathbf{Q}_\theta) dE. \quad (2.19)$$

Remarkably, the second term is independent of the injected input state $|\Psi^{\text{in}}\rangle$. As a matter of fact, this term is solely due to the vacuum fluctuations of the electromagnetic field, as is discussed in more detail in Sec. 2.3. The first term, on the other hand, can be engineered by proper choice of the input state. One is free to select a single operating frequency or choose a frequency window at which one desires to perform micromanipulation. Thus, in the following, we focus on a single frequency component, i.e., monochromatic light.

2.2.3 Optimal Micromanipulation

In most applications, one is limited by the amount of energy that the system under study can get exposed to. Still, for those given resources, one may want to couple to a specific target inside the system as strongly as possible. In this sense, we aim for an *optimal* micromanipulation setup. In other words, given a fixed mean total photon number $\langle \hat{n} \rangle = \nu$, which is proportional to the mean total energy of the incident light (apart from the zero point energy, see Eq. (1.28)), the optimal state ought to exert the highest mean generalized force conjugate to θ on the scattering system, when compared to all other possible input states with the same mean total photon number:

$$\max_{|\psi^{\text{in}}\rangle, \langle \hat{n} \rangle = \nu} \langle \hat{Q}_\theta \rangle. \quad (2.20)$$

In Ref. [20] it is shown that for classical light one obtains the optimal spatial shape of the incident wavefront as the highest eigenvector (as sorted by the eigenvalues) of the corresponding GWS matrix \mathbf{Q}_θ . By employing the QWS operator \hat{Q}_θ we can substantially enlarge the toolbox provided in Ref. [20] by including the quantum properties of the injected light. The QWS operator unites the spatial and the

quantum degrees of freedom of scattered light fields such that we can describe and optimize them jointly to perform both micromanipulation and parameter estimation (see Sec. 3.3) at the optimal level of efficiency. The spatial structure is determined by the selection of occupied modes, whereas the quantum properties result from the quantum states that are fed into those modes.

As is apparent from the classical case, the eigenvectors and eigenvalues of $\mathbf{Q}_\theta = \mathbf{W}\mathbf{A}\mathbf{W}^\dagger$ play an essential role in finding optimal input states. Therefore, we introduce annihilation and creation operators \hat{b}_i and \hat{b}_i^\dagger that correspond to the eigenchannels of \mathbf{Q}_θ . This is achieved by the transformation

$$\begin{bmatrix} \hat{b} \end{bmatrix} := \mathbf{W}^\dagger [\hat{a}] \iff [\hat{a}] = \mathbf{W} \begin{bmatrix} \hat{b} \end{bmatrix}, \quad (2.21)$$

$$\begin{bmatrix} \hat{b}^\dagger \end{bmatrix} = \mathbf{W}^\top [\hat{a}^\dagger] \iff [\hat{a}^\dagger] = \mathbf{W}^* \begin{bmatrix} \hat{b}^\dagger \end{bmatrix}. \quad (2.22)$$

Due to the unitarity of \mathbf{W} , the new operators \hat{b}_i satisfy the same fundamental bosonic commutation relations as the \hat{a}_m :

$$\begin{bmatrix} \hat{b}_i, \hat{b}_{i'}^\dagger \end{bmatrix} = \sum_{m,m'=1}^N W_{m,i}^* W_{m',i'} [\hat{a}_m, \hat{a}_{m'}^\dagger] = \sum_{m=1}^N W_{m,i}^* W_{m,i'} = (\mathbf{W}^\dagger \mathbf{W})_{i,i'} = \delta_{i,i'}. \quad (2.23)$$

These new channel operators constitute the foundation of a new useful representation that we label with the symbol \mathcal{Q} (as opposed to the standard modal representation \mathcal{M}). For instance, we define, respectively, coherent states, squeezed states, Fock states and photon number states as

$$|\beta\rangle^{\mathcal{Q}} := \hat{D}_b(\beta) |\mathbf{0}\rangle, \quad (2.24)$$

$$|\beta, \Xi\rangle^{\mathcal{Q}} := \hat{D}_b(\beta) \hat{S}_b(\Xi) |\mathbf{0}\rangle, \quad (2.25)$$

$$|\mathbf{u}\rangle^{\mathcal{Q}} := \frac{1}{C_{\mathbf{u}}} \prod_{i=1}^N (\hat{b}_i^\dagger)^{u_i} |\mathbf{0}\rangle, \quad (2.26)$$

$$|\phi\rangle^{\mathcal{Q}} := \sum_{\mathbf{u} \in \mathcal{F}_n^N} \phi_{\mathbf{u}} |\mathbf{u}\rangle^{\mathcal{Q}}. \quad (2.27)$$

From a mathematical point of view, the transition (2.21) from the \mathcal{Q} to the \mathcal{M} representation is equivalent to a Bogoliubov transformation (see Eq. (1.58)), where \mathbf{W} takes on the role of the scattering matrix $\mathbf{A} \equiv \mathbf{S}$. We choose the physically irrelevant global phases of the eigenvectors such that $\det(\mathbf{W}) = 1$. Therefore, we can employ the results from Sec. 1.3 to establish the relationship between the state parameters in the different representations:

$$|\alpha\rangle^{\mathcal{M}} = |\beta\rangle^{\mathcal{Q}} \quad \text{for } \alpha = \mathbf{W}\beta, \quad (2.28)$$

$$|\alpha, \mathbf{Z}\rangle^{\mathcal{M}} = |\beta, \Xi\rangle^{\mathcal{Q}} \quad \text{for } \alpha = \mathbf{W}\beta, \mathbf{Z} = \mathbf{W}\Xi\mathbf{W}^\top, \quad (2.29)$$

$$|\psi\rangle^{\mathcal{M}} = |\phi\rangle^{\mathcal{Q}} \quad \text{for } \psi = \mathbf{W}^{(n)}\phi. \quad (2.30)$$

The matrix $\mathbf{W}^{(n)} \in \mathbb{C}^{\binom{N+n-1}{n} \times \binom{N+n-1}{n}}$ is constructed from \mathbf{W} the same way as the n -photon scattering matrix $\mathbf{S}^{(n)}$ is constructed from the classical scattering matrix \mathbf{S} , see Eq. (1.71). For the polar decomposition of the corresponding squeezing matrices $\mathbf{Z} = \mathbf{R}e^{i\Phi}$ and

$$\Xi = \mathbf{P}e^{i\Psi}, \quad (2.31)$$

we find

$$\mathbf{R} = \mathbf{W}\mathbf{P}\mathbf{W}^\dagger, \quad (2.32)$$

$$e^{i\Phi} = \mathbf{W}e^{i\Psi}\mathbf{W}^\top. \quad (2.33)$$

We see that coherent states, squeezed states and photon number states keep their classification across both representations, whereas Fock states are defined only w.r.t. a specific representation. In general, Fock states in a given representation are photon number states in another representation.

In the \mathcal{Q} representation, the QWS operator takes the simple form (see Eq. (2.18))

$$\begin{aligned} \hat{Q}_\theta &= \left[\hat{b}^\dagger\right]^\top \mathbf{W}^\dagger \mathbf{W} \Lambda \mathbf{W}^\dagger \mathbf{W} \left[\hat{b}\right] + \frac{1}{2} \text{tr}(\mathbf{W} \Lambda \mathbf{W}^\dagger) \\ &= \left[\hat{b}^\dagger\right]^\top \Lambda \left[\hat{b}\right] + \frac{1}{2} \text{tr}(\Lambda) \\ &= \sum_{i=1}^N \lambda_i \hat{b}_i^\dagger \hat{b}_i + \frac{1}{2} \sum_{i=1}^N \lambda_i. \end{aligned} \quad (2.34)$$

The operator

$$\hat{n}_i := \hat{b}_i^\dagger \hat{b}_i \quad (2.35)$$

counts the photons in the i^{th} eigenchannel of \mathbf{Q}_θ . We indicate the distinction to the modal photon number operators \hat{n}_m from Eq. (1.26) by using different indices (i or j as compared to m). The total photon number operator is again just the sum over the contributions from the channels:

$$\begin{aligned} \hat{n} &= \sum_{m=1}^N \hat{n}_m = \sum_{m=1}^N \hat{a}_m^\dagger \hat{a}_m = \left[\hat{a}^\dagger\right]^\top \left[\hat{a}\right] = \left[\hat{b}^\dagger\right]^\top \mathbf{W}^\dagger \mathbf{W} \left[\hat{b}\right] = \left[\hat{b}^\dagger\right]^\top \left[\hat{b}\right] \\ &= \sum_{i=1}^N \hat{b}_i^\dagger \hat{b}_i = \sum_{i=1}^N \hat{n}_i. \end{aligned} \quad (2.36)$$

This leads us to the physical interpretation that the QWS operator

$$\hat{Q}_\theta = \sum_{i=1}^N \lambda_i \hat{n}_i + \frac{1}{2} \text{tr}(\Lambda) \quad (2.37)$$

gives a weighted sum of the GWS eigenvalues λ_i , where the weights are given by the photon numbers in the respective eigenchannels, plus a scalar contribution from all eigenchannels. Furthermore, we see that the Fock states in the \mathcal{Q} representation are the eigenvectors of the QWS operator:

$$\hat{Q}_\theta |\mathbf{u}\rangle^{\mathcal{Q}} = \left(\lambda_{\mathbf{u}} + \frac{1}{2} \text{tr}(\mathbf{\Lambda}) \right) |\mathbf{u}\rangle^{\mathcal{Q}}, \quad (2.38)$$

where the eigenvalues are — up to the scalar contribution — given by

$$\lambda_{\mathbf{u}} := \sum_{i=1}^N \lambda_i u_i. \quad (2.39)$$

We now return back to the optimization problem (2.20). We see that the mean force depends only on the mean photon numbers in the GWS eigenchannels:

$$\langle \hat{Q}_\theta \rangle = \sum_{i=1}^N \lambda_i \langle \hat{n}_i \rangle + \frac{1}{2} \text{tr}(\mathbf{\Lambda}). \quad (2.40)$$

The constraint also involves only the the mean photon numbers:

$$\langle \hat{n} \rangle = \sum_{i=1}^N \langle \hat{n}_i \rangle = \nu. \quad (2.41)$$

The weighted sum of eigenvalues in Eq. (2.40) is maximized for

$$\langle \hat{n}_{i_{\max}} \rangle = \nu, \quad (2.42)$$

$$\forall i \neq i_{\max} : \langle \hat{n}_i \rangle = 0, \quad (2.43)$$

where i_{\max} indicates the maximal eigenvalue. Similarly, i_{\min} and i_{hav} indicate the minimal eigenvalue and the eigenvalue with the **highest absolute value**, respectively:

$$i_{\max} := \arg \max_{i \in \{1, \dots, N\}} \{\lambda_i\}_{i=1}^N, \quad (2.44)$$

$$i_{\min} := \arg \min_{i \in \{1, \dots, N\}} \{\lambda_i\}_{i=1}^N, \quad (2.45)$$

$$i_{\text{hav}} := \arg \max_{i \in \{1, \dots, N\}} \{|\lambda_i|\}_{i=1}^N. \quad (2.46)$$

The solution of the maximization problem is specified just by the mean photon numbers in the GWS eigenchannels and not by any higher order statistics. This means that there is a degeneracy regarding the optimal input state: Injecting all photonic resources into the channel corresponding to the highest GWS eigenvalue

$\lambda_{i_{\max}}$ is sufficient for reaching optimality, the specific type of quantum state that is injected into this channel is irrelevant. The optimal state has a well-defined spatial shape which matches the classical optimum. (For numerical examples, see Sec. 2.1.) However, higher moments of the generalized force are influenced by the photon statistics, which is dictated by the injected quantum state, as shown further below. Similar reasoning can also be applied to obtain the minimum rather than the maximum, corresponding to a force acting in the opposite direction.

To become more specific, the mean force for Gaussian input states is given by (see Eq. (1.42))

$${}^{\mathcal{Q}}\langle\boldsymbol{\beta}, \Xi|\hat{Q}_\theta|\boldsymbol{\beta}, \Xi\rangle^{\mathcal{Q}} = \sum_{i=1}^N \lambda_i \left(|\beta_i|^2 + (\sinh^2(\mathbf{P}))_{i,i} \right) + \frac{1}{2} \text{tr}(\boldsymbol{\Lambda}) \quad (2.47)$$

$$= \boldsymbol{\beta}^\dagger \boldsymbol{\Lambda} \boldsymbol{\beta} + \text{tr}(\boldsymbol{\Lambda} \sinh^2(\mathbf{P})) + \frac{1}{2} \text{tr}(\boldsymbol{\Lambda}). \quad (2.48)$$

In the modal representation, this translates to (see Eqs. (2.4), (2.29) and (2.32))

$${}^{\mathcal{M}}\langle\boldsymbol{\alpha}, \mathbf{Z}|\hat{Q}_\theta|\boldsymbol{\alpha}, \mathbf{Z}\rangle^{\mathcal{M}} = \boldsymbol{\alpha}^\dagger \mathbf{Q}_\theta \boldsymbol{\alpha} + \text{tr}(\mathbf{Q}_\theta \sinh^2(\mathbf{R})) + \frac{1}{2} \text{tr}(\mathbf{Q}_\theta). \quad (2.49)$$

For photon number states, the mean force is most conveniently expressed in the \mathcal{Q} representation (see Eq. (2.39)):

$${}^{\mathcal{Q}}\langle\phi|\hat{Q}_\theta|\phi\rangle^{\mathcal{Q}} = \sum_{i=1}^N \lambda_i \sum_{\mathbf{u} \in \mathcal{F}_n^N} |\phi_{\mathbf{u}}|^2 u_i + \frac{1}{2} \text{tr}(\boldsymbol{\Lambda}) \quad (2.50)$$

$$= \sum_{\mathbf{u} \in \mathcal{F}_n^N} |\phi_{\mathbf{u}}|^2 \lambda_{\mathbf{u}} + \frac{1}{2} \text{tr}(\boldsymbol{\Lambda}). \quad (2.51)$$

The considerations above focus on the mean force only. However, for precise nanoscale micromanipulation, like trapping, levitating or cooling particles, the fluctuations of the force must be minimized. These fluctuations are measured by the variance of the generalized force operator \hat{K}_θ . The main idea is to exploit the degeneracy of the optimal input state mentioned after Eq. (2.46). To illustrate this idea, we make the very crude approximation that contributions from different parts of the frequency spectrum are independent of each other. Interspectral correlations always exist [9, 172], but they are neglected here for simplicity. This way the variance of \hat{K}_θ is just the integrated variance of the QWS operator \hat{Q}_θ . (In Sec. 3.3 we showcase the close relationship between this variance and the so-called quantum Fisher information, a central quantity in quantum metrology.) The degeneracy elucidated after Eq. (2.46) gives us room to choose the quantum parameters of the input state in such a way as to minimize the variance of \hat{Q}_θ while keeping its expectation value constant.

For photon number states, this variance can in principle be reduced to zero if all photons are put into a single GWS eigenchannel. Since there is a well-defined number of photons, the variance vanishes in this case. However, if there are more than three photons involved, this becomes impractical in the experiment.

For Gaussian states it turns out that for any fixed mean photon number ν there is a nontrivial mixture of coherent amplitude and squeezing that results in a minimal variance of \hat{Q}_θ , which we derive in the following. Here, we consider only Gaussian states that populate a single channel, namely i_{\max} :

$$\boldsymbol{\beta} = \beta \mathbf{e}_{i_{\max}}, \quad (2.52)$$

$$\boldsymbol{\Xi} = p e^{i\psi} \mathbf{e}_{i_{\max}} \mathbf{e}_{i_{\max}}^\top. \quad (2.53)$$

The variance of \hat{Q}_θ w.r.t. a general multi-mode Gaussian state is calculated in App. C. For the single-mode Gaussian state relevant here, we obtain

$$\begin{aligned} \mathbb{V}_{|\boldsymbol{\beta}, \boldsymbol{\Xi}\rangle^{\mathcal{Q}}} [\hat{Q}_\theta] &= \lambda_{i_{\max}}^2 (|\beta|^2 + \sinh^2(p) + \cosh^2(p) \sinh^2(p) + \sinh^4(p) \\ &\quad - 2 \cosh(p) \sinh(p) \Re(\beta^{*2} e^{i\psi}) + 2|\beta|^2 \sinh^2(p)) \\ &= \lambda_{i_{\max}}^2 (|\beta|^2 \cosh(2p) + 2 \cosh^2(p) \sinh^2(p) \\ &\quad - 2 \cosh(p) \sinh(p) \Re(\beta^{*2} e^{i\psi})). \end{aligned} \quad (2.54)$$

We want to minimize this expression by adjusting the state parameters $\beta \in \mathbb{C}$ (coherent amplitude), $p \geq 0$ (squeezing strength) and $\psi \in [0, 2\pi)$ (double squeezing angle), subject to the constraint

$$\langle \boldsymbol{\beta}, \boldsymbol{\Xi} | \hat{n} | \boldsymbol{\beta}, \boldsymbol{\Xi} \rangle^{\mathcal{Q}} = |\beta|^2 + \sinh^2(p) = \nu. \quad (2.55)$$

The squeezing angle appears only at a single place in Eq. (2.54), so we start our minimization procedure with it. Since $\cosh(p) \sinh(p) \geq 0$, the overall variance is minimized by choosing $\psi = 2 \arg(\beta)$, resulting in $\Re(\beta^{*2} e^{i\psi}) = |\beta|^2$. The condition $\psi/2 = \arg(\beta)$ amounts to amplitude squeezing (see Fig. 1.4(b)). This result agrees with the intuition that the fluctuations in the force are minimized by squeezing the amplitude of the Gaussian input state. The remaining task is to minimize the expression

$$|\beta|^2 e^{-2p} + 2 \cosh^2(p) \sinh^2(p). \quad (2.56)$$

Inserting the constraint into this expression yields

$$\min_{p \in [0, \operatorname{arsinh}(\sqrt{\nu})]} (\nu e^{-2p} + \sinh^2(p) (1 + \sinh(2p))). \quad (2.57)$$

This minimization problem has a unique nontrivial yet analytically expressible solution for all $\nu \geq 0$, found with the help of Wolfram Mathematica:

$$|\beta_{\text{opt}}(\nu)| = \sqrt{\nu - \sinh^2(p_{\text{opt}}(\nu))}, \quad (2.58)$$

$$p_{\text{opt}}(\nu) = \frac{1}{2} \ln \left(\frac{1}{2} \left(\sqrt{g(\nu)} + \sqrt{\frac{4(1+2\nu)}{\sqrt{g(\nu)}} - g(\nu)} \right) \right), \quad (2.59)$$

$$g(\nu) := \frac{4}{h(\nu)} + \frac{h(\nu)}{3}, \quad (2.60)$$

$$h(\nu) := \left(54(1+2\nu)^2 + \sqrt{2916(1+2\nu)^4 - 1728} \right)^{1/3}. \quad (2.61)$$

The functions $g(\nu)$ and $h(\nu)$ are mere mathematical auxiliary functions. A plot of $|\beta_{\text{opt}}(\nu)|$ and $p_{\text{opt}}(\nu)$ is given in Figs. 2.4(a) and 2.4(b), respectively.

We now compare this result to the optimal classical (i.e. “unsqueezed”) coherent state. Demanding $p = 0$ yields $|\beta_{\text{opt}}(\nu)| = \sqrt{\nu}$. We evaluate the square root of the target function, which is the standard deviation of the QWS operator, on the one hand for the best Gaussian state and on the other hand for the best classical coherent state, and show the quotient of these two quantities as a function of ν in Fig. 2.4(c). It turns out that the advantage of the Gaussian state is substantial albeit the comparatively little effort: Beyond a mean photon number of $\nu = 49$, the standard deviation is reduced by more than half despite the required squeezing strength p being not extraordinarily high ($p_{\text{opt}} \approx 7.65$ dB for $\nu = 49$) and growing only logarithmically with ν :

$$p_{\text{opt}}(\nu) = \frac{1}{6} \ln(4\nu) + O\left(\frac{1}{\nu}\right). \quad (2.62)$$

The optimal coherent amplitude is close to the classical one:

$$|\beta_{\text{opt}}(\nu)| = \sqrt{\nu} + O\left(\frac{1}{\nu^{1/6}}\right). \quad (2.63)$$

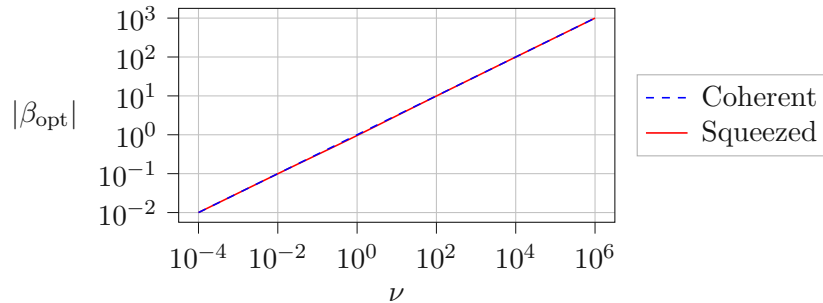
In this section, we demonstrated that knowing the classical scattering matrix and its θ -dependence of a passive linear, unitary, multi-mode system is sufficient for identifying the optimal quantum state for micromanipulation. The mean generalized force is fixed by the mean photon number, but its variance and higher moments can be influenced by shaping the quantum degrees of freedom of the employed light field.

2.3 Vacuum Forces

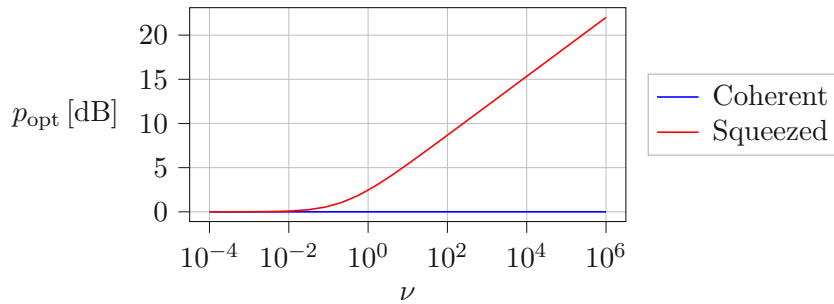
The QWS operator \hat{Q}_θ describes the forces of the radiation field upon the parameter θ . In this section, we aim to clarify the physical meaning of the trace term appearing in Eq. (2.18). Note that this term is precisely the vacuum expectation value of \hat{Q}_θ :

$$\langle \mathbf{0} | \hat{Q}_\theta | \mathbf{0} \rangle = \frac{1}{2} \text{tr}(\mathbf{Q}_\theta). \quad (2.64)$$

(a) Optimal coherent amplitude



(b) Optimal squeezing strength



(c) Noise reduction

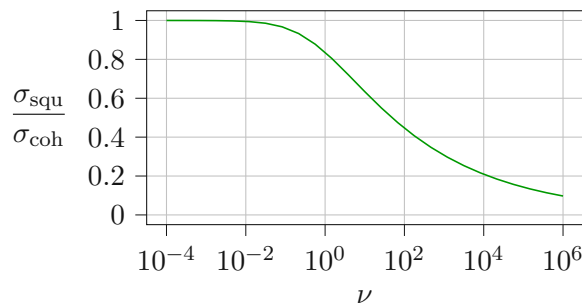


Figure 2.4: Optimal micromanipulation with Gaussian states of light. The fluctuations in the generalized force are minimized after the mean force has been maximized. The only relevant channel is the one corresponding to the largest eigenvalue of the GWS matrix. (a) The absolute values of the coherent amplitudes $|\beta_{\text{opt}}|$ are shown as a function of the mean photon number ν for the optimal coherent state and the optimal squeezed state, respectively. The phases of the coherent amplitudes can be chosen arbitrarily. (b) The squeezing strengths p_{opt} of the optimal coherent state and the optimal squeezed state are shown. The squeezing angle has to be chosen such that the amplitude is squeezed. The optimal coherent state shows no squeezing by definition. (c) Noise reduction factor when using the optimal squeezed input state as compared to the optimal coherent input state. Here, σ denotes the standard deviation of the QWS operator.

One might be inclined to remove this term from Eq. (2.18) because it stems from the factor $\sqrt{\det(\mathbf{S})}$ in Eq. (1.62), see derivation in Eq. (B.20), and neglecting this factor does not change the defining behaviour of \hat{U} given in Eq. (1.58). However, in this section we show that the trace term *does* have a physical meaning with a distinguished history: it describes the forces of the quantum vacuum [53, 54, 173, 174]. These are the generalized van der Waals forces [53, 175], the Casimir forces between two or more dielectric bodies [52] or the Casimir-Polder forces between two molecules [176]. Or, as θ can be rather general, these are the torques between birefringent plates [177], or the capillary forces [53] that lift up water to the leaves of trees (limiting the maximal height to which trees can grow [178]) or they might even constitute the force that accelerates the expansion of the universe [179, 180].

First, we give an intuitive heuristic explanation of the nature of vacuum forces. Zero-point fluctuations of the electromagnetic field manifest themselves as omnipresent virtual photons that equally populate all modes at all frequencies. For a specific frequency, this leads to a (nonvirtual, i.e., real) force which is an equally weighted sum over all contributions from all the modes. Mathematically, this is expressed by the trace

$$\text{tr}(\mathbf{Q}_\theta) = \sum_{m=1}^N \mathbf{e}_m^\dagger \mathbf{Q}_\theta \mathbf{e}_m. \quad (2.65)$$

Here, \mathbf{e}_m are the unit basis vectors describing the modes of the electromagnetic field. The surprising consequence of this trace term is that a finite force is transmitted onto a target even when no light is injected into the system at all.

To see on a more technical level that the trace of the GWS matrix describes the vacuum forces, we re-derive the latter from first principles. Consider the scattering phase η defined as the sum of all eigenphases η_k of the unitary scattering matrix \mathbf{S} with eigenvalues $e^{i\eta_k}$:

$$\eta = \sum_{k=1}^N \eta_k = -i \text{tr}(\ln(\mathbf{S})) = -i \ln(\det(\mathbf{S})). \quad (2.66)$$

The scattering phase, in turn, provides direct access to the density of states $\rho(E)$ according to Krein's trace formula [181, 182],

$$\rho(E) = \rho_0(E) + \frac{1}{2\pi} \partial_E \eta, \quad (2.67)$$

where $\rho_0(E)$ is the density of states for free space which is independent of θ . Since

$$\partial_\theta \eta = -i \text{tr}(\mathbf{S}^\dagger \partial_\theta \mathbf{S}) = \text{tr}(\mathbf{Q}_\theta) \quad (2.68)$$

for arbitrary θ (including $\theta = E$), we have:

$$\rho(E) = \rho_0(E) + \frac{1}{2\pi} \text{tr}(\mathbf{Q}_E). \quad (2.69)$$

Now, the vacuum force K_θ^{vac} upon θ is the negative gradient of the vacuum energy with respect to θ :

$$K_\theta^{\text{vac}} = -\partial_\theta \int_0^\infty \frac{E}{2} \rho(E) dE = -\frac{1}{4\pi} \int_0^\infty E (\partial_E \partial_\theta \eta) dE. \quad (2.70)$$

Integrating by parts and using Eq. (2.68) gives

$$K_\theta^{\text{vac}} = \frac{1}{4\pi} \int_0^\infty \text{tr}(\mathbf{Q}_\theta) dE = \langle 0 | \hat{K}_\theta | 0 \rangle. \quad (2.71)$$

This formula agrees with our finding in Eq. (2.19). It relates the classical GWS matrix \mathbf{Q}_θ to the vacuum force and constitutes the main result of this section. In deriving it by partial integration, we assumed that $\text{tr}(\mathbf{Q}_\theta)$ vanishes for $E \rightarrow \infty$ (or is infinitely oscillatory such that it vanishes effectively). This assumption is based on the physical fact that the vacuum forces originate from reflections between scatterers [54] and that those reflections vanish for $E \rightarrow \infty$ due to dispersion [183]. Our result is in accordance with the established literature dealing with the relationship between scattering theory and vacuum forces [184, 185].

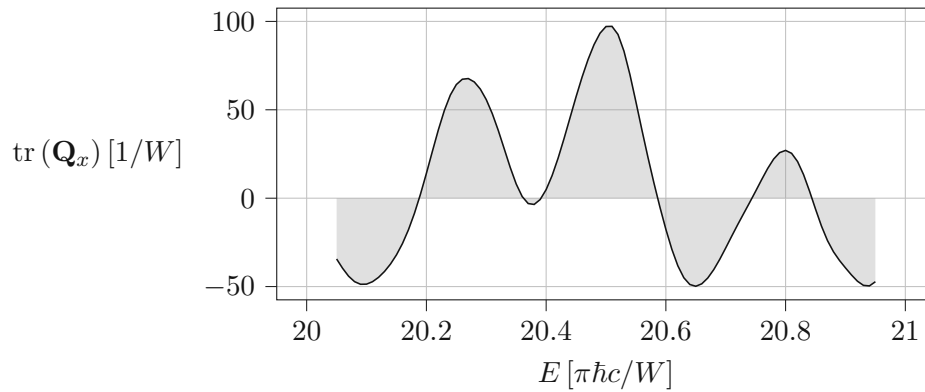
Physically motivated renormalization methods have been suggested right from the beginning of Casimir physics research in the late 1940's. Casimir himself [52] extracted the part of the vacuum energy that can do physical work by taking the difference between a finite and an infinite cavity, which he interpreted as the difference between the sum and the integral of the corresponding eigen-energies, which turns out to agree with the result of zeta function renormalization. Taking the difference between vacuum energies for finite and infinite distances is also the basis for renormalization in modern numerical methods for calculating the Casimir force between arbitrary dielectric bodies [186]. But this renormalization method cannot determine the Casimir force of the dielectric upon itself, in particular in inhomogeneous media [187–189], because one cannot take such media apart to infinity for determining their intrinsic vacuum stresses. As for inhomogeneous media, Ref. [187] shows that the simple ansatz of discretizing such media into small homogeneous sections does not converge in the continuum limit. The QWS operator may serve as a starting point to overcome these problems and to provide an understanding of the physical phenomena that underlie mathematical renormalization procedures [190].

Formula (2.71) may also give practical advantages in calculating vacuum forces, especially when only a few modes are relevant. Consider here, in particular, already established frameworks for calculating Casimir forces as in Ref. [186], which contain expressions seemingly similar to those in Eq. (2.71). Notably, however, such preceding methods involve the Green's function between all surface elements of the discretized bodies, whereas for our approach it is sufficient to know the asymptotic scattering matrix, which is essentially the Green's function between the far field modes.

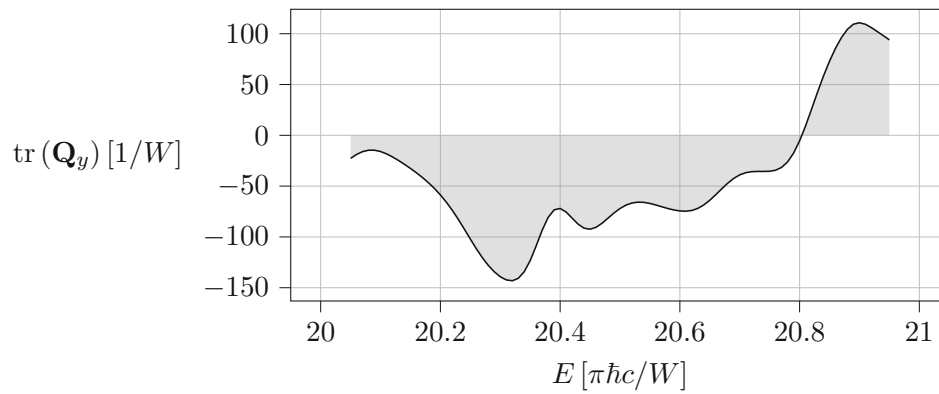
To give a concrete example, we consider the generic setup specified in Subsec. 1.1.2. Placed at the center of a waveguide, a metallic square-shaped scatterer is surrounded by several circular scatterers that cause strong scattering, see also Fig. 1.3. For simplicity, we assume that all scatterers are dispersion-free, i.e., their refractive indices do not depend on the frequency $\omega = E/\hbar$. Figure 2.5(a) displays the spectral contributions to the horizontal component of the vacuum force, which is given by the trace of the corresponding GWS matrix \mathbf{Q}_x (apart from a factor of 4π), see also Eq. (2.71). The plot covers the spectral range where $N = 40$ modes are open. For realistic materials, dispersion provides a cutoff, leading to a finite relevant spectral range. Figures 2.5(b) and 2.5(c) show the spectral contributions to the vertical component of the vacuum force and to the vacuum torque acting on the target, respectively.

In this section, we explained how the QWS operator establishes a connection between vacuum physics and classical electromagnetic scattering. This opens up the possibility to gain a deeper understanding of the physical mechanisms behind renormalization schemes from a new perspective.

(a) Horizontal force



(b) Vertical force



(c) Torque

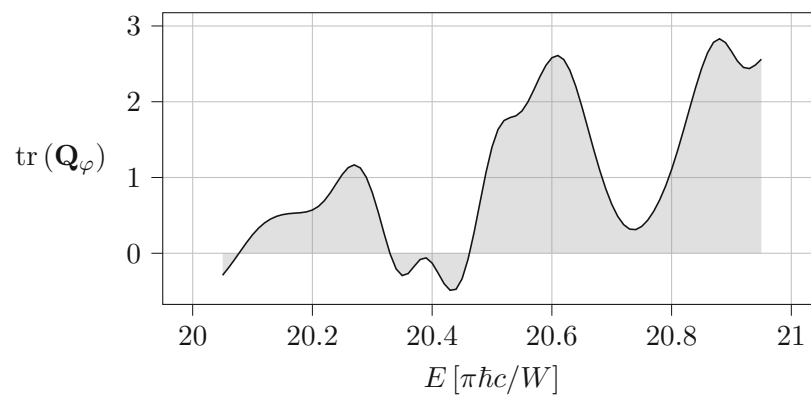


Figure 2.5: Spectral contributions to the vacuum force and the vacuum torque acting on the target from the generic waveguide system introduced in Subsec. 1.1.2. W denotes the width of the waveguide. The grey areas serve as a visual aid to better discern the zero line. (a) Horizontal component of the vacuum force. (b) Vertical component of the vacuum force. (c) Vacuum torque.

Chapter 3

Metrology

In this chapter, we interpret θ as a parameter of a physical system, the value of which we want to estimate. Note that we take a frequentist point of view here, i.e., we assume that the parameter θ has a specific value. For a Bayesian approach, where one assumes a prior distribution $p(\theta)$, we refer to Refs. [191–193].

3.1 Classical Fisher Information

In the following, we give an introduction to the fundamentals of estimation theory. For a more detailed review of this topic, we refer the reader to Refs. [194, 195].

We want to estimate the value of the parameter of interest θ by measuring some observable(s) X on the system. (The framework described below is quite general, but one can think of X as the quadratures of the output light field, for instance.) Usually, those observables are random variables, whose distribution depends on the value of θ , i.e., X is distributed according to some conditional probability distribution $p(X|\theta)$, which is also called “likelihood”. From the collected measurement data X we want to calculate an estimation value for θ , which we denote by $\tilde{\theta}$. This is done using a so-called estimator (function) τ :

$$\tilde{\theta} = \tau(X). \quad (3.1)$$

Since X is a random variable and τ is a deterministic function, the estimation value $\tilde{\theta}$ is a random variable as well, $\tilde{\theta} \sim p(\tilde{\theta}|\theta)$. Two core properties of this distribution are accuracy and precision, see Fig. 3.1. Accuracy is given by the bias b , which is the offset of the mean value μ from the true value θ :

$$\mu := \mathbb{E}_{\tilde{\theta} \sim p(\tilde{\theta}|\theta)} [\tilde{\theta}] = \int \tilde{\theta} p(\tilde{\theta}|\theta) d\tilde{\theta} = \int \tau(X) p(X|\theta) dX, \quad (3.2)$$

$$b := \mu - \theta. \quad (3.3)$$

Precision is determined by the variance σ^2 (or standard deviation σ) of the corresponding distribution:

$$\sigma^2 := \mathbb{V}_{\tilde{\theta} \sim p(\tilde{\theta}|\theta)} [\tilde{\theta}] = \int (\tilde{\theta} - \mu)^2 p(\tilde{\theta}|\theta) d\tilde{\theta} = \int (\tau(X) - \mu)^2 p(X|\theta) dX. \quad (3.4)$$

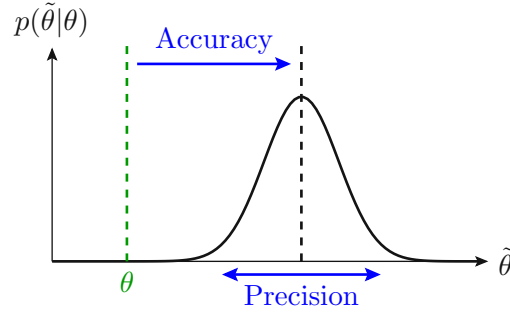


Figure 3.1: The estimation value $\tilde{\theta}$ is distributed according to $p(\tilde{\theta}|\theta)$. For illustrative purposes, this distribution is chosen here as a generic normal distribution. The accuracy of the estimation is given by the difference between the mean estimation value (dashed black line) and the true value θ (dashed green line). The precision of the estimation is determined by the standard deviation of the estimation value.

When taking M independently repeated measurements X_1, \dots, X_M , the arithmetic mean

$$\tau_M(X_1, \dots, X_M) = \frac{1}{M} \sum_{i=1}^M \tau(X_i) \quad (3.5)$$

constitutes an estimator with the same mean as τ and an M -fold reduced variance.

Naively, optimal accuracy and precision are reached if both the bias and the variance vanish, because then $p(\tilde{\theta}|\theta)$ becomes a delta distribution $\delta(\tilde{\theta} - \theta)$ and each estimation is perfect, i.e., $\tilde{\theta} = \theta$. It turns out, however, that in general this optimum can not be reached. On the one hand, the bias can indeed always be brought to zero, in principle. One might think of gauging the measurement device by adding a corresponding shift to the estimator. An estimator with $b = 0$ is called “unbiased”. On the other hand, the variance can — in general — never reach zero. There is a lower bound to it, which is called the Cramér-Rao lower bound (CRLB) [196, 197]. It is given by the inverse of the so-called classical Fisher information (FI) I_θ [198], multiplied by the squared derivative of the mean, all divided by the number M of repeated independent measurements:

$$\sigma^2 \geq \frac{(\partial_\theta \mu)^2}{MI_\theta}. \quad (3.6)$$

For unbiased estimators, $\mu = \theta$ and thus

$$\sigma^2 \geq \frac{1}{MI_\theta}. \quad (3.7)$$

Classical FI tells — on a global level — how much the distribution of the observed data X changes w.r.t. the parameter of interest θ (as is expressed by the derivative

∂_θ):

$$I_\theta := \mathbb{E}_{X \sim p(X|\theta)} [(\partial_\theta \ln(p(X|\theta)))^2] = \int (\partial_\theta \ln(p(X|\theta)))^2 p(X|\theta) dX. \quad (3.8)$$

Behind this mathematical description lies an intuitive picture: If the distribution of the measurement outcome X strongly depends on θ , which is indicated by a high FI I_θ , then one can potentially infer the value of θ with high precision, described by a small value for the variance σ^2 .

Surprisingly, the CRLB $1/MI_\theta$ for unbiased estimators only depends on the conditional distribution $p(X|\theta)$ and not on the specific estimator function. An unbiased estimator is called “efficient” if it reaches the CRLB, i.e., $\sigma^2 = 1/MI_\theta$. If an efficient estimator exists, it is the maximum likelihood estimator (MLE) τ_{MLE} [195], given by

$$\tau_{\text{MLE}}(X) = \arg \max_{\theta} p(X|\theta). \quad (3.9)$$

In any case, the MLE is asymptotically efficient (in the limit of many independently repeated measurements) [195]:

$$\lim_{M \rightarrow \infty} \frac{\sigma_{\text{MLE}}^2}{1/MI_\theta} = 1. \quad (3.10)$$

3.2 Quantum Fisher Information

This section discusses the basics of quantum metrology. A broader introduction to this topic is provided in Refs. [199–204].

In quantum theory, the injected state with which the physical system gets probed is generally described by a density operator $\hat{\rho}^{\text{in}}$. In formal terms, the interaction with the system can be described with a so-called quantum operation \mathcal{E}_θ . This interaction imprints a θ -dependence onto the probe state, which then leaves the system in the state $\hat{\rho}^{\text{out}}(\theta) = \mathcal{E}_\theta(\hat{\rho}^{\text{in}})$. (In the following, we omit to write the θ -dependence explicitly unless it serves conceptual understanding.) Upon this state, a measurement is performed, which is specified by a so-called positive operator-valued measure (POVM) $\hat{\Pi}_X$ satisfying

$$\sum_X \hat{\Pi}_X = \hat{1}, \quad (3.11)$$

and all $\hat{\Pi}_X$ are Hermitian, positive semidefinite operators. A typical choice is to take the projectors $\hat{\Pi}_X = |X\rangle\langle X|$ onto the eigenstates of an observable \hat{X} . The corresponding conditional probability density is given by Born’s rule

$$p(X|\theta) = \text{tr}(\hat{\Pi}_X \hat{\rho}^{\text{out}}(\theta)). \quad (3.12)$$

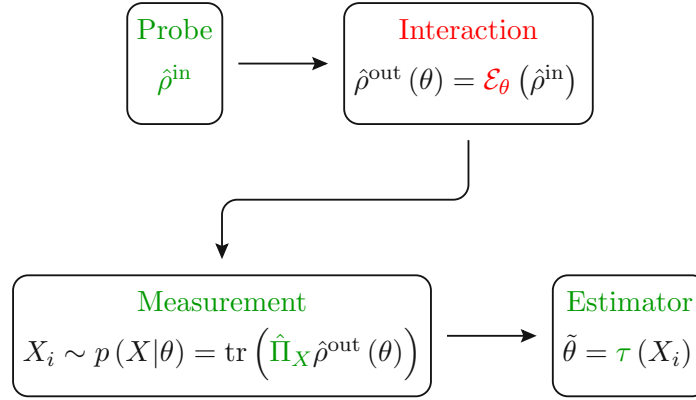


Figure 3.2: Schematic pipeline for a general estimation task in quantum metrology. A probe state $\hat{\rho}^{\text{in}}$ is made to interact with the system under study. This interaction is described by the quantum operation \mathcal{E}_θ , which in turn is parameterized by θ , the value of which we want to estimate. To this end, the output state $\hat{\rho}^{\text{out}}(\theta)$ is measured in a chosen measurement basis $\hat{\Pi}_X$. The results X_i of this measurement are fed into the estimator function τ , which returns the estimation value $\tilde{\theta}$. All fixed elements of the pipeline are coloured in red. All configurable elements of the pipeline are indicated with green colour.

The rest of the process that eventually yields an estimation value $\tilde{\theta}$ is discussed in Sec. 3.1.

We want to set up a pipeline that establishes an estimation scheme with optimal precision. There are essentially three choices that one has to make when building such a protocol, see also Fig. 3.2: (1) the probe state $\hat{\rho}^{\text{in}}$, (2) the measurement scheme as given by the POVM $\hat{\Pi}_X$, and (3) the estimator function τ . Which choices yield the best estimation precision?

We start with the last choice and then make our way to the first. For an efficient estimator to exist, it is a necessary condition that $p(X|\theta)$ is a member of the exponential family [205]. If this condition is not met, it is unclear what the best estimator is. However, as stated at the end of Sec. 3.1, the MLE is at least asymptotically efficient.

By adjusting the measurement scheme and the probe state, one can maximize the FI, providing a minimal CRLB, allowing for a minimal estimation variance σ^2 . It turns out that the optimization over all possible POVMs can be carried out analytically for each fixed probe state [206], resulting in what is called “quantum Fisher information” (QFI)

$$F_\theta := \max_{\hat{\Pi}_X} I_\theta = \text{tr} \left(\hat{L}_\theta^2 \hat{\rho}^{\text{out}} \right), \quad (3.13)$$

where the symmetric logarithmic derivative (SLD) \hat{L}_θ is defined by

$$\partial_\theta \hat{\rho}^{\text{out}} =: \frac{1}{2} \left(\hat{L}_\theta \hat{\rho}^{\text{out}} + \hat{\rho}^{\text{out}} \hat{L}_\theta \right). \quad (3.14)$$

The optimal POVM is given by the set of orthogonal projectors onto the eigenspaces of \hat{L}_θ , see also Subsec. 3.3.4 for the special case of pure probe states and unitary input-output mappings.

At this point, we would like to clarify the potentially misleading terminology here: “Classical” and “quantum” Fisher information refer to the fact that the measurement scheme has been fixed to some specific POVM or that it has been optimized over, respectively. It does *not* refer to the fact that just classical or quantum systems can be described by it. Alternatively, one can also think of QFI as portraying the smallest estimation error possible with a given quantum probe state, whereas classical FI gives the smallest possible error after having chosen a certain measurement scheme. The difference between QFI and classical FI describes the loss in (potential) precision entailed by selecting a specific POVM.

In the general case, $\hat{\rho}^{\text{out}}$ is a mixed state with eigen-decomposition

$$\hat{\rho}^{\text{out}} = \sum_k p_k |v_k\rangle \langle v_k|. \quad (3.15)$$

The QFI can be expressed as [199]

$$F_\theta = 2 \sum_{k,l:p_k+p_l \neq 0} \frac{|\langle v_k | \partial_\theta \hat{\rho}^{\text{out}} | v_l \rangle|^2}{p_k + p_l}. \quad (3.16)$$

Assuming that the support $\mathcal{S} := \{k : p_k \neq 0\}$ does not change with θ , it holds that [207]

$$F_\theta = \sum_{k \in \mathcal{S}} \frac{(\partial_\theta p_k)^2}{p_k} + 4 \sum_{k \in \mathcal{S}} p_k \langle \partial_\theta v_k | \partial_\theta v_k \rangle - 8 \sum_{k,l \in \mathcal{S}} \frac{p_k p_l}{p_k + p_l} |\langle v_l | \partial_\theta v_k \rangle|^2. \quad (3.17)$$

After having optimized over the POVM, the remaining objective is to identify the optimal probe state $\hat{\rho}^{\text{in}}$, which is achieved by maximizing the QFI. Note that the QFI (3.13) depends only on the choice of the probe state and not on the POVM or the estimator. An important mathematical property of the QFI is that it is a convex functional w.r.t. the probe state [208]. This implies that the QFI is always maximized by a pure probe state $\hat{\rho}^{\text{in}} = |\psi^{\text{in}}\rangle \langle \psi^{\text{in}}|$. In the following two sections 3.3 and 3.4, we will showcase concrete examples on how to find optimal probe states.

From Eq. (3.13) it is evident that $I_\theta \leq F_\theta$. For unbiased estimators, this leads to the quantum CRLB $1/MF_\theta$ on the estimation variance:

$$\sigma^2 \geq \frac{1}{MI_\theta} \geq \frac{1}{MF_\theta}. \quad (3.18)$$

In quantum optical metrology, one often distinguishes two different regimes: In the so-called standard quantum limit (SQL), the QFI is proportional to the mean

total photon number $\nu := \langle \psi^{\text{in}} | \hat{n} | \psi^{\text{in}} \rangle$. This occurs when the photons behave in an uncorrelated manner, which is effectively the case in coherent states, for instance. The standard deviation of the estimation scales like $\sigma \propto 1/\sqrt{\nu}$, a well-known result from classical statistics. Employing quantum correlations, one can surpass the SQL and attain what is known as the Heisenberg limit (HL), characterized by $F_\theta \propto \nu^2$ and thus $\sigma \propto 1/\nu$ [209, 210]. Concrete examples are given in the following two sections.

3.3 Unitary Quantum Metrology

In this section, we portray how QFI is obtained in unitary scattering setups. As it turns out, also here the QWS operator is a central quantity. This implies that for passive linear systems, the classical GWS matrix provides sufficient information to get access to the QFI. Based on this connection, we identify quantum states of light that are optimal probes for metrology. We will see that utilizing the quantum degrees of freedom allows for a considerably enhanced precision in measurements.

The discussion in this section is largely based on Ref. [147], where the analytical and numerical calculations were carried out by the author of this thesis, the project was proposed by Stefan Rotter and Ulf Leonhardt and the manuscript was written by the author of this thesis with input from Ulf Leonhardt, Stefan Rotter and Dorian Bouchet.

Independently repeated measurements can always be modelled using a vector-valued random variable $\mathbf{X} = (X_1, \dots, X_M)$ with the conditional distribution being a product of the individual contributions. This case is treated exactly the same as with a single repeated measurement where \mathbf{X} takes the place of the random variable. For this reason we set $M = 1$ in the following.

In this section, we consider the case of a unitary input-output relation

$$|\psi^{\text{out}}\rangle = \hat{U} |\psi^{\text{in}}\rangle, \quad (3.19)$$

where \hat{U} and hence $|\psi^{\text{out}}\rangle$ depend on θ . The QFI is easily calculated using Eq. (3.17):

$$F_\theta = 4 \left(\langle \partial_\theta \psi^{\text{out}} | \partial_\theta \psi^{\text{out}} \rangle - |\langle \psi^{\text{out}} | \partial_\theta \psi^{\text{out}} \rangle|^2 \right). \quad (3.20)$$

Inserting Eq. (3.19) and recalling the definition of the QWS operator (2.6), we arrive at the result that the QFI is essentially the variance of the QWS operator w.r.t. the probe state:

$$F_\theta = 4 \left(\langle \psi^{\text{in}} | \hat{Q}_\theta^2 | \psi^{\text{in}} \rangle - \langle \psi^{\text{in}} | \hat{Q}_\theta | \psi^{\text{in}} \rangle^2 \right) = 4 \mathbb{V}_{|\psi^{\text{in}}\rangle} [\hat{Q}_\theta]. \quad (3.21)$$

The corresponding quantum CRLB from Eq. (3.18) can be formulated as a kind of Heisenberg uncertainty relation [206]:

$$\mathbb{V} [\tilde{\theta}] \mathbb{V} [\hat{Q}_\theta] \geq \frac{1}{4}. \quad (3.22)$$

The striking difference to the standard Heisenberg uncertainty relation is that one of the quantities is not represented by an operator, but by a scalar parameter θ . This is especially interesting if one wants to consider time, which is not describable by a quantum operator [211]. From an intuitive point of view, it is clear that the uncertainty trade-off is established between the measured quantity θ and the conjugate generalized force \hat{Q}_θ , describing the measurement back-action onto the system [212].

We now apply this general framework of unitary quantum metrology to passive linear systems described by a classical scattering matrix \mathbf{S} , see also Sec. 1.3 and Subsec. 2.2.2. When evaluating the QFI (3.21) as the variance of the QWS operator, we notice that the scalar trace term from Eq. (2.18) cancels. Since this term stems from the factor $\sqrt{\det(\mathbf{S})}$ in Eq. (1.62), we omit this factor in the remainder of this chapter.

A quick note on notation: In the following, we are going to write the QFI as a functional of the output state, $F_\theta[\hat{\rho}^{\text{out}}]$ or $F_\theta[|\psi^{\text{out}}\rangle]$, but alternatively also as a functional of the input state, $F_\theta[|\psi^{\text{in}}\rangle]$, or just as F_θ . The respective meaning should be clear from the context. Also, we are going to omit the label “in” unless necessary.

3.3.1 Coherent Probe States

For coherent probe states $|\alpha\rangle^{\mathcal{M}} = |\beta\rangle^{\mathcal{Q}}$, we calculate the variance of the QWS operator in App. C:

$$F_\theta = 4\beta^\dagger \Lambda^2 \beta = 4\alpha^\dagger \mathbf{Q}_\theta^2 \alpha. \quad (3.23)$$

For the conversion between the modal \mathcal{M} representation and the \mathcal{Q} representation, we refer the reader to Subsec. 2.2.3. This result is already obtained in Ref. [23] and clearly shows the close relationship between the notion of QFI and the GWS matrix. The relevant matrix here, \mathbf{Q}_θ^2 , is Hermitian. It has the same eigenvectors as the GWS matrix \mathbf{Q}_θ and its eigenvalues are the squared eigenvalues of \mathbf{Q}_θ . Given a specific mean photon number

$${}^{\mathcal{M}}\langle \alpha | \hat{n} | \alpha \rangle^{\mathcal{M}} = \|\alpha\|^2 = \nu, \quad (3.24)$$

the state that maximizes the QFI (3.23) is given by the eigenvector of the GWS matrix \mathbf{Q}_θ that corresponds to the eigenvalue λ_i with the highest value for λ_i^2 . This is the eigenvalue with the highest absolute value $\lambda_{i_{\text{hav}}}$, see Eq. (2.46). The QFI is thus maximized using the probe state $|\sqrt{\nu} \mathbf{w}_{i_{\text{hav}}}\rangle^{\mathcal{M}}$. For numerical examples showing the spatial structure of such optimal probe states in a complex medium, we refer the reader to Figs. 2.1(b), 2.2(b) and 2.3(a) in Sec. 2.1.

Inserting back into the expression for the QFI, we observe that with the optimal protocol the SQL is achieved (see Fig. 3.3):

$$F_\theta \left[|\sqrt{\nu} \mathbf{w}_{i_{\text{hav}}}\rangle^{\mathcal{M}} \right] = 4\lambda_{i_{\text{hav}}}^2 \nu. \quad (3.25)$$

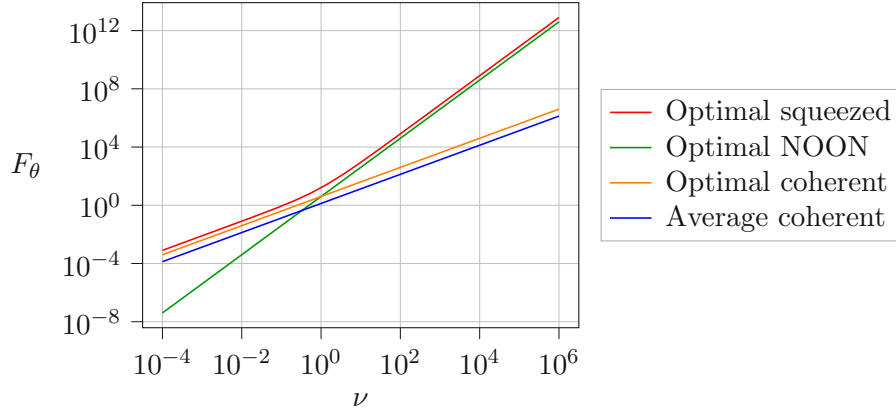


Figure 3.3: Quantum Fisher information F_θ as a function of the mean photon number ν for different choices for the probe state in unitary quantum metrology. Here, we assume that the GWS matrix of the underlying system has a generic eigenvalue spectrum with $\lambda_{i_{\max}} = -\lambda_{i_{\min}} = 1$ and $\langle \lambda_i^2 \rangle_i = 1/3$, corresponding to a uniform distribution $\mathcal{U}(-1, 1)$. The baseline value is set by the mean QFI averaged over all possible coherent probe states (blue line). Employing the optimal coherent probe state yields a constant gain factor over the baseline (orange line). Both strategies involving coherent probe states exhibit the scaling $F_\theta \propto \nu$, indicating the SQL. To reach the HL, one has to resort to quantum correlations in the probe state. Both the optimal NOON state (green line) and the optimal squeezed state (red line) are able to reach the HL, as indicated by the scaling $F_\theta \propto \nu^2$, for large values of ν . The optimal squeezed state yields a QFI that is at least twice as large as the one obtained with the optimal NOON state.

In order to reach Heisenberg scaling $F_\theta \propto \nu^2$, we have to resort to quantum correlations in the probe state, which is addressed and outlined in the following subsections.

3.3.2 Squeezed Probe States

For squeezed probe states $|\alpha, \mathbf{Z}\rangle^{\mathcal{M}} = |\beta, \Xi\rangle^{\mathcal{Q}}$, the variance of the QWS operator is given in Eq. (C.8). It is physically reasonable to assume that the squeezing matrix is diagonal in the \mathcal{Q} representation:

$$\Xi_{i,j} = \xi_i \delta_{i,j} = p_i e^{i\psi_i} \delta_{i,j}. \quad (3.26)$$

This intuitive ansatz is independently verified numerically. We are thus left with (see also Eq. (2.54))

$$F_\theta = 4 \sum_{i=1}^N \lambda_i^2 (|\beta_i|^2 \cosh(2p_i) + 2 \cosh^2(p_i) \sinh^2(p_i) - 2 \cosh(p_i) \sinh(p_i) \Re(\beta_i^{*2} e^{i\psi_i})). \quad (3.27)$$

We want to maximize this expression for a given fixed mean total photon number

$$\langle \beta, \Xi | \hat{n} | \beta, \Xi \rangle = \|\beta\|^2 + \text{tr}(\sinh^2(\mathbf{P})) = \sum_{i=1}^N (|\beta_i|^2 + \sinh^2(p_i)) = \nu. \quad (3.28)$$

The squeezing angles ψ_i and the phases of the coherent amplitudes β_i appear only in a single term in Eq. (3.27), namely $\Re(\beta_i^{*2} e^{i\psi_i}) = |\beta_i|^2 \cos(\psi_i - 2 \arg(\beta_i))$. Since $\cosh(p_i) \sinh(p_i) \geq 0$, the QFI is maximized when this expression is minimized, which is achieved with $\psi_i = 2 \arg(\beta_i) + \pi$. This corresponds to phase squeezing (see Fig. 1.4(b)) and results in

$$F_\theta = 4 \sum_{i=1}^N \lambda_i^2 (|\beta_i|^2 e^{2p_i} + 2 \cosh^2(p_i) \sinh^2(p_i)). \quad (3.29)$$

Numerical studies show that the general solution to this optimization problem is given by the following parameters:

$$\beta = \mathbf{0}, \quad (3.30)$$

$$\Xi = \text{arsinh}(\sqrt{\nu}) \mathbf{e}_{i_{\text{hav}}} \mathbf{e}_{i_{\text{hav}}}^\top. \quad (3.31)$$

The expression $\mathbf{e}_{i_{\text{hav}}} \mathbf{e}_{i_{\text{hav}}}^\top$ represents an $N \times N$ zero matrix with a single one-valued entry in row i_{hav} and column i_{hav} . Thus, the optimal probe state is characterized as follows: All channels are populated by the vacuum state and the whole resources (in terms of the mean photon number or, equivalently, the energy of the light) are used to squeeze the vacuum in the channel corresponding to the eigenvalue of the GWS matrix with the highest absolute value. (Numerical examples showing the spatial structure of such channels in a complex scattering system are given in Figs. 2.1(b), 2.2(b) and 2.3(a) in Sec. 2.1.) Since $\beta = \mathbf{0}$, there is no preferred direction in the photonic quantum phase space spanned by the light quadratures, which is why the squeezing angles are irrelevant in this special case and are thus set to zero without loss of generality. In the \mathcal{M} representation, the optimal parameters are $\alpha = \mathbf{0}$ and $\mathbf{Z} = \text{arsinh}(\sqrt{\nu}) \mathbf{w}_{i_{\text{hav}}} \mathbf{w}_{i_{\text{hav}}}^\top$.

Using this optimal Gaussian probe state, the HL is achieved (see Fig. 3.3):

$$F_\theta \left[|\mathbf{0}, \text{arsinh}(\sqrt{\nu}) \mathbf{w}_{i_{\text{hav}}} \mathbf{w}_{i_{\text{hav}}}^\top \rangle^{\mathcal{M}} \right] = 8 \lambda_{i_{\text{hav}}}^2 \nu (\nu + 1). \quad (3.32)$$

For $\nu > 0$, this value is strictly greater than the QFI (3.25) of the optimal coherent probe state. For $\nu \gg 1$, the QFI (3.32) scales quadratically, $F_\theta \propto \nu^2$, marking the HL. For $\nu \ll 1$, it scales linearly, $F_\theta \propto \nu$, thereby outperforming the optimal photon number state (see next subsection), which scales quadratically over the whole range of ν -values.

The most prominent example for the usage of squeezed light in high precision metrology is in gravitational wave detectors [35, 213–215]. In Ref. [216] it is theoretically shown that for realistic lossy interferometers, squeezed probe states outperform Fock states, NOON states and “any other sophisticated nonclassical quantum states”, see also next subsection.

3.3.3 Photon Number Probe States

For photon number probe states $|\psi\rangle^{\mathcal{M}} = |\phi\rangle^{\mathcal{Q}}$ with n photons, the variance of the QWS operator is straightforward to calculate since the Fock states $|\mathbf{u}\rangle^{\mathcal{Q}}$ are the eigenstates of \hat{Q}_θ with corresponding eigenvalues $\lambda_{\mathbf{u}}$, see Eq. (2.38). The variance of \hat{Q}_θ w.r.t. the state $|\phi\rangle^{\mathcal{Q}}$ equals the variance of the discrete distribution of values $\lambda_{\mathbf{u}}$ with respective probabilities $|\phi_{\mathbf{u}}|^2$:

$$F_\theta \left[|\phi\rangle^{\mathcal{Q}} \right] = 4\mathbb{V}_{|\phi\rangle^{\mathcal{Q}}} \left[\hat{Q}_\theta \right] = 4 \left(\sum_{\mathbf{u} \in \mathcal{F}_n^N} |\phi_{\mathbf{u}}|^2 \lambda_{\mathbf{u}}^2 - \left(\sum_{\mathbf{u} \in \mathcal{F}_n^N} |\phi_{\mathbf{u}}|^2 \lambda_{\mathbf{u}} \right)^2 \right). \quad (3.33)$$

To find the optimal probe state that maximizes this expression, we invoke Popoviciu’s inequality on variances [217], which states that the variance of such a bounded probability distribution $p(\lambda_{\mathbf{u}})$ is bound from above according to

$$\mathbb{V}_{|\phi\rangle^{\mathcal{Q}}} \left[\hat{Q}_\theta \right] \leq \frac{((\lambda_{\mathbf{u}})_{\max} - (\lambda_{\mathbf{u}})_{\min})^2}{4} = n^2 \frac{(\lambda_{i_{\max}} - \lambda_{i_{\min}})^2}{4}. \quad (3.34)$$

This inequality is saturated, i.e., the QFI is maximized, for

$$|\phi_{\mathbf{u}}|^2 = \begin{cases} \frac{1}{2} & \mathbf{u} \in \{n\mathbf{e}_{i_{\max}}, n\mathbf{e}_{i_{\min}}\}, \\ 0 & \text{else,} \end{cases} \quad (3.35)$$

yielding the optimal probe state

$$|\phi\rangle^{\mathcal{Q}} = \frac{1}{\sqrt{2}} \left(e^{i\varphi_{i_{\max}}} |n\mathbf{e}_{i_{\max}}\rangle^{\mathcal{Q}} + e^{i\varphi_{i_{\min}}} |n\mathbf{e}_{i_{\min}}\rangle^{\mathcal{Q}} \right). \quad (3.36)$$

The phase factors $e^{i\varphi_{i_{\max}}}$ and $e^{i\varphi_{i_{\min}}}$ are arbitrary. This state is a special kind of NOON state [218, 219], establishing a maximal degree of entanglement between the two channels corresponding to the largest and the smallest eigenvalue of the GWS matrix. The QFI with respect to this state is

$$F_\theta \left[\frac{1}{\sqrt{2}} \left(e^{i\varphi_{i_{\max}}} |n\mathbf{e}_{i_{\max}}\rangle^{\mathcal{Q}} + e^{i\varphi_{i_{\min}}} |n\mathbf{e}_{i_{\min}}\rangle^{\mathcal{Q}} \right) \right] = (\lambda_{i_{\max}} - \lambda_{i_{\min}})^2 n^2. \quad (3.37)$$

The quadratic scaling $F_\theta \propto n^2$ indicates that the HL is reached using this optimal probe state. However, we find that, regarding the QFI, the optimal Gaussian probe

state with the same mean total photon number $\nu = n$ surpasses the NOON state by a factor of at least 2, see also Fig. 3.3 and Ref. [220]:

$$F_{\theta}^{\text{optimal Gauss}} \geq 2F_{\theta}^{\text{optimal NOON}}. \quad (3.38)$$

NOON states are tricky to prepare in the experiment. Sending two identical photons through a 50 : 50 beam splitter yields a NOON state with $n = 2$, which is also known as the Hong-Ou-Mandel effect [221]. NOON states with $n = 3$ or $n = 4$ can be produced with a probabilistic method using spontaneous parametric down-conversion and post-selection [222, 223]. The current record is $n = 5$, achieved by interference of non-classical light with classical light [224].

For a concrete demonstration of NOON states, we consider the generic setup introduced in Subsec. 1.1.2. A metallic target is placed inside a waveguide, surrounded by other scatterers implementing a disordered medium. θ is chosen as one of three geometrical parameters of the target: horizontal position ($\theta = x$), vertical position ($\theta = y$) or rotational orientation ($\theta = \varphi$). For a single photon ($n = 1$), the spatial structures of the probability densities of the corresponding NOON states are illustrated in Fig. 3.4. The plots make it clear that NOON states build up intensity, i.e., they are highly sensitive, in regions where the target changes, irrespective if this perturbation in θ is positive or negative. To make this more specific, we see, e.g., that for $\theta = x$ the NOON state builds up intensity to the left and the right of the target (see Fig. 3.4(a)). In contrast, eigenstates of the corresponding GWS matrix \mathbf{Q}_x lead to a high intensity only on one side of the target (see Figs. 2.1(b) and 2.1(c)).

3.3.4 Optimal POVM

In this subsection, we determine the optimal POVM for a given pure output state $|\psi^{\text{out}}\rangle = \hat{U} |\psi^{\text{in}}\rangle$. The probe state does not have to be a maximizer of QFI. As stated in Sec. 3.2, the optimal POVM is given by the projectors onto the eigenspaces of the SLD \hat{L}_{θ} . For the pure state $\hat{\rho}^{\text{out}} = |\psi^{\text{out}}\rangle \langle \psi^{\text{out}}|$ we have (see Eq. (3.14))

$$\hat{\rho}^{\text{out}} = \hat{\rho}^{\text{out}2} \quad (3.39)$$

$$\implies \partial_{\theta} \hat{\rho}^{\text{out}} = (\partial_{\theta} \hat{\rho}^{\text{out}}) \hat{\rho}^{\text{out}} + \hat{\rho}^{\text{out}} (\partial_{\theta} \hat{\rho}^{\text{out}}) \quad (3.40)$$

$$\implies \hat{L}_{\theta} = 2\partial_{\theta} \hat{\rho}^{\text{out}} = 2(|\psi^{\text{out}}\rangle \langle \partial_{\theta} \psi^{\text{out}}| + |\partial_{\theta} \psi^{\text{out}}\rangle \langle \psi^{\text{out}}|). \quad (3.41)$$

Since only the two vectors $|\psi^{\text{out}}\rangle$ and $|\partial_{\theta} \psi^{\text{out}}\rangle$ are involved in this expression, we conjecture that also the eigenvectors of \hat{L}_{θ} corresponding to non-zero eigenvalues lie in the span of those two vectors. One can verify that with the results obtained in Eqs. (3.42), (3.49) and (3.50), the SLD as given in Eq. (3.41) is fully retrieved. We use the ansatz

$$\hat{L}_{\theta} = \ell^+ |\ell^+\rangle \langle \ell^+| + \ell^- |\ell^-\rangle \langle \ell^-|, \quad (3.42)$$

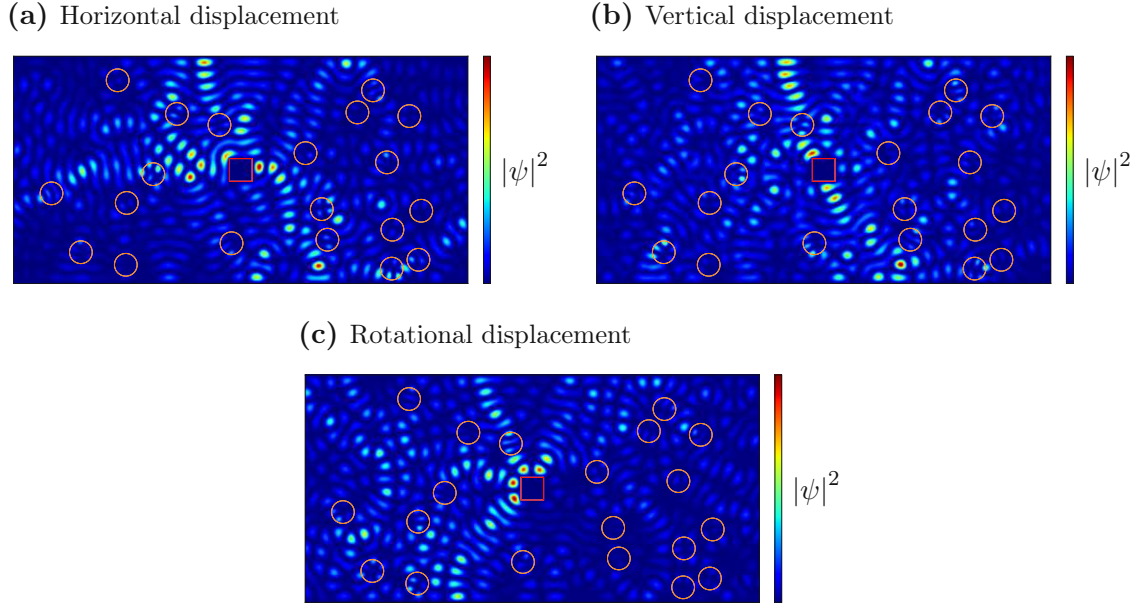


Figure 3.4: Spatial probability densities of single photon NOON states in the system described in Subsec. 1.1.2 for different choices of the parameter θ . (a) The parameter θ is taken as the horizontal position x of the target (red square). (b) The parameter θ is taken as the vertical position y of the target (red square). (c) The parameter θ is taken as the angular orientation φ of the target (red square). All shown NOON states are highly sensitive w.r.t. small positive as well as negative perturbations in θ .

$$|\ell^\pm\rangle = \alpha^\pm |\psi^{\text{out}}\rangle + \beta^\pm |\partial_\theta \psi^{\text{out}}\rangle, \quad (3.43)$$

$$\langle \ell^s | \ell^{s'} \rangle = \delta_{s,s'}, \quad (3.44)$$

and the identities

$$|\partial_\theta \psi^{\text{out}}\rangle = i\hat{U}\hat{Q}_\theta |\psi^{\text{in}}\rangle, \quad (3.45)$$

$$\langle \psi^{\text{out}} | \psi^{\text{out}} \rangle = 1, \quad (3.46)$$

$$\langle \partial_\theta \psi^{\text{out}} | \partial_\theta \psi^{\text{out}} \rangle = \langle \psi^{\text{in}} | \hat{Q}_\theta^2 | \psi^{\text{in}} \rangle, \quad (3.47)$$

$$-\langle \partial_\theta \psi^{\text{out}} | \psi^{\text{out}} \rangle = \langle \psi^{\text{out}} | \partial_\theta \psi^{\text{out}} \rangle = i \langle \psi^{\text{in}} | \hat{Q}_\theta | \psi^{\text{in}} \rangle. \quad (3.48)$$

We have to distinguish two cases: (1) The vectors $|\psi^{\text{out}}\rangle$ and $|\partial_\theta \psi^{\text{out}}\rangle$ are linearly dependent, i.e., there exists some $c \in \mathbb{C}$ such that $|\partial_\theta \psi^{\text{out}}\rangle = c |\psi^{\text{out}}\rangle$. According to Eq. (3.48), c must be purely imaginary since the QWS operator \hat{Q}_θ is Hermitian. But according to Eq. (3.41), we find $\hat{L}_\theta = 4\Re(c) |\psi^{\text{out}}\rangle \langle \psi^{\text{out}}| = 0$, implying that the QFI $F_\theta = \text{tr}(\hat{L}_\theta^2 \hat{\rho}^{\text{out}})$ vanishes.

(2) The vectors $|\psi^{\text{out}}\rangle$ and $|\partial_\theta \psi^{\text{out}}\rangle$ are linearly independent. In this case, the linear equations for the coefficients α^\pm and β^\pm established by the eigenvalue equation $\hat{L}_\theta |\ell^\pm\rangle = \ell^\pm |\ell^\pm\rangle$ can be solved using simple linear algebra. The solution reads (F_θ

being the QFI [225]

$$\ell^\pm = \pm\sqrt{F_\theta}, \quad (3.49)$$

$$|\ell^\pm\rangle = \frac{\pm\sqrt{F_\theta} - 2i\langle\psi^{\text{in}}|\hat{Q}_\theta|\psi^{\text{in}}\rangle}{\sqrt{2F_\theta}}|\psi^{\text{out}}\rangle + \sqrt{\frac{2}{F_\theta}}|\partial_\theta\psi^{\text{out}}\rangle \quad (3.50)$$

$$= \pm\frac{1}{\sqrt{2}}\hat{U}|\psi^{\text{in}}\rangle + i\sqrt{\frac{2}{F_\theta}}\hat{U}\left(\hat{Q}_\theta - \langle\psi^{\text{in}}|\hat{Q}_\theta|\psi^{\text{in}}\rangle\hat{1}\right)|\psi^{\text{in}}\rangle. \quad (3.51)$$

For a fixed working point θ_0 , we choose as an optimal POVM the projectors $|\ell^+(\theta_0)\rangle\langle\ell^+(\theta_0)|$, $|\ell^-(\theta_0)\rangle\langle\ell^-(\theta_0)|$ and $\hat{1} - |\ell^+(\theta_0)\rangle\langle\ell^+(\theta_0)| - |\ell^-(\theta_0)\rangle\langle\ell^-(\theta_0)|$. The output state close to the working point can be linearized according to $|\psi^{\text{out}}(\theta)\rangle = |\psi^{\text{out}}(\theta_0)\rangle + (\theta - \theta_0)|\partial_\theta\psi^{\text{out}}(\theta_0)\rangle + O((\theta - \theta_0)^2)$. From this we can calculate the measurement probabilities close to the working point:

$$p_\pm(\theta) := |\langle\ell^\pm(\theta_0)|\psi^{\text{out}}(\theta)\rangle|^2 = \frac{1}{2} \pm \frac{\sqrt{F_\theta(\theta_0)}}{2}(\theta - \theta_0) + O((\theta - \theta_0)^2). \quad (3.52)$$

This illustrates why a large QFI leads to a good estimation, because then the measurement probabilities change rapidly with small deviations in θ .

For the optimal coherent state $|\beta^{\text{in}}\rangle^{\mathcal{Q}} = |\sqrt{\nu}\mathbf{e}_{i_{\text{hav}}}\rangle^{\mathcal{Q}}$, we find

$$\hat{Q}_\theta|\beta^{\text{in}}\rangle^{\mathcal{Q}} = \sum_{i=1}^N \lambda_i \hat{b}_i^\dagger \hat{b}_i |\sqrt{\nu}\mathbf{e}_{i_{\text{hav}}}\rangle^{\mathcal{Q}} = \lambda_{i_{\text{hav}}} \sqrt{\nu} \hat{b}_{i_{\text{hav}}}^\dagger |\sqrt{\nu}\mathbf{e}_{i_{\text{hav}}}\rangle^{\mathcal{Q}}, \quad (3.53)$$

which is not a coherent state. So the theoretically optimal POVM involves non-coherent states. However, in Ref. [23] it is shown that a homodyne detection measurement with an intense coherent reference beam approximately yields an optimal POVM as well.

The optimal POVM for the NOON state $2^{-1/2}(|n\mathbf{e}_{i_{\text{max}}}\rangle^{\mathcal{Q}} + e^{i\varphi}|n\mathbf{e}_{i_{\text{min}}}\rangle^{\mathcal{Q}})$ can be calculated to be the same corresponding output NOON state, but with different relative phases (the global phase is immaterial here):

$$|\ell^\pm\rangle = \hat{U} \frac{1}{\sqrt{2}} \left(|n\mathbf{e}_{i_{\text{max}}}\rangle^{\mathcal{Q}} \mp ie^{i\varphi} |n\mathbf{e}_{i_{\text{min}}}\rangle^{\mathcal{Q}} \right). \quad (3.54)$$

3.4 Subunitary Quantum Metrology

In most experiments, it is unfeasible to measure the complete unitary optical scattering matrix \mathbf{S} , e.g., due to the limited NA of the illumination or detectors. Also losses, which are omnipresent in realistic physical systems, lead to a subunitary scattering matrix [226, 227]. It has been shown that in specific lossy systems there is a transition from the HL to the SQL [228–233]. Here, we provide a general

description of subunitary multi-mode systems with potentially complicated loss mechanisms, where θ does not necessarily represent a simple phase shift.

As we show in the following, it is in principle always possible to identify pure probe states that are optimal for quantum metrology even in systems with losses or incomplete channel control by knowing just the available subunitary part $\tilde{\mathbf{S}}$ of the scattering matrix. We denote every quantity related to the subunitary part of the system with a tilde.

If one has access to just $M < N$ out of the N output channels (w.l.o.g. the ones with indices $m \in \{1, \dots, M\}$) then the output state is reduced to a mixed state, which is obtained by taking the partial trace of the full pure output state $\hat{\rho}^{\text{out}} = |\psi^{\text{out}}\rangle\langle\psi^{\text{out}}|$ over the unobserved channels:

$$\hat{\rho}^{\text{out}} = \sum_{n_{M+1}=0}^{\infty} \cdots \sum_{n_N=0}^{\infty} {}^{\mathcal{M}}_{M+1}\langle n_{M+1} | \cdots {}^{\mathcal{M}}_N \langle n_N | \hat{\rho}^{\text{out}} | n_N \rangle_N^{\mathcal{M}} \cdots | n_{M+1} \rangle_{M+1}^{\mathcal{M}}. \quad (3.55)$$

Physically, it is evident that this state can only depend on the correspondingly reduced subunitary scattering matrix $\tilde{\mathbf{S}} \in \mathbb{C}^{M \times N}$, and on the probe state $|\psi^{\text{in}}\rangle$. The QFI of a general mixed state is given in Eq. (3.17) and can in general no longer be expressed as the variance of a Hermitian operator, as it is the case in unitary systems.

A restriction of accessible input channels is taken into account in a much more straightforward way: One simply removes the corresponding columns of $\tilde{\mathbf{S}}$ and restricts the space of allowed probe states $|\psi^{\text{in}}\rangle$ accordingly. This is independent of taking partial traces over unobserved output channels. This means that restricting input channels does not alter the mathematical description, so we can just keep N and take it as the number of accessible input channels.

3.4.1 Coherent Probe States

Multi-mode coherent states $|\alpha^{\text{out}}\rangle^{\mathcal{M}}$ are always product states and thus never exhibit entanglement. This leads to the result that the reduced output state is a pure state as well:

$$\begin{aligned} \hat{\rho}^{\text{out}} &= |\alpha_1^{\text{out}}\rangle_1^{\mathcal{M}} \cdots |\alpha_M^{\text{out}}\rangle_M^{\mathcal{M}} {}^{\mathcal{M}}_1 \langle \alpha_1^{\text{out}} | \cdots {}^{\mathcal{M}}_M \langle \alpha_M^{\text{out}} | \cdot \\ &\quad \cdot \left. \prod_{m=M+1}^N \sum_{n_m=0}^{\infty} {}^{\mathcal{M}}_m \langle n_m | \alpha_m^{\text{out}} \rangle_m^{\mathcal{M}} {}^{\mathcal{M}}_m \langle \alpha_m^{\text{out}} | n_m \rangle_m^{\mathcal{M}} \right\} = 1 \\ &= |\alpha_1^{\text{out}}\rangle_1^{\mathcal{M}} \cdots |\alpha_M^{\text{out}}\rangle_M^{\mathcal{M}} {}^{\mathcal{M}}_1 \langle \alpha_1^{\text{out}} | \cdots {}^{\mathcal{M}}_M \langle \alpha_M^{\text{out}} |. \end{aligned} \quad (3.56)$$

The output state is given by the coherent amplitude $\tilde{\alpha}^{\text{out}} = \tilde{\mathbf{S}}\alpha^{\text{in}} \in \mathbb{C}^M$. In App. D we show that the QFI of such a multi-mode coherent state is given by

$$F_\theta \left[|\tilde{\alpha}^{\text{out}}\rangle^{\mathcal{M}} \right] = 4 \|\partial_\theta \tilde{\alpha}^{\text{out}}\|^2 = 4 (\alpha^{\text{in}})^\dagger \left(\partial_\theta \tilde{\mathbf{S}} \right)^\dagger \left(\partial_\theta \tilde{\mathbf{S}} \right) \alpha^{\text{in}}. \quad (3.57)$$

We call

$$\tilde{\mathbf{F}}_\theta := 4 \left(\partial_\theta \tilde{\mathbf{S}} \right)^\dagger \left(\partial_\theta \tilde{\mathbf{S}} \right) \quad (3.58)$$

the reduced FI matrix⁴ [23]. It is Hermitian and positive semidefinite by construction.

Given a fixed mean total input photon number $\|\boldsymbol{\alpha}^{\text{in}}\|^2 = \nu$, the QFI (3.57) is maximized when $\boldsymbol{\alpha}^{\text{in}}$ is proportional to the eigenvector of $\tilde{\mathbf{F}}_\theta$ corresponding to its largest eigenvalue \tilde{f}_{max} . With this optimal choice, the QFI scales linearly with the mean total photon number, $F_\theta = \nu \tilde{f}_{\text{max}}$, which is a hallmark of the SQL.

In the unitary limit, one just has to replace $\tilde{\mathbf{F}}_\theta$ by the full FI matrix $\mathbf{F}_\theta = 4 \left(\partial_\theta \mathbf{S} \right)^\dagger \left(\partial_\theta \mathbf{S} \right)$. This matches with the result previously found in Eq. (3.23) since with the unitarity of \mathbf{S} we find

$$\mathbf{Q}_\theta^2 = -\mathbf{S}^\dagger \left(\partial_\theta \mathbf{S} \right) \mathbf{S}^\dagger \left(\partial_\theta \mathbf{S} \right) = \left(\partial_\theta \mathbf{S} \right)^\dagger \mathbf{S} \mathbf{S}^\dagger \left(\partial_\theta \mathbf{S} \right) = \left(\partial_\theta \mathbf{S} \right)^\dagger \left(\partial_\theta \mathbf{S} \right). \quad (3.59)$$

As a numerical example, we consider the generic system presented in Subsec. 1.1.2. In the center of a waveguide, a metallic target is placed, which is surrounded by other scatterers that provide a complex scattering environment. The parameter θ is either the horizontal position x of the target, its vertical position y , or its rotational orientation φ . We choose the left-sided reflection matrix \mathbf{R} to be the subunitary part of the scattering matrix. The spatial intensity distributions of the respective maximum eigenstates of $\tilde{\mathbf{F}}_\theta$ are plotted in Fig. 3.5. One can see that the wave first has to reach the target at the relevant locations, i.e., where the target changes with θ . Then, the wave has to bring the collected information back to the detector on the left hand side. Indeed, all shown eigenstates exhibit an above-average reflectance.

3.4.2 Squeezed Probe States

As stated in Ref. [234], taking the partial trace over the squeezed state $|\boldsymbol{\alpha}^{\text{out}}, \mathbf{Z}^{\text{out}}\rangle^{\mathcal{M}}$ yields the pure squeezed state $|\tilde{\boldsymbol{\alpha}}^{\text{out}}, \tilde{\mathbf{Z}}^{\text{out}}\rangle^{\mathcal{M}}$ with

$$\tilde{\boldsymbol{\alpha}}^{\text{out}} = \tilde{\mathbf{S}} \boldsymbol{\alpha}^{\text{in}}, \quad (3.60)$$

$$\tilde{\mathbf{Z}}^{\text{out}} = \tilde{\mathbf{S}} \mathbf{Z}^{\text{in}} \tilde{\mathbf{S}}^\top. \quad (3.61)$$

As shown in Ref. [235], the QFI of such a squeezed state can be calculated as

$$F_\theta \left[|\tilde{\boldsymbol{\alpha}}^{\text{out}}, \tilde{\mathbf{Z}}^{\text{out}}\rangle^{\mathcal{M}} \right] = 2 \left(\partial_\theta \tilde{\mathbf{d}} \right)^\dagger \tilde{\boldsymbol{\Sigma}}^{-1} \left(\partial_\theta \tilde{\mathbf{d}} \right) + \frac{1}{4} \text{tr} \left(\left(\tilde{\boldsymbol{\Sigma}}^{-1} \partial_\theta \tilde{\boldsymbol{\Sigma}} \right)^2 \right), \quad (3.62)$$

where

$$\tilde{\mathbf{d}} = \begin{pmatrix} \tilde{\boldsymbol{\alpha}}^{\text{out}} \\ \tilde{\boldsymbol{\alpha}}^{\text{out}*} \end{pmatrix}, \quad (3.63)$$

⁴Not to be confused with the FI matrix from multi-parameter estimation.

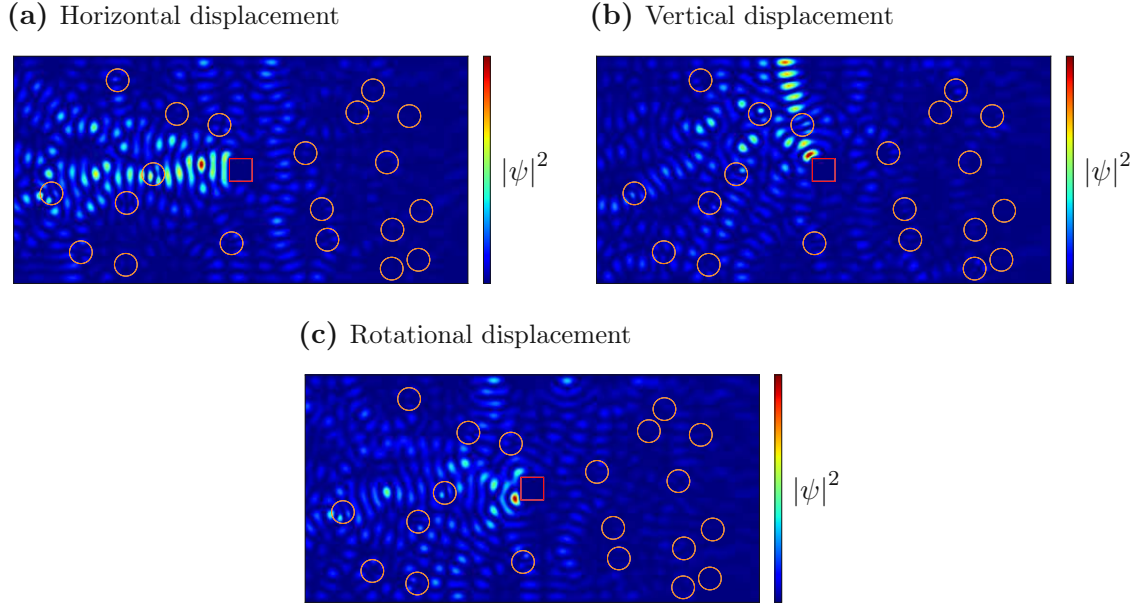


Figure 3.5: Spatial intensity distributions of optimal coherent probe states for measuring different parameters θ of the target (red square). The other scatterers (orange circles) generate a complex scattering environment. It is assumed that waves can be injected and measured only on the left hand side, thereby establishing a subunitary system. (a) $\theta = x$ is the horizontal position of the target. The reflectance of this state is ≈ 0.734 . (b) $\theta = y$ is the vertical position of the target. The reflectance of this state is ≈ 0.650 . (c) $\theta = \varphi$ is the rotational orientation of the target. The reflectance of this state is ≈ 0.595 .

$$\tilde{\Sigma} = \begin{pmatrix} \cosh(2\tilde{\mathbf{R}}^{\text{out}}) & -\sinh(2\tilde{\mathbf{R}}^{\text{out}}) e^{i\tilde{\Phi}^{\text{out}}} \\ -e^{-i\tilde{\Phi}^{\text{out}}} \sinh(2\tilde{\mathbf{R}}^{\text{out}}) & \cosh(2\tilde{\mathbf{R}}^{\text{out}})^{\top} \end{pmatrix}. \quad (3.64)$$

In analogy to coherent probe states, where the transition from a unitary system to a subunitary one is implemented by replacing \mathbf{F}_θ by $\tilde{\mathbf{F}}_\theta$ (see Subsec. 3.4.1), it is conjectured that choosing a squeezed probe state such that (see Eqs. (3.30) and (3.31)) $\boldsymbol{\alpha}^{\text{in}} = \mathbf{0}$ and $\mathbf{Z}^{\text{in}} \propto \tilde{\mathbf{f}}_{\text{max}} \tilde{\mathbf{f}}_{\text{max}}^{\top}$, where $\tilde{\mathbf{f}}_{\text{max}}$ is the eigenvector of the reduced FI matrix $\tilde{\mathbf{F}}_\theta$ corresponding to the highest eigenvalue, leads to good performance, i.e., a high QFI. In order to answer the questions whether this state is truly optimal, how the corresponding QFI scales (SQL vs. HL), and under which circumstances it outperforms the optimal photon number state (like in the unitary case, see Eq. (3.38)), further investigations are required.

3.4.3 Photon Number Probe States

In order to calculate the partial trace over the pure output state

$$\hat{\rho}^{\text{out}} = |\psi^{\text{out}}\rangle^{\mathcal{M}} \langle\psi^{\text{out}}| = \sum_{\mathbf{n}, \mathbf{n}' \in \mathcal{F}_n^N} \psi_{\mathbf{n}}^{\text{out}} \psi_{\mathbf{n}'}^{\text{out}*} |\mathbf{n}\rangle^{\mathcal{M}} \langle\mathbf{n}'| \quad (3.65)$$

with $\psi^{\text{out}} = \mathbf{S}^{(n)}\psi^{\text{in}}$, see Eq. (1.67), we introduce the set of Fock states, where all n photons are in the first M channels, and where all n photons are in the last $N - M$ channels, respectively:

$$\mathcal{F}_n^{N, \leq M} := \{ \mathbf{n} \in \mathcal{F}_n^N | \forall m \in \{M+1, \dots, N\} : n_m = 0 \}, \quad (3.66)$$

$$\mathcal{F}_n^{N, > M} := \{ \mathbf{n} \in \mathcal{F}_n^N | \forall m \in \{1, \dots, M\} : n_m = 0 \}. \quad (3.67)$$

With these definitions, the reduced output state can be calculated as

$$\begin{aligned} \hat{\rho}^{\text{out}} &= \sum_{n_{M+1}=0}^n \cdots \sum_{n_N=0}^n \langle n_{M+1} | \cdots \langle n_N | \hat{\rho}^{\text{out}} | n_N \rangle_N^{\mathcal{M}} \cdots | n_{M+1} \rangle_{M+1}^{\mathcal{M}} \\ &= \sum_{\mathbf{n}, \mathbf{n}' \in \mathcal{F}_n^{N, \leq M}} \psi_{\mathbf{n}}^{\text{out}} \psi_{\mathbf{n}'}^{\text{out}*} |\mathbf{n}\rangle^{\mathcal{M}} \langle\mathbf{n}'| \\ &\quad + \sum_{\mathbf{n}, \mathbf{n}' \in \mathcal{F}_{n-1}^{N, \leq M}} \sum_{\mathbf{n}'' \in \mathcal{F}_1^{N, > M}} \psi_{\mathbf{n}+\mathbf{n}''}^{\text{out}} \psi_{\mathbf{n}'+\mathbf{n}''}^{\text{out}*} |\mathbf{n}\rangle^{\mathcal{M}} \langle\mathbf{n}'| \\ &\quad + \sum_{\mathbf{n}, \mathbf{n}' \in \mathcal{F}_{n-2}^{N, \leq M}} \sum_{\mathbf{n}'' \in \mathcal{F}_2^{N, > M}} \psi_{\mathbf{n}+\mathbf{n}''}^{\text{out}} \psi_{\mathbf{n}'+\mathbf{n}''}^{\text{out}*} |\mathbf{n}\rangle^{\mathcal{M}} \langle\mathbf{n}'| \\ &\quad + \dots \\ &\quad + \sum_{\mathbf{n}, \mathbf{n}' \in \mathcal{F}_1^{N, \leq M}} \sum_{\mathbf{n}'' \in \mathcal{F}_{n-1}^{N, > M}} \psi_{\mathbf{n}+\mathbf{n}''}^{\text{out}} \psi_{\mathbf{n}'+\mathbf{n}''}^{\text{out}*} |\mathbf{n}\rangle^{\mathcal{M}} \langle\mathbf{n}'| \\ &\quad + \left(\sum_{\mathbf{n}'' \in \mathcal{F}_n^{N, > M}} |\psi_{\mathbf{n}''}^{\text{out}}|^2 \right) |\mathbf{0}\rangle \langle\mathbf{0}| \\ &= \sum_{\mu=0}^n \sum_{\mathbf{n}, \mathbf{n}' \in \mathcal{F}_\mu^{N, \leq M}} \sum_{\mathbf{n}'' \in \mathcal{F}_{n-\mu}^{N, > M}} \psi_{\mathbf{n}+\mathbf{n}''}^{\text{out}} \psi_{\mathbf{n}'+\mathbf{n}''}^{\text{out}*} |\mathbf{n}\rangle^{\mathcal{M}} \langle\mathbf{n}'| \\ &=: \sum_{\mu=0}^n \sum_{\mathbf{n}, \mathbf{n}' \in \mathcal{F}_\mu^M} \tilde{\rho}_{\mathbf{n}, \mathbf{n}'}^{\text{out}(\mu)} |\mathbf{n}\rangle^{\mathcal{M}} \langle\mathbf{n}'|. \end{aligned} \quad (3.68)$$

The original entanglement with the unobserved channels in $|\psi^{\text{out}}\rangle^{\mathcal{M}}$ in general gives rise to a mixed state $\hat{\rho}^{\text{out}}$.

At first sight, it seems that this expression explicitly depends on the amplitudes of the output state that we do not have access to, as expressed by the sum $\sum_{\mathbf{n}'' \in \mathcal{F}_{n-\mu}^{N, > M}}$.

However, as is derived in App. E, the density matrix $\tilde{\rho}^{\text{out}(\mu)}$ corresponding to μ output photons is expressible in terms of the reduced subunitary scattering matrix $\tilde{\mathbf{S}}$ and the amplitudes $\psi_{\mathbf{n}}^{\text{in}}$ of the probe state,

$$\begin{aligned} \tilde{\rho}_{\mathbf{n},\mathbf{n}'}^{\text{out}(\mu)} &= \frac{1}{(n-\mu)!} \frac{1}{C_{\mathbf{n}}C_{\mathbf{n}'}} \sum_{\mathbf{p}_1, \dots, \mathbf{p}_n \in \mathcal{F}_1^N} \sum_{\mathbf{q}_1, \dots, \mathbf{q}_n \in \mathcal{F}_1^N} \left(\prod_{k=1}^{\mu} \tilde{S}_{\mathbf{n}_k, \mathbf{p}_k} \right) \Upsilon_{\sum_{k=1}^n \mathbf{p}_k}^{\text{in}} \cdot \\ &\cdot \left(\prod_{k=\mu+1}^n \left(\mathbf{1} - \tilde{\mathbf{S}}^\top \tilde{\mathbf{S}}^* \right)_{\mathbf{p}_k, \mathbf{q}_k} \right) \Upsilon_{\sum_{k=1}^n \mathbf{q}_k}^{\text{in}*} \left(\prod_{k=1}^{\mu} \tilde{S}_{\mathbf{n}'_k, \mathbf{q}_k}^* \right), \end{aligned} \quad (3.69)$$

where we used the convention introduced in Eq. (1.70) and we define

$$\Upsilon_{\mathbf{n}}^{\text{in}} := C_{\mathbf{n}} \psi_{\mathbf{n}}^{\text{in}}. \quad (3.70)$$

When represented in the Fock basis, the reduced output state $\hat{\rho}^{\text{out}}$ has a block structure according to the number μ of photons in the observed output channels. This implies that the QFI decomposes into $n+1$ contributions, corresponding to the $\hat{\rho}^{\text{out}(\mu)}$ for $\mu \in \{0, 1, \dots, n\}$.

For $\mu = n$, i.e., the contribution where no photon is lost, we define $\tilde{\psi}^{\text{out}(n)} \in \mathbb{C}^{|\mathcal{F}_n^M|}$ as

$$\forall \mathbf{n} \in \mathcal{F}_n^M : \tilde{\psi}_{\mathbf{n}}^{\text{out}(n)} := \psi_{\mathbf{n}}^{\text{out}}. \quad (3.71)$$

Accordingly, we define the reduced subunitary n -photon scattering matrix $\tilde{\mathbf{S}}^{(n)} \in \mathbb{C}^{|\mathcal{F}_n^M| \times |\mathcal{F}_n^N|}$ as

$$\forall \mathbf{n} \in \mathcal{F}_n^M \forall \mathbf{n}' \in \mathcal{F}_n^N : \tilde{S}_{\mathbf{n}, \mathbf{n}'}^{(n)} := S_{\mathbf{n}, \mathbf{n}'}^{(n)} = \frac{1}{C_{\mathbf{n}}C_{\mathbf{n}'}} \sum_{\sigma \in \mathfrak{S}_n} \prod_{k=1}^n \tilde{S}_{\mathbf{n}_k, \mathbf{n}'_{\sigma(k)}}. \quad (3.72)$$

This way, we can write $\tilde{\psi}^{\text{out}(n)} = \tilde{\mathbf{S}}^{(n)} \psi^{\text{in}}$ and

$$\tilde{\rho}^{\text{out}(n)} = \tilde{\psi}^{\text{out}(n)} \left(\tilde{\psi}^{\text{out}(n)} \right)^\dagger. \quad (3.73)$$

Mind that in general $\|\tilde{\psi}^{\text{out}(n)}\| \leq 1$, so $\tilde{\rho}^{\text{out}(n)}$ cannot be considered a properly normalized pure state. We call it a “reduced pure state”. The QFI of such a state can be calculated exactly, see App. F:

$$F_\theta [\tilde{\rho}^{\text{out}(n)}] = 4 \left(\partial_\theta \tilde{\psi}^{\text{out}(n)} \right)^\dagger \left(\partial_\theta \tilde{\psi}^{\text{out}(n)} \right) - \frac{4\Re^2 \left(-i \left(\tilde{\psi}^{\text{out}(n)} \right)^\dagger \left(\partial_\theta \tilde{\psi}^{\text{out}(n)} \right) \right)}{\left\| \tilde{\psi}^{\text{out}(n)} \right\|^2}. \quad (3.74)$$

Introducing the reduced n -photon FI matrix

$$\tilde{\mathbf{F}}_\theta^{(n)} := 4 \left(\partial_\theta \tilde{\mathbf{S}}^{(n)} \right)^\dagger \left(\partial_\theta \tilde{\mathbf{S}}^{(n)} \right) \quad (3.75)$$

and the reduced n -photon GWS matrix

$$\tilde{\mathbf{Q}}_\theta^{(n)} := -i \left(\tilde{\mathbf{S}}^{(n)} \right)^\dagger \partial_\theta \tilde{\mathbf{S}}^{(n)}, \quad (3.76)$$

we obtain

$$F_\theta [\tilde{\rho}^{\text{out}(n)}] = (\boldsymbol{\psi}^{\text{in}})^\dagger \tilde{\mathbf{F}}_\theta^{(n)} \boldsymbol{\psi}^{\text{in}} - \frac{4 \left((\boldsymbol{\psi}^{\text{in}})^\dagger \Re \left(\tilde{\mathbf{Q}}_\theta^{(n)} \right) \boldsymbol{\psi}^{\text{in}} \right)^2}{\left\| \tilde{\mathbf{S}}^{(n)} \boldsymbol{\psi}^{\text{in}} \right\|^2} \quad (3.77)$$

with

$$\Re \left(\tilde{\mathbf{Q}}_\theta^{(n)} \right) := \frac{1}{2} \left(\tilde{\mathbf{Q}}_\theta^{(n)} + \left(\tilde{\mathbf{Q}}_\theta^{(n)} \right)^\dagger \right) \quad (3.78)$$

being the Hermitian part of the reduced n -photon GWS matrix.

In the unitary case, Eq. (3.77) is the only contribution to the QFI. Additionally, for unitary n -photon scattering matrices, the n -photon GWS matrix $\mathbf{Q}_\theta^{(n)}$ is Hermitian and the n -photon FI matrix equals $\mathbf{F}_\theta^{(n)} = 4 \left(\mathbf{Q}_\theta^{(n)} \right)^2$ (see Eq. (3.59)) and we are left with

$$F_\theta [\rho^{\text{out}}] = 4 (\boldsymbol{\psi}^{\text{in}})^\dagger \left(\mathbf{Q}_\theta^{(n)} \right)^2 \boldsymbol{\psi}^{\text{in}} - 4 \left((\boldsymbol{\psi}^{\text{in}})^\dagger \mathbf{Q}_\theta^{(n)} \boldsymbol{\psi}^{\text{in}} \right)^2, \quad (3.79)$$

which is equivalent to Eq. (3.33). From the same reasoning as in Subsec. 3.3.3 we can deduce that this QFI is maximal when the probe state is a NOON state, where the relevant two channels are given by the eigenvectors of $\mathbf{Q}_\theta^{(n)}$ corresponding to the minimum and maximum eigenvalue, respectively. Such a NOON state is highly sensitive w.r.t. small changes in the parameter of interest θ , but it is also very fragile against photon loss: If just a single photon escapes from a NOON state, the remaining photons collapse into either of two eigenchannels of $\mathbf{Q}_\theta^{(n-1)}$, leading to a complete loss of sensitivity, i.e., vanishing QFI [236]. In the expression of the QFI for the subunitary system, consisting of Eq. (3.77) and the terms for $\mu < n$, this trade-off between sensitivity and robustness is automatically taken into account.

Similarly to Eq. (3.72), we can express the n -photon matrices $\tilde{\mathbf{Q}}_\theta^{(n)}$ and $\tilde{\mathbf{F}}_\theta^{(n)}$ in terms of the single-photon matrices $\tilde{\mathbf{Q}}_\theta := \tilde{\mathbf{Q}}_\theta^{(1)}$ and $\tilde{\mathbf{F}}_\theta := \tilde{\mathbf{F}}_\theta^{(1)}$. The derivation of the following results is given in App. G:

$$\begin{aligned} \left(\tilde{\mathbf{Q}}_\theta^{(n)} \right)_{\mathbf{n}, \mathbf{n}'} &= \frac{1}{C_n C_{\mathbf{n}'}} \sum_{\sigma \in \mathfrak{S}_n} \sum_{k=1}^n \left(\tilde{\mathbf{Q}}_\theta \right)_{\mathbf{n}_k, \mathbf{n}'_{\sigma(k)}} \prod_{l(\neq k)}^n \left(\tilde{\mathbf{S}}^\dagger \tilde{\mathbf{S}} \right)_{\mathbf{n}_l, \mathbf{n}'_{\sigma(l)}}, \quad (3.80) \\ \left(\tilde{\mathbf{F}}_\theta^{(n)} \right)_{\mathbf{n}, \mathbf{n}'} &= \frac{1}{C_n C_{\mathbf{n}'}} \sum_{\sigma \in \mathfrak{S}_n} \sum_{k=1}^n \left(\tilde{\mathbf{F}}_\theta \right)_{\mathbf{n}_k, \mathbf{n}'_{\sigma(k)}} \prod_{l(\neq k)}^n \left(\tilde{\mathbf{S}}^\dagger \tilde{\mathbf{S}} \right)_{\mathbf{n}_l, \mathbf{n}'_{\sigma(l)}} \end{aligned}$$

$$\begin{aligned}
 & + \frac{4}{C_{\mathbf{n}} C_{\mathbf{n}'}} \sum_{\sigma \in \mathfrak{S}_n} \sum_{k \neq k'}^n \left(\tilde{\mathbf{Q}}_{\theta}^{\dagger} \right)_{\mathbf{n}_k, \mathbf{n}'_{\sigma(k)}} \left(\tilde{\mathbf{Q}}_{\theta} \right)_{\mathbf{n}_{k'}, \mathbf{n}'_{\sigma(k')}} \cdot \\
 & \cdot \prod_{l(\neq k, k')}^n \left(\tilde{\mathbf{S}}^{\dagger} \tilde{\mathbf{S}} \right)_{\mathbf{n}_l, \mathbf{n}'_{\sigma(l)}}. \quad (3.81)
 \end{aligned}$$

As a specific example, we now consider single-photon probe states ($n = 1$). There are two contributions to the total QFI: The contribution from the case when the photon is detected ($\mu = 1$) is given by Eq. (3.77). In case of the photon being lost ($\mu = 0$), the corresponding contribution to the mixed state is (see Eq. (3.69))

$$\tilde{\rho}^{\text{out}(0)} = \sum_{\mathbf{p}, \mathbf{q} \in \mathcal{F}_1^N} \psi_{\mathbf{p}}^{\text{in}} \left(\mathbf{1} - \tilde{\mathbf{S}}^{\top} \tilde{\mathbf{S}}^* \right)_{\mathbf{p}, \mathbf{q}} \psi_{\mathbf{q}}^{\text{in}*} = 1 - (\boldsymbol{\psi}^{\text{in}})^{\dagger} \tilde{\mathbf{S}}^{\dagger} \tilde{\mathbf{S}} \boldsymbol{\psi}^{\text{in}} = 1 - \left\| \tilde{\mathbf{S}} \boldsymbol{\psi}^{\text{in}} \right\|^2. \quad (3.82)$$

We introduce the anti-Hermitian part of $\tilde{\mathbf{Q}}_{\theta}$, multiplied by $-i$, in order to obtain the Hermitian matrix

$$\Im \left(\tilde{\mathbf{Q}}_{\theta} \right) := \frac{1}{2i} \left(\tilde{\mathbf{Q}}_{\theta} - \tilde{\mathbf{Q}}_{\theta}^{\dagger} \right) = -\frac{1}{2} \partial_{\theta} \left(\tilde{\mathbf{S}}^{\dagger} \tilde{\mathbf{S}} \right). \quad (3.83)$$

The QFI of $\tilde{\rho}^{\text{out}(0)}$ is easily calculated (see Eq. (3.17)):

$$F_{\theta} \left[\tilde{\rho}^{\text{out}(0)} \right] = \frac{(\partial_{\theta} \tilde{\rho}^{\text{out}(0)})^2}{\tilde{\rho}^{\text{out}(0)}} = \frac{\left((\boldsymbol{\psi}^{\text{in}})^{\dagger} \left(\partial_{\theta} \left(\tilde{\mathbf{S}}^{\dagger} \tilde{\mathbf{S}} \right) \right) \boldsymbol{\psi}^{\text{in}} \right)^2}{1 - \left\| \tilde{\mathbf{S}} \boldsymbol{\psi}^{\text{in}} \right\|^2}. \quad (3.84)$$

This expression does not vanish in general and it gives the information contained in the escaped photon. A photon, from which one knows that it was scattered into the unobserved channels because one does not detect it, yields information about the scattering system nonetheless.

In total, the QFI adds up to

$$F_{\theta} \left[\tilde{\rho}^{\text{out}} \right] = (\boldsymbol{\psi}^{\text{in}})^{\dagger} \tilde{\mathbf{F}}_{\theta} \boldsymbol{\psi}^{\text{in}} - \frac{4 \left((\boldsymbol{\psi}^{\text{in}})^{\dagger} \Re \left(\tilde{\mathbf{Q}}_{\theta} \right) \boldsymbol{\psi}^{\text{in}} \right)^2}{\left\| \tilde{\mathbf{S}} \boldsymbol{\psi}^{\text{in}} \right\|^2} + \frac{4 \left((\boldsymbol{\psi}^{\text{in}})^{\dagger} \Im \left(\tilde{\mathbf{Q}}_{\theta} \right) \boldsymbol{\psi}^{\text{in}} \right)^2}{1 - \left\| \tilde{\mathbf{S}} \boldsymbol{\psi}^{\text{in}} \right\|^2}. \quad (3.85)$$

The case of a single photon is relatively easy to interpret physically. When maximizing the QFI (3.85), there are different contributions that can lead to an overall increase of the QFI. The first term is proportional to $\left\| \partial_{\theta} \tilde{\boldsymbol{\psi}}^{\text{out}(1)} \right\|^2$ and grows large for a high sensitivity of the output state (in case that the photon is detected) w.r.t. the parameter of interest. Conversely, when inspecting the denominators of the second and the third term, it becomes clear that those terms increase for large

$\|\tilde{\psi}^{\text{out}(1)}\|^2$, which is the probability of detecting the photon in the first place. But the derivative $\partial_\theta \tilde{\psi}^{\text{out}(1)}$ that determines the first term also influences the last two terms. Only the proper combination of these different effects as given in Eq. (3.85) yields the optimal probe state upon maximization.

As already indicated in Refs. [14, 20] (in the context of micromanipulation), the “real” and “imaginary part” of $\tilde{\mathbf{Q}}_\theta$ are connected to the transfer and loss of photons, respectively. This physical interpretation becomes quite clear in the present context of QFI of single photons.

For a numerical example, we resort to the generic setup presented in Subsec. 1.1.2. A waveguide is filled with scatterers forming a complex scattering medium. A metallic target is placed at the center of the waveguide. The parameter θ is chosen as the horizontal position x of the target, its vertical position y , or its angular orientation φ . We assume that we have access to the system only from the left hand side, both for the injection and the detection of single photons, i.e., the subunitary part of the scattering matrix is given by the reflection matrix \mathbf{R} . Here, the optimal probe state can not be determined by solving an eigenvalue problem like in most other scenarios discussed in this thesis. Rather, the QFI in Eq. (3.85) is directly optimized numerically using the dual annealing routine from the `scipy.optimize` package. The spatial probability densities of the optimal single photon probe states for the different choices of θ are shown in Fig. 3.6. Similar to the optimal coherent probe states (see Fig. 3.5), we see that the photon first has to reach the target at the critical locations (where it changes with θ), and then has to transfer the gathered information back to the detector on the left hand side. All optimal probe states considered here lead to a photon detection probability of roughly 0.6.

To finish this subsection, we briefly discuss the case in which one can access just $M = 1$ output channel, e.g., by having a single pixel (or bucket) detector. Then the output signal is a complex scalar $\psi \equiv \tilde{\psi}^{\text{out}} = \tilde{\mathbf{S}}\psi^{\text{in}}$. We now show that the phase of this scalar is irrelevant. Its squared absolute value, the probability of detection $p := |\psi|^2$, and its derivative are enough to specify the QFI. We start by evaluating Eq. (3.85):

$$\begin{aligned}
 F_\theta [\tilde{\rho}^{\text{out}}] &= (\psi^{\text{in}})^\dagger \tilde{\mathbf{F}}_\theta \psi^{\text{in}} - \frac{4\Re^2 \left((\psi^{\text{in}})^\dagger \tilde{\mathbf{Q}}_\theta \psi^{\text{in}} \right)}{|\psi|^2} + \frac{4\Im^2 \left((\psi^{\text{in}})^\dagger \tilde{\mathbf{Q}}_\theta \psi^{\text{in}} \right)}{1 - |\psi|^2} \\
 &= 4|\partial_\theta \psi|^2 - \frac{4\Im^2 (\psi^* \partial_\theta \psi)}{|\psi|^2} + \frac{4\Re^2 (\psi^* \partial_\theta \psi)}{1 - |\psi|^2} \\
 &= \frac{4}{|\psi|^2} \left(|\psi^* \partial_\theta \psi|^2 - \Im^2 (\psi^* \partial_\theta \psi) + \frac{|\psi|^2}{1 - |\psi|^2} \Re^2 (\psi^* \partial_\theta \psi) \right) \\
 &= \frac{4}{|\psi|^2} \left(\Re^2 (\psi^* \partial_\theta \psi) + \frac{|\psi|^2}{1 - |\psi|^2} \Re^2 (\psi^* \partial_\theta \psi) \right)
 \end{aligned}$$

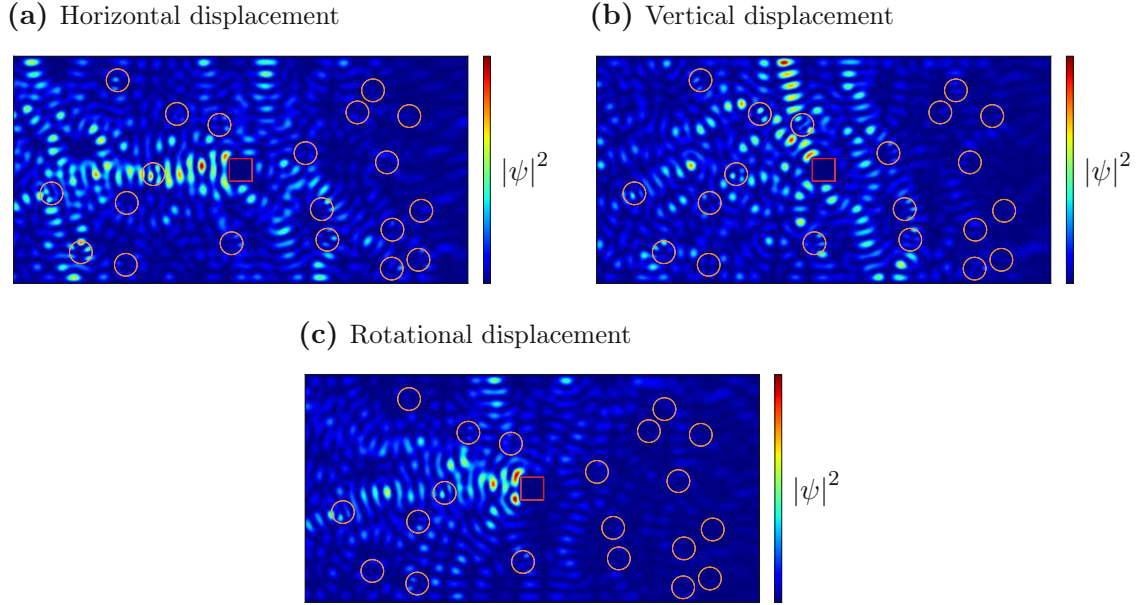


Figure 3.6: Spatial probability densities of optimal single photon probe states for measuring different parameters θ of the target (red square). The other scatterers (orange circles) create a complex scattering environment. It is assumed that the photon can be injected and measured only on the left hand side, thereby establishing a subunitary system. (a) $\theta = x$ is the horizontal position of the target. The probability for detecting the photon is ≈ 0.589 . (b) $\theta = y$ is the vertical position of the target. The probability for detecting the photon is ≈ 0.583 . (c) $\theta = \varphi$ is the rotational orientation of the target. The probability for detecting the photon is ≈ 0.631 .

$$= \frac{4}{|\psi|^2} \frac{1}{1 - |\psi|^2} \Re^2(\psi^* \partial_\theta \psi). \quad (3.86)$$

We set $\psi = |\psi| e^{i\eta}$ and calculate

$$\psi^* \partial_\theta \psi = |\psi| e^{-i\eta} (e^{i\eta} \partial_\theta |\psi| + i |\psi| e^{i\eta} \partial_\theta \eta) = |\psi| \partial_\theta |\psi| + i |\psi|^2 \partial_\theta \eta. \quad (3.87)$$

Inserting $p = |\psi|^2$, we arrive at

$$F_\theta [\hat{\rho}^{\text{out}}] = \frac{4}{|\psi|^2 (1 - |\psi|^2)} (|\psi| \partial_\theta |\psi|)^2 = \frac{(\partial_\theta (|\psi|^2))^2}{|\psi|^2 (1 - |\psi|^2)} = \frac{(\partial_\theta p)^2}{p(1-p)}. \quad (3.88)$$

This result is exactly the (ordinary) FI of a Bernoulli distribution where p is the probability of an event. For the act of measuring a single photon in a single pixel detector with probability p , the Bernoulli distribution is the correct statistical model, reinforcing the validity of the more general expression for the QFI of single photons in Eq. (3.85).

To summarize, in this section we elucidated the fact that in order to achieve optimal quantum metrology in systems with loss or limited access to the optical channels, knowledge of the measurable subunitary classical scattering matrix and its θ -dependence is sufficient.

3.5 Coherent Quantum Fisher Information Flow

So far, we have considered the QFI that corresponds to a light state that has left the system under study and is captured by a detector placed in the far field. However, prior to measurement, the electromagnetic field that carries the QFI propagates through the system. Therefore, it is natural to ask whether one can also formalize the propagation of QFI in the near field, including effects of scattering and interference. In this section, we show that, indeed, this can be done in terms of a continuity equation, which consequently allows the identification of sources and sinks of QFI. In the last paragraph of this section, we argue that such a spatially localized flow of QFI can be established only for coherent states out of the kinds of quantum states considered in this thesis (Gaussian states and definite photon number states). The evolution of such classical light fields is governed by Maxwell's equations

$$\nabla \cdot \mathbf{D} = \rho, \quad \nabla \cdot \mathbf{B} = 0, \quad \nabla \times \mathbf{E} = -\partial_t \mathbf{B}, \quad \nabla \times \mathbf{H} = \mathbf{j} + \partial_t \mathbf{D}. \quad (3.89)$$

For linear, isotropic and static media, we have the constitutive relations

$$\mathbf{D} = \varepsilon \mathbf{E}, \quad \mathbf{B} = \mu \mathbf{H}. \quad (3.90)$$

A central quantity in classical electrodynamics is the Poynting vector $\mathbf{j}_E = \mathbf{E} \times \mathbf{H}$ which describes the flow of energy (hence the subscript E) supported by the electromagnetic field via Poynting's theorem

$$\partial_t \rho_E + \nabla \cdot \mathbf{j}_E = \sigma_E, \quad (3.91)$$

which has the form of a continuity equation, where the energy density is $\rho_E = \frac{1}{2}(\varepsilon \mathbf{E}^2 + \mu \mathbf{H}^2)$ and the source term is given by $\sigma_E = -\mathbf{j} \cdot \mathbf{E}$.

For coherent states $|\alpha\rangle^{\mathcal{M}}$, we already know that the energy is proportional to $\|\alpha\|^2$ and the QFI is proportional to $\|\partial_\theta \alpha\|^2$. Motivated by this simple correspondence, namely replacing fields by their respective θ -derivatives, we can formulate the following ansatz for a continuity equation of QFI (subscript F):

$$\rho_F := \frac{1}{2} (\varepsilon (\partial_\theta \mathbf{E})^2 + \mu (\partial_\theta \mathbf{H})^2), \quad (3.92)$$

$$\mathbf{j}_F := (\partial_\theta \mathbf{E}) \times (\partial_\theta \mathbf{H}). \quad (3.93)$$

Inserting into the corresponding continuity equation

$$\partial_t \rho_F + \nabla \cdot \mathbf{j}_F = \sigma_F, \quad (3.94)$$

we can identify the following source term:

$$\sigma_F = -(\partial_\theta \mathbf{j} + (\partial_\theta \varepsilon) (\partial_t \mathbf{E})) \cdot (\partial_\theta \mathbf{E}) - (\partial_\theta \mu) (\partial_t \mathbf{H}) \cdot (\partial_\theta \mathbf{H}). \quad (3.95)$$

The flux density \mathbf{j}_F describes the local propagation of QFI inside the scattering system, whereas the density ρ_F describes the QFI locally stored in the electromagnetic field and in the dielectric medium. The term σ_F describes local sources and sinks of QFI. Also intuitively, this makes sense since σ_F is (in the absence of external currents) proportional to $\partial_\theta \varepsilon$ and $\partial_\theta \mu$, which are non-zero in those spatial regions that change with θ . It is these locations where QFI is produced (or absorbed), see also Fig. 3.7.

We now apply the formulae above to the waveguide setup as described in Subsec. 1.1.2, where $\mu = \mu_0$, $n^2 = \varepsilon/\varepsilon_0$ and $\mathbf{E} = \psi \mathbf{e}_z$ is the complex-valued monochromatic electric field. The corresponding magnetic field is obtained using the Maxwell-Faraday equation (the third one in Eq. (3.89)):

$$-i\omega\mu_0 \mathbf{H} = \mu_0 \partial_t \mathbf{H} = \partial_t \mathbf{B} = -\nabla \times \mathbf{E} = -\partial_y \psi \mathbf{e}_x + \partial_x \psi \mathbf{e}_y \quad (3.96)$$

$$\iff \mathbf{H} = \frac{1}{i\omega\mu_0} \begin{pmatrix} \partial_y \psi \\ -\partial_x \psi \\ 0 \end{pmatrix}. \quad (3.97)$$

Performing an average over a time period (indicated by an overline), we obtain the QFI density

$$\begin{aligned} \overline{\rho_F} &= \frac{\varepsilon}{4} \Re((\partial_\theta \mathbf{E})^* \cdot (\partial_\theta \mathbf{E})) + \frac{\mu_0}{4} \Re((\partial_\theta \mathbf{H})^* \cdot (\partial_\theta \mathbf{H})) \\ &= \frac{\varepsilon}{4} \|\partial_\theta \mathbf{E}\|^2 + \frac{\mu_0}{4} \|\partial_\theta \mathbf{H}\|^2 \\ &= \frac{\varepsilon}{4} |\partial_\theta \psi|^2 + \frac{1}{4\mu_0 \omega^2} \|\nabla \partial_\theta \psi\|^2 \\ &= \frac{\varepsilon}{4} \left(|\partial_\theta \psi|^2 + \frac{1}{n^2 k^2} \|\nabla \partial_\theta \psi\|^2 \right), \end{aligned} \quad (3.98)$$

the QFI flux density

$$\begin{aligned} \overline{\mathbf{j}_F} &= \frac{1}{2} \Re((\partial_\theta \mathbf{E})^* \times (\partial_\theta \mathbf{H})) \\ &= \frac{1}{2} \Re \left(\frac{1}{i\omega\mu_0} \begin{pmatrix} 0 \\ 0 \\ \partial_\theta \psi^* \end{pmatrix} \times \begin{pmatrix} \partial_y \partial_\theta \psi \\ -\partial_x \partial_\theta \psi \\ 0 \end{pmatrix} \right) \end{aligned}$$

$$\begin{aligned}
 &= \frac{1}{2} \Re \left(\frac{1}{i\omega\mu_0} \begin{pmatrix} (\partial_\theta\psi)^* \partial_x (\partial_\theta\psi) \\ (\partial_\theta\psi)^* \partial_y (\partial_\theta\psi) \\ 0 \end{pmatrix} \right) \\
 &= \frac{1}{2\mu_0\omega} \Im ((\partial_\theta\psi)^* \nabla (\partial_\theta\psi)), \tag{3.99}
 \end{aligned}$$

and the QFI source density

$$\begin{aligned}
 \overline{\sigma_F} &= -(\partial_\theta\varepsilon) \overline{(\partial_t \Re(\mathbf{E})) \cdot (\partial_\theta \Re(\mathbf{E}))} \\
 &= -(\partial_\theta\varepsilon) \omega \overline{\Re(-i\mathbf{E}) \cdot \Re(\partial_\theta \mathbf{E})} \\
 &= -\frac{(\partial_\theta\varepsilon)\omega}{2} \Re(i\mathbf{E}^* \cdot \partial_\theta \mathbf{E}) \\
 &= \frac{(\partial_\theta\varepsilon)\omega}{2} \Im(\psi^* \partial_\theta \psi). \tag{3.100}
 \end{aligned}$$

Mind that the time averaged continuity equation reads $\overline{\nabla \cdot \mathbf{j}_F} = \nabla \cdot \overline{\mathbf{j}_F} = \overline{\sigma_F}$ since $\overline{\partial_t \rho_F} = 0$.

We now make the link to the expression of QFI in the far field, namely $F_\theta = 4\|\partial_\theta \boldsymbol{\alpha}^{\text{out}}\|^2$, by showing that the (time averaged) integrated QFI flux Φ_F flowing out of the system is proportional to F_θ . Since all involved fields are independent of the z -coordinate, we neglect the corresponding integration. The integrated flux into the far field is thus given by (Ω denotes the scattering region)

$$\Phi_F = \oint_{\partial\Omega} \overline{\mathbf{j}_F} \cdot d\mathbf{A} = -\int_0^W \overline{j_{F,x}}(x=0, y) dy + \int_0^W \overline{j_{F,x}}(x=L, y) dy. \tag{3.101}$$

From the mode decomposition from Eqs. (1.13) and (1.14) we obtain:

$$(\partial_\theta\psi)(0, y) = \sum_{m=1}^{N'} (\partial_\theta\alpha_{l,m}^-) \frac{1}{\sqrt{k_m^x}} \psi_m(y), \tag{3.102}$$

$$(\partial_x \partial_\theta\psi)(0, y) = \sum_{m=1}^{N'} (\partial_\theta\alpha_{l,m}^-) \frac{-ik_m^x}{\sqrt{k_m^x}} \psi_m(y), \tag{3.103}$$

$$(\partial_\theta\psi)(L, y) = \sum_{m=1}^{N'} (\partial_\theta\alpha_{r,m}^+) \frac{1}{\sqrt{k_m^x}} \psi_m(y), \tag{3.104}$$

$$(\partial_x \partial_\theta\psi)(L, y) = \sum_{m=1}^{N'} (\partial_\theta\alpha_{r,m}^+) \frac{ik_m^x}{\sqrt{k_m^x}} \psi_m(y). \tag{3.105}$$

Using the orthogonality (1.17) of the waveguide modes, we can calculate

$$\Phi_F = -\frac{1}{2\mu_0\omega} \Im \left(\int_0^W (\partial_\theta\psi)^*(0, y) (\partial_x \partial_\theta\psi)(0, y) dy \right)$$

$$\begin{aligned}
 & + \frac{1}{2\mu_0\omega} \Im \left(\int_0^W (\partial_\theta \psi)^* (L, y) (\partial_x \partial_\theta \psi) (L, y) dy \right) \\
 = & - \frac{1}{2\mu_0\omega} \Im \left(\sum_{m=1}^{N'} (\partial_\theta \alpha_{l,m}^-)^* (-i) (\partial_\theta \alpha_{l,m}^-) \right) \\
 & + \frac{1}{2\mu_0\omega} \Im \left(\sum_{m=1}^{N'} (\partial_\theta \alpha_{r,m}^+)^* (i) (\partial_\theta \alpha_{r,m}^+) \right) \\
 = & \frac{1}{2\mu_0\omega} \left(\|\partial_\theta \alpha_l^-\|^2 + \|\partial_\theta \alpha_r^+\|^2 \right) \\
 = & \frac{1}{2\mu_0\omega} \|\partial_\theta \alpha^{\text{out}}\|^2. \tag{3.106}
 \end{aligned}$$

This result establishes the crucial link between the known expression for QFI in the far field and the newly introduced expression for the QFI flux density \mathbf{j}_F defined in Eq. (3.93) which can be evaluated in the near field also. It confirms that the continuity equation (3.94) gives a proper description of the spatial flow of QFI carried by a coherent state of light through a scattering system.

The author of this thesis co-advised the diploma thesis “Fisher Information Flow in Wave Scattering” by Felix Russo [237], which also provides an experimental demonstration of the above concepts in a microwave waveguide setup, conducted in the group of Ulrich Kuhl at Université Côte d’Azur in Nice (France). Furthermore, the author contributed to the analytical and numerical calculations in Ref. [238], which contains further details on this topic.

In the following, we demonstrate the concept of coherent QFI flow with the generic waveguide example introduced in Subsec. 1.1.2. A metallic square-shaped target is embedded inside a disordered medium realized by circular scatterers. Figure 3.7 shows the time averaged QFI densities $\overline{\rho}_F$ and the associated flux densities $\overline{\mathbf{j}}_F$ for horizontal, vertical and rotational displacements of the target when the respective optimal probe states (the ones that maximize the QFI in the output fields) are injected into the system. The time averaged QFI source densities $\overline{\sigma}_F$ are not plotted because they are concentrated along the edge of the target. From the flux densities it is anyway evident where the QFI is created. The plots clearly illustrate the production of QFI right at the boundary of the target, where it changes most w.r.t. the parameter θ , and how the QFI then propagates through the disordered system, ultimately flowing into the far field.

We close this section by noting that a local continuity equation for QFI makes sense only for coherent states of light. For instance, the QFI of photon number states, as given in Eq. (3.33), contains a 4th order contribution in the amplitudes. But then, the QFI flux density \mathbf{j}_F would also need to have such a contribution such that $\Phi_F \propto F_\theta$. This however makes it impossible to utilize the orthogonality of the mode profiles, a crucial ingredient in the derivation (3.106). The physical reason

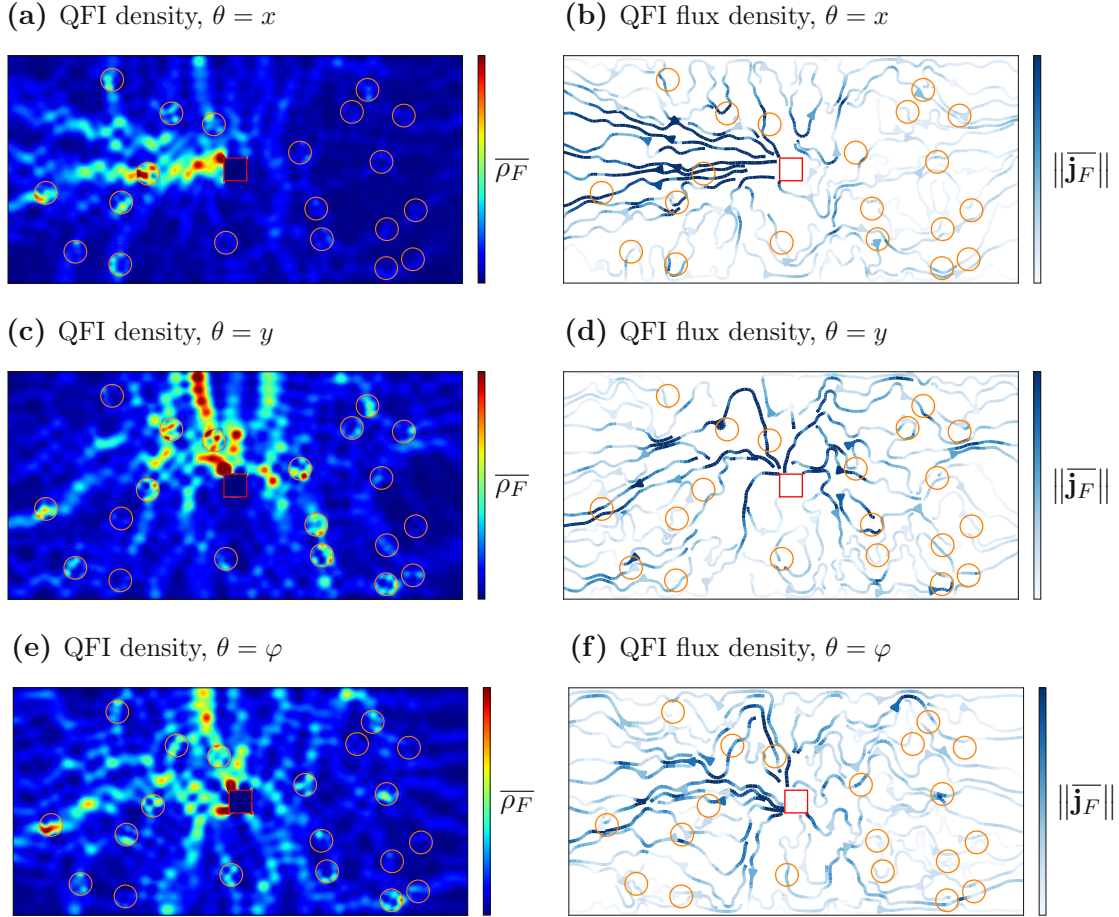


Figure 3.7: Coherent QFI flow in a waveguide system containing a metallic target (red square) and multiple scatterers (orange circles) inducing random scattering. We distinguish three choices for the parameter θ : horizontal position of the target ($\theta = x$, first row), vertical position of the target ($\theta = y$, second row) and the rotational orientation of the target ($\theta = \varphi$, third row). For each parameter θ , the respective optimal probe state (the one maximizing the QFI in the output state) is coupled into the system. The plots show the spatial distributions of the respective time averaged QFI densities $\overline{\rho_F}$ (left column) and the associated time averaged QFI flux densities $\overline{\mathbf{j}_F}$ (right column). The latter are visualized using stream plots, where the colour of the lines encode the norm of the vector field. Close to the target, the fields take on extremely large values, which is why the ranges for $\overline{\rho_F}$ and $\|\overline{\mathbf{j}_F}\|$ represented in the respective colour bars are clipped.

why photon number states (and non-classical states in general) do not allow for a local description of the flow of QFI is that QFI is in general a non-local quantity, reflecting the non-local nature of the wavefunction, which materializes, e.g., in the collapse of the wavefunction upon a performed measurement. What happens in one detector influences the statistics of events in all other detectors. Coherent states, on the other side, behave in a local fashion: The measurement statistics of a detector is independent of the measurement outcome of any other detector.

3.6 Coherent Discrimination

Up to this point, we considered only infinitesimal changes in the parameter of interest θ , as expressed by the derivative ∂_θ . So a natural question could be how to modify the formalism to describe finite differences. The notion of a “finite difference” comprises finite shifts $\Delta\theta$ in the parameter, but also the presence/absence of a target, or the replacement of the whole system by a different system altogether. The aim in all those cases is to distinguish between two different hypotheses H_1 and H_2 , which is called binary decision. This means that the probe state $|\psi^{\text{in}}\rangle$ propagates through one of two systems, where system 1 appears with the prior probability p_1 and system 2 is realized with the prior probability $p_2 = 1 - p_1$. In the absence of any prior information, for instance, one would set $p_1 = p_2 = 1/2$. Based on a measurement of the output state $|\psi_1^{\text{out}}\rangle$ or $|\psi_2^{\text{out}}\rangle$, one tries to predict which of the two systems was present. If the two output states are not orthogonal, there is always a non-zero probability of an incorrect prediction. The average error probability is defined as

$$p_{\text{err}} := p_1 p(H_2|H_1) + p_2 p(H_1|H_2), \quad (3.107)$$

where $p(H_2|H_1)$ is the probability of deciding for hypothesis H_2 , provided that the system is actually a realization of hypothesis H_1 , and vice versa for $p(H_1|H_2)$. This error probability is always larger than a certain minimum value, which is known as the Helstrom bound [199]:

$$p_{\text{err}} \geq \frac{1}{2} \left(1 - \sqrt{1 - 4p_1 p_2 |\langle \psi_1^{\text{out}} | \psi_2^{\text{out}} \rangle|^2} \right). \quad (3.108)$$

The central question is what choice to make for the probe state $|\psi^{\text{in}}\rangle$ such that the Helstrom bound gets as small as possible. Regardless of the values for p_1 and p_2 , this is achieved by minimizing the overlap $|\langle \psi_1^{\text{out}} | \psi_2^{\text{out}} \rangle|^2$.

For coherent states and passive linear scattering systems we have $\alpha_i^{\text{out}} = \mathbf{S}_i \alpha_i^{\text{in}}$, where $i \in \{1, 2\}$ and \mathbf{S}_i is the scattering matrix of system i . It holds that

$${}^{\mathcal{M}}\langle \alpha_1^{\text{out}} | \alpha_2^{\text{out}} \rangle^{\mathcal{M}} = \exp \left(-\frac{1}{2} \left(\|\alpha_1^{\text{out}}\|^2 + \|\alpha_2^{\text{out}}\|^2 - 2\alpha_1^{\text{out}\dagger} \alpha_2^{\text{out}} \right) \right), \quad (3.109)$$

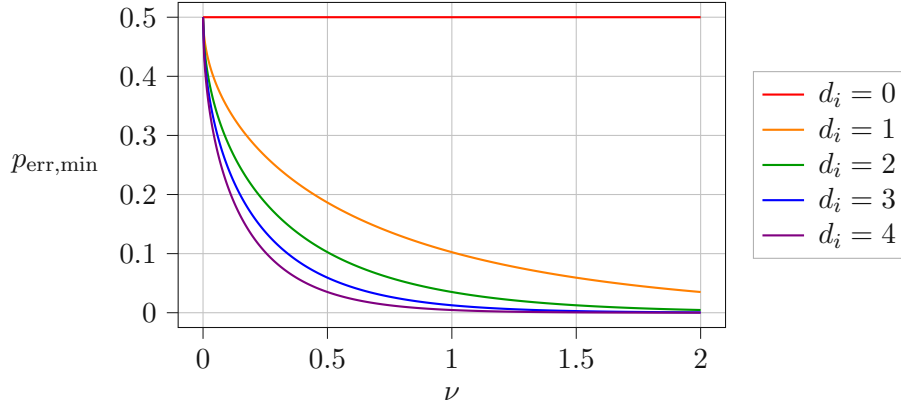


Figure 3.8: Helstrom bound $p_{\text{err},\min}$ as a function of the mean photon number ν for different possible eigenvalues d_i of the matrix \mathbf{D}_{12} , see Eq. (3.112). The prior probabilities are assumed to be balanced, i.e., $p_1 = p_2 = 1/2$.

$$\begin{aligned} \left| \mathcal{M} \langle \boldsymbol{\alpha}_1^{\text{out}} | \boldsymbol{\alpha}_2^{\text{out}} \rangle \mathcal{M} \right|^2 &= \exp \left(- \left(\|\boldsymbol{\alpha}_1^{\text{out}}\|^2 + \|\boldsymbol{\alpha}_2^{\text{out}}\|^2 - 2\Re \left(\boldsymbol{\alpha}_1^{\text{out}\dagger} \boldsymbol{\alpha}_2^{\text{out}} \right) \right) \right) \\ &= \exp \left(- \|\boldsymbol{\alpha}_1^{\text{out}} - \boldsymbol{\alpha}_2^{\text{out}}\|^2 \right). \end{aligned} \quad (3.110)$$

Therefore, the Helstrom bound is optimal when the expression

$$\|\boldsymbol{\alpha}_1^{\text{out}} - \boldsymbol{\alpha}_2^{\text{out}}\|^2 = \boldsymbol{\alpha}^{\text{in}\dagger} (\mathbf{S}_1 - \mathbf{S}_2)^\dagger (\mathbf{S}_1 - \mathbf{S}_2) \boldsymbol{\alpha}^{\text{in}} \quad (3.111)$$

is maximized. The relevant matrix here, namely $\mathbf{D}_{12} := (\mathbf{S}_1 - \mathbf{S}_2)^\dagger (\mathbf{S}_1 - \mathbf{S}_2)$, shows a close resemblance to the FI matrix $\mathbf{F}_\theta = 4 (\partial_\theta \mathbf{S})^\dagger (\partial_\theta \mathbf{S})$, where the derivative is replaced by the finite difference. The optimal probe state $\boldsymbol{\alpha}^{\text{in}}$ for discrimination is proportional to the eigenvector of \mathbf{D}_{12} corresponding to the largest eigenvalue. Denoting the eigenvectors and -values of \mathbf{D}_{12} by \mathbf{d}_i and d_i , respectively, we obtain (ν is the mean photon number)

$$\boldsymbol{\alpha}^{\text{in}} = \sqrt{\nu} \mathbf{d}_i \implies p_{\text{err},\min} = \frac{1}{2} \left(1 - \sqrt{1 - 4p_1 p_2 e^{-\nu d_i}} \right). \quad (3.112)$$

Plots of this function for different possible eigenvalues d_i can be seen in Fig. 3.8. For $\nu d_i \gg 1$, the Helstrom bound can be approximated by

$$p_{\text{err},\min} \approx p_1 p_2 e^{-\nu d_i}. \quad (3.113)$$

An experimental implementation in the optical domain for detecting the presence of a polystyrene bead hidden between two strongly scattering glass diffusers is given in Ref. [239], to which the author contributed in the theoretical analysis.

For a concrete numerical example, we resort to the generic setup presented in Subsec. 1.1.2. A metallic target is positioned in the center of a waveguide. Further scatterers surrounding the target provide a complex scattering environment.

As hypotheses H_1 and H_2 we choose the presence and the absence of the target, respectively. The other scatterers are always in place. Figure 3.9 shows the spatial intensity distributions of the waves that emerge when injecting the eigenstates of \mathbf{D}_{12} corresponding to the maximum and the minimum eigenvalue into both systems (with and without the target). The maximum eigenvalue is $d_{\max} \approx 3.652$. Employing the corresponding eigenstate allows for a highly reliable discrimination between the two hypotheses, even at low light intensities, see also Fig. 3.8. This fact is supported by inspecting the spatial structures of this eigenstate when coupled into the system with and without the scatterer (see Figs. 3.9(a) and 3.9(b), respectively): The wave focuses onto the location of the target, leading to vastly different spatial structures of the emerging wave fields. On the other hand, the minimum eigenvalue of \mathbf{D}_{12} is zero within the given machine precision (double precision). This implies that employing the corresponding eigenstate gives absolutely no additional information (on top of the prior probabilities) on whether the target is present or not. Physically, this is explained by the fact that the light wave avoids any contact with the target, see Fig. 3.9(c), and it therefore makes no difference if the target is removed, see Fig. 3.9(d).

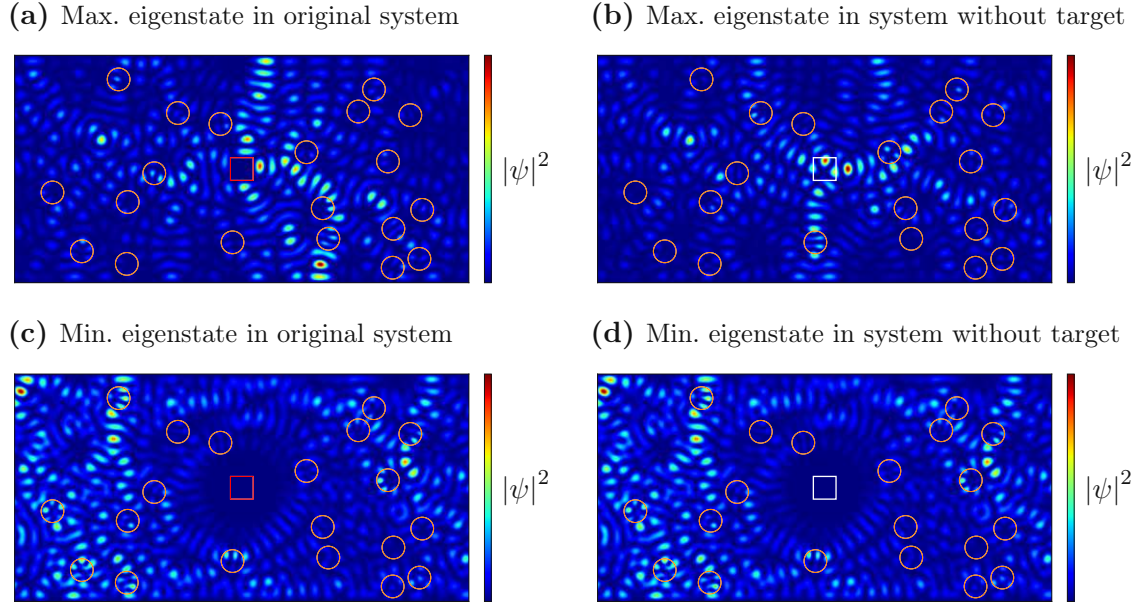


Figure 3.9: Discrimination in the generic waveguide example introduced in Subsec. 1.1.2 to decide if the target (red square) is present or not. The orange circles mark the surrounding scatterers that constitute a complex scattering medium. The maximum eigenvalue of \mathbf{D}_{12} is $d_{\max} \approx 3.652$ and the minimum eigenvalue practically vanishes, $d_{\min} = 0$. The corresponding eigenstates are fed into both systems (with and without the target) and the resulting spatial intensity distributions are shown. **(a)** Maximum eigenstate in system with target. The wave strongly focuses onto the target. **(b)** Maximum eigenstate in system without target. The white square indicates the original location of the target. The emerging wave field is vastly different from **(a)**. **(c)** Minimum eigenstate in system with target. The wave avoids any contact with the target. **(d)** Minimum eigenstate in system without target. The white square indicates the original location of the target. The emerging wave field is the same as in **(c)**.

Chapter 4

Imaging

The aim of imaging is to generate spatial feature maps displaying local properties of a system (e.g., the speed of propagation (SOP) or the reflectance) by measurements that are conducted outside of the system. In most scenarios, the system gets irradiated with a wave (e.g., an electromagnetic or a sound wave), which then undergoes scattering inside the system. The outgoing probe (or a secondary wave that is excited inside the system) is measured in a detector and the measurement results are converted into an image through a specific computational protocol. Imaging finds application in a broad spectrum of disciplines, ranging from material sciences [240–242] over earth sciences [243–245] to life sciences [246–248]. Further reviews on imaging in complex media are given in Refs. [25, 93, 249].

The two most prominent detrimental effects leading to a degradation of the image quality are aberrations and (multiple) scattering. Aberrations are caused by smooth long-range spatial modulations of the SOP which lead to a slight distortion of the wavefront. Mathematically, this can be expressed by a local phase mask. Multiple scattering on the other hand comes about if there are high-contrast modulations of the SOP, causing severe deformations of the wavefront. To give concrete examples: For ultrasound imaging, aberrations would be realized by a layer of fat tissue, whereas the skull with its rich structure provokes multiple scattering.

In most scenarios, one has access to just a single side of the specimen, which is what we assume for the remainder of this chapter. This means that the data available for computing an image consists of (a part of) the spectral reflection matrix $\mathbf{R}(k)$. It turns out that it is quite convenient to formulate imaging techniques based on the reflection matrix [63, 250, 251].

4.1 Confocal Imaging

To demonstrate how such a technique works in practice, we present a very simple imaging method in matrix formulation, namely confocal imaging, which is characterized by focusing the probe wave onto a specific point within the sample and collecting only the part of the reflected wave that originates at the same point [252]. In a matrix imaging framework, this can be expressed by representing $\mathbf{R}(k)$ in the

so-called “focused basis” [63] (although it is not a basis in the strict mathematical sense). In this chapter, we denote matrix indices as arguments in round brackets, e.g., $R(k; m, m') \equiv R_{m, m'}(k)$. The conversion between the mode basis $\{m\}$, in which $\mathbf{R}(k)$ is measured, and the focused basis $\{\mathbf{r}\}$ is mediated by a matrix built from the Green’s function $G(k; m, \mathbf{r})$ which gives the propagation amplitude of the injected mode m with frequency $\omega = ck$ to the location \mathbf{r} inside the sample. Ideally, this would be the exact Green’s function of the complete system, which we assume to be unknown to us. The roughest approximation consists in assuming free propagation. For instance, in the two-dimensional waveguide presented in Subsec. 1.1.2, this would be

$$G_0(k; m, x, y) = \sqrt{\frac{2}{W}} \sin\left(\frac{m\pi y}{W}\right) e^{ik_m x}. \quad (4.1)$$

Care must be taken with proper complex conjugation when changing from the mode basis to the focused basis. It is easy to keep track when formulating it in a quasi-bracket-notation, where $R(k; m, m') \equiv \langle k; m | \mathbf{R} | k; m' \rangle$, $R(k; \mathbf{r}, \mathbf{r}') \equiv \langle k; \mathbf{r} | \mathbf{R} | k; \mathbf{r}' \rangle$ and $G_0(k; m, \mathbf{r}) \equiv \langle k; \mathbf{r} | k; m \rangle$. The first index of the reflection matrix corresponds to outgoing, i.e., left-travelling modes, which is why we have to conjugate the corresponding Green’s function:

$$\begin{aligned} R(k; \mathbf{r}, \mathbf{r}') &= \sum_{m, m'} \langle k; \mathbf{r} | k; m \rangle^* R(k; m, m') \langle k; m' | k; \mathbf{r}' \rangle \\ &= \sum_{m, m'} G_0^*(k; m, \mathbf{r}) R(k; m, m') G_0(k; m', \mathbf{r}'). \end{aligned} \quad (4.2)$$

The matrix element $R(k; \mathbf{r}, \mathbf{r}')$ can be understood in the following way: The monochromatic probe wave with frequency $\omega = ck$ gets coupled into the system in such a way that it would focus onto the point \mathbf{r}' if the medium was replaced by free space. Also in reception, the same spatial gating is applied — but with the focus located at the point \mathbf{r} . The matrix element $R(k; \mathbf{r}, \mathbf{r}')$ gives the amplitude of observing this special output signal provided the \mathbf{r}' -focused probe wave.

In the absence of aberrations and multiple scattering, i.e., in free space, the spatial extent of the focal spot at position \mathbf{r} is limited by diffraction [253]:

$$\Delta y = \frac{\lambda}{2 \sin(\beta(\mathbf{r}))}, \quad (4.3)$$

$$\Delta x = \frac{2\lambda}{\sin^2(\beta(\mathbf{r}))}. \quad (4.4)$$

Here, y denotes the transverse (or lateral) coordinate and x denotes the axial (or depth) coordinate. $\beta(\mathbf{r})$ is half the angle of illumination for the location \mathbf{r} , which also determines the NA of the imaging system. In our waveguide setup, this angle

β is the angle of the classical trajectory of the highest mode that we have access to, see also Fig. 1.2: $\beta = \kappa_{m_{\max}} = \arcsin(m_{\max}\pi/kW)$.

Usually, the axial resolution is worse than the transverse one. In order to enhance the axial resolution, one often replaces the monochromatic probe by a spatially confined pulse. In wavenumber space, the probe signal is characterized by the Fourier transform $f(k)$ of the spatial pulse shape. The modified axial resolution is determined by the inverse of the spectral bandwidth Δk , which is the standard deviation or the full width at half maximum of $|f(k)|$:

$$\Delta x \propto \frac{1}{\Delta k}. \quad (4.5)$$

Keeping only responses with ballistic time for the signal can be achieved by coherently integrating $R(k; \mathbf{r}, \mathbf{r}')$ over the wavenumber, the result of which is called the broadband focused reflection matrix [63]

$$R(\mathbf{r}, \mathbf{r}') = \int_0^\infty R(k; \mathbf{r}, \mathbf{r}') f(k) dk. \quad (4.6)$$

Adding a specific spatial gating, where both the input and the output focus lie at the same point \mathbf{r} , one arrives at the conventional confocal image. It gives a map of the local reflectance of the system and can be expressed as [63]

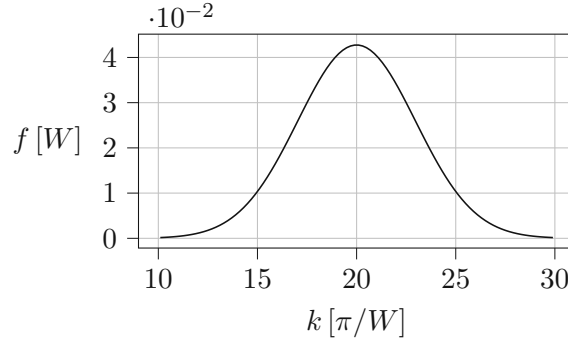
$$I_{\text{confocal}}(\mathbf{r}) = |R(\mathbf{r}, \mathbf{r})|^2. \quad (4.7)$$

In the following, we demonstrate confocal imaging explicitly using the waveguide system described in Subsec. 1.1.2. The only difference is that the square-shaped target is no longer assumed to be metallic, but it gets assigned a refractive index of 1.88, thus making it less reflective. The consequence is that it becomes more challenging to image the target since it leaves a weaker signal in the reflection matrix. On the other hand, the target modified in this way exhibits a richer spectral reflection behaviour, which can be leveraged in the fingerprint imaging method introduced below in Sec. 4.2.

We choose a Gaussian pulse shape such that the axial resolution roughly matches the size of the target and the scatterers, see Fig. 4.1. Furthermore, we assume a limited NA, which is determined by a maximum angle κ_{\max} , i.e., we only consider modes m with $\kappa_m \leq \kappa_{\max} \iff m \leq m_{\max} = \lfloor kW \sin(\kappa_{\max})/\pi \rfloor$. On the level of the reflection matrix in mode basis $R(k; m, m')$, this is implemented by deleting the rows and columns corresponding to $m^{(l)} > m_{\max}$. The confocal images for different values of κ_{\max} are displayed in Fig. 4.2. It is apparent that only the leftmost scatterers are detected reliably. Beyond a certain imaging depth, the image is corrupted due to multiple scattering and thus becomes blurred there.

Furthermore, mind that a confocal image shows the local reflectance, which is why the peaks in the image do not occur at the midpoints of the scatterers. A thorough

(a) Pulse shape in wavenumber space



(b) Pulse shape in real space

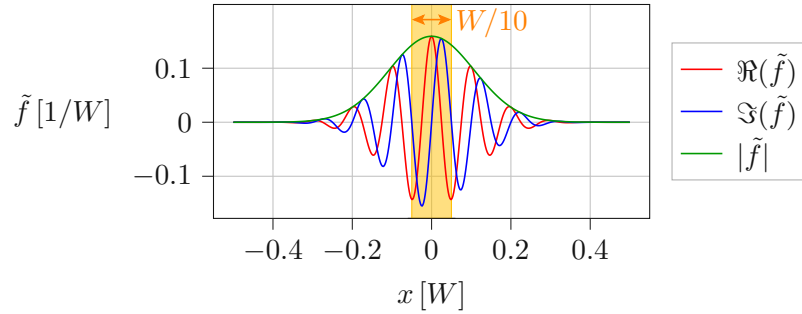


Figure 4.1: Pulse shape used for imaging. W denotes the width of the waveguide. **(a)** In wavenumber space, a Gaussian profile is chosen. It covers a range where between $N' = 10$ and $N' = 30$ modes are open in the left lead (the empty waveguide to the left of the system). **(b)** The Fourier-transformed Gaussian profile is shown in real space. The standard deviation of the envelope $|\tilde{f}|$ is $\Delta x \approx 0.107W$. The orange strip indicates the diameter of the circular scatterers as well as the side length of the square-shaped target, which all equal to $W/10$.

independent investigation of the local reflectance requires Mie theory because both the spatial standard deviation of the pulse, $\Delta x \approx 0.107W$, as well as the wavelength corresponding to the central wavenumber, $k_c = 20\pi/W \implies \lambda_c = 0.1W$, are close to the size of the scatterers, $0.1W$, see also Fig. 4.1(b). Such a detailed analysis using Mie theory is omitted here. Instead, we note that the image of an individual scatterer depends on its shape, size, refractive index and on the pulse shape of the probe wave as well as the NA. As an illustration, we show the confocal images of a single scatterer with different refractive indices in Fig. 4.3.

Confocal imaging relies on ballistic contributions in the reflected signal. Inspecting Fig. 4.2, we observe two effects where multiple scattering leads to a degradation of the image. Firstly, multiple scattering becomes increasingly predominant at larger imaging depths, progressively blurring out the image in the affected regions.

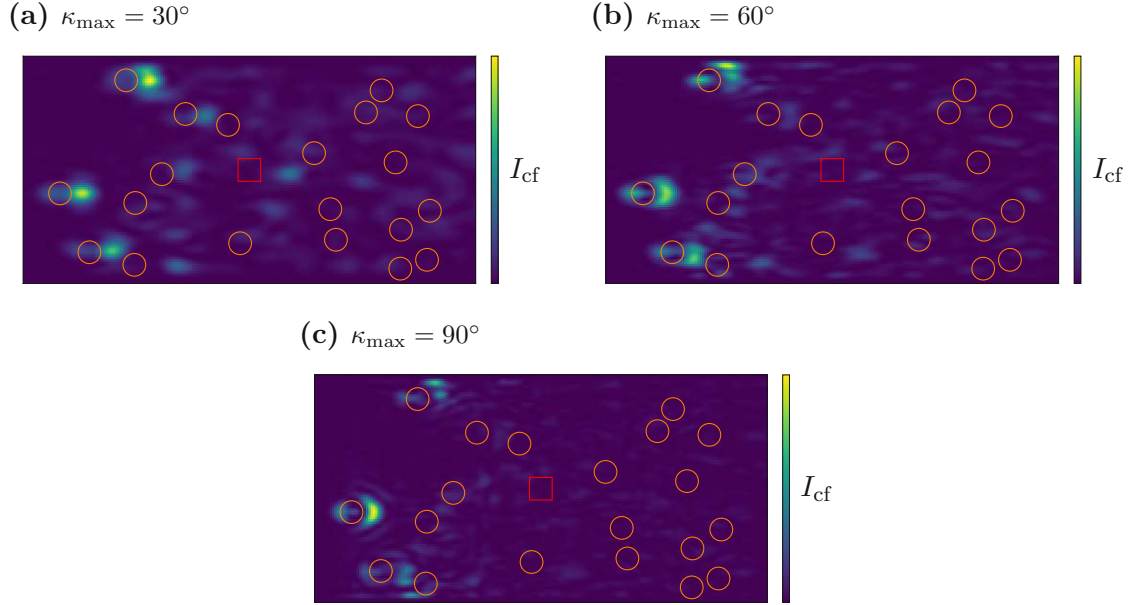


Figure 4.2: Confocal images $I_{\text{cf}} \equiv I_{\text{confocal}}$ of the waveguide system from Subsec. 1.1.2 based on its left-sided reflection matrix \mathbf{R} using a pulsed wave, see Fig. 4.1, for different NAs κ_{max} . Here, the target (red square) has a refractive index of 1.88 instead of being metallic. (a) $\kappa_{\text{max}} = 30^\circ$. Out of the scatterers (orange circles), only the leftmost ones are faithfully reconstructed whereas the rest of the image is blurred. The peaks in the image seem to be shifted relative to the true scatterer positions because the image shows the local reflectance of the system, see also Fig. 4.3. The target is situated at a depth where neither the target itself nor other scatterers are properly detected. (b) Similar to (a), but with $\kappa_{\text{max}} = 60^\circ$. (c) $\kappa_{\text{max}} = 90^\circ$, i.e., all open modes are taken into account. Only the leftmost scatterer shows a pronounced peak while all the other scatterers, including the target, leave no reliable trace in the image. The degradation of the image results from the contributions of the higher modes which are more severely subjected to multiple scattering events.

Secondly, modes with higher mode numbers m have steeper associated angles of propagation κ_m , see Fig. 1.2. In a ray model, those modes traverse the system more often before being back-reflected into the left lead and are thus more strongly influenced by multiple scattering. This effect explains the reduced image quality in Fig. 4.2(c), where all modes are taken into account, as compared to Figs. 4.2(a) and 4.2(b), where higher modes are left out.

According to the Lambert-Beer law, the ballistic contribution essential to confocal imaging typically decreases exponentially $\propto e^{-2x/\ell_t}$ with the imaging depth x in scattering media [25]. The corresponding characteristic length ℓ_t is the transport mean free path. This quantity is the average distance after which the direction of propagation is completely randomized. Another important quantity which de-

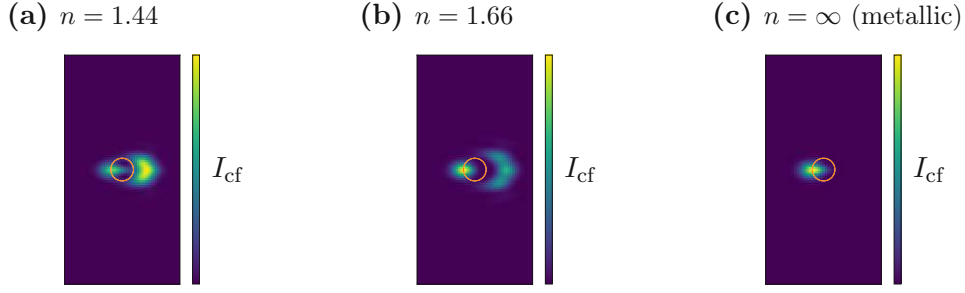


Figure 4.3: Confocal images $I_{\text{cf}} \equiv I_{\text{confocal}}$ of a single scatterer (orange circle) in a waveguide based on its left-sided reflection matrix using a pulsed wave, see Fig. 4.1, for different refractive indices n of the scatterer. The NA is assumed to be given by $\kappa_{\text{max}} = 60^\circ$. **(a)** $n = 1.44$. This corresponds to the scatterers in the original system, see also Fig. 4.2(b). There are two peaks appearing in the image, one at the scatterer’s front side (left) and one at its back side (right). Each peak originates from the reflection off the respective interface. Here, the reflection from the back side is stronger and thus the corresponding peak is more pronounced. **(b)** When the refractive index is increased to $n = 1.66$, the reflection from the scatterer’s front side and hence the corresponding peak become dominant. Meanwhile, the peak at the back side dissolves into a blurry arc. The gap between this arc and the contour of the actual scatterer is explained by the mismatch between the free propagation assumed in the construction of the confocal image and the actual refractive index of the scatterer; see also the discussion in the paragraph before Eq. (4.1). **(c)** When the scatterer becomes metallic ($n = \infty$), there is just a single peak at its front side because the wave cannot penetrate the scatterer and thus cannot be reflected from its back side.

describes the scattering strength of the system is the scattering mean free path ℓ_s , which gives the average distance between two scattering events. The anisotropy factor $g := \langle \cos(\gamma) \rangle$, which gives the average cosine of the scattering angle γ , relates the two lengths ℓ_t and ℓ_s through $\ell_t = \ell_s / (1 - g)$ [10]. In a medium with isotropic scattering it holds that $g = 0 \implies \ell_t = \ell_s$, whereas for strong forward scattering $g \approx 1 \implies \ell_t \gg \ell_s$. Typically, isotropic scattering happens whenever the individual scatterers are much smaller than the wavelength (Rayleigh scattering), whereas scatterers that are much larger than the wavelength usually lead to forward scattering. In generic biological tissues one finds for visible or near-infrared light $g \approx 0.9$, $\ell_s \approx 100 \mu\text{m}$ and $\ell_t \approx 1 \text{mm}$ [254], see also Fig. 4.4. The accompanying refractive index is to a good approximation given by $n \approx 1.33w + 1.514(1 - w)$, where $w \in [0, 1]$ indicates the water content of the tissue [254]. Regarding ultrasound, biological tissues show a variety of values for the SOP, but soft tissues usually have a value around 1540 m/s [58]. It is much less common to characterize biological samples by their acoustical scattering parameters as was done in Ref. [255] for rat lung tissue, for which the following results were found: $g \approx 0$ and $\ell_s \approx \ell_t \approx 332 \mu\text{m}$.

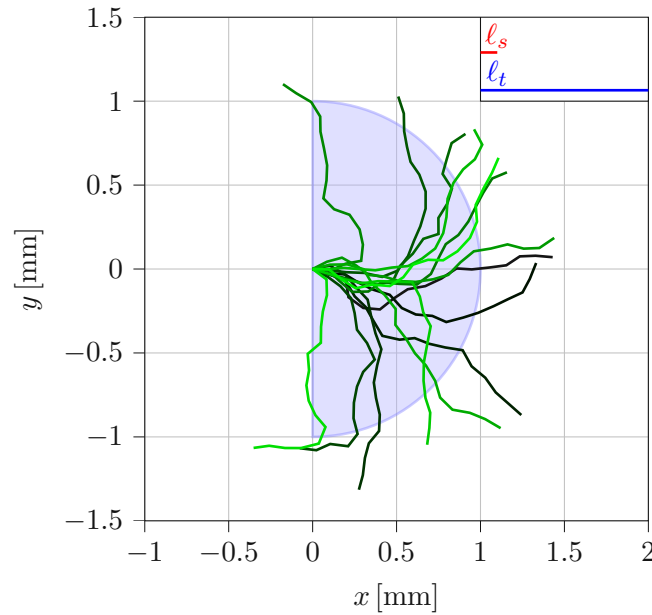


Figure 4.4: Visual depiction of the scattering mean free path ℓ_s and the transport mean free path ℓ_t . Here, the values are set to $\ell_s = 100 \mu\text{m}$ and $\ell_t = 1 \text{ mm}$, which are typical values for the propagation of light in biological specimen. Fifteen randomly generated ray paths are shown in different shades of green. Each path starts at the origin, pointing to the right. The sizes of the individual steps are drawn from a uniform distribution $\mathcal{U}(90 \mu\text{m}, 110 \mu\text{m})$. The direction of each step is chosen relative to the direction of the previous step such that the anisotropy factor takes on the value $g = 0.9$. This is accomplished by drawing the relative scattering angles from the normal distribution $\mathcal{N}(\mu = 0, \sigma = \sqrt{2 \ln(1/g)})$. The scattering mean free path ℓ_s corresponds to the length of the red line. The transport mean free path ℓ_t is indicated by the blue line and the blue semicircle whose radius is ℓ_t . After the distance ℓ_t , the propagation directions of the rays are completely randomized.

Confocal imaging is an appropriate imaging modality in scenarios where the back-reflected signal is dominated by ballistic contributions, which is the case whenever the imaging depth is smaller than the transport mean free path ℓ_t . For deep imaging or in strongly scattering media, however, the desired imaging depth might be considerably larger than ℓ_t . There are two main ideas on how to tackle this challenge. One approach is enhancing the ballistic contribution in the back-reflected signal or filtering away the contributions that stem from multiple scattering, as is done in Refs. [256–258]. The other approach consists in leveraging the multiple scattering contributions, as opposed to trying to suppress them. These contributions contain vastly more information than the ballistic signal. This becomes clear when considering confocal imaging, where through the spatial gating mechanism all the off-diagonal elements of the broadband focused reflection matrix are discarded.

The problem with the rich and valuable information contained in the multiple scattered component is that it is scrambled within the back-reflected signal, so one has to come up with clever ways of extracting this information. Examples for such strategies are given in Refs. [63, 64, 259].

4.2 Fingerprint Imaging

In a joint project together with the group of Alexandre Aubry at Institut Langevin (ESPCI Paris), the author of this thesis contributed conceptual ideas to the development of a new ultrasound imaging technique that utilizes multiple scattering components. Under the supervision of the author of this thesis, David Furlinger contributed numerical investigations in the course of his bachelor thesis “Object-Adapted Imaging Using Scattering Invariant Modes” [260]. With the group of Alexandre Aubry, we filed a patent entitled “Procede pour caracteriser un objet cible dans un milieu” (“Method for characterizing a target object in a medium”) that comprises this method we call here “fingerprint imaging” for reasons that will become clear below.

Inspired by the so-called “scattering invariant modes” (SIMs) [261], we devised an imaging method that is able to locate specific targets within a scattering environment. A SIM has the defining property that it produces nearly identical output fields when it gets injected into two different scattering systems. Specifically, this even works when one of the systems is a target scatterer buried deep inside a disordered medium and the other system consists of the target alone, surrounded by free space. In this case, a SIM that is injected into one of these systems yields essentially the same output scattered wave, independent of whether the surrounding disorder is present or not. Numerical studies carried out in Ref. [261] demonstrated that on top of this defining property, the wave fields show high correlations also within the scattering medium. A first imaging approach based on these correlations gave promising numerical results, but required a measurement behind the medium and the presence of fluorescent particles inside of it [261].

Here, we propose to work without fluorescent deposits, but only with the information stored in the reflection matrix \mathbf{R} of the system under study, which we assume to be accessible from only one side. Our aim is to detect and locate a particular target inside the system using the individual scattering characteristics encoded within the reflection matrix of the bare target. To achieve this goal, we require some means of assessing the similarity between the original system under study and the target on the level of their reflection matrices. To this end, we introduce special states that we call here “reflection invariant modes” (RIMs). They are defined with respect to a reference system, which consists of just the target that we wish to detect and locate, see also Fig. 4.5. The reference target is characterized by specific parameters like its position, rotational orientation, size or local SOP.

Here, we only consider the position \mathbf{r} of the reference target. The background of the reference system is most conveniently chosen to be a homogeneous medium. In more refined versions of the proposed imaging method, the reference background can be tailored depending on the level of knowledge about the background medium in the original system. The reflection matrix $\mathbf{R}_{\text{ref}}(\mathbf{r})$ of the reference system can be established through measurement of a corresponding real-world system or through numerical computations. Shifting the target, i.e., relocating it at different positions \mathbf{r} , can, for instance, be performed virtually in post-processing using the focused basis, see Sec. 4.1. Other possibilities for virtually shifting the target, particularly suited for the waveguide system, are the transformations given below in Eqs. (4.12) and (4.13). The RIMs $\mathbf{a}_i(\mathbf{r})$ are defined as eigenvectors of the matrix $\mathbf{R}_{\text{ref}}^\dagger(\mathbf{r})\mathbf{R}$:

$$\mathbf{R}_{\text{ref}}^\dagger(\mathbf{r})\mathbf{R}\mathbf{a}_i(\mathbf{r}) = a_i(\mathbf{r})\mathbf{a}_i(\mathbf{r}). \quad (4.8)$$

For each position \mathbf{r} of the reference object, the eigenvalues $a_i(\mathbf{r})$ are a measure for how well the reference system emulates the original system when being probed with the RIMs. In this way, these eigenvalues measure the correlations between those two systems, which are strongest when the reference position \mathbf{r} matches the true position of the object in the original system. Thus, plotting the spatial dependence of the complex eigenvalues $a_i(\mathbf{r})$ or a suitable combination of them, provides us with a map for the likelihood of the target's location, see also Fig. 4.5. Specifically, here we consider the coherent summation over all eigenvalues (which is given by the trace) as well as an integration over the wavenumber spectrum, weighted by the Fourier transform $f(k)$ of the spatial shape of the probe pulse. Additionally, we normalize w.r.t. the respective total reflectances. Introducing the Frobenius⁵ inner product, including a weighted wavenumber integration,

$$\langle \mathbf{A}, \mathbf{B} \rangle_f := \int_0^\infty \text{tr}(\mathbf{A}^\dagger(k)\mathbf{B}(k))f(k)dk, \quad (4.9)$$

the computational procedure for fingerprint imaging can be written concisely as

$$I_{\text{fingerprint}}(\mathbf{r}) = \frac{|\langle \mathbf{R}_{\text{ref}}(\mathbf{r}), \mathbf{R} \rangle_f|^2}{\langle \mathbf{R}_{\text{ref}}(\mathbf{r}), \mathbf{R}_{\text{ref}}(\mathbf{r}) \rangle_f \langle \mathbf{R}, \mathbf{R} \rangle_f}. \quad (4.10)$$

This expression can be interpreted as the squared cosine similarity between $\mathbf{R}_{\text{ref}}(\mathbf{r})$ and \mathbf{R} w.r.t. the inner product $\langle \cdot, \cdot \rangle_f$ defined in Eq. (4.9).

Using different reference objects allows for multi-channel images with each channel corresponding to an individual object. Now the terminology of ‘‘fingerprint imaging’’ should make sense: For each target, a fingerprint is recorded in the form of a corresponding reference reflection matrix $\mathbf{R}_{\text{ref}}(\mathbf{r})$. One can then search for this fingerprint within a given reflection matrix \mathbf{R} .

⁵It is called after Frobenius because $\text{tr}(\mathbf{A}^\dagger\mathbf{A}) = \|\mathbf{A}\|_{\text{F}}^2$.

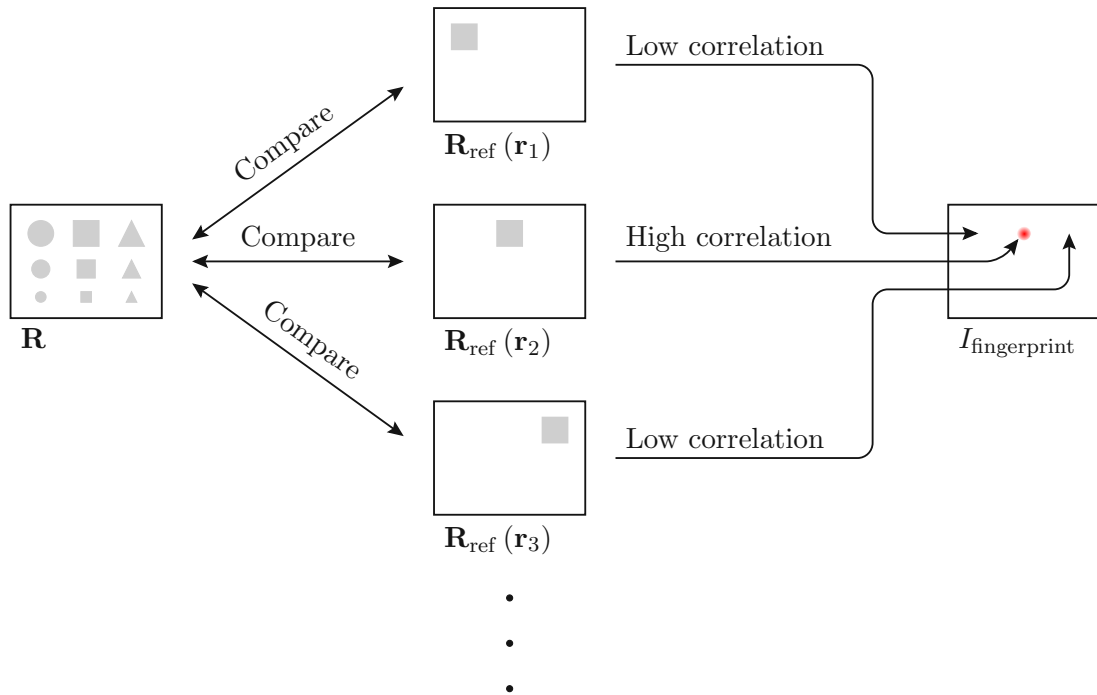


Figure 4.5: Working principle of the fingerprint imaging method. In the left column, the configuration of the original system is shown. Here, it consists of nine scatterers with different shapes and sizes. The system is characterized by its reflection matrix \mathbf{R} . The large square is selected as the reference target. In the middle column, three reference systems with the reference target located at different positions \mathbf{r}_i are shown. (These reference systems are only an exemplary selection of potentially infinitely many.) Each reference system has an associated reflection matrix $\mathbf{R}_{\text{ref}}(\mathbf{r}_i)$ and is compared to the original system via the eigenvalues of the matrix $\mathbf{R}_{\text{ref}}^\dagger(\mathbf{r}_i)\mathbf{R}$. This comparison yields a correlation value which is displayed at the corresponding pixel in the fingerprint image (right column). The correlation is high whenever the reference position \mathbf{r}_i matches the position of a reference target in the original system.

One of the major advantages of this method is that it is free of labels (like localized guide stars or fluorescence), but still target-specific. Furthermore, the whole procedure works in post-processing once the reflection matrix has been recorded, i.e., the explicit experimental implementation of a RIM using wavefront shaping tools is not required.

The fingerprint imaging technique can be refined in different ways. By removing the specular echo, which is not really unique for a given target, finer characteristic features of the target are accentuated. Also, depending on the knowledge about the original system under study, the model of the reference system may be improved.

As an explicit example, we now perform fingerprint imaging in the waveguide system introduced in Subsec. 1.1.2, the only difference being that the target is not

metallic any more, but it has a refractive index of 1.88. This way, the target is equipped with richer reflection characteristics, e.g., more resonances, as compared to a metallic target. The shape $f(k)$ of the pulsed probe wave is chosen to be the same as in Sec. 4.1, see also Fig. 4.1. The NA is assumed to be limited by $\kappa_{\max} = 30^\circ$, i.e., only modes m with $\kappa_m \leq 30^\circ$ are taken into account. We select two different reference objects, namely the square-shaped target and a single circular scatterer. The reference matrices $\mathbf{R}_{\text{ref}}(\mathbf{r})$ do not have to be calculated numerically for each position \mathbf{r} . With the help of two transformations, the number of simulated reference systems can be considerably reduced.

Firstly, if we know the reflection matrix for the target being located at position $\mathbf{r} = (x, y)$, then the reflection matrix for the “mirrored” position $(x, W - y)$ can be derived from $\mathbf{R}_{\text{ref}}(\mathbf{r})$. This can be done only for reference objects that are themselves mirror-symmetric w.r.t. the axial coordinate. We note that under this mirror transformation $y \mapsto W - y$, the transverse profiles (see Eq. (1.16)) of the modes with even m change sign while the profiles of the modes with odd m remain unaffected:

$$\psi_m(W - y) = (-1)^{m-1} \psi_m(y). \quad (4.11)$$

On the level of the reflection matrix, this transformation is implemented by flipping the sign of all matrix entries that are indexed with an even and an odd mode:

$$(\mathbf{R}_{\text{ref}}(x, W - y))_{m,m'} = (-1)^{m+m'} (\mathbf{R}_{\text{ref}}(x, y))_{m,m'}. \quad (4.12)$$

Secondly, we can virtually shift the reference object in the axial direction (i.e., in the x coordinate). Suppose we know $\mathbf{R}_{\text{ref}}(x, y)$. The reference system where the object is moved to the position $(x + \Delta x, y)$ can be interpreted as the concatenation of an empty waveguide of length Δx and the original system where the reference object is located at (x, y) . The scattering matrix of the empty waveguide is known analytically (see Eq. (1.21)). The so-called Redheffer star product [262, 263] is an operation that yields the scattering matrix of a concatenated system from the scattering matrices of the constituents. In the case considered here, the Redheffer star product simplifies to

$$(\mathbf{R}_{\text{ref}}(x + \Delta x, y))_{m,m'} = (\mathbf{R}_{\text{ref}}(x, y))_{m,m'} e^{ik_m^x \Delta x} e^{ik_{m'}^x \Delta x}. \quad (4.13)$$

It should be noted that this transformation is valid also for $\Delta x < 0$.

Figure 4.6(a) shows the fingerprint image where the reference object is chosen as the square-shaped target. Close to the true target position, a distinct peak emerges. On the other hand, peaks also form at some locations that are associated to the circular scatterers. This drawback can be remedied by considering also the fingerprint image where the reference object is chosen as one of the circular scatterers, see Fig. 4.6(b). There we see that the leftmost scatterers are reconstructed very well. In a next step, we merge the individual fingerprint images into a combined

two-channel image. This is achieved by taking the pixel-wise maximum of both fingerprint images, keeping track of where each pixel came from (i.e., the target- or the scatterer-related fingerprint image — this information is encoded in the colour of the final image), see Fig. 4.6(c). We see that for the leftmost scatterers, the scatterer channel overrules the target channel. This behaviour can be verified independently by considering the fingerprint images of the individual reference objects alone, see Fig. 4.7. Coming back to the two-channel image of the original system in Fig. 4.6(c), we notice that also the target is imaged reliably by a predominant peak in the target channel, though this peak is not so sharp and a bit shifted. This, however, is a considerable improvement when compared to the corresponding confocal image in Fig. 4.6(d), where the target leaves no trace whatsoever.

As illustrated in the example above, fingerprint imaging exhibits considerable advantages over confocal imaging. It provides a technique that is object-specific by making use of the multiple scattering characteristics of each object considered, without relying on any particular guide star placed inside the system under investigation. Employing multiple reference objects makes it possible to produce multi-channel images where the different objects are associated to different channels. Fingerprint imaging is applied in post-processing, i.e., it does not require any particular wavefront shaping during the measurement process. Lastly, it should be pointed out that the method is not restricted to the positions of the reference objects, but any object-related parameter such as orientation, size or local SOP may be used to create maps of likelihoods assigned to the respective parameters.

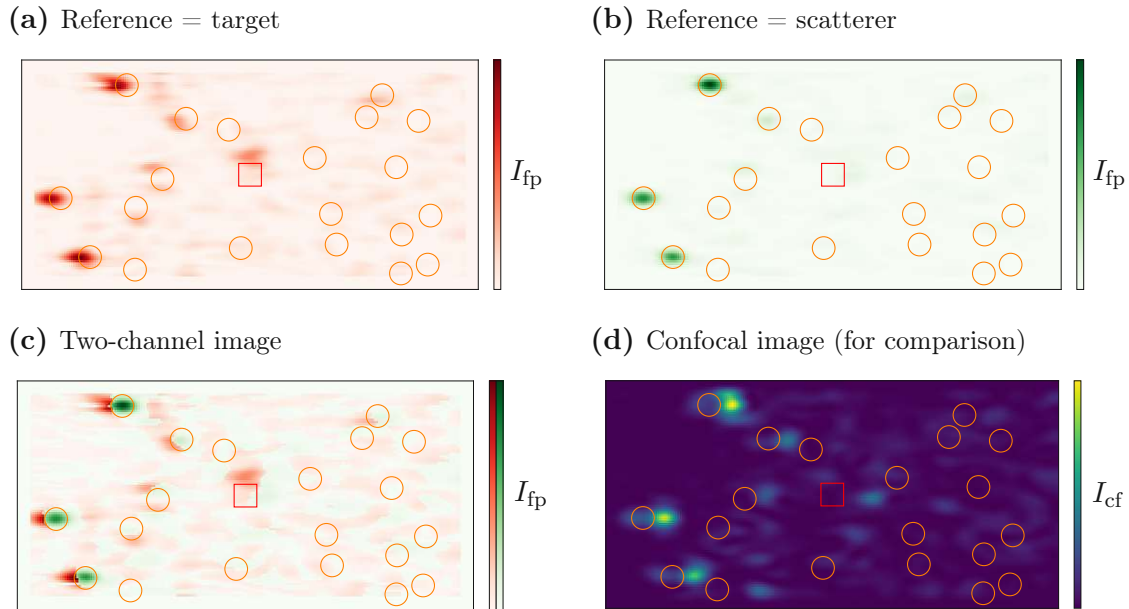


Figure 4.6: Fingerprint images $I_{\text{fp}} \equiv I_{\text{fingerprint}}$ of the waveguide system from Subsec. 1.1.2 based on its left-sided reflection matrix \mathbf{R} using a pulsed wave, see Fig. 4.1, for different reference objects. Here, the target (red square) has a refractive index of 1.88 instead of being metallic. The NA is given by $\kappa_{\text{max}} = 30^\circ$. **(a)** The target is chosen as the reference object. Apart from the peak close to the true position of the target, there are also a few erroneous peaks that are not related to the target, but rather to the circular scatterers (orange circles). **(b)** A single scatterer is chosen as the reference object. The leftmost scatterers get imaged very clearly. **(c)** The two images in **(a)** and **(b)** are merged into a two-channel image by taking the pixel-wise maximum, where the origin of the respective maximum pixel is encoded in the colour (red for reference = target, green for reference = scatterer). The leftmost peaks are now correctly attributed to the circular scatterers (see also Fig. 4.7(c)). Also the presence of the target is successfully detected. Its predicted location is a bit shifted though. **(d)** For direct comparison, the confocal image with the same imaging parameters, Fig. 4.2(a), is shown again. Here, the target does not appear in the image.

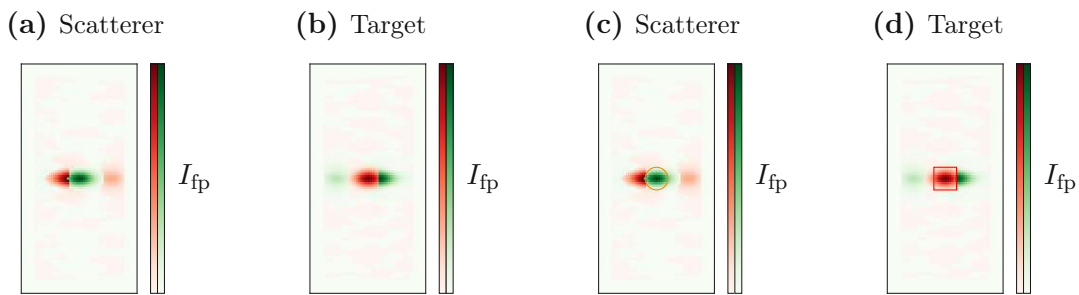


Figure 4.7: Fingerprint images $I_{\text{fp}} \equiv I_{\text{fingerprint}}$ of the individual reference objects, namely a single circular scatterer and the square-shaped target (with refractive index 1.88), when being placed in the center of an otherwise empty waveguide. The imaging parameters (e.g., pulse shape, NA) are the same as in Fig. 4.6(c). For the red channel, the target is taken as the reference object. For the green channel, a scatterer is taken as the reference object. (a) Two-channel fingerprint image of a single circular scatterer. The peak in the target channel (red) is partly covered by the dominant peak in the scatterer channel (green). (b) Two-channel fingerprint image of the square-shaped target. The peak in the scatterer channel (green) is partly covered by the dominant peak in the target channel (red). (c) Same as (a), including the contour of the true scatterer. (d) Same as (b), including the contour of the true target.

Chapter 5

Machine Learning

In the course of his diploma thesis “Inverse Scattering in One-dimensional Random Media Using Deep Learning” [264], the author of this thesis introduced machine learning (ML), specifically deep learning (DL), to the research in the group of Stefan Rotter. The diploma thesis [264] contains a concise introduction to DL. For a more in-depth treatment of ML and DL, the reader is recommended to read the literature in Refs. [265–270].

During his PhD studies, the author of this thesis supervised a handful of DL-related projects, which are outlined in the following sections in chronological order.

5.1 Two-Dimensional Inverse Scattering

In his project thesis “Use of Machine Learning in 2D inverse Scattering” [271], Günther Hackl further developed the methods established in [264] and generalized them to two-dimensional systems. An artificial neural network (ANN) was trained to predict the location of circular scatterers based on the scattering matrix of the system as an input. Different network architectures were tested, including sequential and non-sequential fully connected neural networks (FCNNs) as well as convolutional neural networks (CNNs).

A non-sequential FCNN has the huge advantage, as compared to a sequential one, that it allows for separate input layers that are merged at a later stage in the network. This makes it easier to feed input data with different dimensions, like scattering matrices at different frequencies with different sizes, into the network. Additionally, far less connections between the input layer(s) and the first hidden layer(s) are required in this architecture, leading to a drastically decreased number of trainable parameters without any noticeable drop in performance.

The FCNNs used in [271] are bound to estimate the position of a fixed number of scatterers since they directly give the predicted coordinates in their output layers. The CNN, on the other hand, is able to predict the location of an arbitrary number of scatterers. This is because it maps a two-dimensional image, namely the confocal image (see Sec. 4.1), to another two-dimensional image of the same dimensions, which shows the probability of each pixel belonging to a target scatterer. Using

a confocal image as the input for the CNN can be viewed as a deterministic pre-processing step preparing the data from the scattering matrices.

The vast amount of training data required for the learning procedure is produced using a trick: The systems for the training data set are assembled from lateral slices containing a single scatterer or free space. One then just needs to calculate the scattering matrices of a single scatterer at few different positions numerically. The scattering matrix of free space is known analytically. The individual scattering matrices of the slices can then be combined using the Redheffer star product to yield the scattering matrix of the total system [262, 263].

Firstly, the performance of each trained network is tested on data that is similar to the training data, but which is not part of the training data set, i.e., the network has not encountered the testing data during the learning procedure. Both the non-sequential FCNN and the CNN achieve excellent results, see Figs. 5.1(a) and 5.2(a).

Secondly, for each architecture, its generalizability is examined, i.e., how well it can deal with data that lies outside of the training data distribution. For instance, the shape or the size of a scatterer is changed or an additional scatterer is introduced into the system. The non-sequential FCNN can cope well with different shapes and it achieves acceptable results for different sizes, see Figs. 5.1(b) and 5.1(c). By construction, the FCNN can predict only the position of a fixed amount of scatterers, but it comes up with an interesting solution when the input scattering matrix stems from a system with an additional scatterer: In its prediction, it places one scatterer exactly in the midpoint between two scatterers from the ground truth, all the other ones are predicted as normal, see Fig. 5.1(d). The CNN, on the other hand, can reliably predict the positions of all scatterers, even if an additional one is introduced, unless one of the scatterers “hides” behind another one. In this scenario, the signal from the “hidden” scatterer is virtually non-existent in the single-sided reflection matrix, which is used to construct the input confocal image, so also the CNN fails to reconstruct this scatterer, see Fig. 5.2(d). The CNN shows acceptable results when tested on scatterers with different shapes or sizes. It is able to predict the locations of the scatterers, but fails to give the correct shapes (it mostly draws the shape in the size that it was trained on), yet it does not produce any unwanted artefacts in regions where no scatterer is located, see Figs. 5.2(b) and 5.2(c).

This project demonstrates that ANNs provide a valuable tool in two-dimensional inverse scattering problems. Non-sequential networks are a lightweight alternative to sequential ones whenever the input data allow for a sensible subdivision into separate blocks. They show virtually the same performance as their sequential counterparts. Employing suitable pre-processing, such as constructing a confocal image, opens up the possibility of using architectures that show a greater flexibility in their predictions, like CNNs.

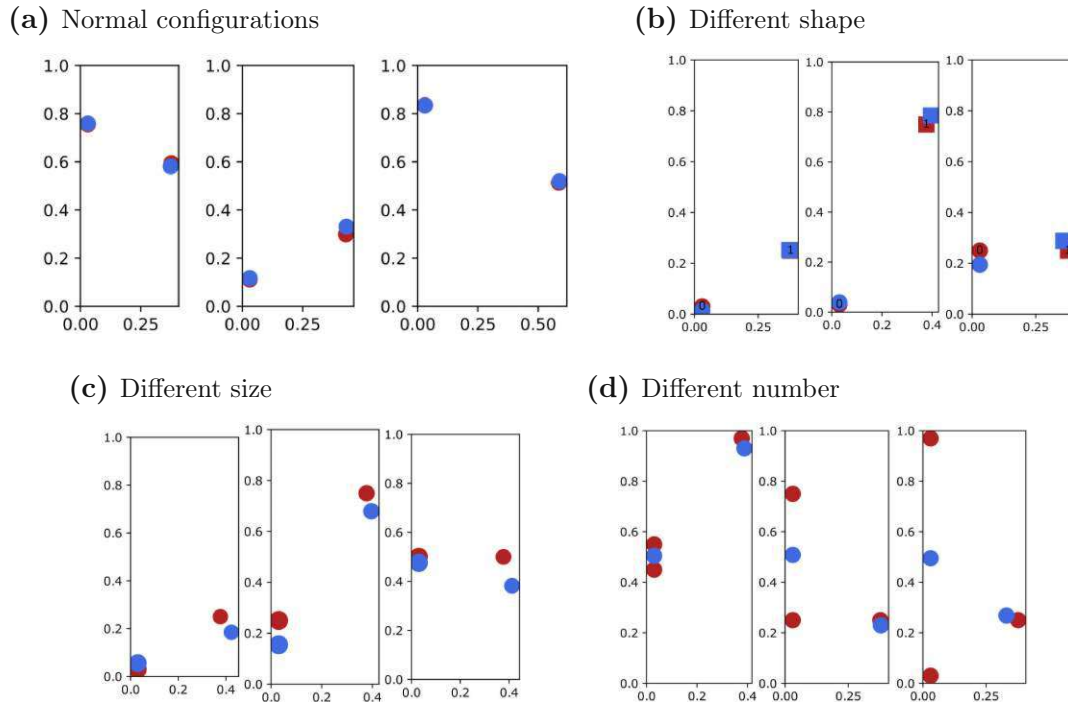


Figure 5.1: Testing the non-sequential FCNN that was trained to predict the coordinates of two circular scatterers from the corresponding scattering matrix. The ground truths are indicated in red, whereas the predictions are shown in blue. (a) The FCNN is tested on data similar to the one it has been trained on. (b) The shape of one scatterer is changed to a square. The predictions are still reliable. (c) The size of one of the scatterers is increased by 15%. The performance of the FCNN degrades noticeably. (d) An additional scatterer is introduced. The FCNN is forced to predict the coordinates of only two scatterers. The solution it chooses consists in placing a scatterer in the midpoint between two original scatterers. Note: Adapted from [271].

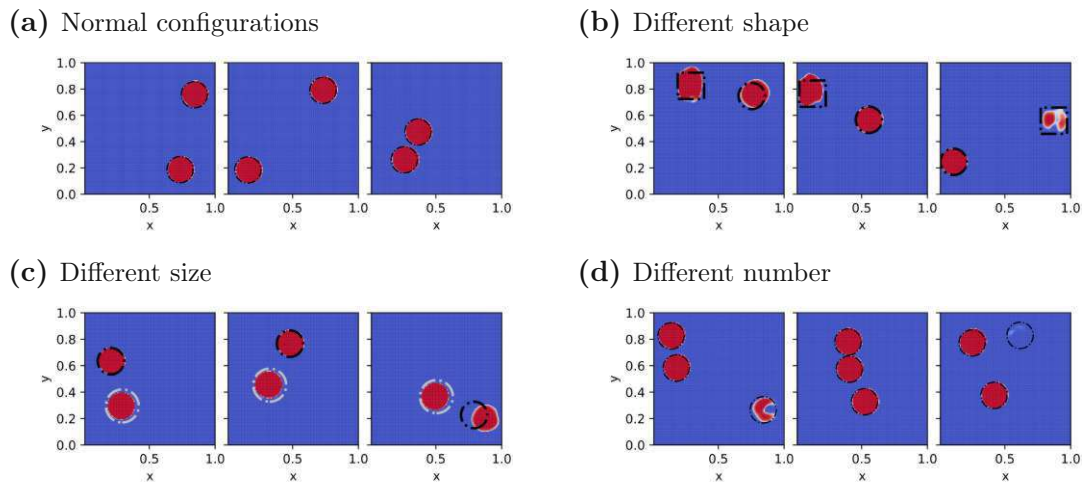


Figure 5.2: Testing the CNN that was trained to predict the pixels that are occupied by circular scatterers from the corresponding scattering matrix. In the training data set, only two circles with the same size are present. The ground truths are indicated by dash-dotted lines, whereas the predictions are shown in red (belonging to a scatterer) and blue (belonging to the background). **(a)** The CNN is tested on data similar to the one it has been trained on. **(b)** The shape of one scatterer is changed to a square. The CNN correctly predicts the positions of the scatterers, but it fails to reconstruct the square shape. **(c)** The size of one of the scatterers is increased by 25% (marked in grey). Most of the time, the CNN correctly predicts the positions of the scatterers, but it fails to reconstruct the larger size. **(d)** An additional scatterer is introduced. The CNN yields reliable results, except for scatterers that are concealed by other scatterers. Note: Adapted from [271].

5.2 Design of Refractive Index for Constant-Intensity Waves

Constant-intensity (CI) waves $\psi(\mathbf{r})$ are, as the name suggests, characterized by having a constant spatial intensity distribution. Without loss of generality, we set this constant value to one, i.e., $|\psi(\mathbf{r})|^2 = 1$. A prime example for CI waves are plane waves in free space. However, in random media, CI waves do not occur in general, but only under very specific circumstances. Which systems allow for CI waves? Let us consider only one-dimensional systems in the following. The ansatz [272]

$$\psi(x) = \exp\left(ik \int_0^x W(x') dx'\right) \quad (5.1)$$

with some real-valued generating function $W(x)$ is a CI wave by construction. Inserting this ansatz into the Helmholtz equation (1.8) yields the corresponding refractive index landscape [272]

$$n^2(x) = W^2(x) - \frac{i}{k} \partial_x W(x). \quad (5.2)$$

Unless $\partial_x W(x) = 0$ (which is the case only for completely homogeneous media), only non-Hermitian systems with gain and loss (as expressed by the imaginary refractive index) support CI waves.

One interesting physical property of CI waves worth highlighting is that they propagate through the medium with perfect transmission, i.e., under the absence of any back-reflection [272]. This has been implemented and verified experimentally using sound waves [273]. Surprisingly, even Hermitian systems that exhibit strong interference effects or even Anderson localization, can be turned into systems that support fully delocalized, perfectly transmitting CI waves by adding the appropriate gain-loss profile.

Whereas it is straightforward to derive the refractive index landscape $n(x)$ for a given generating function $W(x)$, it is much more challenging to find a gain-loss profile $n_i(x)$ to a given real refractive index $n_r(x)$ such that the combined landscape $n(x) = n_r(x) + in_i(x)$ supports a CI wave. The mathematical reason for this is that the underlying differential equations are nonlinear. Trying to solve these differential equations numerically entirely fails to deliver satisfactory results [274]. Ref. [272] provides an iterative scheme that does yield the correct result, but it remains unmentioned how fast and stable this procedure converges and how sensitive it is with respect to the initial guess. A simple implementation of this iterative scheme indicates poor convergence behaviour [274].

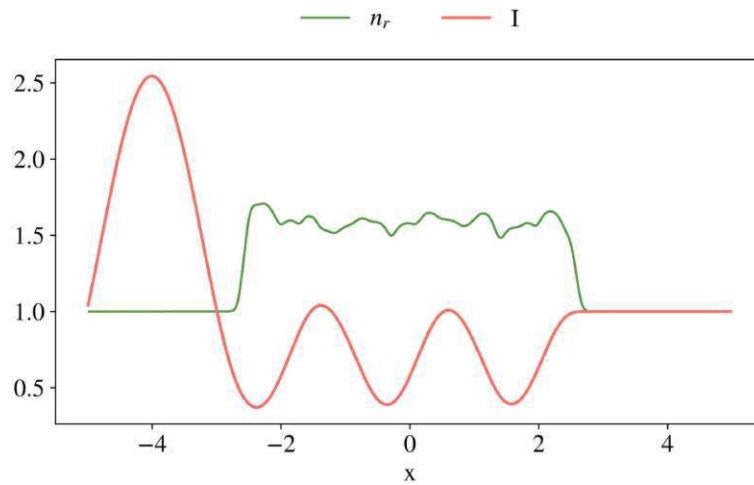
In his project thesis “Constant-Intensity Refractive Indices created with Deep Learning” [274], Felix Wagner addressed this issue by devising a non-iterative DL-based approach. The input of the ANN is some given real refractive index

$n_r(x)$ together with a wavenumber k , and the output is the predicted imaginary refractive index $n_i(x)$ which, when added to $n_r(x)$, should yield a landscape that supports a CI wave. Training data is easy to produce in this case: From a great many randomly chosen generating functions $W(x)$ and wavenumbers k , one can directly construct valid input-output pairs $((k, n_r(x)), n_i(x))$ with minute numerical effort. The refractive indices $n_r(x)$ and $n_i(x)$ are interpreted as sequential data, namely as functions of a suitably discretized space coordinate x_i : $(\dots, n_{r/i}(x_{i-1}), n_{r/i}(x_i), n_{r/i}(x_{i+1}), \dots)$. The architecture predestined for sequential data (which also encompasses text data or time series) is a recurrent neural network. To be more specific, long short-term memory (LSTM) is used in Ref. [274]. The loss function that is minimized during the training process of the ANN is the mean squared error (MSE) between the predicted $n_i(x)$ and the corresponding ground truth. Once training is finished, the performance of the ANN is evaluated by a physical figure of merit, which the ANN did not explicitly learn to optimize. This figure of merit is chosen to be the reflectance that a wave with wavenumber k experiences when injected into the system which is assembled from the given $n_r(x)$ and the predicted $n_i(x)$. The reflectance should be zero in the ideal case. For weakly scattering systems, the ANN achieves a mean reflectance in the order of 10^{-4} , see Fig. 5.3. Compared to the reflectance of the corresponding Hermitian systems (defined by $n(x) = n_r(x)$), this is a decrease by two orders of magnitude. For highly disordered media, whose Hermitian counterparts have reflectance values of approximately 0.97, the ANN is still able to decrease this value by two orders of magnitude, see Fig. 5.4.

Also a CNN is employed to learn the mapping from $(k, n_r(x))$ to $n_i(x)$. It shows results comparable to those of LSTM. However, the CNN introduces minute gain in the asymptotic region (where the refractive index should be $n(x) = 1$). This unwanted effect does not occur with LSTM, which is why the use of LSTM is recommended for the specific task discussed in this section.

This project shows that ANNs constitute a suitable method for solving nonlinear problems appearing in one-dimensional wave scattering. DL-based approaches have multiple advantages over standard numerical procedures: Firstly, they are much faster in producing a solution once the ANN has been trained. Secondly, they are less prone to unstable behaviour. Thirdly, they are able to filter out the unique physically relevant solution in cases where multiple mathematically possible solutions exist.

(a) Hermitian refractive index and corresponding wave intensity



(b) ANN prediction

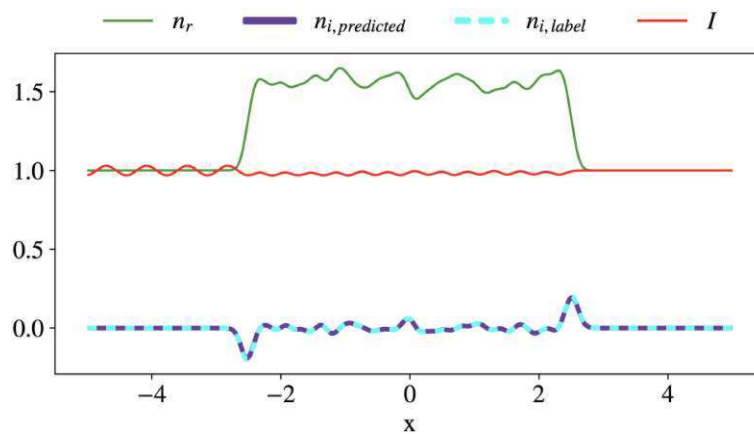
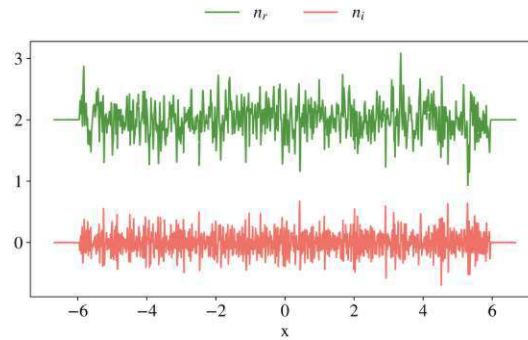
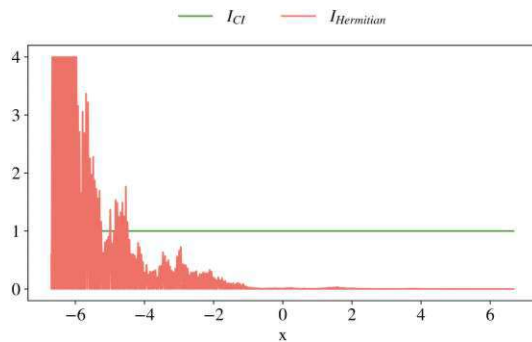


Figure 5.3: Testing the ANN that was trained to predict the imaginary part to a given Hermitian refractive index, such that the total complex-valued refractive index landscape supports a CI wave. (a) A generic Hermitian, i.e., real-valued refractive index (green line) is shown together with the intensity distribution (red line) of a plane wave injected from the left. The large intensity peak to the left of the index profile indicates that the incoming wave is superimposed by a non-negligible reflected wave. In the absence of a reflected wave, the intensity to the left of the system would be constant. (b) The green and the dashed cyan line respectively display the real and the imaginary part of a refractive index that supports a CI wave. The trained ANN receives the real part as an input and returns a prediction for the corresponding imaginary part (purple line). This prediction closely matches the ground truth (dashed cyan line). The red line shows the intensity distribution of a plane wave that is injected from the left into the system constructed from the given real part and the imaginary part as predicted by the ANN. The small oscillations to the left of the system indicate a weak reflection. Note: Adapted from [274].

(a) Highly fluctuating refractive index supporting a CI wave



(b) Intensity in Hermitian counterpart



(c) Intensity in ANN-predicted system

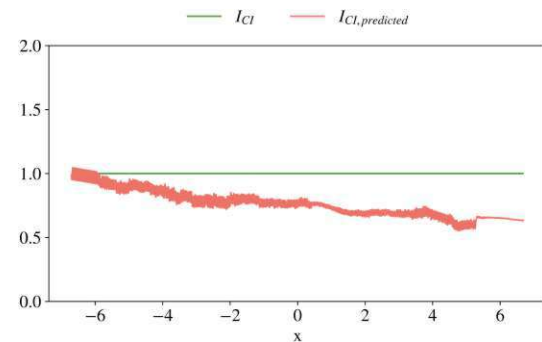


Figure 5.4: Testing the ANN that was trained to predict the imaginary part to a given Hermitian refractive index, such that the total complex-valued refractive index landscape supports a CI wave. **(a)** Example of a highly fluctuating refractive index landscape (green line: real part, red line: imaginary part) that supports a CI wave. **(b)** A plane wave is injected into the corresponding Hermitian system from the left. The emerging intensity distribution (red line) is highly oscillatory and localized in the left region of the strongly scattering system. Practically the whole impinging wave is back-reflected. The green line shows the constant intensity distribution of a CI wave as a reference. **(c)** The Hermitian refractive index is combined with the imaginary part that is predicted by the ANN. Now, the intensity of a plane wave injected from the left (red line) shows no localization any more and it is much closer to that of a true CI wave (green line). About 70 % of the wave get transmitted. Due to the loss and gain in the system, the reflectance is different from 0.3, it amounts to roughly 10^{-2} . Note: Adapted from [274].

5.3 Completing Classical Scattering Matrices for Micromanipulation

In his project thesis “Missing Data Imputation and Prediction of Scattering Matrices using Machine Learning” [275], Jens Burkhart investigated the ability of ML techniques to mitigate experimental shortcomings in real-world applications of classical optical micromanipulation protocols based on the GWS matrix (see Sec. 2.1). These protocols rely on the fact that the GWS matrix is Hermitian, which is the case whenever the scattering matrix is unitary. However, under realistic conditions, the measurement setup usually gives access just to a subunitary part of the full optical scattering matrix, e.g., due to a limited NA of the optical instruments.

In Ref. [275], a simple proof-of-principle system, namely a waveguide containing a single circular dielectric scatterer with arbitrary location, is considered. The parameter θ represents a displacement of the scatterer in a random direction. It is assumed that waves can be injected into the waveguide just from the left hand side. Thus, the relevant part of the GWS matrix is its upper left block $\mathbf{Q}_\theta^{\text{UL}} := -i(\mathbf{R}^\dagger \partial_\theta \mathbf{R} + \mathbf{T}^\dagger \partial_\theta \mathbf{T})$. Furthermore, it is assumed that the scattered waves can be measured only on the right hand side, i.e., only (a part of) the transmitted wave is captured. In a first step, the effect of having a limited NA — both at the input and at the output — is considered, where only part of the transmission matrix \mathbf{T} is measurable. To be more specific, the four highest out of twenty waveguide modes are discarded, such that only 64% of the full transmission matrix is known. A CNN is trained to fill in the missing entries of \mathbf{T} . Knowledge of the reflection matrix \mathbf{R} is essential in order to construct the relevant part $\mathbf{Q}_\theta^{\text{UL}}$ of the GWS matrix. But in the considered setup, \mathbf{R} cannot be measured directly. So in a second step, another CNN is trained to predict \mathbf{R} corresponding to a given transmission matrix \mathbf{T} , which may be complete in the first place or completed by the first CNN. The mean absolute error is chosen as the loss function for the learning procedure of both CNNs. The trained CNNs are evaluated with physically more meaningful figures of merit. Unitarity demands that $\mathbf{R}^\dagger \mathbf{R} + \mathbf{T}^\dagger \mathbf{T} = \mathbf{1}$, so the first figure of merit is chosen as the Frobenius norm $f_1 := \|\mathbf{R}^\dagger \mathbf{R} + \mathbf{T}^\dagger \mathbf{T} - \mathbf{1}\|_{\text{F}}$. With the initially incomplete transmission matrices, the sample average of f_1 amounts to $\langle f_1 \rangle \approx 3.7$. Using the completed transmission matrices together with the predicted reflection matrices, this value is reduced down to $\langle f_1 \rangle \approx 0.22$. The second figure of merit is chosen as the ratio between the achieved momentum transfer and the best possible momentum transfer. Based on the initial incomplete transmission matrix or on the predictions for \mathbf{T} and \mathbf{R} by the CNNs, the matrix $\tilde{\mathbf{Q}}_\theta^{\text{UL}}$ is assembled. Its eigenvector $\tilde{\mathbf{w}}_{\text{max}}$ corresponding to the highest eigenvalue (according to its real part) is injected into the system, leading to a true momentum transfer of $\tilde{\mathbf{w}}_{\text{max}}^\dagger \mathbf{Q}_\theta^{\text{UL}} \tilde{\mathbf{w}}_{\text{max}}$. The maximum momentum transfer is given by the largest eigenvalue λ_{max} of $\mathbf{Q}_\theta^{\text{UL}}$. Thus, the second figure of merit is $f_2 := \tilde{\mathbf{w}}_{\text{max}}^\dagger \mathbf{Q}_\theta^{\text{UL}} \tilde{\mathbf{w}}_{\text{max}} / \lambda_{\text{max}}$. If only the initial

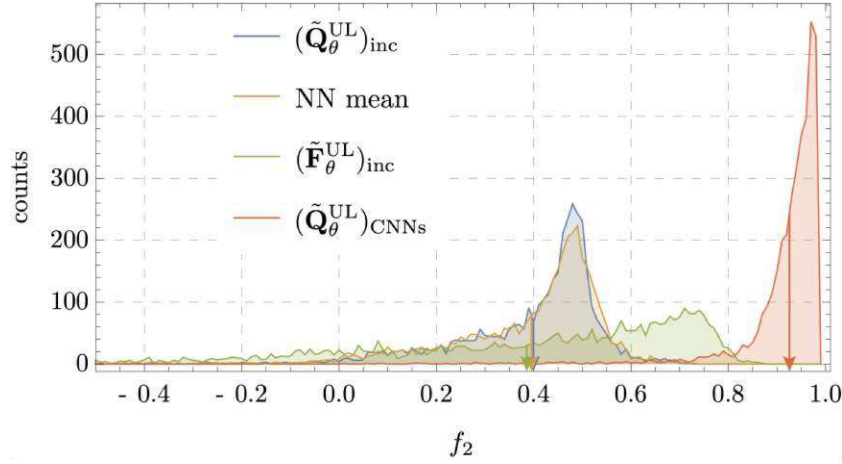


Figure 5.5: Improved micromanipulation in a system with limited mode access. The eigenvector of a matrix (indicated in the legend and described below) corresponding to the highest eigenvalue (according to its real part) is injected into the system. The ratio of the achieved momentum transfer over the highest possible momentum transfer is denoted as f_2 and plotted on the horizontal axis. (The aim is to achieve high values for f_2 .) The vertical axis shows the absolute frequency of the f_2 -values (in bins of size 10^{-2}) appearing within a set of 3678 samples for each method. For the blue curve, the underlying matrix is $(\tilde{\mathbf{Q}}_\theta^{\text{UL}})_{\text{inc}} = -i\mathbf{T}_{\text{inc}}^\dagger \partial_\theta \mathbf{T}_{\text{inc}}$, where \mathbf{T}_{inc} is the original incomplete transmission matrix. The orange curve can be ignored here (for an explanation, see Ref. [275]). For the green curve, the underlying matrix is the FI matrix $(\tilde{\mathbf{F}}_\theta^{\text{UL}})_{\text{inc}} = 4(\partial_\theta \mathbf{T}_{\text{inc}})^\dagger (\partial_\theta \mathbf{T}_{\text{inc}})$. For the red curve, the underlying matrix is $\tilde{\mathbf{Q}}_\theta^{\text{UL}}$ (the expression is given in the main text) composed of the full transmission and reflection matrix, both as predicted by the trained CNNs. The vertical arrows in the respective colours indicate the corresponding mean values. Note: Adapted from [275].

incomplete transmission matrices are available, f_2 averages to a value of $\langle f_2 \rangle \approx 0.40$. Incorporating the CNN predictions, this value increases to $\langle f_2 \rangle \approx 0.93$, see also Fig. 5.5.

This project clearly demonstrates the benefit that can be gained from employing DL-based scattering matrix completion routines for micromanipulation tasks under real-world conditions where only a certain part of the scattering matrix is available.

5.4 Artificial Neural Networks as Efficient Estimators

This project was an international collaboration between Dorian Bouchet from Université Grenoble Alpes in Grenoble (France), Ilya Starshynov and Daniele Faccio from the University of Glasgow in Glasgow (United Kingdom) and Günther Hackl,

Maximilian Weimar, the author of this thesis and Stefan Rotter from TU Wien in Vienna (Austria). Dorian Bouchet conceived the project, the group in Glasgow conducted the experiments, whereas our group in Vienna developed the theoretical tools.

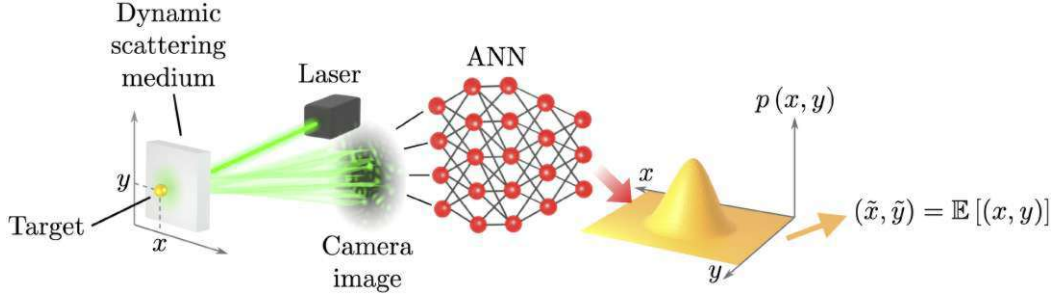
The general task in this project is to estimate the position of a target behind a dynamically changing disordered scattering layer from recorded reflection speckle patterns using an ANN, see Fig. 5.6(a). We show that the performance of the ANN practically reaches the CRLB, which is a fundamental limit given by the physical properties of the scattering medium and the optical setup.

A plain monochromatic laser beam, which is not shaped in any specific way, serves as a probe. The dynamic scattering medium is implemented by a suspension that gets pumped through a cuvette. Varying the concentration of the suspension changes the optical thickness, which is defined as the physical thickness of the scattering layer divided by the transport mean free path of the laser light in the suspension. The optical thickness gives a measure for the scattering strength of the medium. In the experiment, the optical thickness takes on the following values: 0 (no scattering), 1.7, 2.5, 3.3, 4.2, 5.0. The target is realized as a collection of reflective pixels on a digital micromirror device placed on the far side of the scattering layer. The reflected light field propagates through the disordered medium once again before being captured by a complementary metal-oxide-semiconductor camera. The intensity profile recorded by the camera shows typical speckle patterns which are more pronounced for stronger scattering, i.e., larger optical thicknesses [1], see Fig. 5.6(b).

Constructing an estimator that predicts the target position from a given speckle image may seem like an immensely cumbersome task. ANNs are the prime tools for deducing rules that replicate an unknown input-output relation (here from speckle to target position) from just a set of exemplary input-output pairs. However, ANNs can not become arbitrarily potent, they are limited by the CRLB, see Sec. 3.1. Assuming that the ANN is unbiased, the CRLB is given by the statistical properties of the measured intensity images, which are in turn determined by the physical properties of the dynamic disordered medium and the optical setup. Therefore, the CRLB can already be calculated from the recorded speckles prior to training any ANN, and it establishes the same bound for any ANN that might be employed. On the positive side, we demonstrate that ANNs can practically reach the CRLB, even when applied to complex real-world systems.

The position of the target is composed of two parameters, namely the x - and the y -coordinate. They are collected in the vector parameter $\boldsymbol{\theta} = (x, y)^\top$. The (vectorized) intensity image captured by the camera is denoted by \mathbf{s} . It is a random variable, subject to the statistical fluctuations generated predominantly by the ever changing disorder in the scattering layer. The CRLB for such a multi-parameter

(a) Schematic experimental setup and ANN workflow



(b) Exemplary speckle images

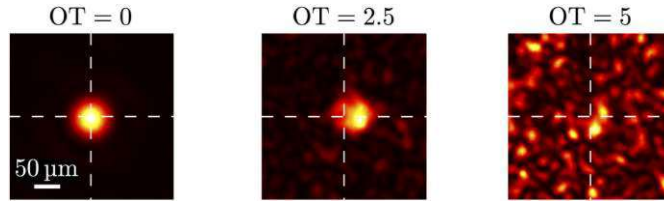


Figure 5.6: An ANN is trained to predict the position of a target hidden behind a scattering layer from recorded speckle images. (a) A laser beam (green) hits a dynamically changing scattering medium (light grey). Part of the transmitted light gets reflected by a target (gold sphere) placed at position (x, y) and propagates through the scattering layer again. A camera records an image of the reflected light wave, which gets fed into the ANN (red circles and black lines). The ANN returns a probability distribution (yellow surface) for the target position. The final prediction is taken as the mean value of this distribution. (b) For three values of the optical thickness (OT), an exemplary speckle image is shown. Note: Courtesy of Ilya Starshynov.

configuration is determined by the FI matrix [195]

$$\mathbf{I}_{\theta} := \mathbb{E}_{s \sim p(s|\theta)} \left[(\nabla_{\theta} \ln(p(s|\theta))) (\nabla_{\theta} \ln(p(s|\theta)))^{\top} \right]. \quad (5.3)$$

Assuming an unbiased estimator and a single repeated independent measurement, the standard deviation σ_i of the predicted value $\tilde{\theta}_i$ is bound from below by [195]

$$\sigma_i \geq \sqrt{(\mathbf{I}_{\theta}^{-1})_{i,i}}. \quad (5.4)$$

First, we focus on the right hand side of the last equation, namely on the calculation of the FI matrix. There are two symmetries in the physical setup that we exploit for this calculation. Firstly, the two coordinates are what is called “information orthogonal” to each other. Physically, this means that the FI of one coordinate is independent of whether the value of the other coordinate is known or not. Mathematically, this is expressed by vanishing off-diagonal elements in the

FI matrix, resulting in $(\mathbf{I}_{\boldsymbol{\theta}}^{-1})_{i,i} = 1/(\mathbf{I}_{\boldsymbol{\theta}})_{i,i}$. Secondly, the speckle images are translationally invariant in the sense that a shifted speckle pattern can also originate from a correspondingly shifted target together with a suitably changed disorder realization. Utilizing this invariance, we can assume that the FI is constant over all target positions and thus it suffices to calculate the FI only for a single target location. For each optical thickness, we record $1.25 \cdot 10^5$ speckle images with a fixed target, but a changing scattering layer. We approximate the $\boldsymbol{\theta}$ -derivative in Eq. (5.3) by a finite difference, which — again due to the translational invariance — can be implemented by virtually shifting the speckle images by a small amount in post-processing.

Since we do not have a good physical model for the probability distribution $p(\mathbf{s}|\boldsymbol{\theta})$, we have to resort to a general model-free procedure for approximating the FI from given measurement data. In the following, we provide such a procedure by establishing an upper and a lower bound to the true FI, as well as an adequate approximation based on a decomposition of the data into maximally independent components.

Having just a finite set of measured speckles $\{\mathbf{s}\}$ at hand, one could approximate the distribution $p(\mathbf{s}|\boldsymbol{\theta})$ by histograms. However, such histograms are too rough an approximation for high-dimensional data. One idea is to resort to one-dimensional data, which allow for a reliable characterization through histograms. Each image pixel s_k represents a one-dimensional variable, so one could approximate $p(\mathbf{s}|\boldsymbol{\theta})$ by the product of its marginals $p_k(s_k|\boldsymbol{\theta})$. This approach however completely ignores the dependencies between the pixels that potentially occur since a speckle pattern consists of grains with finite size [1]. If the camera pixels are smaller than such a grain, neighbouring pixels carry the same information. According to this physical heuristic, the sum of the FIs of the individual marginals is greater than (or equal to) the true FI, thereby establishing an upper bound:

$$(\mathbf{I}_{\boldsymbol{\theta}})_{i,i} \leq \sum_k \mathbb{E}_{s_k \sim p_k(s_k|\boldsymbol{\theta})} [(\partial_{\theta_i} \ln(p_k(s_k|\boldsymbol{\theta})))^2]. \quad (5.5)$$

We can push the expression on the right hand side of the previous equation closer to the true FI by transforming the data \mathbf{s} such that the dependencies between the components are minimal. This can be achieved with principal component analysis (PCA) [276] or, as was done in this project, with independent component analysis (ICA) [277]. While PCA yields an orthogonal transformation that renders the covariance matrix of the transformed data diagonal (elimination of first order correlations), ICA attempts to find a linear transformation $\mathbf{t} = \mathbf{A}\mathbf{s}$ such that the components of \mathbf{t} are maximally independent (eliminating also higher order correlations). This is done by optimizing a suitable statistical quantity like mutual information. As there may still be some dependence between the components of \mathbf{t} ,

the sum of the marginal FIs only provides an approximation to the true FI:

$$(\mathbf{I}_\theta)_{i,i} \approx \sum_k \mathbb{E}_{t_k \sim q_k(t_k|\theta)} [(\partial_{\theta_i} \ln(q_k(t_k|\theta)))^2]. \quad (5.6)$$

We found that in the current context, approximating the marginals $q_k(t_k|\theta)$ with histograms using equal frequency binning works better as compared to equal width binning. The derivative ∂_{θ_i} in Eq. (5.6) is approximated by a symmetric finite difference $\Delta\theta_i$. A good value for the step size $\Delta\theta_i$ is recognizable by a plateau that emerges when plotting the calculated FI as a function of $\Delta\theta_i$. If the step size is too small, the statistical fluctuations dominate the signal and thus corrupt the finite difference. Too large step sizes result in a poor approximation of the derivative.

A lower bound to FI is provided by the so-called linear Fisher information (LFI) [278]. It is called “linear” because it constitutes a CRLB for local *linear* estimators [279]. (This is just to explain the terminology — we do not use any linear estimators here.) The LFI L_{θ_i} is calculated from the mean value $\boldsymbol{\mu}$ and the covariance matrix $\boldsymbol{\Sigma}$ of the data (here the speckle images \mathbf{s}):

$$L_{\theta_i} := (\partial_{\theta_i} \boldsymbol{\mu})^\top \boldsymbol{\Sigma}^{-1} (\partial_{\theta_i} \boldsymbol{\mu}). \quad (5.7)$$

LFI can also be understood in the following way: We fit the data with a multivariate Gaussian distribution and take the FI that arises from the θ_i -dependence of the first moment, which exactly matches L_{θ_i} . The LFI gives a lower bound to the true FI,

$$(\mathbf{I}_\theta)_{i,i} \geq L_{\theta_i}, \quad (5.8)$$

but it is just the first in a series of increasing lower bounds, based on taking into account ever increasing moments of the underlying probability distribution [280]. Yet, high moments of high-dimensional variables are hard to estimate from empirical sample statistics. Hence, we stick with the LFI which already yields satisfactory results.

In the present physical setup, the approximation (5.6) and the lower bound (5.8) are close to each other, such that we can be confident that Eq. (5.6) yields a reliable estimate of the true FI.

We now turn towards the left hand side of Eq. (5.4), namely the performance of the ANN. As an architecture we choose a special version of a CNN, namely a densely connected convolutional network [281]. Justified by the translational invariance property of the speckle patterns, we can employ data augmentation to establish an appropriate training data set: We record $1.25 \cdot 10^5$ images with just a single fixed target position and virtually shift the images in post-processing to obtain data points for different target positions. This allows us to place the target at arbitrary positions, also at locations not realizable by the digital micromirror device. Conversely, after being trained, the ANN is exclusively tested on real-world data, i.e., on images where the target is physically moved. Evaluating the

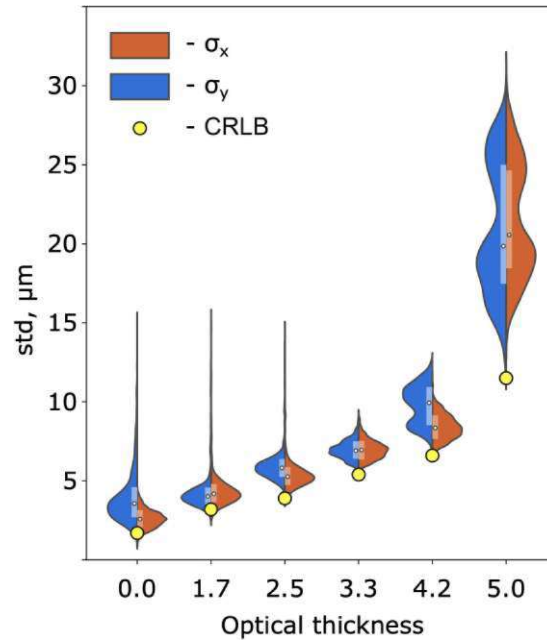


Figure 5.7: Assessment of the performance of the ANNs trained to predict the position of a target hidden behind a scattering layer from recorded speckle images. For each optical thickness (horizontal axis), 25 trained ANNs are tested. The curves show the distribution of standard deviations (vertical axis) of the ANN predictions of the x components (orange) and the y components (blue) of the target position. The white dots and the attached vertical bars represent the respective quartiles. The yellow circles indicate the CRLB. Note: Courtesy of Ilya Starshynov.

performance of the ANN demands far less data than the training process. For each of the 25 chosen target locations arranged in a 5 by 5 grid (and for each optical thickness), we recorded $5 \cdot 10^3$ speckles.

The results for the CRLB and the standard deviations of 25 ANNs (differing by their random initializations) are compared in Fig. 5.7 for each optical thickness. We find that, depending on the parameter initialization, the ANNs come more or less close to the CRLB. There are very few outliers, where the ANN seems to perform better than what is allowed by the CRLB. These outliers can be explained by overestimating the CRLB or/and underestimating the standard deviations of the ANNs due to the finite amount of data and small deviations from the translational invariance, which cause the augmented training data to be an imperfect representation of the testing images stemming from physically shifted targets. Altogether, these are very impressive results considering the fact that the ANNs train essentially only on augmented data, and yet they are able to learn a highly complex relationship realized by a real-world physical system.

To sum up, this project shows that the performance of ANNs can not become

arbitrarily powerful, but it is limited by the CRLB. This bound is a fundamental principle rooted in statistical mathematics, but it also has implications for physical systems. We provide means to approximate the CRLB from the given data without the need for an analytical model of the data distribution. On the other hand, we also show that it is feasible for ANNs to come close to the CRLB, even when being challenged by an intricate physical problem.

5.5 Fisher Information Flow Through Artificial Neural Networks

In his diploma thesis “Fisher Information Flow in Neural Networks” [282], Maximilian Weimar demonstrated that the concept of FI flow portrayed in Sec. 3.5 can be extended from physical waves to the flow of data through the layers of an ANN, thereby providing a better understanding of the inner workings of an ANN. In contrast to the conservation of FI in linear Hermitian wave propagation, FI is in general not conserved in ANNs since they constitute non-invertible mappings.

Usually, data is processed in a layer-wise manner inside an ANN. We indicate the hidden layers with the index $l \in \{1, \dots, N_{\text{hid}}\}$. The distribution of the input data determines its FI I_{θ}^{in} . This data is successively transformed from layer to layer on its way through the ANN. In each hidden layer l , the corresponding data distribution entails a FI I_{θ}^l . The same holds for the output layer, where we denote the corresponding FI by I_{θ}^{out} . The transformed data distributions in the hidden layers are in general intractable. However, it turns out that the individual FIs are sufficiently well approximated by the corresponding LFIs (see Sec. 5.4) or specific refinements thereof, which are explained in Ref. [282]. Additionally, there is a general relationship between the FIs of adjacent layers: The transformations from layer to layer are deterministic and θ -independent. In such a setting, the so-called data processing inequality holds [283] and it implies that FI can only decrease when the data is being transformed during propagation through the ANN, or at best stay constant:

$$I_{\theta}^{\text{in}} \geq I_{\theta}^1 \geq \dots \geq I_{\theta}^{N_{\text{hid}}} \geq I_{\theta}^{\text{out}}. \quad (5.9)$$

Since, however, the Cramér-Rao inequality states that the inverse FI of the data is a lower bound to the precision of the final (unbiased) estimate, an ANN that is well-trained to make very precise estimates on θ must necessarily make sure that the FI content in the data stays constant or drops only minimally. These heuristic considerations are confirmed by the empirical findings in Ref. [282], see also Fig. 5.8. In an untrained ANN, FI rapidly decays with increasing layer depth. Once the ANN has learned to estimate θ well, FI is close to being completely preserved over the layers. Although conserving FI is not the primary goal of the training procedure, the ANN is capable of extracting the essential information from the

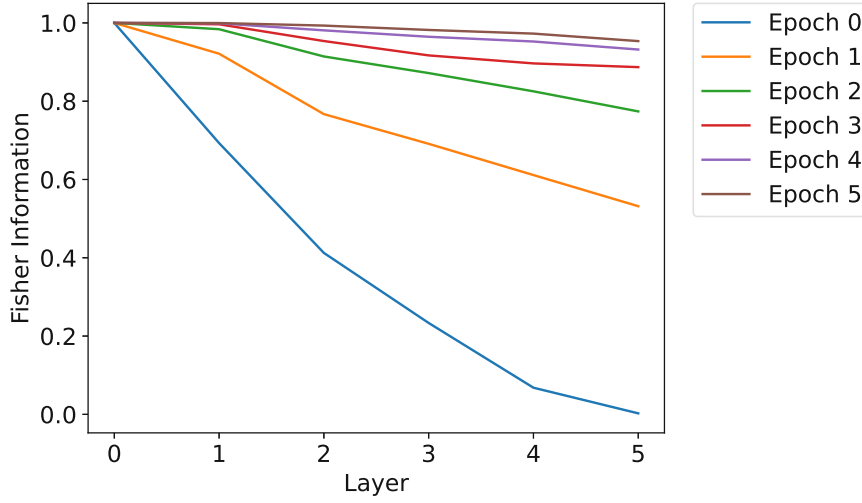


Figure 5.8: FI flow through an ANN during the training procedure. At different stages of learning (expressed by the epoch number), the normalized FI of the processed data is shown for each layer of the ANN (encompassing the input layer, four hidden layers and the output layer). The normalization of the FI consists in dividing by the FI in the input layer. Initially, virtually no FI reaches the output layer. As training progresses, the flow of FI through the ANN increases until the ANN reaches a configuration that allows it to preserve most of the FI through all the layers. More details can be found in Ref. [282]. Note: Adapted from [282].

data despite the decrease in dimensionality from the input to the output layer.

A wide-spread loss function for estimation tasks⁶ is the MSE, which can be decomposed into a bias and a variance term (see also Eqs. (3.3) and (3.4)):

$$\text{MSE} := \mathbb{E} \left[\left(\tilde{\theta} - \theta \right)^2 \right] = \left(\mathbb{E} \left[\tilde{\theta} \right] - \theta \right)^2 + \mathbb{E} \left[\left(\tilde{\theta} - \mathbb{E} \left[\tilde{\theta} \right] \right)^2 \right] = b^2 + \sigma^2. \quad (5.10)$$

Employing the CRLB (3.6), the MSE is bound from below by

$$\text{MSE} \geq b^2 + \frac{(1 + \partial_{\theta} b)^2}{I_{\theta}}. \quad (5.11)$$

Assuming that the ANN is unbiased, i.e., $b = 0$, we see that the inverse FI provides a lower bound to the MSE loss function:

$$b = 0 \implies \text{MSE} \geq \frac{1}{I_{\theta}}. \quad (5.12)$$

The ANN is close to efficient if the MSE loss function comes close to this lower bound. This establishes a convenient indicator for when to stop the training procedure. Usually, one monitors this procedure by evaluating the loss function on a

⁶In ML terminology, estimation tasks can be understood as a type of regression problem.

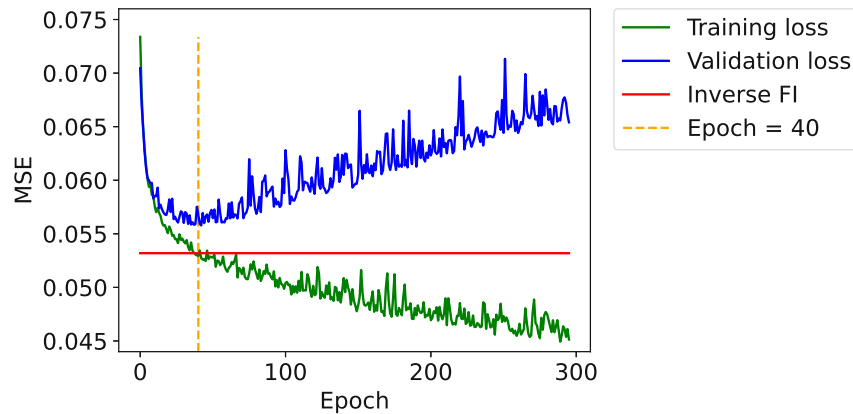


Figure 5.9: Early stopping using FI. An ANN is trained (using the MSE as the loss function) and driven into overfitting on purpose. Overfitting occurs when the validation loss (blue line) starts to increase (after a period of decrease) while the training loss (green line) keeps decreasing. The point where the ANN enters overfitting (around epoch 40, orange dashed line) coincides with the point where the training loss falls below the inverse FI of the underlying data (red line). More details can be found in Ref. [282]. Note: Adapted from [282].

separate validation data set. This is called the “validation loss”, as opposed to the “training loss”, which is the loss function evaluated on the training data. The ANN overfits to the training data whenever the validation loss starts increasing while the training loss still decreases. Utilizing the inequality from above, we can formulate an approximate criterion for overfitting, namely whenever the training MSE loss falls below $1/I_\theta$. This lower bound can be calculated prior to the training process and is independent of the used network architecture. In particular, one can safely use all the available data both for determining the FI as well as for training the ANN, i.e., it becomes dispensable to split the data into a training and a validation data set. Figure 5.9 shows an example demonstrating that the training MSE falling below the inverse FI is a good indicator for overfitting.

To conclude, we establish the understanding that FI is a quantity that can flow through an ANN, linked to the regular data flow. A crucial fundamental principle is that FI can never increase while propagating through an ANN. It turns out that a well-trained ANN is associated with the (near) conservation of FI throughout the network. At the same time, the FI of the input data poses a limit to the capability of the ANN via the CRLB. Knowing this bound equips one with the ability to assess the efficacy of ANNs on a standalone basis, without the need for comparison to other algorithms. As a consequence, this enables the detection of overfitting during the training process without the use of validation data, namely whenever the ANN’s performance on the training data surpasses the CRLB.

Conclusions and Outlook

In this thesis, we discuss different manifestations of waves propagating in inhomogeneous media and corresponding applications thereof. The treated phenomena encompass the propagation of optical light and ultrasound through complex media and the propagation of data through artificial neural networks. A number of insights are demonstrated on numerically simulated examples and tested in real-world experiments.

The optical scattering matrix is a convenient tool encoding the propagation of both classical (i.e., coherent) and quantum light through linear media in a representation whose reference points are located in the far field. It can readily be measured experimentally and it serves as the starting point for a wide range of protocols that aim at identifying states of light with desired properties. An example for this is micromanipulation, where the aim is to exert a specific force, torque or pressure onto a selected target. In this case, the GWS matrix is the quantity derived from the scattering matrix that provides the relevant information about the local forces.

By virtue of correspondence, we introduce the QWS operator that extends the GWS matrix and makes it applicable to quantum light as well. The QWS operator describes the forces that quantum light exerts on classical objects, thereby establishing a versatile framework for identifying quantum states of light that have a desired effect on the target object. We show that harnessing the quantum degrees of freedom of the light field leads to an improvement in micromanipulation procedures. In particular, the fluctuations in the optical force can be considerably reduced compared to classical coherent light. The influence of the quantum degrees of freedom of light onto the optical forces could be studied in future experiments using the Kapitza-Dirac effect, i.e., the diffraction of matter from a grating created by a standing laser wave. On the theoretical side, it would be interesting to investigate the properties of the QWS operator for unitary processes that are not expressible by a classical scattering matrix, e.g., active linear systems like parametric amplifiers. In the field of vacuum physics, the QWS operator provides a promising starting point for a theory to explain and understand the physical origins of mathematical renormalization procedures.

We establish a link from the QWS operator to (quantum) metrology through the notion of QFI. The latter imposes a limit on the precision that can be reached in measurement setups. To achieve the physically best possible precision, the QFI needs to be maximized by tuning the spatial as well as the quantum degrees of

freedom of the optical probe field such that the corresponding output state becomes extremely sensitive to small changes in the quantity to be measured. The QWS operator, which provides a versatile framework already for micromanipulation, can also be used to establish a useful platform for finding quantum states of light that yield maximum values of the QFI — even in complex, open scattering systems. By exploiting the quantum degrees of freedom of light, the measurement precision can be significantly enhanced compared to classical light probes. Several questions are still unanswered in the domain of subunitary quantum metrology, where the full unitary scattering matrix is not accessible. Both for squeezed and photon number states, the optimal probe states have to be determined using numerical optimization routines. It is not yet clear how stable the found solutions are against small perturbations in the measured scattering matrix or how imperfections in the preparation of the optimal probe states impact their performance. It is desirable to find heuristic solutions that are both easy to calculate and stable against different noise sources.

Coherent light is special because it allows for the definition of a spatial quantum Fisher information flow that satisfies a continuity equation, allowing us to identify the sources and sinks of information and to formulate a law of conserved quantum Fisher information in parts of the medium that do not change with the parameter of interest, but may otherwise cause strong scattering.

The scattering matrix proves to be applicable also to problems, where one wants to detect discrete changes in the system instead of continuous ones. The corresponding pivotal matrix is simply a discretized version of the matrix that yields the quantum Fisher information in the continuous case.

Scattering matrices are a convenient tool also for characterizing the propagation of ultrasound waves, which are an indispensable resource in medical diagnosis and therapy. In biomedical imaging, one is typically constrained to a single side of the specimen. Therefore, only the reflection matrix is available, or, in the case of a limited NA, even only a part of the reflection matrix. Many imaging techniques like confocal imaging rely on a single-scattering approximation, i.e., they assume that the wave that hits the detector underwent a single reflecting event during its propagation through the medium. We introduce a target-specific imaging method that also takes multiple scattering events into account, which are characteristic for the particular target. In the future, this method can be further enhanced by constructing better models for the background medium or linking it with complementary methods that yield information about the background medium through the knowledge of a guide star.

Artificial neural networks have proven to be ideal for solving problems in the area of wave propagation. In one project, we employ such a network for estimating the location of a reflective target hidden behind a scattering layer. We show that its performance is close to optimal, i.e., it is practically able to reach the Cramér-Rao lower bound, which is determined by the Fisher information contained in the recor-

ded speckle images. Considering the layer-wise transformations of the data in the neural network, the corresponding Fisher information can be traced through the layers of the network as well. This insight establishes the means to take a peek into the inner workings of artificial neural networks. It remains an open task to investigate the flow of Fisher information through non-sequential network architectures like those containing skip connections (also called residual connections). How does the Fisher information branch and recombine in such architectures? Another open problem is the development of a corresponding scheme for classification tasks. We already know that the so-called Bayes error provides a lower bound to the error probability of any decision algorithm, similar to the Cramér-Rao lower bound for the precision when estimating a continuous parameter, and that this Bayes error obeys a data processing inequality. On the other hand, it is not yet clear whether there is an easily calculable bound on the Bayes error similar to the linear Fisher information, and how good an approximation such a bound provides. It is also desirable to find a lower bound for common classification loss functions, such as the cross-entropy, in order to obtain a precomputable criterion for early stopping.

The author of these lines hopes that this thesis provides a comprehensible study comprising different topics such as wave physics, quantum optics and machine learning, thereby building up and reinforcing communication channels between diverse groups working in the areas mentioned, and eventually sparking new interdisciplinary developments where all parties involved can benefit from each other.

Appendix A

Expectation Values for Gaussian States

In the following we derive some relevant expectation values for multi-mode Gaussian states $|\boldsymbol{\alpha}, \mathbf{Z}\rangle^{\mathcal{M}}$. Reference [100] provides the identities

$$\hat{a}_m \hat{D}_a(\boldsymbol{\alpha}) = \alpha_m \hat{D}_a(\boldsymbol{\alpha}) + \hat{D}_a(\boldsymbol{\alpha}) \hat{a}_m, \quad (\text{A.1})$$

$$\begin{aligned} \hat{a}_m \hat{S}_a(\mathbf{Z}) &= \sum_{m'=1}^N (\cosh(\mathbf{R}))_{m,m'} \hat{S}_a(\mathbf{Z}) \hat{a}_{m'} \\ &\quad - \sum_{m'=1}^N (\sinh(\mathbf{R}) e^{i\Phi})_{m,m'} \hat{S}_a(\mathbf{Z}) \hat{a}_{m'}^\dagger, \end{aligned} \quad (\text{A.2})$$

$$\begin{aligned} \hat{a}_m \hat{D}_a(\boldsymbol{\alpha}) \hat{S}_a(\mathbf{Z}) &= \alpha_m \hat{D}_a(\boldsymbol{\alpha}) \hat{S}_a(\mathbf{Z}) + \sum_{m'=1}^N (\cosh(\mathbf{R}))_{m,m'} \hat{D}_a(\boldsymbol{\alpha}) \hat{S}_a(\mathbf{Z}) \hat{a}_{m'} \\ &\quad - \sum_{m'=1}^N (\sinh(\mathbf{R}) e^{i\Phi})_{m,m'} \hat{D}_a(\boldsymbol{\alpha}) \hat{S}_a(\mathbf{Z}) \hat{a}_{m'}^\dagger, \end{aligned} \quad (\text{A.3})$$

where $\mathbf{Z} = \mathbf{R}e^{i\Phi}$ is the polar decomposition of the squeezing matrix. “cosh” and “sinh” are to be applied as proper matrix functions, e.g., $\cosh(\mathbf{R}) = (e^{\mathbf{R}} + e^{-\mathbf{R}})/2$.

Using $\hat{a}_m |0\rangle = 0$ and denoting the Fock state with a single photon in mode m by $|\mathbf{e}_m\rangle^{\mathcal{M}} = \hat{a}_m^\dagger |0\rangle$, we calculate

$$\begin{aligned} \hat{a}_m |\boldsymbol{\alpha}, \mathbf{Z}\rangle^{\mathcal{M}} &= \hat{a}_m \hat{D}_a(\boldsymbol{\alpha}) \hat{S}_a(\mathbf{Z}) |0\rangle \\ &= \alpha_m \hat{D}_a(\boldsymbol{\alpha}) \hat{S}_a(\mathbf{Z}) |0\rangle \\ &\quad - \sum_{m'=1}^N (\sinh(\mathbf{R}) e^{i\Phi})_{m,m'} \hat{D}_a(\boldsymbol{\alpha}) \hat{S}_a(\mathbf{Z}) |\mathbf{e}_{m'}\rangle^{\mathcal{M}}. \end{aligned} \quad (\text{A.4})$$

Since both the displacement operator and the squeezing operator are unitary, they transform the orthonormal Fock basis into another orthonormal basis. With this insight we immediately obtain:

$${}^{\mathcal{M}}\langle \boldsymbol{\alpha}, \mathbf{Z} | \hat{a}_m | \boldsymbol{\alpha}, \mathbf{Z} \rangle^{\mathcal{M}} = \alpha_m, \quad (\text{A.5})$$

$${}^{\mathcal{M}}\langle \boldsymbol{\alpha}, \mathbf{Z} | \hat{a}_m^\dagger | \boldsymbol{\alpha}, \mathbf{Z} \rangle^{\mathcal{M}} = \alpha_m^*. \quad (\text{A.6})$$

Utilizing the linearity of expectation values, we get (see Eqs. (1.31) and (1.32))

$${}^{\mathcal{M}}\langle \boldsymbol{\alpha}, \mathbf{Z} | \hat{q}_m(\varphi) | \boldsymbol{\alpha}, \mathbf{Z} \rangle^{\mathcal{M}} = \frac{1}{\sqrt{2}} (e^{-i\varphi} \alpha_m + e^{i\varphi} \alpha_m^*), \quad (\text{A.7})$$

$${}^{\mathcal{M}}\langle \boldsymbol{\alpha}, \mathbf{Z} | \hat{p}_m(\varphi) | \boldsymbol{\alpha}, \mathbf{Z} \rangle^{\mathcal{M}} = \frac{-i}{\sqrt{2}} (e^{-i\varphi} \alpha_m - e^{i\varphi} \alpha_m^*). \quad (\text{A.8})$$

The expectation value of the photon number operator $\hat{n}_m = \hat{a}_m^\dagger \hat{a}_m$ is the same as the squared norm of the vector in Eq. (A.4). Due to orthonormality we can simply read off the coefficients:

$${}^{\mathcal{M}}\langle \boldsymbol{\alpha}, \mathbf{Z} | \hat{n}_m | \boldsymbol{\alpha}, \mathbf{Z} \rangle^{\mathcal{M}} = \left\| \hat{a}_m | \boldsymbol{\alpha}, \mathbf{Z} \rangle^{\mathcal{M}} \right\|^2 = |\alpha_m|^2 + \sum_{m'=1}^N \left| (\sinh(\mathbf{R}) e^{i\Phi})_{m,m'} \right|^2. \quad (\text{A.9})$$

Using the Hermiticity of \mathbf{R} and the unitarity of $e^{i\Phi}$, we can simplify the last term:

$$\begin{aligned} {}^{\mathcal{M}}\langle \boldsymbol{\alpha}, \mathbf{Z} | \hat{n}_m | \boldsymbol{\alpha}, \mathbf{Z} \rangle^{\mathcal{M}} &= |\alpha_m|^2 + \sum_{m'=1}^N \left| (\sinh(\mathbf{R}) e^{i\Phi})_{m,m'} \right|^2 \\ &= |\alpha_m|^2 + \sum_{m'=1}^N (\sinh(\mathbf{R}) e^{i\Phi})_{m,m'} (\sinh(\mathbf{R}) e^{i\Phi})_{m,m'}^* \\ &= |\alpha_m|^2 + \left(\sinh(\mathbf{R}) e^{i\Phi} (\sinh(\mathbf{R}) e^{i\Phi})^\dagger \right)_{m,m} \\ &= |\alpha_m|^2 + \left(\sinh(\mathbf{R}) e^{i\Phi} e^{-i\Phi} \sinh(\mathbf{R}) \right)_{m,m} \\ &= |\alpha_m|^2 + (\sinh^2(\mathbf{R}))_{m,m}. \end{aligned} \quad (\text{A.10})$$

This result proves Eq. (1.42). Equation (1.43) is obtained by summation over m .

In order to obtain the expectation value of \hat{a}_m^2 , we start by applying \hat{a}_m to Eq. (A.4) and using Eq. (A.3). We use $\hat{a}_{m''} | \mathbf{e}_{m'} \rangle^{\mathcal{M}} = \delta_{m'',m'} | \mathbf{0} \rangle$ and $\hat{a}_{m''}^\dagger | \mathbf{e}_{m'} \rangle^{\mathcal{M}} = \sqrt{\delta_{m'',m'} + 1} | \mathbf{e}_{m'} + \mathbf{e}_{m''} \rangle^{\mathcal{M}}$, see Eqs. (1.50) and (1.51).

$$\begin{aligned} \hat{a}_m^2 | \boldsymbol{\alpha}, \mathbf{Z} \rangle^{\mathcal{M}} &= \alpha_m \hat{a}_m \hat{D}_a(\boldsymbol{\alpha}) \hat{S}_a(\mathbf{Z}) | \mathbf{0} \rangle \\ &\quad - \sum_{m'=1}^N (\sinh(\mathbf{R}) e^{i\Phi})_{m,m'} \hat{a}_m \hat{D}_a(\boldsymbol{\alpha}) \hat{S}_a(\mathbf{Z}) | \mathbf{e}_{m'} \rangle^{\mathcal{M}} \\ &= \alpha_m^2 \hat{D}_a(\boldsymbol{\alpha}) \hat{S}_a(\mathbf{Z}) | \mathbf{0} \rangle \\ &\quad - \alpha_m \sum_{m''=1}^N (\sinh(\mathbf{R}) e^{i\Phi})_{m,m''} \hat{D}_a(\boldsymbol{\alpha}) \hat{S}_a(\mathbf{Z}) | \mathbf{e}_{m''} \rangle^{\mathcal{M}} \end{aligned}$$

$$\begin{aligned}
 & - \sum_{m'=1}^N (\sinh(\mathbf{R}) e^{i\Phi})_{m,m'} \alpha_m \hat{D}_a(\boldsymbol{\alpha}) \hat{S}_a(\mathbf{Z}) |\mathbf{e}_{m'}\rangle^{\mathcal{M}} \\
 & - \sum_{m'=1}^N (\sinh(\mathbf{R}) e^{i\Phi})_{m,m'} \cdot \\
 & \quad \cdot \sum_{m''=1}^N (\cosh(\mathbf{R}))_{m,m''} \hat{D}_a(\boldsymbol{\alpha}) \hat{S}_a(\mathbf{Z}) \hat{a}_{m''} |\mathbf{e}_{m'}\rangle^{\mathcal{M}} \\
 & + \sum_{m'=1}^N (\sinh(\mathbf{R}) e^{i\Phi})_{m,m'} \cdot \\
 & \quad \cdot \sum_{m''=1}^N (\sinh(\mathbf{R}) e^{i\Phi})_{m,m''} \hat{D}_a(\boldsymbol{\alpha}) \hat{S}_a(\mathbf{Z}) \hat{a}_{m''}^\dagger |\mathbf{e}_{m'}\rangle^{\mathcal{M}} \\
 = & \alpha_m^2 \hat{D}_a(\boldsymbol{\alpha}) \hat{S}_a(\mathbf{Z}) |\mathbf{0}\rangle \\
 & - 2\alpha_m \sum_{m'=1}^N (\sinh(\mathbf{R}) e^{i\Phi})_{m,m'} \hat{D}_a(\boldsymbol{\alpha}) \hat{S}_a(\mathbf{Z}) |\mathbf{e}_{m'}\rangle^{\mathcal{M}} \\
 & - \sum_{m'=1}^N (\sinh(\mathbf{R}) e^{i\Phi})_{m,m'} (\cosh(\mathbf{R}))_{m,m'} \hat{D}_a(\boldsymbol{\alpha}) \hat{S}_a(\mathbf{Z}) |\mathbf{0}\rangle \\
 & + \sum_{m',m''=1}^N (\sinh(\mathbf{R}) e^{i\Phi})_{m,m'} (\sinh(\mathbf{R}) e^{i\Phi})_{m,m''} \cdot \\
 & \quad \cdot \sqrt{\delta_{m'',m'} + 1} \hat{D}_a(\boldsymbol{\alpha}) \hat{S}_a(\mathbf{Z}) |\mathbf{e}_{m'} + \mathbf{e}_{m''}\rangle^{\mathcal{M}} \\
 = & \left(\alpha_m^2 - \left(\sinh(\mathbf{R}) e^{i\Phi} \cosh(\mathbf{R})^\top \right)_{m,m} \right) \hat{D}_a(\boldsymbol{\alpha}) \hat{S}_a(\mathbf{Z}) |\mathbf{0}\rangle \\
 & - 2\alpha_m \sum_{m'=1}^N (\sinh(\mathbf{R}) e^{i\Phi})_{m,m'} \hat{D}_a(\boldsymbol{\alpha}) \hat{S}_a(\mathbf{Z}) |\mathbf{e}_{m'}\rangle^{\mathcal{M}} \\
 & + \sqrt{2} \sum_{m'=1}^N (\sinh(\mathbf{R}) e^{i\Phi})_{m,m'} (\sinh(\mathbf{R}) e^{i\Phi})_{m,m'} \cdot \\
 & \quad \cdot \hat{D}_a(\boldsymbol{\alpha}) \hat{S}_a(\mathbf{Z}) |2\mathbf{e}_{m'}\rangle^{\mathcal{M}} \\
 & + \sum_{m' \neq m''}^N (\sinh(\mathbf{R}) e^{i\Phi})_{m,m'} (\sinh(\mathbf{R}) e^{i\Phi})_{m,m''} \cdot \\
 & \quad \cdot \hat{D}_a(\boldsymbol{\alpha}) \hat{S}_a(\mathbf{Z}) |\mathbf{e}_{m'} + \mathbf{e}_{m''}\rangle^{\mathcal{M}}. \tag{A.11}
 \end{aligned}$$

Multiplying ${}^{\mathcal{M}}\langle \boldsymbol{\alpha}, \mathbf{Z} | = \langle \mathbf{0} | \hat{S}_a^\dagger(\mathbf{Z}) \hat{D}_a^\dagger(\boldsymbol{\alpha})$ from the left and complex conjugation

yields

$${}^{\mathcal{M}}\langle \boldsymbol{\alpha}, \mathbf{Z} | \hat{a}_m^2 | \boldsymbol{\alpha}, \mathbf{Z} \rangle^{\mathcal{M}} = \alpha_m^2 - \left(\sinh(\mathbf{R}) e^{i\Phi} \cosh(\mathbf{R})^\top \right)_{m,m}, \quad (\text{A.12})$$

$$\begin{aligned} {}^{\mathcal{M}}\langle \boldsymbol{\alpha}, \mathbf{Z} | \hat{a}_m^{\dagger 2} | \boldsymbol{\alpha}, \mathbf{Z} \rangle^{\mathcal{M}} &= \alpha_m^{*2} - \left(\sinh(\mathbf{R})^* e^{-i\Phi^*} \cosh(\mathbf{R})^\dagger \right)_{m,m} \\ &= \alpha_m^{*2} - \left(\sinh(\mathbf{R})^\top e^{-i\Phi^\top} \cosh(\mathbf{R}) \right)_{m,m} \\ &= \alpha_m^{*2} - \left(\cosh(\mathbf{R})^\top e^{-i\Phi} \sinh(\mathbf{R}) \right)_{m,m}. \end{aligned} \quad (\text{A.13})$$

For the second moments of the quadratures we use

$$\begin{aligned} \hat{q}_m^2(\varphi) &= \frac{1}{2} \left(e^{-2i\varphi} \hat{a}_m^2 + e^{2i\varphi} \hat{a}_m^{\dagger 2} + \hat{a}_m^\dagger \hat{a}_m + \hat{a}_m \hat{a}_m^\dagger \right) \\ &= \frac{1}{2} \left(e^{-2i\varphi} \hat{a}_m^2 + e^{2i\varphi} \hat{a}_m^{\dagger 2} + 2\hat{a}_m^\dagger \hat{a}_m + 1 \right) \end{aligned} \quad (\text{A.14})$$

and $\hat{p}_m(\varphi) = \hat{q}_m(\varphi + \pi/2)$:

$$\begin{aligned} {}^{\mathcal{M}}\langle \boldsymbol{\alpha}, \mathbf{Z} | \hat{q}_m^2(\varphi) | \boldsymbol{\alpha}, \mathbf{Z} \rangle^{\mathcal{M}} &= \frac{1}{2} e^{-2i\varphi} \alpha_m^2 - \frac{1}{2} e^{-2i\varphi} \left(\sinh(\mathbf{R}) e^{i\Phi} \cosh(\mathbf{R})^\top \right)_{m,m} \\ &\quad + \frac{1}{2} e^{2i\varphi} \alpha_m^{*2} - \frac{1}{2} e^{2i\varphi} \left(\cosh(\mathbf{R})^\top e^{-i\Phi} \sinh(\mathbf{R}) \right)_{m,m} \\ &\quad + |\alpha_m|^2 + \left(\sinh^2(\mathbf{R}) \right)_{m,m} + \frac{1}{2}, \end{aligned} \quad (\text{A.15})$$

$$\begin{aligned} {}^{\mathcal{M}}\langle \boldsymbol{\alpha}, \mathbf{Z} | \hat{p}_m^2(\varphi) | \boldsymbol{\alpha}, \mathbf{Z} \rangle^{\mathcal{M}} &= -\frac{1}{2} e^{-2i\varphi} \alpha_m^2 + \frac{1}{2} e^{-2i\varphi} \left(\sinh(\mathbf{R}) e^{i\Phi} \cosh(\mathbf{R})^\top \right)_{m,m} \\ &\quad - \frac{1}{2} e^{2i\varphi} \alpha_m^{*2} + \frac{1}{2} e^{2i\varphi} \left(\cosh(\mathbf{R})^\top e^{-i\Phi} \sinh(\mathbf{R}) \right)_{m,m} \\ &\quad + |\alpha_m|^2 + \left(\sinh^2(\mathbf{R}) \right)_{m,m} + \frac{1}{2}. \end{aligned} \quad (\text{A.16})$$

Finally, we give a proof of Eqs. (1.44) and (1.45): Assume that $\mathbf{Z} = \text{diag}(\zeta_1, \dots, \zeta_N)$ with $\zeta_m = r_m e^{i\varphi_m}$. Then:

$$\begin{aligned} \mathbb{V}_{|\boldsymbol{\alpha}, \mathbf{Z}\rangle^{\mathcal{M}}} [\hat{q}_m(\varphi_m/2)] &= {}^{\mathcal{M}}\langle \boldsymbol{\alpha}, \mathbf{Z} | \hat{q}_m^2(\varphi_m/2) | \boldsymbol{\alpha}, \mathbf{Z} \rangle^{\mathcal{M}} \\ &\quad - \left({}^{\mathcal{M}}\langle \boldsymbol{\alpha}, \mathbf{Z} | \hat{q}_m(\varphi_m/2) | \boldsymbol{\alpha}, \mathbf{Z} \rangle^{\mathcal{M}} \right)^2 \\ &= \frac{1}{2} e^{-i\varphi_m} \alpha_m^2 - \frac{1}{2} e^{-i\varphi_m} \sinh(r_m) e^{i\varphi_m} \cosh(r_m) \\ &\quad + \frac{1}{2} e^{i\varphi_m} \alpha_m^{*2} - \frac{1}{2} e^{i\varphi_m} \cosh(r_m) e^{-i\varphi_m} \sinh(r_m) \\ &\quad + |\alpha_m|^2 + \sinh^2(r_m) + \frac{1}{2} - \frac{1}{2} \left(e^{-i\varphi_m/2} \alpha_m + e^{i\varphi_m/2} \alpha_m^* \right)^2 \end{aligned}$$

$$\begin{aligned}
 &= \frac{1}{2} + \sinh^2(r_m) - \sinh(r_m) \cosh(r_m) \\
 &= \frac{2 + (e^{r_m} - e^{-r_m})(e^{r_m} - e^{-r_m} - e^{r_m} - e^{-r_m})}{4} \\
 &= \frac{2 - 2(e^{r_m} - e^{-r_m})e^{-r_m}}{4} \\
 &= \frac{e^{-2r_m}}{2}.
 \end{aligned} \tag{A.17}$$

Similarly,

$$\mathbb{V}_{|\alpha, \mathbf{z}\rangle^{\mathcal{M}}} [\hat{p}_m(\varphi_m/2)] = \frac{1}{2} + \sinh^2(r_m) + \sinh(r_m) \cosh(r_m) = \frac{e^{2r_m}}{2}. \tag{A.18}$$

Appendix B

QWS Operator in Terms of the GWS Matrix

We first prove two lemmata before we give a proof of Eq. (2.18).

B.1 First Lemma

Let $Y(\theta)$ be a θ -dependent matrix or operator, then

$$e^{-Y(\theta)} \frac{\partial e^{Y(\theta)}}{\partial \theta} = \int_0^1 e^{-tY(\theta)} Y'(\theta) e^{tY(\theta)} dt \quad (\text{B.1})$$

$$= \sum_{r=0}^{\infty} \frac{(-1)^r}{(r+1)!} [Y(\theta), Y'(\theta)]_r, \quad (\text{B.2})$$

where the prime \prime denotes differentiation w.r.t. θ and $[\cdot, \cdot]_r$ is the r -fold nested commutator, defined by

$$[Y, Z]_0 := Z, \quad (\text{B.3})$$

$$[Y, Z]_r := [Y, [Y, Z]_{r-1}]. \quad (\text{B.4})$$

Eq. (B.1) is derived in Ref. [284] (appendix B) and Eq. (B.2) is obtained using the Hadamard lemma

$$e^A B e^{-A} = \sum_{r=0}^{\infty} \frac{1}{r!} [A, B]_r. \quad (\text{B.5})$$

B.2 Second Lemma

The second lemma we need for our proof is that for all $\mathbf{L}, \mathbf{J} \in \mathbb{C}^{N \times N}$:

$$\left[[\hat{a}^\dagger]^\top \mathbf{L} [\hat{a}], [\hat{a}^\dagger]^\top \mathbf{J} [\hat{a}] \right] = [\hat{a}^\dagger]^\top [\mathbf{L}, \mathbf{J}] [\hat{a}]. \quad (\text{B.6})$$

Note that the commutator on the left hand side is the commutator of quantum operators whereas the commutator on the right hand side acts on matrices. This

relation simply states that when some matrix \mathbf{L} is translated into a quantum operator via $[\hat{a}^\dagger]^\top \mathbf{L} [\hat{a}]$, then the commutation relations of the bosonic creation and annihilation operators $\hat{a}_m^{(\dagger)}$ correctly encode the ordinary matrix commutation rules.

In order to prove this lemma we need the easily deducible commutator

$$[\hat{a}_m^\dagger \hat{a}_{m'}, \hat{a}_\mu^\dagger \hat{a}_{\mu'}] = \delta_{m',\mu} \hat{a}_m^\dagger \hat{a}_{\mu'} - \delta_{m,\mu'} \hat{a}_\mu^\dagger \hat{a}_{m'}. \quad (\text{B.7})$$

Using the abbreviations

$$\hat{L} := [\hat{a}^\dagger]^\top \mathbf{L} [\hat{a}] = \sum_{m,m'=1}^N L_{m,m'} \hat{a}_m^\dagger \hat{a}_{m'}, \quad (\text{B.8})$$

$$\hat{J} := [\hat{a}^\dagger]^\top \mathbf{J} [\hat{a}] = \sum_{m,m'=1}^N J_{m,m'} \hat{a}_m^\dagger \hat{a}_{m'}, \quad (\text{B.9})$$

$$\mathbf{C} := [\mathbf{L}, \mathbf{J}] \iff C_{m,m'} = \sum_{\mu'=1}^N L_{m,\mu'} J_{\mu',m'} - \sum_{\mu=1}^N J_{m,\mu} L_{\mu,m'}, \quad (\text{B.10})$$

the lemma is proven as follows:

$$\begin{aligned} [\hat{L}, \hat{J}] &= \sum_{m,m',\mu,\mu'=1}^N L_{m,m'} J_{\mu,\mu'} [\hat{a}_m^\dagger \hat{a}_{m'}, \hat{a}_\mu^\dagger \hat{a}_{\mu'}] \\ &= \sum_{m,m',\mu'=1}^N L_{m,m'} J_{m',\mu'} \hat{a}_m^\dagger \hat{a}_{\mu'} - \sum_{m,m',\mu=1}^N L_{m,m'} J_{\mu,m} \hat{a}_\mu^\dagger \hat{a}_{m'} \\ &= \sum_{m,m'=1}^N \left(\sum_{\mu'=1}^N L_{m,\mu'} J_{\mu',m'} - \sum_{\mu=1}^N L_{\mu,m'} J_{m,\mu} \right) \hat{a}_m^\dagger \hat{a}_{m'} \\ &= \sum_{m,m'=1}^N C_{m,m'} \hat{a}_m^\dagger \hat{a}_{m'}. \end{aligned} \quad (\text{B.11})$$

A corollary (a simple but important consequence) of this lemma is that the same relation also holds for the nested commutators defined in Eqs. (B.3) and (B.4):

$$[[\hat{a}^\dagger]^\top \mathbf{L} [\hat{a}], [\hat{a}^\dagger]^\top \mathbf{J} [\hat{a}]]_r = [\hat{a}^\dagger]^\top [\mathbf{L}, \mathbf{J}]_r [\hat{a}]. \quad (\text{B.12})$$

This can be proven by induction.

B.3 The Proof

If $\mathbf{S}(\theta)$ is a unitary scattering matrix, then

$$\mathbf{L}(\theta) := -i \ln(\mathbf{S}(\theta)) \quad (\text{B.13})$$

is a Hermitian matrix. The GWS matrix is obtained as (see Eqs. (2.2), (B.1) and (B.2))

$$\mathbf{Q}_\theta(\theta) = \int_0^1 e^{-it\mathbf{L}(\theta)} \mathbf{L}'(\theta) e^{it\mathbf{L}(\theta)} dt \quad (\text{B.14})$$

$$= \sum_{r=0}^{\infty} \frac{(-i)^r}{(r+1)!} [\mathbf{L}(\theta), \mathbf{L}'(\theta)]_r. \quad (\text{B.15})$$

Note that the GWS matrix is *not* just the derivative of the logarithm of the scattering matrix, i.e., in general $\mathbf{Q}_\theta(\theta) \neq \mathbf{L}'(\theta)$.

In order to calculate the QWS operator, we first express the corresponding unitary operator $\hat{U}(\theta)$ in terms of $\mathbf{L}(\theta)$, see Eq. (1.62):

$$\hat{U}(\theta) = e^{i[\hat{a}^\dagger]^\top \mathbf{L}(\theta)[\hat{a}]} e^{\frac{i}{2} \text{tr}(\mathbf{L}(\theta))}. \quad (\text{B.16})$$

Using the product rule of differentiation, we can split the QWS operator $\hat{Q}_\theta(\theta) = -i\hat{U}^\dagger(\theta) \partial_\theta \hat{U}(\theta)$ into the sum of two expressions:

$$\hat{Q}_\theta(\theta) = -ie^{-i[\hat{a}^\dagger]^\top \mathbf{L}(\theta)[\hat{a}]} \frac{\partial}{\partial \theta} e^{i[\hat{a}^\dagger]^\top \mathbf{L}(\theta)[\hat{a}]} \quad (\text{B.17})$$

$$-ie^{-\frac{i}{2} \text{tr}(\mathbf{L}(\theta))} \frac{\partial}{\partial \theta} e^{\frac{i}{2} \text{tr}(\mathbf{L}(\theta))}. \quad (\text{B.18})$$

The first term (B.17) has the form $e^{-Y(\theta)} \partial_\theta e^{Y(\theta)}$ so we can use the first lemma from above (see Eq. (B.2)). We also employ the second lemma (see Eq. (B.12)) in the following calculation:

$$\begin{aligned} \hat{Q}_\theta^I(\theta) &:= -ie^{-i[\hat{a}^\dagger]^\top \mathbf{L}(\theta)[\hat{a}]} \frac{\partial}{\partial \theta} e^{i[\hat{a}^\dagger]^\top \mathbf{L}(\theta)[\hat{a}]} \\ &= \sum_{r=0}^{\infty} \frac{(-i)^r}{(r+1)!} \left[[\hat{a}^\dagger]^\top \mathbf{L}(\theta)[\hat{a}], [\hat{a}^\dagger]^\top \mathbf{L}'(\theta)[\hat{a}] \right]_r \\ &= \sum_{r=0}^{\infty} \frac{(-i)^r}{(r+1)!} [\hat{a}^\dagger]^\top [\mathbf{L}(\theta), \mathbf{L}'(\theta)]_r [\hat{a}] \\ &= [\hat{a}^\dagger]^\top \left(\sum_{r=0}^{\infty} \frac{(-i)^r}{(r+1)!} [\mathbf{L}(\theta), \mathbf{L}'(\theta)]_r \right) [\hat{a}] \end{aligned}$$

$$= [\hat{a}^\dagger]^\top \mathbf{Q}_\theta(\theta) [\hat{a}]. \quad (\text{B.19})$$

In the last step we used Eq. (B.15).

The second term (B.18) is related to the trace of the GWS matrix:

$$\begin{aligned} \hat{Q}_\theta^{\text{II}}(\theta) &:= -ie^{-\frac{i}{2} \text{tr}(\mathbf{L}(\theta))} \frac{\partial}{\partial \theta} e^{\frac{i}{2} \text{tr}(\mathbf{L}(\theta))} \\ &= \frac{1}{2} \frac{\partial \text{tr}(\mathbf{L}(\theta))}{\partial \theta} \\ &= \frac{1}{2} \text{tr}(\mathbf{L}'(\theta)) \\ &= \frac{1}{2} \int_0^1 \text{tr}(e^{-it\mathbf{L}(\theta)} \mathbf{L}'(\theta) e^{it\mathbf{L}(\theta)}) dt \\ &= \frac{1}{2} \text{tr}(\mathbf{Q}_\theta(\theta)). \end{aligned} \quad (\text{B.20})$$

In the last step we used Eq. (B.14).

Appendix C

Variance of the QWS Operator for Gaussian States

Using Eqs. (2.37), (2.35) and (2.23), the general variance of the QWS operator is calculated as follows:

$$\begin{aligned}
 \mathbb{V}[\hat{Q}_\theta] &= \langle \hat{Q}_\theta^2 \rangle - \langle \hat{Q}_\theta \rangle^2 \\
 &= \left\langle \sum_{i,j=1}^N \lambda_i \lambda_j \hat{n}_i \hat{n}_j + \text{tr}(\Lambda) \sum_{i=1}^N \lambda_i \hat{n}_i + \frac{1}{4} \text{tr}^2(\Lambda) \right\rangle \\
 &\quad - \left\langle \sum_{i=1}^N \lambda_i \hat{n}_i + \frac{1}{2} \text{tr}(\Lambda) \right\rangle^2 \\
 &= \sum_{i,j=1}^N \lambda_i \lambda_j (\langle \hat{n}_i \hat{n}_j \rangle - \langle \hat{n}_i \rangle \langle \hat{n}_j \rangle) \\
 &= \sum_{i,j=1}^N \lambda_i \lambda_j \left(\langle \hat{b}_i^\dagger (\delta_{i,j} + \hat{b}_j^\dagger \hat{b}_i) \hat{b}_j \rangle - \langle \hat{n}_i \rangle \langle \hat{n}_j \rangle \right) \\
 &= \sum_{i=1}^N \lambda_i^2 \langle \hat{n}_i \rangle + \sum_{i,j=1}^N \lambda_i \lambda_j \left(\langle \hat{b}_i^\dagger \hat{b}_j^\dagger \hat{b}_i \hat{b}_j \rangle - \langle \hat{n}_i \rangle \langle \hat{n}_j \rangle \right). \tag{C.1}
 \end{aligned}$$

For Gaussian states, we already know from Eq. (1.42) that

$$\langle \hat{b}_i \hat{b}_j | \boldsymbol{\beta}, \boldsymbol{\Xi} | \hat{n}_i | \boldsymbol{\beta}, \boldsymbol{\Xi} \rangle^{\mathcal{Q}} = |\beta_i|^2 + (\sinh^2(\mathbf{P}))_{i,i}. \tag{C.2}$$

Using Eqs. (A.4), (A.3), (1.50) and (1.51), which all hold equally well in the \mathcal{Q} representation, we obtain

$$\begin{aligned}
 \hat{b}_i \hat{b}_j | \boldsymbol{\beta}, \boldsymbol{\Xi} \rangle^{\mathcal{Q}} &= \beta_j \hat{b}_i \hat{D}_b(\boldsymbol{\beta}) \hat{S}_b(\boldsymbol{\Xi}) | \mathbf{0} \rangle - \sum_{j'=1}^N (\sinh(\mathbf{P}) e^{i\Psi})_{j,j'} \hat{b}_i \hat{D}_b(\boldsymbol{\beta}) \hat{S}_b(\boldsymbol{\Xi}) | \mathbf{e}_{j'} \rangle^{\mathcal{Q}} \\
 &= \beta_i \beta_j \hat{D}_b(\boldsymbol{\beta}) \hat{S}_b(\boldsymbol{\Xi}) | \mathbf{0} \rangle - \beta_j \sum_{i'=1}^N (\sinh(\mathbf{P}) e^{i\Psi})_{i,i'} \hat{D}_b(\boldsymbol{\beta}) \hat{S}_b(\boldsymbol{\Xi}) | \mathbf{e}_{i'} \rangle^{\mathcal{Q}}
 \end{aligned}$$

$$\begin{aligned}
 & - \sum_{j'=1}^N (\sinh(\mathbf{P}) e^{i\Psi})_{j,j'} \beta_i \hat{D}_b(\boldsymbol{\beta}) \hat{S}_b(\boldsymbol{\Xi}) |\mathbf{e}_{j'}\rangle^{\mathcal{Q}} \\
 & - \sum_{j'=1}^N (\sinh(\mathbf{P}) e^{i\Psi})_{j,j'} \sum_{i'=1}^N (\cosh(\mathbf{P}))_{i,i'} \hat{D}_b(\boldsymbol{\beta}) \hat{S}_b(\boldsymbol{\Xi}) \hat{b}_{i'} |\mathbf{e}_{j'}\rangle^{\mathcal{Q}} \\
 & + \sum_{j'=1}^N (\sinh(\mathbf{P}) e^{i\Psi})_{j,j'} \sum_{i'=1}^N (\sinh(\mathbf{P}) e^{i\Psi})_{i,i'} \hat{D}_b(\boldsymbol{\beta}) \hat{S}_b(\boldsymbol{\Xi}) \hat{b}_{i'}^\dagger |\mathbf{e}_{j'}\rangle^{\mathcal{Q}} \\
 = & \beta_i \beta_j \hat{D}_b(\boldsymbol{\beta}) \hat{S}_b(\boldsymbol{\Xi}) |\mathbf{0}\rangle \\
 & - \sum_{i'=1}^N \left(\beta_j (\sinh(\mathbf{P}) e^{i\Psi})_{i,i'} + \beta_i (\sinh(\mathbf{P}) e^{i\Psi})_{j,i'} \right) \cdot \\
 & \quad \cdot \hat{D}_b(\boldsymbol{\beta}) \hat{S}_b(\boldsymbol{\Xi}) |\mathbf{e}_{i'}\rangle^{\mathcal{Q}} \\
 & - \sum_{i'=1}^N (\sinh(\mathbf{P}) e^{i\Psi})_{j,i'} (\cosh(\mathbf{P}))_{i,i'} \hat{D}_b(\boldsymbol{\beta}) \hat{S}_b(\boldsymbol{\Xi}) |\mathbf{0}\rangle \\
 & + \sum_{i',j'=1}^N (\sinh(\mathbf{P}) e^{i\Psi})_{i,i'} (\sinh(\mathbf{P}) e^{i\Psi})_{j,j'} \cdot \\
 & \quad \cdot \sqrt{\delta_{i',j'} + 1} \hat{D}_b(\boldsymbol{\beta}) \hat{S}_b(\boldsymbol{\Xi}) |\mathbf{e}_{i'} + \mathbf{e}_{j'}\rangle^{\mathcal{Q}} \\
 = & \left(\beta_i \beta_j - \left(\cosh(\mathbf{P}) e^{i\Psi^\top} \sinh(\mathbf{P})^\top \right)_{i,j} \right) \hat{D}_b(\boldsymbol{\beta}) \hat{S}_b(\boldsymbol{\Xi}) |\mathbf{0}\rangle \\
 & - \sum_{i'=1}^N \left(\beta_i (\sinh(\mathbf{P}) e^{i\Psi})_{j,i'} + \beta_j (\sinh(\mathbf{P}) e^{i\Psi})_{i,i'} \right) \cdot \\
 & \quad \cdot \hat{D}_b(\boldsymbol{\beta}) \hat{S}_b(\boldsymbol{\Xi}) |\mathbf{e}_{i'}\rangle^{\mathcal{Q}} \\
 & + \sqrt{2} \sum_{i'=1}^N (\sinh(\mathbf{P}) e^{i\Psi})_{i,i'} (\sinh(\mathbf{P}) e^{i\Psi})_{j,i'} \hat{D}_b(\boldsymbol{\beta}) \hat{S}_b(\boldsymbol{\Xi}) |2\mathbf{e}_{i'}\rangle^{\mathcal{Q}} \\
 & + \sum_{i' \neq j'}^N (\sinh(\mathbf{P}) e^{i\Psi})_{i,i'} (\sinh(\mathbf{P}) e^{i\Psi})_{j,j'} \cdot \\
 & \quad \cdot \hat{D}_b(\boldsymbol{\beta}) \hat{S}_b(\boldsymbol{\Xi}) |\mathbf{e}_{i'} + \mathbf{e}_{j'}\rangle^{\mathcal{Q}} . \tag{C.3}
 \end{aligned}$$

In the following calculation, we use the identity

$$\sum_{i'=1}^N \left| (\sinh(\mathbf{P}) e^{i\Psi})_{i,i'} \right|^2 = (\sinh^2(\mathbf{P}))_{i,i} \tag{C.4}$$

found in Eq. (A.10). Additionally, we use

$$\begin{aligned}
\sum_{i'=1}^N (\sinh(\mathbf{P}) e^{i\Psi})_{i,i'} (\sinh(\mathbf{P}) e^{i\Psi})_{j,i'}^* &= \left(\sinh(\mathbf{P}) e^{i\Psi} (\sinh(\mathbf{P}) e^{i\Psi})^\dagger \right)_{i,j} \\
&= \left(\sinh(\mathbf{P}) e^{i\Psi} e^{-i\Psi} \sinh(\mathbf{P}) \right)_{i,j} \\
&= \left(\sinh^2(\mathbf{P}) \right)_{i,j}. \tag{C.5}
\end{aligned}$$

The expectation value of $\hat{b}_i^\dagger \hat{b}_j^\dagger \hat{b}_i \hat{b}_j$ is the squared norm of the vector in Eq. (C.3):

$$\begin{aligned}
\mathcal{Q} \langle \boldsymbol{\beta}, \Xi | \hat{b}_i^\dagger \hat{b}_j^\dagger \hat{b}_i \hat{b}_j | \boldsymbol{\beta}, \Xi \rangle \mathcal{Q} &= \left\| \hat{b}_i \hat{b}_j | \boldsymbol{\beta}, \Xi \rangle \mathcal{Q} \right\|^2 \\
&= \left| \beta_i \beta_j - \left(\cosh(\mathbf{P}) e^{i\Psi^\top} \sinh(\mathbf{P})^\top \right)_{i,j} \right|^2 \\
&\quad + \sum_{i'=1}^N \left| \beta_i (\sinh(\mathbf{P}) e^{i\Psi})_{j,i'} + \beta_j (\sinh(\mathbf{P}) e^{i\Psi})_{i,i'} \right|^2 \\
&\quad + 2 \sum_{i'=1}^N \left| (\sinh(\mathbf{P}) e^{i\Psi})_{i,i'} (\sinh(\mathbf{P}) e^{i\Psi})_{j,i'} \right|^2 \\
&\quad + \sum_{i' \neq j'}^N \left| (\sinh(\mathbf{P}) e^{i\Psi})_{i,i'} (\sinh(\mathbf{P}) e^{i\Psi})_{j,j'} \right|^2 \\
&= |\beta_i \beta_j|^2 + \left| \left(\cosh(\mathbf{P}) e^{i\Psi^\top} \sinh(\mathbf{P})^\top \right)_{i,j} \right|^2 \\
&\quad - 2 \Re \left(\beta_i^* \beta_j^* \left(\cosh(\mathbf{P}) e^{i\Psi^\top} \sinh(\mathbf{P})^\top \right)_{i,j} \right) \\
&\quad + |\beta_i|^2 (\sinh^2(\mathbf{P}))_{j,j} + |\beta_j|^2 (\sinh^2(\mathbf{P}))_{i,i} \\
&\quad + 2 \Re \left(\beta_i^* \beta_j (\sinh^2(\mathbf{P}))_{i,j} \right) \\
&\quad + \sum_{i'=1}^N \left| (\sinh(\mathbf{P}) e^{i\Psi})_{i,i'} (\sinh(\mathbf{P}) e^{i\Psi})_{j,i'} \right|^2 \\
&\quad + (\sinh^2(\mathbf{P}))_{i,i} (\sinh^2(\mathbf{P}))_{j,j}. \tag{C.6}
\end{aligned}$$

From this expression we subtract

$$\begin{aligned}
\mathcal{Q} \langle \boldsymbol{\beta}, \Xi | \hat{n}_i | \boldsymbol{\beta}, \Xi \rangle \mathcal{Q} \mathcal{Q} \langle \boldsymbol{\beta}, \Xi | \hat{n}_j | \boldsymbol{\beta}, \Xi \rangle \mathcal{Q} &= |\beta_i \beta_j|^2 + (\sinh^2(\mathbf{P}))_{i,i} (\sinh^2(\mathbf{P}))_{j,j} \\
&\quad + |\beta_i|^2 (\sinh^2(\mathbf{P}))_{j,j} \\
&\quad + |\beta_j|^2 (\sinh^2(\mathbf{P}))_{i,i} \tag{C.7}
\end{aligned}$$

to obtain:

$$\begin{aligned}
 \mathbb{V}_{|\beta, \Xi\rangle} [\hat{Q}_\theta] &= \sum_{i=1}^N \lambda_i^2 \left(|\beta_i|^2 + (\sinh^2(\mathbf{P}))_{i,i} \right) \\
 &+ \sum_{i,j=1}^N \lambda_i \lambda_j \left(\left| \left(\cosh(\mathbf{P}) e^{i\Psi^\top} \sinh(\mathbf{P})^\top \right)_{i,j} \right|^2 \right. \\
 &\quad \left. + \sum_{i'=1}^N \left| (\sinh(\mathbf{P}) e^{i\Psi})_{i,i'} (e^{-i\Psi} \sinh(\mathbf{P}))_{i',j} \right|^2 \right. \\
 &\quad \left. - 2\Re \left(\beta_i^* \beta_j^* \left(\cosh(\mathbf{P}) e^{i\Psi^\top} \sinh(\mathbf{P})^\top \right)_{i,j} \right) \right. \\
 &\quad \left. + 2\Re \left(\beta_i^* \beta_j (\sinh^2(\mathbf{P}))_{i,j} \right) \right). \tag{C.8}
 \end{aligned}$$

Appendix D

QFI of Coherent States

First, we calculate the QFI of a single-mode coherent state $|\alpha(\theta)\rangle$ using the orthonormal Fock basis and Eq. (3.20).

$$|\alpha(\theta)\rangle = e^{-\frac{|\alpha(\theta)|^2}{2}} \sum_{n=0}^{\infty} \frac{\alpha^n(\theta)}{\sqrt{n!}} |n\rangle, \quad (\text{D.1})$$

$$\begin{aligned} |\partial_\theta \alpha(\theta)\rangle &= -\frac{1}{2} e^{-\frac{|\alpha(\theta)|^2}{2}} (\partial_\theta |\alpha(\theta)|^2) \sum_{n=0}^{\infty} \frac{\alpha^n(\theta)}{\sqrt{n!}} |n\rangle \\ &\quad + e^{-\frac{|\alpha(\theta)|^2}{2}} (\partial_\theta \alpha(\theta)) \sum_{n=1}^{\infty} \frac{n \alpha^{n-1}(\theta)}{\sqrt{n!}} |n\rangle, \end{aligned} \quad (\text{D.2})$$

$$\begin{aligned} \langle \partial_\theta \alpha(\theta) | \partial_\theta \alpha(\theta) \rangle &= \frac{1}{4} e^{-|\alpha(\theta)|^2} (\partial_\theta |\alpha(\theta)|^2)^2 \sum_{n=0}^{\infty} \frac{|\alpha(\theta)|^{2n}}{n!} \\ &\quad + e^{-|\alpha(\theta)|^2} |\partial_\theta \alpha(\theta)|^2 \sum_{n=1}^{\infty} \frac{n^2 |\alpha(\theta)|^{2(n-1)}}{n!} \\ &\quad - \frac{1}{2} e^{-|\alpha(\theta)|^2} (\partial_\theta |\alpha(\theta)|^2) \left(\frac{\partial_\theta \alpha(\theta)}{\alpha(\theta)} + \frac{\partial_\theta \alpha^*(\theta)}{\alpha^*(\theta)} \right) \sum_{n=1}^{\infty} \frac{n |\alpha(\theta)|^{2n}}{n!} \\ &= \frac{1}{4} (\partial_\theta |\alpha(\theta)|^2)^2 + (1 + |\alpha(\theta)|^2) |\partial_\theta \alpha(\theta)|^2 \\ &\quad - \frac{1}{2} |\alpha(\theta)|^2 (\partial_\theta |\alpha(\theta)|^2) \left(\frac{\partial_\theta \alpha(\theta)}{\alpha(\theta)} + \frac{\partial_\theta \alpha^*(\theta)}{\alpha^*(\theta)} \right), \end{aligned} \quad (\text{D.3})$$

$$\begin{aligned} \langle \alpha(\theta) | \partial_\theta \alpha(\theta) \rangle &= -\frac{1}{2} e^{-|\alpha(\theta)|^2} (\partial_\theta |\alpha(\theta)|^2) \sum_{n=0}^{\infty} \frac{|\alpha(\theta)|^{2n}}{n!} \\ &\quad + e^{-|\alpha(\theta)|^2} \frac{\partial_\theta \alpha(\theta)}{\alpha(\theta)} \sum_{n=1}^{\infty} \frac{n |\alpha(\theta)|^{2n}}{n!} \end{aligned}$$

$$= -\frac{1}{2} (\partial_\theta |\alpha(\theta)|^2) + |\alpha(\theta)|^2 \frac{\partial_\theta \alpha(\theta)}{\alpha(\theta)}, \quad (\text{D.4})$$

$$\begin{aligned} |\langle \alpha(\theta) | \partial_\theta \alpha(\theta) \rangle|^2 &= \frac{1}{4} (\partial_\theta |\alpha(\theta)|^2)^2 + |\alpha(\theta)|^2 |\partial_\theta \alpha(\theta)|^2 \\ &\quad - \frac{1}{2} |\alpha(\theta)|^2 (\partial_\theta |\alpha(\theta)|^2) \left(\frac{\partial_\theta \alpha(\theta)}{\alpha(\theta)} + \frac{\partial_\theta \alpha^*(\theta)}{\alpha^*(\theta)} \right). \end{aligned} \quad (\text{D.5})$$

For the QFI we obtain the simple result

$$F_\theta [|\alpha(\theta)\rangle] = 4 (\langle \partial_\theta \alpha(\theta) | \partial_\theta \alpha(\theta) \rangle - |\langle \alpha(\theta) | \partial_\theta \alpha(\theta) \rangle|^2) = 4 |\partial_\theta \alpha(\theta)|^2. \quad (\text{D.6})$$

The QFI of a multi-mode coherent state $|\boldsymbol{\alpha}(\theta)\rangle = |\alpha_1(\theta)\rangle_1 \dots |\alpha_N(\theta)\rangle_N$ amounts to the sum of the QFIs of the individual components:

$$|\partial_\theta \boldsymbol{\alpha}(\theta)\rangle = \sum_{m=1}^N \dots |\alpha_{m-1}(\theta)\rangle_{m-1} |\partial_\theta \alpha_m(\theta)\rangle_m |\alpha_{m+1}(\theta)\rangle_{m+1} \dots, \quad (\text{D.7})$$

$$\begin{aligned} \langle \partial_\theta \boldsymbol{\alpha}(\theta) | \partial_\theta \boldsymbol{\alpha}(\theta) \rangle &= \sum_{m=1}^N {}_m \langle \partial_\theta \alpha_m(\theta) | \partial_\theta \alpha_m(\theta) \rangle_m \\ &\quad + \sum_{m \neq m'}^N {}_m \langle \alpha_m(\theta) | \partial_\theta \alpha_m(\theta) \rangle_m \cdot \\ &\quad \cdot {}_{m'} \langle \partial_\theta \alpha_{m'}(\theta) | \alpha_{m'}(\theta) \rangle_{m'}, \end{aligned} \quad (\text{D.8})$$

$$\langle \boldsymbol{\alpha}(\theta) | \partial_\theta \boldsymbol{\alpha}(\theta) \rangle = \sum_{m=1}^N {}_m \langle \alpha_m(\theta) | \partial_\theta \alpha_m(\theta) \rangle_m, \quad (\text{D.9})$$

$$|\langle \boldsymbol{\alpha}(\theta) | \partial_\theta \boldsymbol{\alpha}(\theta) \rangle|^2 = \sum_{m, m'=1}^N {}_m \langle \alpha_m(\theta) | \partial_\theta \alpha_m(\theta) \rangle_m {}_{m'} \langle \partial_\theta \alpha_{m'}(\theta) | \alpha_{m'}(\theta) \rangle_{m'}, \quad (\text{D.10})$$

$$\begin{aligned} F_\theta [|\boldsymbol{\alpha}(\theta)\rangle] &= 4 (\langle \partial_\theta \boldsymbol{\alpha}(\theta) | \partial_\theta \boldsymbol{\alpha}(\theta) \rangle - |\langle \boldsymbol{\alpha}(\theta) | \partial_\theta \boldsymbol{\alpha}(\theta) \rangle|^2) \\ &= 4 \left(\sum_{m=1}^N {}_m \langle \partial_\theta \alpha_m(\theta) | \partial_\theta \alpha_m(\theta) \rangle_m \right. \\ &\quad \left. - \sum_{m=1}^N {}_m \langle \alpha_m(\theta) | \partial_\theta \alpha_m(\theta) \rangle_m {}_m \langle \partial_\theta \alpha_m(\theta) | \alpha_m(\theta) \rangle_m \right) \\ &= 4 \sum_{m=1}^N ({}_m \langle \partial_\theta \alpha_m(\theta) | \partial_\theta \alpha_m(\theta) \rangle_m - |{}_m \langle \alpha_m(\theta) | \partial_\theta \alpha_m(\theta) \rangle_m|^2) \\ &= \sum_{m=1}^N F_\theta [|\alpha_m(\theta)\rangle_m] = 4 \sum_{m=1}^N |\partial_\theta \alpha_m(\theta)|^2 = 4 \|\partial_\theta \boldsymbol{\alpha}(\theta)\|^2. \end{aligned} \quad (\text{D.11})$$

Appendix E

General Reduced Photon Number States

The multinomial coefficient

$$\binom{n}{p_1, \dots, p_N} = \frac{n!}{C_{\mathbf{p}}^2} \quad (\text{E.1})$$

gives the number of possibilities of distributing n photons into N modes, such that in mode m there are p_m photons. Thus, for any vector $\mathbf{f} \in \mathbb{C}^{|\mathcal{F}_n^N|}$:

$$\forall \mathbf{p} \in \mathcal{F}_n^N : f_{\mathbf{p}} = \frac{C_{\mathbf{p}}^2}{n!} \sum_{\mathbf{p}_1, \dots, \mathbf{p}_n \in \mathcal{F}_1^N}^{\sum_{k=1}^n \mathbf{p}_k = \mathbf{p}} f_{\sum_{k=1}^n \mathbf{p}_k}. \quad (\text{E.2})$$

From this it follows that we can split a sum over \mathcal{F}_n^N into sums over \mathcal{F}_1^N in the following way:

$$\sum_{\mathbf{p} \in \mathcal{F}_n^N} f_{\mathbf{p}} = \frac{1}{n!} \sum_{\mathbf{p}_1, \dots, \mathbf{p}_n \in \mathcal{F}_1^N} C_{\sum_{k=1}^n \mathbf{p}_k}^2 f_{\sum_{k=1}^n \mathbf{p}_k}. \quad (\text{E.3})$$

Similarly,

$$\sum_{\mathbf{n}'' \in \mathcal{F}_{n-\mu}^{N, > M}} f_{\mathbf{n}''} = \frac{1}{(n-\mu)!} \sum_{\mathbf{n}''_{\mu+1}, \dots, \mathbf{n}''_1 \in \mathcal{F}_1^{N, > M}} C_{\sum_{k=\mu+1}^n \mathbf{n}''_k}^2 f_{\sum_{k=\mu+1}^n \mathbf{n}''_k}. \quad (\text{E.4})$$

With this and $\psi^{\text{out}} = \mathbf{S}^{(n)} \psi^{\text{in}}$ we can calculate:

$$\begin{aligned} \tilde{\rho}_{\mathbf{n}, \mathbf{n}'}^{\text{out}(\mu)} &= \sum_{\mathbf{n}'' \in \mathcal{F}_{n-\mu}^{N, > M}} \psi_{\mathbf{n}+\mathbf{n}''}^{\text{out}} \psi_{\mathbf{n}'+\mathbf{n}''}^{\text{out}*} \\ &= \sum_{\mathbf{n}'' \in \mathcal{F}_{n-\mu}^{N, > M}} \sum_{\mathbf{p}, \mathbf{q} \in \mathcal{F}_n^N} S_{\mathbf{n}+\mathbf{n}'', \mathbf{p}}^{(n)} S_{\mathbf{n}'+\mathbf{n}'', \mathbf{q}}^{(n)*} \psi_{\mathbf{p}}^{\text{in}} \psi_{\mathbf{q}}^{\text{in}*} \\ &= \frac{1}{(n!)^2 (n-\mu)!} \sum_{\mathbf{p}_1, \dots, \mathbf{p}_n \in \mathcal{F}_1^N} \sum_{\mathbf{q}_1, \dots, \mathbf{q}_n \in \mathcal{F}_1^N} C_{\sum_{k=1}^n \mathbf{p}_k}^2 C_{\sum_{k=1}^n \mathbf{q}_k}^2 \psi_{\sum_{k=1}^n \mathbf{p}_k}^{\text{in}} \psi_{\sum_{k=1}^n \mathbf{q}_k}^{\text{in}*}. \end{aligned}$$

$$\begin{aligned}
 & \cdot \sum_{\mathbf{n}''_{\mu+1}, \dots, \mathbf{n}''_n \in \mathcal{F}_1^{N, > M}} C_{\sum_{k=\mu+1}^n \mathbf{n}''_k}^2 S_{\mathbf{n} + \sum_{k=\mu+1}^n \mathbf{n}''_k, \sum_{k=1}^n \mathbf{p}_k}^{(n)} \cdot \\
 & \cdot S_{\mathbf{n}' + \sum_{k=\mu+1}^n \mathbf{n}''_k, \sum_{k=1}^n \mathbf{q}_k}^{(n)*} \quad (E.5)
 \end{aligned}$$

Using the fact that $\mathbf{n} \in \mathcal{F}_\mu^{N, \leq M}$, $\mathbf{n}'' \in \mathcal{F}_{n-\mu}^{N, > M} \implies C_{\mathbf{n} + \mathbf{n}''} = C_{\mathbf{n}} C_{\mathbf{n}''}$, we express the n -photon scattering matrix $\mathbf{S}^{(n)}$ in terms of the single-photon scattering matrix \mathbf{S} using Eq. (1.71):

$$\begin{aligned}
 S_{\mathbf{n} + \sum_{k=\mu+1}^n \mathbf{n}''_k, \sum_{k=1}^n \mathbf{p}_k}^{(n)} &= \frac{1}{C_{\mathbf{n}} C_{\sum_{k=\mu+1}^n \mathbf{n}''_k} C_{\sum_{k=1}^n \mathbf{p}_k}} \cdot \\
 & \cdot \sum_{\sigma \in \mathcal{G}_n} \left(\prod_{k=1}^{\mu} S_{\mathbf{n}_k, \mathbf{p}_{\sigma(k)}} \right) \left(\prod_{k=\mu+1}^n S_{\mathbf{n}''_k, \mathbf{p}_{\sigma(k)}} \right). \quad (E.6)
 \end{aligned}$$

Before we proceed, we note that in the sum

$$\sum_{\mathbf{p}_1, \dots, \mathbf{p}_n \in \mathcal{F}_1^N} f_{\sum_{k=1}^n \mathbf{p}_k} A_{\mathbf{p}_1, \dots, \mathbf{p}_n} \quad (E.7)$$

we can replace $A_{\mathbf{p}_1, \dots, \mathbf{p}_n}$ by its symmetric part (since $f_{\sum_{k=1}^n \mathbf{p}_k}$ acts as a symmetrizer):

$$\sum_{\mathbf{p}_1, \dots, \mathbf{p}_n \in \mathcal{F}_1^N} f_{\sum_{k=1}^n \mathbf{p}_k} A_{\mathbf{p}_1, \dots, \mathbf{p}_n} = \frac{1}{n!} \sum_{\mathbf{p}_1, \dots, \mathbf{p}_n \in \mathcal{F}_1^N} f_{\sum_{k=1}^n \mathbf{p}_k} \sum_{\sigma \in \mathcal{G}_n} A_{\mathbf{p}_{\sigma(1)}, \dots, \mathbf{p}_{\sigma(n)}}. \quad (E.8)$$

We apply this identity “in reverse” and further use Eq. (3.70) to obtain:

$$\begin{aligned}
 \tilde{\rho}_{\mathbf{n}, \mathbf{n}'}^{\text{out}(\mu)} &= \frac{1}{(n-\mu)!} \frac{1}{C_{\mathbf{n}} C_{\mathbf{n}'}} \sum_{\mathbf{p}_1, \dots, \mathbf{p}_n \in \mathcal{F}_1^N} \sum_{\mathbf{q}_1, \dots, \mathbf{q}_n \in \mathcal{F}_1^N} \Upsilon_{\sum_{k=1}^n \mathbf{p}_k}^{\text{in}} \Upsilon_{\sum_{k=1}^n \mathbf{q}_k}^{\text{in}*} \cdot \\
 & \cdot \sum_{\mathbf{n}''_{\mu+1}, \dots, \mathbf{n}''_n \in \mathcal{F}_1^{N, > M}} \left(\prod_{k=1}^{\mu} S_{\mathbf{n}_k, \mathbf{p}_k} \right) \left(\prod_{k=\mu+1}^n S_{\mathbf{n}''_k, \mathbf{p}_k} \right) \cdot \\
 & \cdot \left(\prod_{k=1}^{\mu} S_{\mathbf{n}'_k, \mathbf{q}_k}^* \right) \left(\prod_{k=\mu+1}^n S_{\mathbf{n}''_k, \mathbf{q}_k}^* \right) \\
 &= \frac{1}{(n-\mu)!} \frac{1}{C_{\mathbf{n}} C_{\mathbf{n}'}} \sum_{\mathbf{p}_1, \dots, \mathbf{p}_n \in \mathcal{F}_1^N} \sum_{\mathbf{q}_1, \dots, \mathbf{q}_n \in \mathcal{F}_1^N} \Upsilon_{\sum_{k=1}^n \mathbf{p}_k}^{\text{in}} \Upsilon_{\sum_{k=1}^n \mathbf{q}_k}^{\text{in}*} \cdot \\
 & \cdot \left(\prod_{k=1}^{\mu} S_{\mathbf{n}_k, \mathbf{p}_k} S_{\mathbf{n}'_k, \mathbf{q}_k}^* \right) \prod_{k=\mu+1}^n \sum_{\mathbf{n}''_k \in \mathcal{F}_1^{N, > M}} S_{\mathbf{n}''_k, \mathbf{p}_k} S_{\mathbf{n}''_k, \mathbf{q}_k}^*. \quad (E.9)
 \end{aligned}$$

At this stage we can employ the unitarity of the (full) scattering matrix, $\mathbf{S}^\top \mathbf{S}^* = \mathbf{1}$,

$$\delta_{\mathbf{p}_k, \mathbf{q}_k} = \sum_{\mathbf{n}'' \in \mathcal{F}_1^N} S_{\mathbf{n}'', \mathbf{p}_k} S_{\mathbf{n}'', \mathbf{q}_k}^* = \sum_{\mathbf{n}'' \in \mathcal{F}_1^M} S_{\mathbf{n}'', \mathbf{p}_k} S_{\mathbf{n}'', \mathbf{q}_k}^* + \sum_{\mathbf{n}'' \in \mathcal{F}_1^{N, > M}} S_{\mathbf{n}'', \mathbf{p}_k} S_{\mathbf{n}'', \mathbf{q}_k}^*, \quad (E.10)$$

and replace \mathbf{S} by the reduced scattering matrix $\tilde{\mathbf{S}}$:

$$\begin{aligned} \tilde{\rho}_{\mathbf{n}, \mathbf{n}'}^{\text{out}(\mu)} &= \frac{1}{(n - \mu)!} \frac{1}{C_{\mathbf{n}} C_{\mathbf{n}'}} \sum_{\mathbf{p}_1, \dots, \mathbf{p}_n \in \mathcal{F}_1^N} \sum_{\mathbf{q}_1, \dots, \mathbf{q}_n \in \mathcal{F}_1^N} \left(\prod_{k=1}^{\mu} \tilde{S}_{\mathbf{n}_k, \mathbf{p}_k} \right) \Upsilon_{\sum_{k=1}^n \mathbf{p}_k}^{\text{in}} \cdot \\ &\cdot \left(\prod_{k=\mu+1}^n \left(\mathbf{1} - \tilde{\mathbf{S}}^\top \tilde{\mathbf{S}}^* \right)_{\mathbf{p}_k, \mathbf{q}_k} \right) \Upsilon_{\sum_{k=1}^n \mathbf{q}_k}^{\text{in}*} \left(\prod_{k=1}^{\mu} \tilde{S}_{\mathbf{n}'_k, \mathbf{q}_k}^* \right). \end{aligned} \quad (\text{E.11})$$

Appendix F

QFI of Reduced Pure States

We call

$$\rho = \psi\psi^\dagger \quad (\text{F.1})$$

with $\|\psi\| \leq 1$ a reduced pure state. The eigen-decomposition (see Eq. (3.15)) of this state is

$$\rho = p\mathbf{v}\mathbf{v}^\dagger \quad (\text{F.2})$$

with

$$p = \|\psi\|^2, \quad (\text{F.3})$$

$$\mathbf{v} = \frac{\psi}{\|\psi\|}. \quad (\text{F.4})$$

We use Eq. (3.17) to calculate the QFI of ρ :

$$\partial_\theta p = \partial_\theta (\psi^\dagger \psi) = (\partial_\theta \psi)^\dagger \psi + \psi^\dagger (\partial_\theta \psi), \quad (\text{F.5})$$

$$\partial_\theta \mathbf{v} = \frac{\|\psi\| \partial_\theta \psi - (\partial_\theta \|\psi\|) \psi}{\|\psi\|^2}, \quad (\text{F.6})$$

$$\begin{aligned}
 (\partial_\theta \mathbf{v})^\dagger (\partial_\theta \mathbf{v}) &= \frac{\|\psi\|^2 (\partial_\theta \psi)^\dagger (\partial_\theta \psi) + (\partial_\theta \|\psi\|)^2 \|\psi\|^2}{\|\psi\|^4} \\
 &\quad - \frac{\|\psi\| (\partial_\theta \|\psi\|) \left((\partial_\theta \psi)^\dagger \psi + \psi^\dagger (\partial_\theta \psi) \right)}{\|\psi\|^4} \\
 &= \frac{(\partial_\theta \psi)^\dagger (\partial_\theta \psi)}{\|\psi\|^2} + \frac{\left(\frac{1}{2} \partial_\theta (\|\psi\|^2) \right)^2}{\|\psi\|^4} - \frac{\left(\frac{1}{2} \partial_\theta (\|\psi\|^2) \right) (\partial_\theta (\|\psi\|^2))}{\|\psi\|^4} \\
 &= \frac{(\partial_\theta \psi)^\dagger (\partial_\theta \psi)}{\|\psi\|^2} - \frac{(\partial_\theta (\|\psi\|^2))^2}{4 \|\psi\|^4}, \quad (\text{F.7})
 \end{aligned}$$

$$\mathbf{v}^\dagger (\partial_\theta \mathbf{v}) = \frac{\|\psi\| \psi^\dagger (\partial_\theta \psi) - (\partial_\theta \|\psi\|) \|\psi\|^2}{\|\psi\|^3}$$

$$\begin{aligned}
 &= \frac{\boldsymbol{\psi}^\dagger (\partial_\theta \boldsymbol{\psi}) - \frac{1}{2} (\partial_\theta (\|\boldsymbol{\psi}\|^2))}{\|\boldsymbol{\psi}\|^2} \\
 &= \frac{\boldsymbol{\psi}^\dagger (\partial_\theta \boldsymbol{\psi}) - (\partial_\theta \boldsymbol{\psi})^\dagger \boldsymbol{\psi}}{2 \|\boldsymbol{\psi}\|^2} \\
 &= \frac{i\Im (\boldsymbol{\psi}^\dagger (\partial_\theta \boldsymbol{\psi}))}{\|\boldsymbol{\psi}\|^2}. \tag{F.8}
 \end{aligned}$$

In total, we obtain

$$\begin{aligned}
 F_\theta [\boldsymbol{\psi} \boldsymbol{\psi}^\dagger] &= \frac{(\partial_\theta p)^2}{p} + 4p (\partial_\theta \mathbf{v})^\dagger (\partial_\theta \mathbf{v}) - 4p |\mathbf{v}^\dagger (\partial_\theta \mathbf{v})|^2 \\
 &= \frac{(\partial_\theta \|\boldsymbol{\psi}\|^2)^2}{\|\boldsymbol{\psi}\|^2} + 4 (\partial_\theta \boldsymbol{\psi})^\dagger (\partial_\theta \boldsymbol{\psi}) - \frac{(\partial_\theta (\|\boldsymbol{\psi}\|^2))^2}{\|\boldsymbol{\psi}\|^2} - \frac{4\Im^2 (\boldsymbol{\psi}^\dagger (\partial_\theta \boldsymbol{\psi}))}{\|\boldsymbol{\psi}\|^2} \\
 &= 4 (\partial_\theta \boldsymbol{\psi})^\dagger (\partial_\theta \boldsymbol{\psi}) - \frac{4\Re^2 (-i\boldsymbol{\psi}^\dagger (\partial_\theta \boldsymbol{\psi}))}{\|\boldsymbol{\psi}\|^2}. \tag{F.9}
 \end{aligned}$$

Appendix G

Multi-Photon GWS and FI Matrix

The reduced n -photon scattering matrix and its derivative w.r.t. θ are respectively given by

$$\tilde{S}_{\mathbf{p},\mathbf{q}}^{(n)} = \frac{1}{C_{\mathbf{p}}C_{\mathbf{q}}} \sum_{\sigma \in \mathfrak{S}_n} \prod_{k=1}^n \tilde{S}_{\mathbf{p}_k, \mathbf{q}_{\sigma(k)}}, \quad (\text{G.1})$$

$$\partial_{\theta} \tilde{S}_{\mathbf{p},\mathbf{q}}^{(n)} = \frac{1}{C_{\mathbf{p}}C_{\mathbf{q}}} \sum_{\sigma \in \mathfrak{S}_n} \sum_{k=1}^n \left(\partial_{\theta} \tilde{S}_{\mathbf{p}_k, \mathbf{q}_{\sigma(k)}} \right) \left(\prod_{l(\neq k)}^n \tilde{S}_{\mathbf{p}_l, \mathbf{q}_{\sigma(l)}} \right). \quad (\text{G.2})$$

G.1 Multi-Photon GWS Matrix

The reduced single-photon GWS matrix is given by

$$\left(\tilde{\mathbf{Q}}_{\theta} \right)_{\mathbf{p},\mathbf{q}} = -i \sum_{\mathbf{r} \in \mathcal{F}_1^M} \tilde{S}_{\mathbf{r},\mathbf{p}}^* \partial_{\theta} \tilde{S}_{\mathbf{r},\mathbf{q}} \quad (\text{G.3})$$

$$\iff \left(\tilde{\mathbf{Q}}_{\theta}^{\dagger} \right)_{\mathbf{p},\mathbf{q}} = i \sum_{\mathbf{r} \in \mathcal{F}_1^M} \left(\partial_{\theta} \tilde{S}_{\mathbf{r},\mathbf{p}}^* \right) \tilde{S}_{\mathbf{r},\mathbf{q}}. \quad (\text{G.4})$$

Using Eqs. (E.3), (G.1), (G.2) and (G.3), we can calculate:

$$\begin{aligned} \left(\tilde{\mathbf{Q}}_{\theta}^{(n)} \right)_{\mathbf{p},\mathbf{q}} &= -i \sum_{\mathbf{r} \in \mathcal{F}_n^M} \tilde{S}_{\mathbf{r},\mathbf{p}}^{(n)*} \partial_{\theta} \tilde{S}_{\mathbf{r},\mathbf{q}}^{(n)} \\ &= -\frac{i}{n!} \sum_{\mathbf{r}_1, \dots, \mathbf{r}_n \in \mathcal{F}_1^M} C_{\sum_{k=1}^n \mathbf{r}_k}^2 \tilde{S}_{\sum_{k=1}^n \mathbf{r}_k, \mathbf{p}}^{(n)*} \partial_{\theta} \tilde{S}_{\sum_{k=1}^n \mathbf{r}_k, \mathbf{q}}^{(n)} \\ &= -\frac{i}{n!} \sum_{\mathbf{r}_1, \dots, \mathbf{r}_n \in \mathcal{F}_1^M} C_{\sum_{k=1}^n \mathbf{r}_k}^2 \left(\frac{1}{C_{\sum_{k=1}^n \mathbf{r}_k} C_{\mathbf{p}}} \sum_{\sigma \in \mathfrak{S}_n} \left(\prod_{l=1}^n \tilde{S}_{\mathbf{r}_l, \mathbf{p}_{\sigma(l)}}^* \right) \right) \\ &\quad \cdot \left(\frac{1}{C_{\sum_{k=1}^n \mathbf{r}_k} C_{\mathbf{q}}} \sum_{\pi \in \mathfrak{S}_n} \sum_{k=1}^n \left(\partial_{\theta} \tilde{S}_{\mathbf{r}_k, \mathbf{q}_{\pi(k)}} \right) \left(\prod_{l(\neq k)}^n \tilde{S}_{\mathbf{r}_l, \mathbf{q}_{\pi(l)}} \right) \right) \end{aligned}$$

$$\begin{aligned}
 &= -\frac{i}{n!} \frac{1}{C_{\mathbf{p}} C_{\mathbf{q}}} \sum_{\mathbf{r}_1, \dots, \mathbf{r}_n \in \mathcal{F}_1^M} \sum_{\sigma, \pi \in \mathfrak{S}_n} \sum_{k=1}^n \tilde{S}_{\mathbf{r}_k, \mathbf{p}_{\sigma(k)}}^* \left(\partial_{\theta} \tilde{S}_{\mathbf{r}_k, \mathbf{q}_{\pi(k)}} \right) \\
 &\quad \cdot \left(\prod_{l(\neq k)}^n \tilde{S}_{\mathbf{r}_l, \mathbf{p}_{\sigma(l)}}^* \right) \left(\prod_{l(\neq k)}^n \tilde{S}_{\mathbf{r}_l, \mathbf{q}_{\pi(l)}} \right) \\
 &= \frac{1}{n!} \frac{1}{C_{\mathbf{p}} C_{\mathbf{q}}} \sum_{\sigma, \pi \in \mathfrak{S}_n} \sum_{k=1}^n \left(\tilde{Q}_{\theta} \right)_{\mathbf{p}_{\sigma(k)}, \mathbf{q}_{\pi(k)}} \cdot \\
 &\quad \cdot \sum_{\mathbf{r}_1, \dots, \mathbf{r}_n \setminus \{\mathbf{r}_k\} \in \mathcal{F}_1^M} \left(\prod_{l(\neq k)}^n \tilde{S}_{\mathbf{r}_l, \mathbf{p}_{\sigma(l)}}^* \tilde{S}_{\mathbf{r}_l, \mathbf{q}_{\pi(l)}} \right) \\
 &= \frac{1}{n!} \frac{1}{C_{\mathbf{p}} C_{\mathbf{q}}} \sum_{\sigma, \pi \in \mathfrak{S}_n} \sum_{k=1}^n \left(\tilde{Q}_{\theta} \right)_{\mathbf{p}_{\sigma(k)}, \mathbf{q}_{\pi(k)}} \prod_{l(\neq k)}^n \sum_{\mathbf{r}_l \in \mathcal{F}_1^M} \tilde{S}_{\mathbf{r}_l, \mathbf{p}_{\sigma(l)}}^* \tilde{S}_{\mathbf{r}_l, \mathbf{q}_{\pi(l)}}. \quad (\text{G.5})
 \end{aligned}$$

By $\mathfrak{S}_n^{k' \rightarrow k'}$ we denote the set of permutations which map k to k' . With this we can proceed:

$$\begin{aligned}
 \left(\tilde{Q}_{\theta}^{(n)} \right)_{\mathbf{p}, \mathbf{q}} &= \frac{1}{n!} \frac{1}{C_{\mathbf{p}} C_{\mathbf{q}}} \sum_{\pi \in \mathfrak{S}_n} \sum_{k=1}^n \sum_{k'=1}^n \sum_{\sigma \in \mathfrak{S}_n^{k' \rightarrow k'}} \left(\tilde{Q}_{\theta} \right)_{\mathbf{p}_{k'}, \mathbf{q}_{\pi(\sigma^{-1}(k'))}} \prod_{l(\neq k')}^n \left(\tilde{S}^{\dagger} \tilde{S} \right)_{\mathbf{p}_{\sigma(l)}, \mathbf{q}_{\pi(l)}} \\
 &= \frac{1}{n!} \frac{1}{C_{\mathbf{p}} C_{\mathbf{q}}} \sum_{\pi \in \mathfrak{S}_n} \sum_{k'=1}^n \sum_{k=1}^n \sum_{\sigma \in \mathfrak{S}_n^{k' \rightarrow k'}} \left(\tilde{Q}_{\theta} \right)_{\mathbf{p}_{k'}, \mathbf{q}_{\pi(\sigma^{-1}(k'))}} \cdot \\
 &\quad \cdot \prod_{l'(\neq k')}^n \left(\tilde{S}^{\dagger} \tilde{S} \right)_{\mathbf{p}_{l'}, \mathbf{q}_{\pi(\sigma^{-1}(l'))}} \\
 &= \frac{1}{n!} \frac{1}{C_{\mathbf{p}} C_{\mathbf{q}}} \sum_{\pi \in \mathfrak{S}_n} \sum_{k'=1}^n \sum_{\sigma \in \mathfrak{S}_n} \left(\tilde{Q}_{\theta} \right)_{\mathbf{p}_{k'}, \mathbf{q}_{\pi(\sigma^{-1}(k'))}} \prod_{l'(\neq k')}^n \left(\tilde{S}^{\dagger} \tilde{S} \right)_{\mathbf{p}_{l'}, \mathbf{q}_{\pi(\sigma^{-1}(l'))}} \\
 &= \frac{1}{n!} \frac{1}{C_{\mathbf{p}} C_{\mathbf{q}}} \sum_{\sigma \in \mathfrak{S}_n} \sum_{\pi \in \mathfrak{S}_n} \sum_{k=1}^n \left(\tilde{Q}_{\theta} \right)_{\mathbf{p}_k, \mathbf{q}_{\pi(\sigma^{-1}(k))}} \prod_{l(\neq k)}^n \left(\tilde{S}^{\dagger} \tilde{S} \right)_{\mathbf{p}_l, \mathbf{q}_{\pi(\sigma^{-1}(l))}}. \quad (\text{G.6})
 \end{aligned}$$

For each fixed $\sigma \in \mathfrak{S}_n$, the sum $\sum_{\pi \in \mathfrak{S}_n}$ runs over all permutations in \mathfrak{S}_n . We perform an “index shift” and replace π by $\pi \circ \sigma$:

$$\begin{aligned}
 \left(\tilde{Q}_{\theta}^{(n)} \right)_{\mathbf{p}, \mathbf{q}} &= \frac{1}{n!} \frac{1}{C_{\mathbf{p}} C_{\mathbf{q}}} \sum_{\sigma \in \mathfrak{S}_n} \sum_{\pi \in \mathfrak{S}_n} \sum_{k=1}^n \left(\tilde{Q}_{\theta} \right)_{\mathbf{p}_k, \mathbf{q}_{\pi(k)}} \prod_{l(\neq k)}^n \left(\tilde{S}^{\dagger} \tilde{S} \right)_{\mathbf{p}_l, \mathbf{q}_{\pi(l)}} \\
 &= \frac{1}{C_{\mathbf{p}} C_{\mathbf{q}}} \sum_{\pi \in \mathfrak{S}_n} \sum_{k=1}^n \left(\tilde{Q}_{\theta} \right)_{\mathbf{p}_k, \mathbf{q}_{\pi(k)}} \prod_{l(\neq k)}^n \left(\tilde{S}^{\dagger} \tilde{S} \right)_{\mathbf{p}_l, \mathbf{q}_{\pi(l)}}. \quad (\text{G.7})
 \end{aligned}$$

This completes the proof of Eq. (3.80).

G.2 Multi-Photon FI Matrix

The reduced single-photon FI matrix is given by

$$\left(\tilde{\mathbf{F}}_{\theta}\right)_{\mathbf{p},\mathbf{q}} = 4 \sum_{\mathbf{r} \in \mathcal{F}_1^M} \left(\partial_{\theta} \tilde{S}_{\mathbf{r},\mathbf{p}}^*\right) \left(\partial_{\theta} \tilde{S}_{\mathbf{r},\mathbf{q}}\right). \quad (\text{G.8})$$

Using Eqs. (E.3), (G.2), (G.3) and (G.4) we can calculate:

$$\begin{aligned} \left(\tilde{\mathbf{F}}_{\theta}^{(n)}\right)_{\mathbf{p},\mathbf{q}} &= 4 \sum_{\mathbf{r} \in \mathcal{F}_n^M} \left(\partial_{\theta} \tilde{S}_{\mathbf{r},\mathbf{p}}^{(n)*}\right) \left(\partial_{\theta} \tilde{S}_{\mathbf{r},\mathbf{q}}^{(n)}\right) \\ &= \frac{4}{n!} \sum_{\mathbf{r}_1, \dots, \mathbf{r}_n \in \mathcal{F}_1^M} C_{\sum_{k=1}^n \mathbf{r}_k}^2 \left(\partial_{\theta} \tilde{S}_{\sum_{k=1}^n \mathbf{r}_k, \mathbf{p}}^{(n)*}\right) \left(\partial_{\theta} \tilde{S}_{\sum_{k=1}^n \mathbf{r}_k, \mathbf{q}}^{(n)}\right) \\ &= \frac{4}{n!} \sum_{\mathbf{r}_1, \dots, \mathbf{r}_n \in \mathcal{F}_1^M} C_{\sum_{k=1}^n \mathbf{r}_k}^2 \cdot \\ &\quad \cdot \left(\frac{1}{C_{\sum_{k=1}^n \mathbf{r}_k} C_{\mathbf{p}}} \sum_{\sigma \in \mathfrak{S}_n} \sum_{k=1}^n \left(\partial_{\theta} \tilde{S}_{\mathbf{r}_k, \mathbf{p}_{\sigma(k)}}^*\right) \left(\prod_{l(\neq k)}^n \tilde{S}_{\mathbf{r}_l, \mathbf{p}_{\sigma(l)}}^*\right) \right) \cdot \\ &\quad \cdot \left(\frac{1}{C_{\sum_{k=1}^n \mathbf{r}_k} C_{\mathbf{q}}} \sum_{\pi \in \mathfrak{S}_n} \sum_{k'=1}^n \left(\partial_{\theta} \tilde{S}_{\mathbf{r}_{k'}, \mathbf{q}_{\pi(k')}}\right) \left(\prod_{l'(\neq k')}^n \tilde{S}_{\mathbf{r}_{l'}, \mathbf{q}_{\pi(l')}}\right) \right) \\ &= \frac{4}{n!} \frac{1}{C_{\mathbf{p}} C_{\mathbf{q}}} \sum_{\mathbf{r}_1, \dots, \mathbf{r}_n \in \mathcal{F}_1^M} \sum_{\sigma, \pi \in \mathfrak{S}_n} \sum_{k, k'=1}^n \left(\partial_{\theta} \tilde{S}_{\mathbf{r}_k, \mathbf{p}_{\sigma(k)}}^*\right) \left(\partial_{\theta} \tilde{S}_{\mathbf{r}_{k'}, \mathbf{q}_{\pi(k')}}\right) \cdot \\ &\quad \cdot \left(\prod_{l(\neq k)}^n \tilde{S}_{\mathbf{r}_l, \mathbf{p}_{\sigma(l)}}^*\right) \left(\prod_{l'(\neq k')}^n \tilde{S}_{\mathbf{r}_{l'}, \mathbf{q}_{\pi(l')}}\right) \\ &= \frac{4}{n!} \frac{1}{C_{\mathbf{p}} C_{\mathbf{q}}} \sum_{\mathbf{r}_1, \dots, \mathbf{r}_n \in \mathcal{F}_1^M} \sum_{\sigma, \pi \in \mathfrak{S}_n} \sum_{k=1}^n \left(\partial_{\theta} \tilde{S}_{\mathbf{r}_k, \mathbf{p}_{\sigma(k)}}^*\right) \left(\partial_{\theta} \tilde{S}_{\mathbf{r}_k, \mathbf{q}_{\pi(k)}}\right) \cdot \\ &\quad \cdot \left(\prod_{l(\neq k)}^n \tilde{S}_{\mathbf{r}_l, \mathbf{p}_{\sigma(l)}}^* \tilde{S}_{\mathbf{r}_l, \mathbf{q}_{\pi(l)}}\right) \\ &\quad + \frac{4}{n!} \frac{1}{C_{\mathbf{p}} C_{\mathbf{q}}} \sum_{\mathbf{r}_1, \dots, \mathbf{r}_n \in \mathcal{F}_1^M} \sum_{\sigma, \pi \in \mathfrak{S}_n} \sum_{k \neq k'}^n \left(\partial_{\theta} \tilde{S}_{\mathbf{r}_k, \mathbf{p}_{\sigma(k)}}^*\right) \tilde{S}_{\mathbf{r}_k, \mathbf{q}_{\pi(k)}} \tilde{S}_{\mathbf{r}_{k'}, \mathbf{p}_{\sigma(k')}}^* \cdot \\ &\quad \cdot \left(\partial_{\theta} \tilde{S}_{\mathbf{r}_{k'}, \mathbf{q}_{\pi(k')}}\right) \left(\prod_{l(\neq k, k')}^n \tilde{S}_{\mathbf{r}_l, \mathbf{p}_{\sigma(l)}}^* \tilde{S}_{\mathbf{r}_l, \mathbf{q}_{\pi(l)}}\right) \end{aligned}$$

$$\begin{aligned}
 &= \frac{1}{n!} \frac{1}{C_{\mathbf{p}} C_{\mathbf{q}}} \sum_{\sigma, \pi \in \mathfrak{S}_n} \sum_{k=1}^n \left(\tilde{\mathbf{F}}_{\theta} \right)_{\mathbf{p}_{\sigma(k)}, \mathbf{q}_{\pi(k)}} \cdot \\
 &\quad \cdot \sum_{\mathbf{r}_1, \dots, \mathbf{r}_n \setminus \{\mathbf{r}_k\} \in \mathcal{F}_1^M} \left(\prod_{l(\neq k)}^n \tilde{S}_{\mathbf{r}_l, \mathbf{p}_{\sigma(l)}}^* \tilde{S}_{\mathbf{r}_l, \mathbf{q}_{\pi(l)}} \right) \\
 &+ \frac{4}{n!} \frac{1}{C_{\mathbf{p}} C_{\mathbf{q}}} \sum_{\sigma, \pi \in \mathfrak{S}_n} \sum_{k \neq k'}^n \left(\tilde{\mathbf{Q}}_{\theta}^{\dagger} \right)_{\mathbf{p}_{\sigma(k)}, \mathbf{q}_{\pi(k)}} \left(\tilde{\mathbf{Q}}_{\theta} \right)_{\mathbf{p}_{\sigma(k')}, \mathbf{q}_{\pi(k')}} \cdot \\
 &\quad \cdot \sum_{\mathbf{r}_1, \dots, \mathbf{r}_n \setminus \{\mathbf{r}_k, \mathbf{r}_{k'}\} \in \mathcal{F}_1^M} \left(\prod_{l(\neq k, k')}^n \tilde{S}_{\mathbf{r}_l, \mathbf{p}_{\sigma(l)}}^* \tilde{S}_{\mathbf{r}_l, \mathbf{q}_{\pi(l)}} \right) \\
 &= \frac{1}{n!} \frac{1}{C_{\mathbf{p}} C_{\mathbf{q}}} \sum_{\sigma, \pi \in \mathfrak{S}_n} \sum_{k=1}^n \left(\tilde{\mathbf{F}}_{\theta} \right)_{\mathbf{p}_{\sigma(k)}, \mathbf{q}_{\pi(k)}} \prod_{l(\neq k)}^n \sum_{\mathbf{r}_l \in \mathcal{F}_1^M} \tilde{S}_{\mathbf{r}_l, \mathbf{p}_{\sigma(l)}}^* \tilde{S}_{\mathbf{r}_l, \mathbf{q}_{\pi(l)}} \\
 &+ \frac{4}{n!} \frac{1}{C_{\mathbf{p}} C_{\mathbf{q}}} \sum_{\sigma, \pi \in \mathfrak{S}_n} \sum_{k \neq k'}^n \left(\tilde{\mathbf{Q}}_{\theta}^{\dagger} \right)_{\mathbf{p}_{\sigma(k)}, \mathbf{q}_{\pi(k)}} \left(\tilde{\mathbf{Q}}_{\theta} \right)_{\mathbf{p}_{\sigma(k')}, \mathbf{q}_{\pi(k')}} \cdot \\
 &\quad \cdot \prod_{l(\neq k, k')}^n \sum_{\mathbf{r}_l \in \mathcal{F}_1^M} \tilde{S}_{\mathbf{r}_l, \mathbf{p}_{\sigma(l)}}^* \tilde{S}_{\mathbf{r}_l, \mathbf{q}_{\pi(l)}} \\
 &= \frac{1}{n!} \frac{1}{C_{\mathbf{p}} C_{\mathbf{q}}} \sum_{\sigma, \pi \in \mathfrak{S}_n} \sum_{k=1}^n \left(\tilde{\mathbf{F}}_{\theta} \right)_{\mathbf{p}_{\sigma(k)}, \mathbf{q}_{\pi(k)}} \prod_{l(\neq k)}^n \left(\tilde{\mathbf{S}}^{\dagger} \tilde{\mathbf{S}} \right)_{\mathbf{p}_{\sigma(l)}, \mathbf{q}_{\pi(l)}} \\
 &+ \frac{4}{n!} \frac{1}{C_{\mathbf{p}} C_{\mathbf{q}}} \sum_{\sigma, \pi \in \mathfrak{S}_n} \sum_{k \neq k'}^n \left(\tilde{\mathbf{Q}}_{\theta}^{\dagger} \right)_{\mathbf{p}_{\sigma(k)}, \mathbf{q}_{\pi(k)}} \left(\tilde{\mathbf{Q}}_{\theta} \right)_{\mathbf{p}_{\sigma(k')}, \mathbf{q}_{\pi(k')}} \cdot \\
 &\quad \cdot \prod_{l(\neq k, k')}^n \left(\tilde{\mathbf{S}}^{\dagger} \tilde{\mathbf{S}} \right)_{\mathbf{p}_{\sigma(l)}, \mathbf{q}_{\pi(l)}}. \tag{G.9}
 \end{aligned}$$

The first summand is equivalent to what was calculated for $\tilde{\mathbf{Q}}_{\theta}^{(n)}$ above:

$$\left(\tilde{\mathbf{F}}_{\theta}^{(n),1} \right)_{\mathbf{p}, \mathbf{q}} = \frac{1}{C_{\mathbf{p}} C_{\mathbf{q}}} \sum_{\sigma \in \mathfrak{S}_n} \sum_{k=1}^n \left(\tilde{\mathbf{F}}_{\theta} \right)_{\mathbf{p}_k, \mathbf{q}_{\sigma(k)}} \prod_{l(\neq k)}^n \left(\tilde{\mathbf{S}}^{\dagger} \tilde{\mathbf{S}} \right)_{\mathbf{p}_l, \mathbf{q}_{\sigma(l)}}. \tag{G.10}$$

The second summand is treated similarly as in the last lines of the calculation of $\tilde{\mathbf{Q}}_{\theta}^{(n)}$ in Sec. G.1:

$$\begin{aligned}
 \left(\tilde{\mathbf{F}}_{\theta}^{(n),2} \right)_{\mathbf{p}, \mathbf{q}} &= \frac{4}{n!} \frac{1}{C_{\mathbf{p}} C_{\mathbf{q}}} \sum_{\pi \in \mathfrak{S}_n} \sum_{k \neq k'}^n \sum_{\kappa \neq \kappa'}^n \sum_{\sigma \in \mathfrak{S}_n^{k \rightarrow \kappa, k' \rightarrow \kappa'}} \left(\tilde{\mathbf{Q}}_{\theta}^{\dagger} \right)_{\mathbf{p}_{\kappa}, \mathbf{q}_{\pi(\sigma^{-1}(\kappa))}} \cdot \\
 &\quad \cdot \left(\tilde{\mathbf{Q}}_{\theta} \right)_{\mathbf{p}_{\kappa'}, \mathbf{q}_{\pi(\sigma^{-1}(\kappa'))}} \prod_{l(\neq k, k')}^n \left(\tilde{\mathbf{S}}^{\dagger} \tilde{\mathbf{S}} \right)_{\mathbf{p}_{\sigma(l)}, \mathbf{q}_{\pi(l)}}
 \end{aligned}$$

$$\begin{aligned}
 &= \frac{4}{n!} \frac{1}{C_{\mathbf{p}} C_{\mathbf{q}}} \sum_{\pi \in \tilde{\mathfrak{S}}_n} \sum_{\kappa \neq \kappa'}^n \sum_{k \neq k'}^n \sum_{\sigma \in \tilde{\mathfrak{S}}_n^{k \mapsto \kappa, k' \mapsto \kappa'}} \left(\tilde{\mathbf{Q}}_{\theta}^{\dagger} \right)_{\mathbf{p}_{\kappa}, \mathbf{q}_{\pi(\sigma^{-1}(\kappa))}} \cdot \\
 &\quad \cdot \left(\tilde{\mathbf{Q}}_{\theta} \right)_{\mathbf{p}_{\kappa'}, \mathbf{q}_{\pi(\sigma^{-1}(\kappa'))}} \prod_{l' (\neq \kappa, \kappa')}^n \left(\tilde{\mathbf{S}}^{\dagger} \tilde{\mathbf{S}} \right)_{\mathbf{p}_{l'}, \mathbf{q}_{\pi(\sigma^{-1}(l'))}} \\
 &= \frac{4}{n!} \frac{1}{C_{\mathbf{p}} C_{\mathbf{q}}} \sum_{\pi \in \tilde{\mathfrak{S}}_n} \sum_{\kappa \neq \kappa'}^n \sum_{\sigma \in \tilde{\mathfrak{S}}_n} \left(\tilde{\mathbf{Q}}_{\theta}^{\dagger} \right)_{\mathbf{p}_{\kappa}, \mathbf{q}_{\pi(\sigma^{-1}(\kappa))}} \left(\tilde{\mathbf{Q}}_{\theta} \right)_{\mathbf{p}_{\kappa'}, \mathbf{q}_{\pi(\sigma^{-1}(\kappa'))}} \cdot \\
 &\quad \cdot \prod_{l' (\neq \kappa, \kappa')}^n \left(\tilde{\mathbf{S}}^{\dagger} \tilde{\mathbf{S}} \right)_{\mathbf{p}_{l'}, \mathbf{q}_{\pi(\sigma^{-1}(l'))}} \\
 &= \frac{4}{C_{\mathbf{p}} C_{\mathbf{q}}} \sum_{\pi \in \tilde{\mathfrak{S}}_n} \sum_{k \neq k'}^n \left(\tilde{\mathbf{Q}}_{\theta}^{\dagger} \right)_{\mathbf{p}_k, \mathbf{q}_{\pi(k)}} \left(\tilde{\mathbf{Q}}_{\theta} \right)_{\mathbf{p}_{k'}, \mathbf{q}_{\pi(k')}} \cdot \\
 &\quad \cdot \prod_{l (\neq k, k')}^n \left(\tilde{\mathbf{S}}^{\dagger} \tilde{\mathbf{S}} \right)_{\mathbf{p}_l, \mathbf{q}_{\pi(l)}} \cdot \tag{G.11}
 \end{aligned}$$

This completes the proof of Eq. (3.81).

Acknowledgements

My deepest gratitude goes to my supervisor Stefan Rotter, who has been guiding me through good and tough times, and from whom I have been learning not only technical expertise in various fields of physics, but also important soft skills for communicating within scientific communities. I also appreciate the insights he has given me into the inner workings of scientific research, e.g., how funding is obtained or how to navigate the publication process, both as an author and as a referee. Classical music, in which Stefan and I share a strong interest, has proved to be a useful allegory for scientific research and its challenges.

Sincere thanks also go out to my colleagues within the group, Andre Brandstötter, Oliver Diekmann, David Globosits, Helmut Hörner, Michael Horodynski, Jakob Hüpf, Ivor Krešić, Matthias Kühmayer, Kevin Pichler, Alexander Schumer, Maximilian Weimar and Matthias Zens, who have created an extremely pleasant, open and cooperative working atmosphere. In particular, I would like to highlight my office neighbour Maximilian Weimar, who always had an open ear for technical or personal concerns and who could lighten up the office routine with both entertaining or in-depth discussions, as well as Andre Brandstötter, Matthias Kühmayer and Matthias Zens, who were providing great mental and emotional support during the Corona times.

Cheers to all the students whose projects I had the honour to (co-)supervise: Jens Burkhart (project student), Tim Ehret (project student), David Förlinger (bachelor student), Günther Hackl (project student and diploma student), Sébastien Lucas (internship student), Thomas Ranner (bachelor student), Felix Russo (diploma student), Felix Wagner (project student) and Maximilian Weimar (diploma student). The discussions with them contributed also to my own understanding of physics and life. In particular, Sébastien Lucas, who had been part of the group for just 3 months, has become a great friend, with whom I can talk about truly everything, which I am exceedingly grateful for.

Due thanks go to the external collaborators who shared parts of their expertise with me and helped me embed my scientific findings into their respective research areas. In the field of ultrasound imaging, I am grateful to have had the opportunity to work with Alexandre Aubry, Antton Goicoechea, Flavien Bureau, Arthur Le Ber and Elsa Giraudat from Institut Langevin in Paris (France). I owe the introduction to quantum optics and vacuum physics to Ulf Leonhardt from the Weizmann Institute of Science in Rehovot (Israel). In the area of (quantum) metrology, Dorian Bouchet from Université Grenoble Alpes in Grenoble (France) has been an invaluable

Acknowledgements

able advisor. For their meticulous experimental work, I acknowledge Daniele Faccio and Ilya Starshynov from the University of Glasgow in Glasgow (UK) as well as Ulrich Kuhl from Université Côte d’Azur in Nice (France).

A huge shout-out goes to the secretaries of the Institute for Theoretical Physics at TU Wien, Heike Höller, Almaz Murshudova, Sylvia Riedler, Andrea Smith-Stachowski and Ingrid Unger, who have always been keeping the administrative, sometimes cumbersome apparatus running. I have the impression that there is not a single question to which they do not have an answer. Special thanks go out to Ingrid Unger, who not only supported me with advice concerning my employment and the FWF project by which I was being financed, but she was also helping to keep the spirits up in the otherwise deserted institute during the Corona times with card games.

I acknowledge the Austrian Science Fund (Fonds zur Förderung der wissenschaftlichen Forschung, FWF) for funding my research through Project No. P 32300-N27 (WaveLand).

The computational results presented herein were achieved in part using the Vienna Scientific Cluster (VSC).

I have to thank my grey key for having given me both short walks to obtain food and a breathtaking view of Vienna.

Last but not least, I want to express my highest gratefulness to my family, especially my parents and my siblings, and friends. They have always offered me emotional, culinary, recreational and financial support whenever I needed it. Without them, studying and working at university under such stable and reliable conditions would not have been possible.

References

- [1] J. W. Goodman, *Speckle Phenomena in Optics: Theory and Applications*, 2nd ed. (SPIE Press, 2020).
- [2] R. Carminati and J. C. Schotland, *Principles of Scattering and Transport of Light* (Cambridge University Press, 2021).
- [3] R. K. Tyson and B. W. Frazier, *Principles of Adaptive Optics*, 5th ed. (CRC Press, 2022).
- [4] I. M. Vellekoop and A. P. Mosk, “Focusing coherent light through opaque strongly scattering media”, *Opt. Lett.* **32**, 2309–2311 (2007).
- [5] S. M. Popoff, G. Lerosey, M. Fink, A. C. Boccara and S. Gigan, “Image transmission through an opaque material”, *Nat. Commun.* **1**, 81 (2010).
- [6] S. M. Popoff *et al.*, “Measuring the Transmission Matrix in Optics: An Approach to the Study and Control of Light Propagation in Disordered Media”, *Phys. Rev. Lett.* **104**, 100601 (2010).
- [7] H. Yu *et al.*, “Measuring Large Optical Transmission Matrices of Disordered Media”, *Phys. Rev. Lett.* **111**, 153902 (2013).
- [8] A. Drémeau *et al.*, “Reference-less measurement of the transmission matrix of a highly scattering material using a DMD and phase retrieval techniques”, *Opt. Express* **23**, 11898–11911 (2015).
- [9] A. P. Mosk, A. Lagendijk, G. Lerosey and M. Fink, “Controlling waves in space and time for imaging and focusing in complex media”, *Nat. Photonics* **6**, 283–292 (2012).
- [10] S. Rotter and S. Gigan, “Light fields in complex media: Mesoscopic scattering meets wave control”, *Rev. Mod. Phys.* **89**, 015005 (2017).
- [11] H. Cao, A. P. Mosk and S. Rotter, “Shaping the propagation of light in complex media”, *Nat. Phys.* **18**, 994–1007 (2022).
- [12] O. Katz, E. Small, Y. Bromberg and Y. Silberberg, “Focusing and compression of ultrashort pulses through scattering media”, *Nat. Photonics* **5**, 372–377 (2011).
- [13] R. Horstmeyer, H. Ruan and C. Yang, “Guidestar-assisted wavefront-shaping methods for focusing light into biological tissue”, *Nat. Photonics* **9**, 563–571 (2015).

- [14] P. Ambichl *et al.*, “Focusing inside Disordered Media with the Generalized Wigner-Smith Operator”, *Phys. Rev. Lett.* **119**, 033903 (2017).
- [15] C. Bradac, “Nanoscale Optical Trapping: A Review”, *Adv. Opt. Mater.* **6**, 1800005 (2018).
- [16] I. A. Favre-Bulle, A. B. Stilgoe, E. K. Scott and H. Rubinsztein-Dunlop, “Optical trapping *in vivo*: theory, practice, and applications”, *Nanophotonics* **8**, 1023–1040 (2019).
- [17] C. Gonzalez-Ballester, M. Aspelmeyer, L. Novotny, R. Quidant and O. Romero-Isart, “Levitodynamics: Levitation and control of microscopic objects in vacuum”, *Science* **374**, eabg3027 (2021).
- [18] K. Dholakia and T. Čižmár, “Shaping the future of manipulation”, *Nat. Photonics* **5**, 335–342 (2011).
- [19] D. Palima and J. Glückstad, “Gearing up for optical microrobotics: micro-manipulation and actuation of synthetic microstructures by optical forces”, *Laser Photonics Rev.* **7**, 478–494 (2013).
- [20] M. Horodyski *et al.*, “Optimal wave fields for micromanipulation in complex scattering environments”, *Nat. Photonics* **14**, 149–153 (2020).
- [21] F. Balzarotti *et al.*, “Nanometer resolution imaging and tracking of fluorescent molecules with minimal photon fluxes”, *Science* **355**, 606–612 (2017).
- [22] T. Juffmann, A. de los Ríos Sommer and S. Gigan, “Local Optimization of Wave-fronts for optimal sensitivity PHase Imaging (LowPhi)”, *Opt. Commun.* **454**, 124484 (2020).
- [23] D. Bouchet, S. Rotter and A. P. Mosk, “Maximum information states for coherent scattering measurements”, *Nat. Phys.* **17**, 564–568 (2021).
- [24] O. Katz, E. Small and Y. Silberberg, “Looking around corners and through thin turbid layers in real time with scattered incoherent light”, *Nat. Photonics* **6**, 549–553 (2012).
- [25] J. Bertolotti and O. Katz, “Imaging in complex media”, *Nat. Phys.* **18**, 1008–1017 (2022).
- [26] S. Rotter, P. Ambichl and F. Libisch, “Generating Particlelike Scattering States in Wave Transport”, *Phys. Rev. Lett.* **106**, 120602 (2011).
- [27] B. Gérardin *et al.*, “Particlelike wave packets in complex scattering systems”, *Phys. Rev. B* **94**, 014209 (2016).
- [28] A. Brandstötter, A. Girschik, P. Ambichl and S. Rotter, “Shaping the branched flow of light through disordered media”, *Proc. Natl. Acad. Sci. U.S.A.* **116**, 13260–13265 (2019).

-
- [29] U. Delić *et al.*, “Cooling of a levitated nanoparticle to the motional quantum ground state”, *Science* **367**, 892–895 (2020).
- [30] L. Magrini *et al.*, “Real-time optimal quantum control of mechanical motion at room temperature”, *Nature* **595**, 373–377 (2021).
- [31] F. Tebbenjohanns, M. L. Mattana, M. Rossi, M. Frimmer and L. Novotny, “Quantum control of a nanoparticle optically levitated in cryogenic free space”, *Nature* **595**, 378–382 (2021).
- [32] A. H. Safavi-Naeini *et al.*, “Squeezed light from a silicon micromechanical resonator”, *Nature* **500**, 185–189 (2013).
- [33] N. Treps *et al.*, “A Quantum Laser Pointer”, *Science* **301**, 940–943 (2003).
- [34] M. A. Taylor *et al.*, “Biological measurement beyond the quantum limit”, *Nat. Photonics* **7**, 229–233 (2013).
- [35] J. Aasi *et al.*, “Enhanced sensitivity of the LIGO gravitational wave detector by using squeezed states of light”, *Nat. Photonics* **7**, 613–619 (2013).
- [36] M. I. Kolobov, ed., *Quantum Imaging* (Springer, New York, NY, 2007).
- [37] M. J. Padgett and R. W. Boyd, “An introduction to ghost imaging: quantum and classical”, *Phil. Trans. R. Soc. A.* **375**, 20160233 (2017).
- [38] P.-A. Moreau, E. Toninelli, T. Gregory and M. J. Padgett, “Imaging with quantum states of light”, *Nat. Rev. Phys.* **1**, 367–380 (2019).
- [39] H. Defienne, M. Barbieri, I. A. Walmsley, B. J. Smith and S. Gigan, “Two-photon quantum walk in a multimode fiber”, *Sci. Adv.* **2**, e1501054 (2016).
- [40] T. A. W. Wolterink *et al.*, “Programmable two-photon quantum interference in 10^3 channels in opaque scattering media”, *Phys. Rev. A* **93**, 053817 (2016).
- [41] H. Defienne, M. Reichert and J. W. Fleischer, “Adaptive Quantum Optics with Spatially Entangled Photon Pairs”, *Phys. Rev. Lett.* **121**, 233601 (2018).
- [42] M. Hiekkamäki, F. Bouchard and R. Fickler, “Photonic Angular Superresolution Using Twisted N00N States”, *Phys. Rev. Lett.* **127**, 263601 (2021).
- [43] J. Carpenter *et al.*, “Mode multiplexed single-photon and classical channels in a few-mode fiber”, *Opt. Express* **21**, 28794–28800 (2013).
- [44] T. J. Huisman, S. R. Huisman, A. P. Mosk and P. W. H. Pinkse, “Controlling single-photon Fock-state propagation through opaque scattering media”, *Appl. Phys. B* **116**, 603–607 (2014).
- [45] H. Defienne *et al.*, “Nonclassical light manipulation in a multiple-scattering medium”, *Opt. Lett.* **39**, 6090–6093 (2014).
- [46] S. Leedumrongwatthanakun *et al.*, “Programmable linear quantum networks with a multimode fibre”, *Nat. Photonics* **14**, 139–142 (2020).

- [47] H. Defienne, M. Reichert, J. W. Fleischer and D. Faccio, “Quantum image distillation”, *Sci. Adv.* **5**, eaax0307 (2019).
- [48] O. Lib, G. Hasson and Y. Bromberg, “Real-time shaping of entangled photons by classical control and feedback”, *Sci. Adv.* **6**, eabb6298 (2020).
- [49] N. H. Valencia, S. Goel, W. McCutcheon, H. Defienne and M. Malik, “Unscrambling entanglement through a complex medium”, *Nat. Phys.* **16**, 1112–1116 (2020).
- [50] S. Pang and A. N. Jordan, “Optimal adaptive control for quantum metrology with time-dependent Hamiltonians”, *Nat. Commun.* **8**, 14695 (2017).
- [51] L. J. Fiderer, J. M. E. Fraïsse and D. Braun, “Maximal Quantum Fisher Information for Mixed States”, *Phys. Rev. Lett.* **123**, 250502 (2019).
- [52] H. B. G. Casimir, “On the attraction between two perfectly conducting plates”, *Proc. Kon. Nederland. Akad. Wetensch.* **51**, 793–795 (1948).
- [53] S. Y. Buhmann, *Dispersion Forces* (Springer-Verlag Berlin Heidelberg, 2012).
- [54] W. M. R. Simpson and U. Leonhardt, eds., *Forces of the Quantum Vacuum* (World Scientific, 2015).
- [55] J. Fujimoto and W. Drexler, “Introduction to Optical Coherence Tomography”, in *Optical Coherence Tomography* (Springer-Verlag Berlin Heidelberg, 2008) Chap. 1.
- [56] T. L. Szabo, *Diagnostic Ultrasound Imaging: Inside Out*, 2nd ed. (Academic Press, 2014).
- [57] J. A. Jensen, “Medical ultrasound imaging”, *Prog. Biophys. Mol. Biol.* **93**, 153–165 (2007).
- [58] H. Azhari, *Basics of Biomedical Ultrasound for Engineers* (John Wiley & Sons, Inc., 2010).
- [59] A. Rix *et al.*, “Advanced Ultrasound Technologies for Diagnosis and Therapy”, *J. Nucl. Med.* **59**, 740–746 (2018).
- [60] S. Gummadi *et al.*, “Advances in Modern Clinical Ultrasound”, *Adv. Ultrasound Diagn. Ther.* **2**, 51–63 (2018).
- [61] J. Baun, “Advances in Ultrasound Imaging Architecture: The Future Is Now”, *J. Diagn. Med. Sonogr.* **37**, 312–314 (2021).
- [62] A. Aubry and A. Derode, “Detection and imaging in a random medium: A matrix method to overcome multiple scattering and aberration”, *J. Appl. Phys.* **106**, 044903 (2009).
- [63] W. Lambert, L. A. Cobus, M. Couade, M. Fink and A. Aubry, “Reflection Matrix Approach for Quantitative Imaging of Scattering Media”, *Phys. Rev. X* **10**, 021048 (2020).

-
- [64] W. Lambert, L. A. Cobus, T. Frappart, M. Fink and A. Aubry, “Distortion matrix approach for ultrasound imaging of random scattering media”, *Proc. Natl. Acad. Sci. U.S.A.* **117**, 14645–14656 (2020).
- [65] A. Turpin, I. Vishniakou and J. d. Seelig, “Light scattering control in transmission and reflection with neural networks”, *Opt. Express* **26**, 30911–30929 (2018).
- [66] U. S. Kamilov, D. Liu, H. Mansour and P. T. Boufounos, “A Recursive Born Approach to Nonlinear Inverse Scattering”, *IEEE Signal Process. Lett.* **23**, 1052–1056 (2016).
- [67] Y. Sun, Z. Xia and U. S. Kamilov, “Efficient and accurate inversion of multiple scattering with deep learning”, *Opt. Express* **26**, 14678–14688 (2018).
- [68] Y. Li, Y. Xue and L. Tian, “Deep speckle correlation: a deep learning approach toward scalable imaging through scattering media”, *Optica* **5**, 1181–1190 (2018).
- [69] G. Barbastathis, A. Ozcan and G. Situ, “On the use of deep learning for computational imaging”, *Optica* **6**, 921–943 (2019).
- [70] H. Almansouri, S. Venkatakrishnan, G. Buzzard, C. Bouman and H. Santos-Villalobos, “Deep Neural Networks for Non-Linear Model-Based Ultrasound Reconstruction”, in *2018 IEEE Global Conference on Signal and Information Processing (GlobalSIP)* (2018), pp. 6–10.
- [71] M. Micucci and A. Iula, “Recent Advances in Machine Learning Applied to Ultrasound Imaging”, *Electronics* **11**, 1800 (2022).
- [72] P. Zelger *et al.*, “Three-dimensional localization microscopy using deep learning”, *Opt. Express* **26**, 33166–33179 (2018).
- [73] E. Nehme *et al.*, “DeepSTORM3D: dense 3D localization microscopy and PSF design by deep learning”, *Nat. Methods* **17**, 734–740 (2020).
- [74] D. Liu, Y. Tan, E. Khoram and Z. Yu, “Training Deep Neural Networks for the Inverse Design of Nanophotonic Structures”, *ACS Photonics* **5**, 1365–1369 (2018).
- [75] J. Peurifoy *et al.*, “Nanophotonic particle simulation and inverse design using artificial neural networks”, *Sci. Adv.* **4**, eaar4206 (2018).
- [76] S. So, T. Badloe, J. Noh, J. Bravo-Abad and J. Rho, “Deep learning enabled inverse design in nanophotonics”, *Nanophotonics* **9**, 1041–1057 (2020).
- [77] W. Ma *et al.*, “Deep learning for the design of photonic structures”, *Nat. Photonics* **15**, 77–90 (2021).
- [78] L. De Marinis, M. Cococcioni, P. Castoldi and N. Andriolli, “Photonic Neural Networks: A Survey”, *IEEE Access* **7**, 175827–175841 (2019).

- [79] G. Wetzstein *et al.*, “Inference in artificial intelligence with deep optics and photonics”, *Nature* **588**, 39–47 (2020).
- [80] H. Zhang *et al.*, “An optical neural chip for implementing complex-valued neural network”, *Nat. Commun.* **12**, 457 (2021).
- [81] I. A. D. Williamson *et al.*, “Reprogrammable Electro-Optic Nonlinear Activation Functions for Optical Neural Networks”, *IEEE J. Sel. Top. Quantum Electron.* **26**, 1–12 (2020).
- [82] X. Xu *et al.*, “Photonic Perceptron Based on a Kerr Microcomb for High-Speed, Scalable, Optical Neural Networks”, *Laser Photonics Rev.* **14**, 2000070 (2020).
- [83] F. Xia *et al.*, “Deep Learning with Passive Optical Nonlinear Mapping”, (2023), [arXiv:2307.08558](https://arxiv.org/abs/2307.08558).
- [84] T. W. Hughes, M. Minkov, Y. Shi and S. Fan, “Training of photonic neural networks through in situ backpropagation and gradient measurement”, *Optica* **5**, 864–871 (2018).
- [85] T. Zhou *et al.*, “In situ optical backpropagation training of diffractive optical neural networks”, *Photonics Res.* **8**, 940–953 (2020).
- [86] S. Pai *et al.*, “Experimentally realized in situ backpropagation for deep learning in photonic neural networks”, *Science* **380**, 398–404 (2023).
- [87] J. D. Jackson, *Classical Electrodynamics*, 3rd ed. (John Wiley & Sons, Inc., 1999).
- [88] N. D. Mermin, *Quantum Computer Science: An Introduction* (Cambridge University Press, 2007).
- [89] R. W. Boyd, *Nonlinear Optics*, 3rd ed. (Academic Press, 2008).
- [90] S. Buddhiraju, A. Song, G. T. Papadakis and S. Fan, “Nonreciprocal Metamaterial Obeying Time-Reversal Symmetry”, *Phys. Rev. Lett.* **124**, 257403 (2020).
- [91] J.-F. Morizur *et al.*, “Programmable unitary spatial mode manipulation”, *J. Opt. Soc. Am. A* **27**, 2524–2531 (2010).
- [92] A. B. Ayoub and D. Psaltis, “High speed, complex wavefront shaping using the digital micro-mirror device”, *Sci. Rep.* **11**, 18837 (2021).
- [93] S. Gigan *et al.*, “Roadmap on wavefront shaping and deep imaging in complex media”, *J. Phys. Photonics* **4**, 042501 (2022).
- [94] A. I. Lvovsky and M. G. Raymer, “Continuous-variable optical quantum-state tomography”, *Rev. Mod. Phys.* **81**, 299–332 (2009).
- [95] J. Schöberl, “C++11 Implementation of Finite Elements in NGSolve”, ASC Report No. 30/2014, 2014.

-
- [96] M. Kühmayer, “Optimal Wave Fields in Complex Scattering Environments”, PhD thesis (TU Wien, 2022).
- [97] S. Rahimi-Keshari *et al.*, “Direct characterization of linear-optical networks”, *Opt. Express* **21**, 13450–13458 (2013).
- [98] U. Leonhardt, *Essential Quantum Optics* (Cambridge University Press, 2010).
- [99] C. Fabre and N. Treps, “Modes and states in quantum optics”, *Rev. Mod. Phys.* **92**, 035005 (2020).
- [100] X. Ma and W. Rhodes, “Multimode squeeze operators and squeezed states”, *Phys. Rev. A* **41**, 4625–4631 (1990).
- [101] H. Vahlbruch, M. Mehmet, K. Danzmann and R. Schnabel, “Detection of 15 dB Squeezed States of Light and their Application for the Absolute Calibration of Photoelectric Quantum Efficiency”, *Phys. Rev. Lett.* **117**, 110801 (2016).
- [102] A. Kronwald, F. Marquardt and A. A. Clerk, “Dissipative optomechanical squeezing of light”, *New J. Phys.* **16**, 063058 (2014).
- [103] U. L. Andersen, T. Gehring, C. Marquardt and G. Leuchs, “30 years of squeezed light generation”, *Phys. Scr.* **91**, 053001 (2016).
- [104] R. Schnabel, “Squeezed states of light and their applications in laser interferometers”, *Phys. Rep.* **684**, 1–51 (2017).
- [105] J.-F. Morizur, S. Armstrong, N. Treps, J. Janousek and H.-A. Bachor, “Spatial reshaping of a squeezed state of light”, *Eur. Phys. J. D* **61**, 237–239 (2011).
- [106] M. Semmler *et al.*, “Single-mode squeezing in arbitrary spatial modes”, *Opt. Express* **24**, 7633–7642 (2016).
- [107] L. Ma *et al.*, “Generation of squeezed states of light in arbitrary complex amplitude transverse distribution”, *Photon. Res.* **8**, 1422–1427 (2020).
- [108] M. Lassen *et al.*, “Tools for Multimode Quantum Information: Modulation, Detection, and Spatial Quantum Correlations”, *Phys. Rev. Lett.* **98**, 083602 (2007).
- [109] G. Cariolaro and G. Pierobon, “Bloch-Messiah reduction of Gaussian unitaries by Takagi factorization”, *Phys. Rev. A* **94**, 062109 (2016).
- [110] M. Reck, A. Zeilinger, H. J. Bernstein and P. Bertani, “Experimental realization of any discrete unitary operator”, *Phys. Rev. Lett.* **73**, 58–61 (1994).
- [111] W. R. Clements, P. C. Humphreys, B. J. Metcalf, W. S. Kolthammer and I. A. Walmsley, “Optimal design for universal multiport interferometers”, *Optica* **3**, 1460–1465 (2016).

- [112] W. Qin *et al.*, “Multimode quantum squeezing generation via multiple four-wave mixing processes within a single atomic vapor cell”, *J. Opt. Soc. Am. B* **39**, 2769–2778 (2022).
- [113] M. D. Eisaman, J. Fan, A. Migdall and S. V. Polyakov, “Invited Review Article: Single-photon sources and detectors”, *Rev. Sci. Instrum.* **82**, 071101 (2011).
- [114] B. T. H. Varcoe, S. Brattke, M. Weidinger and H. Walther, “Preparing pure photon number states of the radiation field”, *Nature* **403**, 743–746 (2000).
- [115] M. Cooper, L. J. Wright, C. Söller and B. J. Smith, “Experimental generation of multi-photon Fock states”, *Opt. Express* **21**, 5309–5317 (2013).
- [116] K. R. Brown, K. M. Dani, D. M. Stamper-Kurn and K. B. Whaley, “Deterministic optical Fock-state generation”, *Phys. Rev. A* **67**, 043818 (2003).
- [117] K. R. Motes *et al.*, “Efficient recycling strategies for preparing large Fock states from single-photon sources: Applications to quantum metrology”, *Phys. Rev. A* **94**, 012344 (2016).
- [118] M. Uria, P. Solano and C. Hermann-Avigliano, “Deterministic Generation of Large Fock States”, *Phys. Rev. Lett.* **125**, 093603 (2020).
- [119] A. Valencia, A. Ceré, X. Shi, G. Molina-Terriza and J. P. Torres, “Shaping the Waveform of Entangled Photons”, *Phys. Rev. Lett.* **99**, 243601 (2007).
- [120] P. Boucher, H. Defienne and S. Gigan, “Engineering spatial correlations of entangled photon pairs by pump beam shaping”, *Opt. Lett.* **46**, 4200–4203 (2021).
- [121] H. Defienne and S. Gigan, “Spatially entangled photon-pair generation using a partial spatially coherent pump beam”, *Phys. Rev. A* **99**, 053831 (2019).
- [122] W. Zhang, R. Fickler, E. Giese, L. Chen and R. W. Boyd, “Influence of pump coherence on the generation of position-momentum entanglement in optical parametric down-conversion”, *Opt. Express* **27**, 20745–20753 (2019).
- [123] K. Vogel and H. Risken, “Determination of quasiprobability distributions in terms of probability distributions for the rotated quadrature phase”, *Phys. Rev. A* **40**, 2847–2849 (1989).
- [124] U. Leonhardt, “Quantum-State Tomography and Discrete Wigner Function”, *Phys. Rev. Lett.* **74**, 4101–4105 (1995).
- [125] M. Collett, R. Loudon and C. Gardiner, “Quantum Theory of Optical Homodyne and Heterodyne Detection”, *J. Mod. Opt.* **34**, 881–902 (1987).
- [126] K. J. Blow, R. Loudon, S. J. D. Phoenix and T. J. Shepherd, “Continuum fields in quantum optics”, *Phys. Rev. A* **42**, 4102–4114 (1990).

-
- [127] U. Leonhardt, “Quantum physics of simple optical instruments”, *Rep. Prog. Phys.* **66**, 1207–1249 (2003).
- [128] U. Leonhardt and A. Neumaier, “Explicit effective Hamiltonians for general linear quantum-optical networks”, *J. Opt. B: Quantum Semiclass. Opt.* **6**, L1–L4 (2003).
- [129] M. Lobino *et al.*, “Complete Characterization of Quantum-Optical Processes”, *Science* **322**, 563–566 (2008).
- [130] S. Rahimi-Keshari *et al.*, “Quantum process tomography with coherent states”, *New J. Phys.* **13**, 013006 (2011).
- [131] K. V. Jacob, A. E. Mirasola, S. Adhikari and J. P. Dowling, “Direct characterization of linear and quadratically nonlinear optical systems”, *Phys. Rev. A* **98**, 052327 (2018).
- [132] T. Takagi, “On an Algebraic Problem Related to an Analytic Theorem of Carathéodory and Fejér and on an Allied Theorem of Landau”, *Japan J. Math.* **1**, 83–93 (1924).
- [133] A. M. Chebotarev and A. E. Teretenkov, “Singular value decomposition for the Takagi factorization of symmetric matrices”, *Appl. Math. Comput.* **234**, 380–384 (2014).
- [134] S. Scheel, “Permanents in linear optical networks”, (2004), [arXiv:quant-ph/0406127](https://arxiv.org/abs/quant-ph/0406127).
- [135] H. Defienne, “Quantum walks of photons in disordered media”, PhD thesis (Université Pierre et Marie Curie, 2015).
- [136] A. Ashkin, J. M. Dziedzic, J. E. Bjorkholm and S. Chu, “Observation of a single-beam gradient force optical trap for dielectric particles”, *Opt. Lett.* **11**, 288–290 (1986).
- [137] J. E. Curtis, B. A. Koss and D. G. Grier, “Dynamic holographic optical tweezers”, *Opt. Commun.* **207**, 169–175 (2002).
- [138] R. Bowman *et al.*, “Position clamping in a holographic counterpropagating optical trap”, *Opt. Express* **19**, 9908–9914 (2011).
- [139] D. B. Phillips *et al.*, “Shape-induced force fields in optical trapping”, *Nat. Photonics* **8**, 400–405 (2014).
- [140] D. G. Grier, “A revolution in optical manipulation”, *Nature* **424**, 810–816 (2003).
- [141] K. Dholakia and P. Reece, “Optical micromanipulation takes hold”, *Nano Today* **1**, 18–27 (2006).

- [142] G. Thalhammer, R. Steiger, S. Bernet and M. Ritsch-Marte, “Optical macro-tweezers: trapping of highly motile micro-organisms”, *J. Opt.* **13**, 044024 (2011).
- [143] T. Li, S. Kheifets and M. G. Raizen, “Millikelvin cooling of an optically trapped microsphere in vacuum”, *Nat. Phys.* **7**, 527–530 (2011).
- [144] C. N. LaFratta, “Optical tweezers for medical diagnostics”, *Anal. Bioanal. Chem.* **405**, 5671–5677 (2013).
- [145] S. Kheifets, A. Simha, K. Melin, T. Li and M. G. Raizen, “Observation of Brownian Motion in Liquids at Short Times: Instantaneous Velocity and Memory Loss”, *Science* **343**, 1493–1496 (2014).
- [146] T. Čížmár, M. Mazilu and K. Dholakia, “In situ wavefront correction and its application to micromanipulation”, *Nat. Photonics* **4**, 388–394 (2010).
- [147] L. M. Rachbauer, D. Bouchet, U. Leonhardt and S. Rotter, “Finding optimal quantum states for optical micromanipulation and metrology in scattering problems: tutorial”, submitted to *J. Opt. Soc. Am. B* (2024).
- [148] L. Eisenbud, “The Formal Properties of Nuclear Collisions”, unpublished, PhD thesis (Princeton University, 1948).
- [149] E. P. Wigner, “Lower Limit for the Energy Derivative of the Scattering Phase Shift”, *Phys. Rev.* **98**, 145–147 (1955).
- [150] F. T. Smith, “Lifetime Matrix in Collision Theory”, *Phys. Rev.* **118**, 349–356 (1960).
- [151] H. G. Winful, “Delay Time and the Hartman Effect in Quantum Tunneling”, *Phys. Rev. Lett.* **91**, 260401 (2003).
- [152] T. Kottos, “Statistics of resonances and delay times in random media: beyond random matrix theory”, *J. Phys. A: Math. Gen.* **38**, 10761–10786 (2005).
- [153] S. Fan and J. M. Kahn, “Principal modes in multimode waveguides”, *Opt. Lett.* **30**, 135–137 (2005).
- [154] J. Hüpfel *et al.*, “Optimal Cooling of Multiple Levitated Particles through Far-Field Wavefront Shaping”, *Phys. Rev. Lett.* **130**, 083203 (2023).
- [155] M. W. Matthès, Y. Bromberg, J. de Rosny and S. M. Popoff, “Learning and Avoiding Disorder in Multimode Fibers”, *Phys. Rev. X* **11**, 021060 (2021).
- [156] B. Judkewitz, Y. M. Wang, R. Horstmeyer, A. Mathy and C. Yang, “Speckle-scale focusing in the diffusive regime with time reversal of variance-encoded light (TROVE)”, *Nat. Photonics* **7**, 300–305 (2013).
- [157] E. H. Zhou, H. Ruan, C. Yang and B. Judkewitz, “Focusing on moving targets through scattering samples”, *Optica* **1**, 227–232 (2014).

-
- [158] C. Ma, X. Xu, Y. Liu and L. V. Wang, “Time-reversed adapted-perturbation (TRAP) optical focusing onto dynamic objects inside scattering media”, *Nat. Photonics* **8**, 931–936 (2014).
- [159] H. Ruan *et al.*, “Focusing light inside scattering media with magnetic-particle-guided wavefront shaping”, *Optica* **4**, 1337–1343 (2017).
- [160] C. Bechinger *et al.*, “Active particles in complex and crowded environments”, *Rev. Mod. Phys.* **88**, 045006 (2016).
- [161] G. Frangipane *et al.*, “Invariance properties of bacterial random walks in complex structures”, *Nat. Commun.* **10**, 2442 (2019).
- [162] A. Das and S. Okubo, *Lie Groups and Lie Algebras for Physicists* (World Scientific Publishing Co. Pte. Ltd., 2014).
- [163] M. Asjad, S. Zippilli and D. Vitali, “Suppression of Stokes scattering and improved optomechanical cooling with squeezed light”, *Phys. Rev. A* **94**, 051801 (2016).
- [164] J. B. Clark, F. Lecocq, R. W. Simmonds, J. Aumentado and J. D. Teufel, “Sideband cooling beyond the quantum backaction limit with squeezed light”, *Nature* **541**, 191–195 (2017).
- [165] M. Asjad, N. E. Abari, S. Zippilli and D. Vitali, “Optomechanical cooling with intracavity squeezed light”, *Opt. Express* **27**, 32427–32444 (2019).
- [166] J. Monsel *et al.*, “Optomechanical cooling with coherent and squeezed light: The thermodynamic cost of opening the heat valve”, *Phys. Rev. A* **103**, 063519 (2021).
- [167] J. J. M. Verbaarschot, H. A. Weidenmüller and M. R. Zirnbauer, “Grassmann integration in stochastic quantum physics: The case of compound-nucleus scattering”, *Phys. Rep.* **129**, 367–438 (1985).
- [168] Y. V. Fyodorov and H.-J. Sommers, “Statistics of resonance poles, phase shifts and time delays in quantum chaotic scattering: Random matrix approach for systems with broken time-reversal invariance”, *J. Math. Phys.* **38**, 1918–1981 (1997).
- [169] F.-M. Dittes, “The decay of quantum systems with a small number of open channels”, *Phys. Rep.* **339**, 215–316 (2000).
- [170] P. Jordan, “Der Zusammenhang der symmetrischen und linearen Gruppen und das Mehrkörperproblem”, *Zeitschrift für Physik* **94**, 531–535 (1935).
- [171] J. Schwinger, “On Angular Momentum”, U.S. Atomic Energy Commission Report Nr. NYO-3071, 1952.
- [172] P. Ambichl *et al.*, “Super- and Anti-Principal-Modes in Multimode Waveguides”, *Phys. Rev. X* **7**, 041053 (2017).

- [173] S. Scheel and S. Y. Buhmann, “Macroscopic Quantum Electrodynamics - Concepts and Applications”, *Acta Phys. Slovaca* **58**, 675–809 (2008).
- [174] A. W. Rodriguez, F. Capasso and S. G. Johnson, “The Casimir effect in microstructured geometries”, *Nat. Photonics* **5**, 211–221 (2011).
- [175] I. Dzyaloshinskii, E. Lifshitz and L. Pitaevskii, “The general theory of van der Waals forces”, *Adv. in Phys.* **10**, 165–209 (1961).
- [176] H. B. G. Casimir and D. Polder, “The Influence of Retardation on the London-van der Waals Forces”, *Phys. Rev.* **73**, 360–372 (1948).
- [177] D. A. T. Somers, J. L. Garrett, K. J. Palm and J. N. Munday, “Measurement of the Casimir torque”, *Nature* **564**, 386–389 (2018).
- [178] G. W. Koch, S. C. Sillett, G. M. Jennings and S. D. Davis, “The limits to tree height”, *Nature* **428**, 851–854 (2004).
- [179] U. Leonhardt, “Lifshitz theory of the cosmological constant”, *Ann. Phys.* **411**, 167973 (2019).
- [180] U. Leonhardt, “Casimir cosmology”, *Int. J. Mod. Phys. A* **37**, 2241006 (2022).
- [181] M. S. Birman and M. G. Krein, “On the theory of wave operators and scattering operators”, *Dokl. Akad. Nauk SSSR* **144**, 475–478 (1962).
- [182] J. S. Faulkner, “Scattering theory and cluster calculations”, *J. Phys. C: Solid State Phys.* **10**, 4661 (1977).
- [183] L. D. Landau and E. M. Lifshitz, “The generalised susceptibility”, in *Statistical Physics. Part 1*, 3rd ed. (Pergamon Press, 1980) Chap. 123.
- [184] A. Lambrecht, P. A. M. Neto and S. Reynaud, “The Casimir effect within scattering theory”, *New J. Phys.* **8**, 243 (2006).
- [185] A. Wirzba, “The Casimir effect as a scattering problem”, *J. Phys. A: Math. Theor.* **41**, 164003 (2008).
- [186] M. T. H. Reid, A. W. Rodriguez, J. White and S. G. Johnson, “Efficient Computation of Casimir Interactions between Arbitrary 3D Objects”, *Phys. Rev. Lett.* **103**, 040401 (2009).
- [187] W. M. R. Simpson, S. A. R. Horsley and U. Leonhardt, “Divergence of Casimir stress in inhomogeneous media”, *Phys. Rev. A* **87**, 043806 (2013).
- [188] I. Griniasty and U. Leonhardt, “Casimir stress inside planar materials”, *Phys. Rev. A* **96**, 032123 (2017).
- [189] I. Y. Efrat and U. Leonhardt, “Van der Waals anomaly: Analog of dark energy with ultracold atoms”, *Phys. Rev. B* **104**, 235432 (2021).
- [190] H. Hörner, L. M. Rachbauer, S. Rotter and U. Leonhardt, “Van der Waals chain: A simple model for Casimir forces in dielectrics”, *Phys. Rev. B* **108**, 235430 (2023).

-
- [191] E. Martínez-Vargas, C. Pineda, F. Leyvraz and P. Barberis-Blostein, “Quantum estimation of unknown parameters”, *Phys. Rev. A* **95**, 012136 (2017).
- [192] J. Rubio and J. Dunningham, “Bayesian multiparameter quantum metrology with limited data”, *Phys. Rev. A* **101**, 032114 (2020).
- [193] S. Morelli, A. Usui, E. Agudelo and N. Friis, “Bayesian parameter estimation using Gaussian states and measurements”, *Quantum Sci. Technol.* **6**, 025018 (2021).
- [194] S. M. Kay, *Fundamentals of Statistical Signal Processing: Estimation Theory* (Prentice-Hall, Inc., 1993).
- [195] H. L. V. Trees, K. L. Bell and Z. Tian, *Detection, Estimation, and Modulation Theory, Part 1 - Detection, Estimation, and Filtering Theory*, 2nd ed. (John Wiley & Sons, Inc., 2013).
- [196] C. R. Rao, “Information and the Accuracy Attainable in the Estimation of Statistical Parameters”, *Bull. Calcutta Math. Soc.* **37**, 81–91 (1945).
- [197] H. Cramér, *Mathematical Methods of Statistics* (Princeton University Press, 1999).
- [198] R. A. Fisher, “On the mathematical foundations of theoretical statistics”, *Philos. Trans. R. Soc. A* **222**, 309–368 (1922).
- [199] C. W. Helstrom, *Quantum Detection and Estimation Theory* (Academic Press, 1976).
- [200] M. G. A. Paris, “Quantum Estimation for Quantum Technology”, *Int. J. Quantum Inf.* **7**, 125–137 (2009).
- [201] V. Giovannetti, S. Lloyd and L. Maccone, “Advances in quantum metrology”, *Nat. Photonics* **5**, 222–229 (2011).
- [202] J. Liu, H. Yuan, X.-M. Lu and X. Wang, “Quantum Fisher information matrix and multiparameter estimation”, *J. Phys. A: Math. Theor.* **53**, 023001 (2020).
- [203] E. Polino, M. Valeri, N. Spagnolo and F. Sciarrino, “Photonic quantum metrology”, *AVS Quantum Sci.* **2**, 024703 (2020).
- [204] M. Barbieri, “Optical Quantum Metrology”, *PRX Quantum* **3**, 010202 (2022).
- [205] A. V. Fend, “On the Attainment of Cramér-Rao and Bhattacharyya Bounds for the Variance of an Estimate”, *Ann. Math. Stat.* **30**, 381–388 (1959).
- [206] S. L. Braunstein and C. M. Caves, “Statistical distance and the geometry of quantum states”, *Phys. Rev. Lett.* **72**, 3439–3443 (1994).
- [207] J. Liu, X.-X. Jing, W. Zhong and X.-G. Wang, “Quantum Fisher Information for Density Matrices with Arbitrary Ranks”, *Commun. Theor. Phys.* **61**, 45 (2014).

- [208] A. Fujiwara, “Quantum channel identification problem”, *Phys. Rev. A* **63**, 042304 (2001).
- [209] M. J. Holland and K. Burnett, “Interferometric detection of optical phase shifts at the Heisenberg limit”, *Phys. Rev. Lett.* **71**, 1355–1358 (1993).
- [210] V. Giovannetti, S. Lloyd and L. Maccone, “Quantum-Enhanced Measurements: Beating the Standard Quantum Limit”, *Science* **306**, 1330–1336 (2004).
- [211] H. Paul, “Über quantenmechanische Zeitoperatoren”, *Ann. Phys. (Berl.)* **464**, 252–261 (1962).
- [212] A. A. Clerk, M. H. Devoret, S. M. Girvin, F. Marquardt and R. J. Schoelkopf, “Introduction to quantum noise, measurement, and amplification”, *Rev. Mod. Phys.* **82**, 1155–1208 (2010).
- [213] C. M. Caves, “Quantum-mechanical noise in an interferometer”, *Phys. Rev. D* **23**, 1693–1708 (1981).
- [214] L. Barsotti, J. Harms and R. Schnabel, “Squeezed vacuum states of light for gravitational wave detectors”, *Rep. Prog. Phys.* **82**, 016905 (2018).
- [215] M. Tse *et al.*, “Quantum-Enhanced Advanced LIGO Detectors in the Era of Gravitational-Wave Astronomy”, *Phys. Rev. Lett.* **123**, 231107 (2019).
- [216] R. Demkowicz-Dobrzański, K. Banaszek and R. Schnabel, “Fundamental quantum interferometry bound for the squeezed-light-enhanced gravitational wave detector GEO 600”, *Phys. Rev. A* **88**, 041802 (2013).
- [217] T. Popoviciu, “Sur les équations algébriques ayant toutes leurs racines réelles”, *Mathematica* **9**, 129–145 (1935).
- [218] A. N. Boto *et al.*, “Quantum Interferometric Optical Lithography: Exploiting Entanglement to Beat the Diffraction Limit”, *Phys. Rev. Lett.* **85**, 2733–2736 (2000).
- [219] H. Lee, P. Kok and J. P. Dowling, “A quantum Rosetta stone for interferometry”, *J. Mod. Opt.* **49**, 2325–2338 (2002).
- [220] J. A. H. Nielsen, J. S. Neergaard-Nielsen, T. Gehring and U. L. Andersen, “Deterministic Quantum Phase Estimation beyond N00N States”, *Phys. Rev. Lett.* **130**, 123603 (2023).
- [221] C. K. Hong, Z. Y. Ou and L. Mandel, “Measurement of subpicosecond time intervals between two photons by interference”, *Phys. Rev. Lett.* **59**, 2044–2046 (1987).
- [222] M. W. Mitchell, J. S. Lundeen and A. M. Steinberg, “Super-resolving phase measurements with a multiphoton entangled state”, *Nature* **429**, 161–164 (2004).

-
- [223] P. Walther *et al.*, “De Broglie wavelength of a non-local four-photon state”, *Nature* **429**, 158–161 (2004).
- [224] I. Afek, O. Ambar and Y. Silberberg, “High-NOON States by Mixing Quantum and Classical Light”, *Science* **328**, 879–881 (2010).
- [225] T. Matsubara, P. Facchi, V. Giovannetti and K. Yuasa, “Optimal Gaussian metrology for generic multimode interferometric circuit”, *New J. Phys.* **21**, 033014 (2019).
- [226] L. Knöll, S. Scheel, E. Schmidt, D.-G. Welsch and A. V. Chizhov, “Quantum-state transformation by dispersive and absorbing four-port devices”, *Phys. Rev. A* **59**, 4716–4726 (1999).
- [227] M. Patra and C. W. J. Beenakker, “Propagation of squeezed radiation through amplifying or absorbing random media”, *Phys. Rev. A* **61**, 063805 (2000).
- [228] R. Demkowicz-Dobrzański *et al.*, “Quantum phase estimation with lossy interferometers”, *Phys. Rev. A* **80**, 013825 (2009).
- [229] M. Kacprowicz, R. Demkowicz-Dobrzański, W. Wasilewski, K. Banaszek and I. A. Walmsley, “Experimental quantum-enhanced estimation of a lossy phase shift”, *Nat. Photonics* **4**, 357–360 (2010).
- [230] J. Kołodyński and R. Demkowicz-Dobrzański, “Phase estimation without a priori phase knowledge in the presence of loss”, *Phys. Rev. A* **82**, 053804 (2010).
- [231] B. M. Escher, R. L. de Matos Filho and L. Davidovich, “General framework for estimating the ultimate precision limit in noisy quantum-enhanced metrology”, *Nat. Phys.* **7**, 406–411 (2011).
- [232] R. Demkowicz-Dobrzański, J. Kołodyński and M. Guță, “The elusive Heisenberg limit in quantum-enhanced metrology”, *Nat. Commun.* **3**, 1063 (2012).
- [233] Y. M. Zhang, X. W. Li, W. Yang and G. R. Jin, “Quantum Fisher information of entangled coherent states in the presence of photon loss”, *Phys. Rev. A* **88**, 043832 (2013).
- [234] G. Adesso, S. Ragy and A. R. Lee, “Continuous Variable Quantum Information: Gaussian States and Beyond”, *Open Syst. Inf. Dyn.* **21**, 1440001 (2014).
- [235] D. Šafránek, “Estimation of Gaussian quantum states”, *J. Phys. A: Math. Theor.* **52**, 035304 (2019).
- [236] U. Dorner *et al.*, “Optimal Quantum Phase Estimation”, *Phys. Rev. Lett.* **102**, 040403 (2009).
- [237] F. Russo, “Fisher Information Flow in Wave Scattering”, Diploma Thesis (TU Wien, 2022).

- [238] J. Hüpfel *et al.*, “Continuity Equation for the Flow of Fisher Information in Wave Scattering”, (2023), [arXiv:2309.00010](#).
- [239] D. Bouchet, L. M. Rachbauer, S. Rotter, A. P. Mosk and E. Bossy, “Optimal Control of Coherent Light Scattering for Binary Decision Problems”, *Phys. Rev. Lett.* **127**, 253902 (2021).
- [240] O. Büyüköztürk, “Imaging of concrete structures”, *NDT & E International* **31**, 233–243 (1998).
- [241] S. Gholizadeh, “A review of non-destructive testing methods of composite materials”, *Procedia Structural Integrity* **1**, 50–57 (2016).
- [242] B. Wang, S. Zhong, T.-L. Lee, K. S. Fancey and J. Mi, “Non-destructive testing and evaluation of composite materials/structures: A state-of-the-art review”, *Advances in Mechanical Engineering* **12**, 1687814020913761 (2020).
- [243] A. D. Parsekian, K. Singha, B. J. Minsley, W. S. Holbrook and L. Slater, “Multiscale geophysical imaging of the critical zone”, *Rev. Geophys.* **53**, 1–26 (2015).
- [244] J. Tromp, “Seismic wavefield imaging of Earth’s interior across scales”, *Nat. Rev. Earth Environ.* **1**, 40–53 (2020).
- [245] Z.-C. Li and Y.-M. Qu, “Research progress on seismic imaging technology”, *Petroleum Science* **19**, 128–146 (2022).
- [246] M. A. Flower, ed., *Webb’s Physics of Medical Imaging*, 2nd ed. (CRC Press, 2012).
- [247] J. Wallyn, N. Anton, S. Akram and T. F. Vandamme, “Biomedical Imaging: Principles, Technologies, Clinical Aspects, Contrast Agents, Limitations and Future Trends in Nanomedicines”, *Pharm. Res.* **36**, 78 (2019).
- [248] J. Kubby, S. Gigan and M. Cui, eds., *Wavefront Shaping for Biomedical Imaging* (Cambridge University Press, 2019).
- [249] S. Yoon *et al.*, “Deep optical imaging within complex scattering media”, *Nat. Rev. Phys.* **2**, 141–158 (2020).
- [250] W. Lambert, J. Robin, L. A. Cobus, M. Fink and A. Aubry, “Ultrasound Matrix Imaging—Part I: The Focused Reflection Matrix, the F-Factor and the Role of Multiple Scattering”, *IEEE Trans. Med. Imaging* **41**, 3907–3920 (2022).
- [251] W. Lambert, L. A. Cobus, J. Robin, M. Fink and A. Aubry, “Ultrasound Matrix Imaging—Part II: The Distortion Matrix for Aberration Correction Over Multiple Isoplanatic Patches”, *IEEE Trans. Med. Imaging* **41**, 3921–3938 (2022).
- [252] M. Minsky, *Microscopy apparatus*, US Patent 3013467 (1961).

-
- [253] T. Latychevskaia, “Lateral and axial resolution criteria in incoherent and coherent optics and holography, near- and far-field regimes”, *Appl. Opt.* **58**, 3597–3603 (2019).
- [254] S. L. Jacques, “Optical properties of biological tissues: a review”, *Phys. Med. Biol.* **58**, R37 (2013).
- [255] K. Mohanty, J. Blackwell, T. Egan and M. Muller, “Characterization of the Lung Parenchyma Using Ultrasound Multiple Scattering”, *Ultrasound Med. Biol.* **43**, 993–1003 (2017).
- [256] S. Kang *et al.*, “Imaging deep within a scattering medium using collective accumulation of single-scattered waves”, *Nat. Photonics* **9**, 253–258 (2015).
- [257] A. Badon *et al.*, “Smart optical coherence tomography for ultra-deep imaging through highly scattering media”, *Sci. Adv.* **2**, e1600370 (2016).
- [258] S. Kang *et al.*, “High-resolution adaptive optical imaging within thick scattering media using closed-loop accumulation of single scattering”, *Nat. Commun.* **8**, 2157 (2017).
- [259] A. Badon *et al.*, “Distortion matrix concept for deep optical imaging in scattering media”, *Sci. Adv.* **6**, eaay7170 (2020).
- [260] D. Furlinger, “Object-Adapted Imaging Using Scattering Invariant Modes”, unpublished, Bachelor Thesis (TU Wien, 2022).
- [261] P. Pai, J. Bosch, M. Kühmayer, S. Rotter and A. P. Mosk, “Scattering invariant modes of light in complex media”, *Nat. Photonics* **15**, 431–434 (2021).
- [262] R. Redheffer, “Inequalities for a Matrix Riccati Equation”, *J. Math. Mech.* **8**, 349–367 (1959).
- [263] R. C. Rumpf, “Improved Formulation of Scattering Matrices for Semi-Analytical Methods that is Consistent with Convention”, *Prog. Electromagn. Res. B* **35**, 241–261 (2011).
- [264] L. M. Rachbauer, “Inverse Scattering in One-dimensional Random Media Using Deep Learning”, Diploma Thesis (TU Wien, 2019).
- [265] Y. LeCun, Y. Bengio and G. Hinton, “Deep learning”, *Nature* **521**, 436–444 (2015).
- [266] I. Goodfellow, Y. Bengio and A. Courville, *Deep Learning* (MIT Press, 2016).
- [267] M. Mohri, A. Rostamizadeh and A. Talwalkar, *Foundations of Machine Learning*, 2nd ed. (MIT Press, 2018).
- [268] E. Stevens, L. Antiga and T. Viehmann, *Deep Learning with PyTorch* (Manning Publications, 2020).
- [269] M. Kubat, *An Introduction to Machine Learning*, 3rd ed. (Springer Nature Switzerland AG, 2021).

- [270] F. Chollet, *Deep Learning with Python*, 2nd ed. (Manning Publications, 2021).
- [271] G. Hackl, “Use of Machine Learning in 2D inverse Scattering”, unpublished, Project Thesis (TU Wien, 2020).
- [272] K. G. Makris, A. Brandstötter, P. Ambichl, Z. H. Musslimani and S. Rotter, “Wave propagation through disordered media without backscattering and intensity variations”, *Light Sci. Appl.* **6**, e17035–e17035 (2017).
- [273] E. Rivet *et al.*, “Constant-pressure sound waves in non-Hermitian disordered media”, *Nat. Phys.* **14**, 942–947 (2018).
- [274] F. Wagner, “Constant-Intensity Refractive Indices created with Deep Learning”, unpublished, Project Thesis (TU Wien, 2020).
- [275] J. Burkhart, “Missing Data Imputation and Prediction of Scattering Matrices using Machine Learning”, unpublished, Project Thesis (TU Wien, 2021).
- [276] I. T. Jolliffe and J. Cadima, “Principal component analysis: a review and recent developments”, *Philos. Trans. R. Soc. A* **374**, 20150202 (2016).
- [277] A. Hyvärinen and E. Oja, “Independent component analysis: algorithms and applications”, *Neural Netw.* **13**, 411–430 (2000).
- [278] M. Stein, A. Mezghani and J. A. Nossek, “A Lower Bound for the Fisher Information Measure”, *IEEE Signal Process. Lett.* **21**, 796–799 (2014).
- [279] I. Kanitscheider, R. Coen-Cagli, A. Kohn and A. Pouget, “Measuring Fisher Information Accurately in Correlated Neural Populations”, *PLOS Comput. Biol.* **11**, e1004218 (2015).
- [280] R. G. Jarrett, “Bounds and expansions for Fisher information when the moments are known”, *Biometrika* **71**, 101–113 (1984).
- [281] G. Huang, Z. Liu, L. Van Der Maaten and K. Q. Weinberger, “Densely Connected Convolutional Networks”, in *2017 IEEE Conference on Computer Vision and Pattern Recognition (CVPR)* (2017), pp. 2261–2269.
- [282] M. Weimar, “Fisher Information Flow in Neural Networks”, Diploma Thesis (TU Wien, 2022).
- [283] R. Zamir, “A proof of the Fisher information inequality via a data processing argument”, *IEEE Trans. Inf. Theory* **44**, 1246–1250 (1998).
- [284] R. F. Snider, “Perturbation Variation Methods for a Quantum Boltzmann Equation”, *J. Math. Phys.* **5**, 1580–1587 (1964).

List of Publications

1. D. Bouchet, L. M. Rachbauer, S. Rotter, A. P. Mosk and E. Bossy, “Optimal Control of Coherent Light Scattering for Binary Decision Problems”, *Phys. Rev. Lett.* **127**, 253902 (2021).
2. H. Hörner, L. M. Rachbauer, S. Rotter and U. Leonhardt, “Van der Waals chain: A simple model for Casimir forces in dielectrics”, *Phys. Rev. B* **108**, 235430 (2023).
3. L. M. Rachbauer, D. Bouchet, U. Leonhardt and S. Rotter, “Finding optimal quantum states for optical micromanipulation and metrology in scattering problems: tutorial”, submitted to *J. Opt. Soc. Am. B*.
4. J. Hüpfel, F. Russo, L. M. Rachbauer, D. Bouchet, J. Lu, U. Kuhl and S. Rotter, “Continuity Equation for the Flow of Fisher Information in Wave Scattering”, under review in *Nat. Phys.*, [arXiv:2309.00010](https://arxiv.org/abs/2309.00010).
5. I. Starshynov, M. Weimar, L. M. Rachbauer, G. Hackl, D. Faccio, S. Rotter and D. Bouchet, “Unveiling fundamental limits of deep neural networks: a Fisher information analysis in complex scattering systems”, in preparation.
6. M. Weimar, L. M. Rachbauer, D. Bouchet and S. Rotter, “Fisher information flow in artificial neural networks”, in preparation.
7. A. Le Ber, A. Goicoechea, L. M. Rachbauer, X. Jia, M. Fink, S. Rotter, A. Tourin and A. Aubry, “Matrix projection method for quantitative ultrasound imaging”, in preparation.
8. L. M. Rachbauer and S. Rotter, “Subunitary Quantum Metrology”, in preparation.

Curriculum Vitae

Personal Data

Name: Dipl.-Ing. Lukas Michael Rachbauer

Address:

Date of birth:

Place of birth:

Nationality:

Mobile number:

Email address:

Education

- since July 2019 **Doctoral programme in Engineering Sciences: Technical Physics**
TU Wien, Institute for Theoretical Physics
Advisor: Stefan Rotter
PhD thesis: Classical and Quantum Waves in Complex Environments
- 2016 – 2019 **Master of Science (Dipl.-Ing.) in Technical Physics**
TU Wien, Institute for Theoretical Physics
Graduation with distinction (19.06.2019)
Advisor: Stefan Rotter
Diploma thesis: Inverse Scattering in One-dimensional Random Media
Using Deep Learning
- 2014 – 2016 **Bachelor of Science in Technical Physics**
Johannes Kepler University Linz, Institute for Theoretical Physics
Graduation with distinction (04.03.2016)
Advisor: Robert Zillich
Bachelor thesis: Wave Packet Molecular Dynamics for Bosons
- 2012 – 2014 **Teacher Education Studies in Physics and Mathematics**
Johannes Kepler University Linz
Not completed
- 2007 – 2011 **High school (science branch)**
ORG Vöcklabruck
Graduation with distinction (16.06.2011)

Work Experience

- since July 2019 **Project assistant (FWF)**
TU Wien, Institute for Theoretical Physics
- March 2017 – July 2019 **Teaching assistant**
TU Wien, Institute for Theoretical Physics
Tutor in Quantum Mechanics I+II, Electrodynamics I+II and
Statistical Physics I+II
- Oct. 2014 – Jan. 2016 **Teaching assistant**
Johannes Kepler University Linz, Institute for Theoretical
Physics
Tutor in Theoretical Mechanics, Theoretical Quantum Mech-
anics and Theoretical Electrodynamics
- Nov. 2011 – July 2012 **Civilian service**
Lebenshilfe Oberösterreich, Werkstätte Regau
Support of disabled people in the wood workshop
- Aug. 2010 **Summer job**
Schloss Esterházy, Eisenstadt
Summer job in sales in the castle boutique

Scientific Contributions

- 2 scientific publications in peer-reviewed journals as well as 1 paper under review, 1 submitted tutorial and 4 manuscripts in preparation, see [List of Publications](#)
- 1 patented invention (my personal legal share is claimed in its entirety by TU Wien)
- 3 talks and 3 poster presentations at national and international conferences, seminar series and summer schools (Austria, Germany, France), see below

Conferences and Seminars

- 14 Nov. 2023 **Seminar series** “*Vienna Theory Lunch Seminar*”, Vienna, Austria
Invited talk “*Micromanipulation, Quantum Metrology and Vacuum Forces: A Unified Perspective Based on the Scattering Matrix*”
- 18–22 June 2023 **Conference** “*EGAS 54*”, Strasbourg, France
Poster presentation “*The Quantum Wigner-Smith Operator: Micro-
manipulation, Metrology and Vacuum Forces*”
- 28–31 March 2023 **Conference** “*Quantum Control of Light*”, Bad Honnef, Germany
Poster presentation “*The Quantum Wigner-Smith Operator: Micro-
manipulation, Metrology and Vacuum Forces*”
- 16 Nov. 2022 **Seminar series** “*Advances in Quantum Science and Quantum Tech-
nology*”, Vienna, Austria
Contributed talk “*The Quantum Wigner-Smith Operator: Micro-
manipulation, Metrology and Vacuum Forces*”

-
- 12–16 Sept. 2022 **Summer school** “*Waves in complex media: From spatial to temporal degrees of freedom*”, Cargèse, France
Poster presentation “*The Quantum Wigner-Smith Operator: Optimal Micromanipulation, Metrology and Vacuum Forces*”
- 30 May 2022 **Seminar series** “*VCQ Colloquium*”, Vienna, Austria
Contributed student talk “*Fisher Information for Optimal Sensing and Particle Manipulation*”
- 23–27 July 2018 **Summer school** “*DeepLearn 2018*”, Genoa, Italy

Awards and Additional Information

Merit scholarships (“Leistungsstipendien”) at Johannes Kepler University Linz (2013 and 2014) and TU Wien (2017)

Participation in the talents program (“Talente-Programm”): Practice of self-presentation in application situations and two days of visiting the company “Wiener Stadtwerke” (2019)

Membership in the “Vienna Center for Quantum Science and Technology” (VCQ) (2019 – 2023)

Programming Skills

Python: advanced
Deep Learning: advanced
Mathematica: advanced
GeoGebra: advanced
C/C++: basic knowledge
Matlab: basic knowledge
Fortran: basic knowledge

Languages

German: native speaker
English: fluent
Latin: basic knowledge

Interests and Abilities

Music: Playing the piano (advanced level), singing (choir, bass)
Podcasts: Politics, science, music, health topics, philosophy, true crime (with focus on the legal system, expert witnesses or historical events)
Sports: Strength training, hiking, running
Games: Board games, card games
Movies: Crime thriller, fantasy, science-fiction, documentary, comedy
Reading: Popular science, science-related thrillers, fantasy novels, biographies